

**CHARACTERIZATION OF AMBIENT GROUND-MOTION USING
SPECTRAL ANALYSIS TECHNIQUES - NUMERICAL MODELING,
DATA PROCESSING AND APPLICATION TO LOW-FREQUENCY
PASSIVE SEISMIC**

A dissertation submitted to
ETH ZURICH

for the degree of
Doctor of Sciences

presented by
MARC-ANDRÉ LAMBERT
Dipl. Natw. ETH Zurich

born 27th November 1976

citizen of
Vernier (GE)

Accepted on the recommendation of

Prof. Dr. Jean-Pierre Burg	ETH Zurich	examiner
Prof. Dr. Stefan M. Schmalholz	University of Lausanne	co-examiner
Prof. Dr. Serge Shapiro	Freie Universität Berlin	co-examiner
PD Dr. Erik H. Saenger	ETH Zurich	co-examiner

Essentially, all models are wrong, but some are useful.

George E.P. Box

Table of Contents

Abstract	ix
Zusammenfassung	xi
1. Introduction	1
1.1. Background	1
1.2. Research framework and related projects	3
1.3. Motivation	4
1.4. Thesis outline	5
References	6
2. Impact of surface layers on H/V spectra	9
2.1. INTRODUCTION	9
2.2. FIELD DATA	11
2.3. THEORY	13
2.3.1. Body wave interpretation	13
2.3.2. Surface wave interpretation	16
2.3.3. Discussion	17
2.4. NUMERICAL MODEL	18
2.5. CONCLUSIONS	21
References	24
3. Using spectral analysis for detecting wave-field modifications	27
3.1. INTRODUCTION	29
3.2. METHOD	31
3.2.1. Data generation	31
3.2.2. Data processing	32
3.3. EMBEDDED INHOMOGENEITY	33
3.4. EMBEDDED ZONES OF SEISMIC EMISSION	40
3.4.1. Two-dimensional models	41
3.4.2. Three-dimensional model	51
3.5. DISCUSSION	53

3.6. CONCLUSIONS	57
References	58
4. Low-frequency microtremor anomalies at an oil and gas field	63
4.1. INTRODUCTION	64
4.2. THE VOITSDORF SURVEY	65
4.2.1. Study site	65
4.2.2. Data acquisition	66
4.3. ANALYSIS OF SPECTRAL ATTRIBUTES	69
4.3.1. Data example	69
4.3.2. Spectral attributes	71
4.3.3. Attribute profiles	73
4.3.4. Spatial variability of the attribute profiles	73
4.3.5. Temporal variability of the attribute profiles	75
4.3.6. Characteristic profiles	75
4.4. DISCUSSION OF FIELD RESULTS	78
4.4.1. Reservoir location	78
4.4.2. Observations on individual attributes	79
4.5. NUMERICAL STUDY ON FREQUENCY PATTERNS	80
4.6. DISCUSSION ON THE ORIGIN OF THE SIGNALS	84
4.7. CONCLUSIONS	85
References	86
5. Noise reduction techniques and mapping inhomogeneity	91
5.1. INTRODUCTION	92
5.2. DATA	95
5.2.1. Anthropogenic noise	95
5.2.2. Features of interest	97
5.2.3. Spectral attributes	99
5.2.4. Spatial and temporal patterns of raw-data attributes	102
5.3. NOISE FILTERING	102
5.3.1. Single station techniques	103
5.3.2. Linear array techniques	111
5.4. DISCUSSION	114
5.5. CONCLUSIONS	120
References	122
6. Discussion	127
References	132

7. Conclusions	135
Appendices	137
A. Reply to comment	139
A.1. INTRODUCTION	139
A.2. RESPONSE TO SPECIFIC COMMENTS	140
A.2.1. Attributes 1 and 2	140
A.2.2. Attributes 3 and 4	140
A.2.3. The influence of shallow structures	141
A.2.4. The Voitsdorf site	143
A.2.5. Selection of applicable literature	143
A.2.6. The nature of 1-10 Hz microtremors	144
A.2.7. Our research organization and earlier work	144
A.3. CONTEXT FOR THE STUDY AND AIMS OF OUR RESEARCH	145
A.4. CONCLUSIONS AND OUTLOOK	146
References	147
B. Fourier transform	151
C. Frequency-shift pattern	153
C.1. OBSERVATION	153
C.2. EXPLANATION	154
C.2.1. Hypothesis 1: Numerical artefacts	154
C.2.2. Hypothesis 2: Effects of the free surface	156
C.2.3. Hypothesis 3: Near-field effects	156
C.2.4. Hypothesis 4: Variation of arrival-time differences	158
C.3. CONCLUSIONS	162
References	163
Acknowledgements	166
Curriculum Vitae	167

Abstract

The omnipresent ambient seismic wave-field at the Earth's surface is a superposition of waves generated by surface and subsurface seismic sources and it is permanently modified by the interaction with subsurface structures. Passive recordings of the ambient ground-motion therefore contain valuable information on underground structures and processes.

Travel-time based seismic methods are not directly applicable to extract such information because distinct events, such as earthquakes or hammer blows, are usually absent in the quasi-stationary ambient ground-motion. Instead, temporally stable wave-field patterns in frequency and space can be used to learn about the subsurface. Such spectral analysis methods have the potential to provide information on vertical inhomogeneities, such as horizontal reflectors (e.g. horizontal-to-vertical spectral ratio method). However, in this thesis emphasis is placed on wave-field modifications due to horizontal inhomogeneities with particular focus on characterizing spatial wave-field variations. Quantifying temporally stable characteristics is not an easy task because the data is often contaminated by transient noise originating from active sources at the surface. The applicability of standard noise filtering techniques (e.g. F-K filtering) is limited because of the small number of synchronized data points and the coarse spatial sampling that have been typical for passive seismic surveys. Furthermore, the surface wave-field is often strongly influenced by shallow structures, which can mask information from greater depth.

To address the above issues, spectral attributes are introduced and applied to quantify and map temporally stable spatial wave-field patterns along the surface. Numerical wave propagation simulations are used to examine different types of subsurface wave-field modification that can cause such patterns. The synthetic data is analyzed in order to explore potentials and limitations of the spectral analysis method. The methodology is also applied to real ambient ground-motion data recorded at an oil and gas field in Austria.

The horizontal location of subsurface wave-field modifications could be successfully detected in simple numerical models featuring a uniform medium and no active noise sources at the surface. Attribute patterns showed indication of the origin of both, active modification (zones of seismic emission) and passive modification (interaction with an inclusion of high attenuation). A realistic velocity distribution and surface noise sources considerably reduced the significance of the results. F-K filtering applied to linear array data successfully recovered information that was beforehand masked by surface noise. F-K filtering failed to suppress surface noise, on the other hand, in cases of inadequate array geometry. Spectral attributes were indicative

of a deep inclusion, despite the presence of a low-velocity surface layer with a strong influence on the wave-field characteristic. Measurements at an oil and gas field show temporally stable attribute patterns in space. Transient and stationary anthropogenic noise in the data could be reduced by applying single station and linear array processing techniques. The interpretation of the observed spatial patterns in terms of subsurface structures and processes showed no fully conclusive results. In particular, patterns collocated with the horizontal location of known hydrocarbon reservoirs could not be unambiguously linked to the presence of the reservoirs.

Spectral analysis is a suitable method to assess the ambient wave-field's characteristic in time, frequency and space. Attribute-based interpretation of temporally stable modifications in frequency and space can provide valuable subsurface information. To minimize possible anthropogenic noise contamination, data should be acquired in quiet areas and/or during the most quiet time periods (usually at night). In addition, large and densely spaced receiver arrays (e.g. regular grids) are recommended to allow effectively filter surface noise. The numerical results indicate that information on both, shallow and deep structures can be simultaneously present in the same data. The difficult task of distinguishing information in attribute profiles on the basis of its origin may be tackled using *a priori* information and statistical correlation methods.

Zusammenfassung

Das allgegenwärtige seismische Umgebungs-Wellenfeld an der Erdoberfläche ist eine Überlagerung von Wellen, welche an der Oberfläche und im Untergrund erzeugt werden, und das Wellenfeld wird permanent durch Interaktion mit Untergrundstrukturen modifiziert. Passive Aufzeichnungen der Umgebungs-Bodenbewegung beinhalten deshalb wertvolle Informationen über eine Vielzahl von Untergrundstrukturen und -prozessen.

Seismische Methoden basierend auf Laufzeiten sind nicht direkt anwendbar, um solche Informationen zu extrahieren, weil ausgeprägte Events, wie z.B. Erdbeben oder Hammerschläge, in der quasi-stationären Umgebungs-Bodenbewegung normalerweise nicht vorkommen. An Stelle dessen können zeitlich stabile Wellenfeld-Muster in Frequenz und Raum verwendet werden, um Informationen über den Untergrund in Erfahrung zu bringen. Solche spektrale Analysemethoden haben das Potenzial, Informationen über vertikale Inhomogenitäten, wie horizontale Reflektoren, zu liefern (z.B. horizontal-to-vertical spectral ratio Methode). In dieser Doktorarbeit sind jedoch hauptsächlich Wellenfeldmodifikationen aufgrund horizontaler Inhomogenitäten von Interesse, und der Schwerpunkt liegt daher auf der Charakterisierung von örtlichen Variationen im Wellenfeld. Die Quantifizierung von zeitlich stabilen Charakteristiken ist nicht einfach, weil die Daten oft durch Störungen kontaminiert sind, welche von aktiven Quellen an der Oberfläche herrühren. Die Verwendbarkeit von üblichen Filtertechniken um solche Störungen zu entfernen (z.B. F-K Filter) ist eingeschränkt, weil synchronisierte, passive seismische Messungen bisher typischerweise nur mit wenigen, weit auseinanderliegenden Messpunkte gemacht werden. Ausserdem ist das Wellenfeld an der Oberfläche oft stark von untiefen Strukturen beeinflusst, was Information aus grösserer Tiefe verdecken kann.

Um obigen Belangen Rechnung zu tragen werden spektrale Attribute eingeführt und verwendet um zeitlich stabile Wellenfeld-Muster entlang der Oberfläche zu quantifizieren und abzubilden. Numerische Wellenausbreitungs-Simulationen werden verwendet um unterschiedliche Typen von Wellenfeldmodifikationen im Untergrund, welche für solche Oberflächen-Muster verantwortlich sein können, zu untersuchen. Die synthetischen Daten werden analysiert um die Möglichkeiten und die Grenzen der spektralen Analysemethode zu erforschen. Zusätzlich wird die Methodik auch auf reelle Messungen der Bodenbewegung an einem Öl- und Gasfeld in Oesterreich angewendet.

Die horizontale Position von unterirdischen Wellenfeldmodifikationen konnte in einfachen numerischen Modellen mit gleichförmigem Untergrund und ohne aktive Noise-Quellen an der

Oberfläche erfolgreich detektiert werden. Attribut-Muster zeigten den Ursprung sowohl aktiver Modifikationen (Zonen seismischer Abstrahlung) als auch passiver Modifikationen (Interaktion mit einer Inklusion hoher Dämpfung) an. Eine realistische Geschwindigkeitsverteilung und Noise-Quellen an der Oberfläche reduzierten die Signifikanz der Ergebnisse beträchtlich. Durch Anwendung eines F-K Filters auf Daten eines linearen Arrays konnten Informationen, welche zunächst von Oberflächen-Noise überdeckt waren, zurückgewonnen werden. Der F-K Filter versagte hingegen im Falle von ungeeigneter Array-Geometrie. Spektrale Attribute zeigten die horizontale Position einer Inklusion in der Tiefe an, trotz zusätzlicher Anwesenheit einer Tiefgeschwindigkeitsschicht an der Oberfläche, welche das Wellenfeld stark beeinflusste. Messungen an einem Öl- und Gasfeld zeigen zeitlich stabile Attribut-Muster im Raum. Stationärer und instationärer anthropogener Noise in den Daten konnte durch Anwendung von Einzelstations- und Arraymethoden reduziert werden. Die Interpretation beobachteter, räumlicher Muster in Bezug auf unterirdische Strukturen und Prozesse ist nicht schlüssig. Muster, welche mit der horizontalen Position bekannter Kohlenwasserstoff-Reservoirs zusammenfallen, können insbesondere nicht endgültig mit der Anwesenheit der Reservoirs in Verbindung gebracht werden.

Die spektrale Analyse ist eine geeignete Methode, um die Charakteristik des Umgebungs-Wellenfeldes in der Zeit, in der Frequenz und im Raum zu beurteilen. Die Interpretation von zeitlich stabilen Modifikationen in Frequenz und Raum, basierend auf spektralen Attributen, kann wertvolle Informationen über den Untergrund liefern. Um eine mögliche Kontaminierung durch anthropogene Störungen zu minimieren, sollten Messungen nach Möglichkeit in lärmarmen Gebieten und/oder während den ruhigsten Zeiten (meistens in der Nacht) durchgeführt werden. Des Weiteren sind grosse Arrays mit geringen Stationsabständen zu empfehlen (z.B. reguläres Gitter), damit Oberflächen-Noise effizient herausgefiltert werden kann. Die numerischen Resultate zeigen, dass Information über oberflächennahe und tiefe Strukturen gleichzeitig in denselben Daten vorhanden sein können. Die schwierige Aufgabe, solche Informationen in Attribut-Profilen voneinander zu unterscheiden, kann durch *a priori* Information und statistische Korrelationsmethoden in Angriff genommen werden.

1. Introduction

Foreword. This thesis analyzes ambient ground-motion measured at the Earth's surface for identifying underground structures and processes. It explores the potential and limitations of spectral analysis techniques in extracting information on seismic wave-field modifications that occur in the subsurface. In particular, possible effects related to the presence of hydrocarbon reservoirs are investigated. The study is relevant for research and application in the field of low-frequency passive seismic. This introduction gives a general overview of the background of the study. It explains the context and motivation and provides a short outline of the thesis.

1.1 Background

One of the main goals in geophysics is to investigate properties of structures and processes in the Earth's subsurface. This includes for example observation of tectonic plate motion, studying earthquakes and volcanic tremor, exploration of potential hydrocarbon reservoirs and mineral deposits, estimating the thicknesses of soils and aquifers and delineating landfills and voids. For such purposes, seismic methods are among the most successful ones because seismic waves are sensitive to physical properties of the material they propagate through. As a consequence, they carry information on characteristics, location, depth and size of underground structures. For most applications, seismic waves are generated with controlled sources, such as explosives, sledgehammers or seismic vibrators. However, some methods do not use active sources but instead "listen" to naturally occurring signals or artificial seismic background noise (passive seismic methods). Passive seismic signals can either be transient (e.g. earthquakes, microseismicity) or quasi-stationary. The latter includes, among others:

- (i) Omnipresent natural background noise, e.g. the oceanic microseism ([Cessaro, 1994](#), and references therein),
- (ii) Artificial (e.g. urban) background noise, also termed as microtremor ([Bonney-Claudet et al., 2006](#), and references therein),
- (iii) Volcanic tremor (e.g. [Chouet, 1996](#)),
- (iv) Non-volcanic tremor (e.g. [Obara, 2002](#)).

In this thesis the terms *ambient wave-field* and *ambient ground-motion* are used to refer to a wave-field that can contain a superposition of the above quasi-stationary signals.

As pointed out in a recent review paper by [Bonnetfoy-Claudet et al. \(2006\)](#), it was realized more than 60 years ago that the usually weak, but omnipresent ambient ground-motion is more than just noise and can be useful for geophysical applications. However, due to the availability of digital recording systems and the development of digital signal processing, analysis of ambient seismic signals became popular only after 1970. It was then applied to a variety of problems in seismology and in exploration and engineering geophysics. Nowadays, such methods are routinely applied, also because of the relatively easy acquisition of large-quantity, high-quality passive data-sets.

Conventional time-domain methods, such as travel-time inversion, can not be applied straightforward to ambient ground-motion data because distinct events in the time traces are absent and the signal-to-noise ratio (S/N-ratio) is usually low. Therefore, most passive methods either use correlation-based (“interferometry”) or spectral (“spectroscopy”) analysis techniques. Correlation-based techniques attempt to retrieve the Green’s function between receivers from the quasi-stationary signal ([Clearbout, 1968](#); [Schuster, 2009](#)), which can be used to reconstruct travel-times of seismic phases. For example, [Brown et al. \(2009\)](#) applies waveform cross-correlation to non-volcanic tremor to measure relative arrival times of P- and S-waves and then performed a travel-time inversion to locate the origin of deep low-frequency earthquakes. [Shapiro et al. \(2005\)](#) performed surface-wave tomography with cross-correlations of low-frequency passive data to determine seismic velocities down to depths of more than 20 km. [Draganov et al. \(2007\)](#) used cross-correlations of passive seismic recordings at frequencies between 2 and 10 Hz to retrieve P-wave reflections with travel-times as great as 2 seconds.

Spectral analysis techniques, on the other hand, consider the signals’ amplitude distribution in the Fourier domain. For example, the horizontal-to-vertical (H/V) spectral ratio technique was introduced for estimating earthquake amplification factors from ambient ground-motion in areas with little seismicity (see [Bard, 1999](#), and references therein). Peaks in H/V spectral ratio curves are also used to map the sediment-bedrock interface down to depths of more than 1000 m ([Parolai et al., 2002](#)). More advanced array methods, such as the frequency-wavenumber analysis, were developed to invert for the vertical S-wave velocity profile of horizontally layered structures ([Okada, 2003](#), and references therein). Horizontal inhomogeneity can be analyzed by studying lateral variations of the wave-field in the frequency domain. [Nasseri-Moghaddam et al. \(2007\)](#), for example, analyzed spatial patterns of frequency domain parameters derived from ambient ground-motion recordings to detect the location of an underground cavity that acts as a Rayleigh wave scatterer.

All these applications show that ambient ground-motion can be a useful source of information for a variety of subsurface structures and processes. Similar spectral analysis techniques

as above have recently been suggested in several independent studies as being useful for the detection of hydrocarbon reservoirs (e.g., [Dangel et al., 2003](#); [van Mastrigt & Al-Dulaijan, 2008](#); [Artman et al., 2010](#)). These empirical studies have reported an apparent correlation between spectral patterns in low-frequency (<10 Hz) passive ground-motion recordings at the Earth's surface and the lateral location of the reservoirs. Therefore, it is speculated that the observed patterns may indeed be related to the presence of subsurface reservoirs and, as a consequence, could be used for reservoir detection.

The physical justification of using spectral analysis for reservoir detection is based on the assumptions that reservoirs can have different seismic properties (e.g., impedance, velocity, attenuation) than the surrounding rocks and that physical processes can occur in reservoirs (e.g., microseismicity, fluid flow, fluid oscillation) that occur with different intensity than in the surrounding rocks. The presence of reservoirs can, therefore, modify the ambient seismic wave-field and these modifications may be detectable in passive ground-motion measurements at the Earth's surface. However, analysis of low-frequency ambient ground-motion for hydrocarbon exploration (in the following termed *low-frequency passive seismic*) is a recent field of research. At the current stage, it is based on empirical observations and can only be treated using statistical interpretation methods. A suitable approach is applying methods that are already used for quantitative interpretation of conventional seismic data. An extensive description of such methods is given in [Avseth et al. \(2005\)](#). A first attempt of using statistical methods to compute hydrocarbon probability maps from passive seismic data has been presented in [Riahi et al. \(2009\)](#).

1.2 Research framework and related projects

This dissertation is completed within the framework of a project supported by the Swiss Commission for Technology and Innovation (CTI). CTI promotes knowledge and technology transfer between companies and universities, in this case between Spectraseis and ETH Zurich, by bringing them together as partners on applied research and development projects. The title of the project is "Determination of site-specific topographic, geological, and noise effects for the improvement of oil and gas detection based on hydrocarbon microtremor analysis" and included two doctoral theses. It is the second of a series of four CTI-projects focusing on aspects of low-frequency passive seismic. The topics of the other projects cover numerical methods, wave-field decomposition using large field arrays, and low frequency attenuation laboratory measurements.

Another related project is the Low-Frequency-Seismic-Partnership (LFSP), a joint industry project for research and development of low-frequency seismic technologies for application to hydrocarbon reservoir detection and characterization. This project was formed 1 September 2009 and is currently supported by six oil and gas operating companies. The scope of this program covers application elements of low-frequency seismic technologies, such as data acquisition and

processing, as well as fundamental theoretical studies, in partnership with researchers at Spectraseis, ETH Zurich and the University of Bern. The project will run for three years. Results of this thesis provide potentially useful contributions to the LFSP. In particular the findings on noise filtering, grid geometries and low-frequency spectral attributes will be applicable.

1.3 Motivation

Technological improvements, such as portable 3-component seismometers, digital recording systems, large data storage capacities and digital signal processing, considerably increased the available quantity and quality of passive seismic data in the last few decades. At the same time, many new applications have been developed and demonstrated that the ambient wave-field is much more than just seismic noise. However, extracting and interpreting useful information by analyzing low-frequency passive measurements is still not an easy task because distinct events in the time traces are usually absent in ambient ground-motion recordings and the signal-to-noise ratio is low. Furthermore, the surface wave-field is often strongly influenced by shallow structures, which is a problem when looking for signals originating from depth. To address these issues, a methodology is developed and evaluated in this thesis that allows quantifying spatial and temporal variation of the ambient wave-field. The methodology uses spectral attributes to quantify and map spectral characteristics of the wave-field in space and time. Lateral variation of temporally stable, i.e. quasi-stationary, characteristics can be indicative of subsurface inhomogeneities. However, lateral variation of spectral attributes can also be caused by lateral variation of local surface noise sources. Therefore, processing techniques are developed for reducing the effects of anthropogenic noise on passive seismic signals. The techniques are designed to take into account the small number of synchronized data points and the coarse spatial sampling that have been typical for low-frequency passive seismic surveys.

A specific motivation for this thesis is the lack of a sufficient number of wave propagation studies for evaluating the applicability of low-frequency passive seismic for hydrocarbon reservoir exploration. Spectral analysis of ambient ground-motion for such purposes is a novel technique. Its capabilities and the possibly underlying physical mechanisms are a current field of research. This study presents a series of numerical wave propagation simulations to investigate how and under what conditions subsurface quasi-stationary wave-field modifications can be detected at the surface. These simulations of standard seismic wave propagation provide a theoretical basis to discuss both, potential physical mechanisms and the applicability of spectral analysis for improving reservoir detection. Together with the proposed spectral analysis methodology, these numerical results may contribute towards a better understanding of observed low-frequency spectral anomalies above oil and gas fields.

1.4 Thesis outline

The thesis consists of this general introduction (**Chapter 1**), followed by four chapters that contain the main work of this study. At the end, there is a general discussion and a conclusions section, followed by the appendices. The chapters 3, 4, 5 and appendix A are written as individual paper manuscripts to be published in peer-reviewed scientific journals. The structure of those chapters therefore may include an individual abstract, introduction and conclusion.

Chapter 2 explores the impact of a low-velocity surface layer on H/V spectral ratios of ambient ground-motion. A surface layer on top of stiffer rocks is an important scenario because it is one of the most common shallow structures in nature and can have a strong influence on the characteristic of the surface wave-field. A field data example is presented and observed H/V-peaks are matched with known low-velocity layers. Data processing steps to obtain average H/V ratios from continuous measurements are explained. The theoretical background of H/V amplification is briefly reviewed and a numerical study is presented that models the phenomenon. Also, the question to what extent H/V spectral ratio curves are useful to estimate resonance frequencies and amplification factors of measurement sites is discussed.

Chapter 3 presents a synthetic study for evaluating the applicability of spectral analysis techniques to detect the origin of subsurface wave-field modifications. A methodology is introduced that uses three independent spectral attributes to quantify lateral variations in the quasi-stationary wave-field. Two types of wave-field modification are considered: (i) models with an embedded inclusion of high attenuation and sources below the inclusion (passive modification) and (ii) models with embedded zones of seismic emission (active modification). Additional complexity, such as shallow structures, realistic subsurface properties and surface noise, are introduced to explore some of the limitations of the approach. F-K filtering is applied to enhance the S/N-ratio and to retrieve signatures in attribute profiles that are otherwise overwhelmed by noise.

Chapter 4 reports the findings of a low-frequency passive seismic survey in 2007 at an oil and gas field in Voitsdorf, Austria. Four spectral attributes that quantify properties of the wave-field are introduced and the algorithm to compute the attribute values from ambient ground-motion recordings is provided. The temporal and spatial variation of the attribute values is examined to assess their significance for quantifying spatial variations of the wave-field at the surface. A physical justification for using the attributes as indicators for subsurface processes is provided by means of numerical modeling.

Chapter 5 presents data from a more recent survey at the Voitsdorf oil and gas field in 2008. The focus of this chapter is on noise reduction techniques and on a more advanced methodology for mapping horizontal inhomogeneity. Three surface noise types of anthropogenic origin were identified in the ambient ground-motion recordings: (i) local transient noise, (ii) stationary narrow-band noise and (iii) correlated transient noise. Four noise reduction techniques are

presented to remove these types of noise. Two of the techniques are applicable to recordings of single stations. The other two techniques are two-dimensional filters which are applicable to attribute sections derived from linear arrays.

The general discussion in **Chapter 6** highlights some of the critical aspects of spectral analysis techniques and addresses the question whether low-frequency passive seismic can be potentially useful for exploration purposes. **Chapter 7** summarizes the main conclusions of this thesis.

Appendix A is a reply to a comment on the paper presented in Chapter 4 (Lambert et al., 2009). The reply responds to specific comments in Green & Greenhalgh (2010) and a short explanation of the context and the general aims of the study presented in Lambert et al. (2009) is provided. **Appendix B** describes the Fourier transform used in this thesis to compute frequency spectra. In particular, the scaling of the transform and the units in the Fourier domain are described. Finally, **Appendix C** provides the explanation for the frequency-shift pattern observed in the synthetic data in Chapter 4.

Additional work that is part of this dissertation was published in Saenger et al. (2009).

References

- Artman, B., Goertz, A., Schechinger, B., Krajewski, P. & Koerbe, M. (2010). *Joint interpretation of multiple passive seismic data volumes*. 72th EAGE meeting, Barcelona, Spain, Expanded Abstracts, p. F009.
- Avseth, P., Mukerji, T. & Mavko, G. (2005). *Quantitative Seismic Interpretation – Applying Rock Physics Tools to Reduce Interpretation Risk*. Cambridge University Press. ISBN 0521816017.
- Bard, P.-Y. (1999). *Microtremor measurements: A tool for site effect estimation?* In: The Effects of Surface Geology on Seismic Motion (eds K. Irikura, K. Kudo, K. Okada and T. Sasatami) [Balkema, Rotterdam, The Netherlands.], pp. 1251–1279.
- Bonnefoy-Claudet, S., Cotton, F. & Bard, P. (2006). *The nature of noise wavefield and its applications for site effects studies: A literature review*. Earth-Science Reviews, **79**, 205–227.
- Brown, J. R., Beroza, G. C., Ide, S., Ohta, K., Shelly, D. R., Schwartz, S. Y., Rabbel, W., Thorwart, M. & Kao, H. (2009). *Deep low-frequency earthquakes in tremor localize to the plate interface in multiple subduction zones*. Geophysical Research Letters, **36**, L19306.

- Cessaro, R. K. (1994). *Sources of Primary and Secondary Microseisms*. Bull. Seism. Soc. Am., **84**(1), 142–148.
- Chouet, B. (1996). *Long-period volcano seismicity: Its source and use in eruption forecasting*. Nature, **380**, 309–315.
- Clearbout, J. (1968). *Synthesis of a layered medium from its acoustic transmission response*. Geophysics, **33**, 264–269.
- Dangel, S., Shaepman, M. E., Stoll, E. P., Carniel, R., Barzandji, O., Rode, E.-D. & Singer, J. M. (2003). *Phenomenology of tremor-like signals observed over hydrocarbon reservoirs*. J. Volcanol. Geothermal Res., **128**, 135–158.
- Draganov, D., Wapenaar, K., Mulder, W., Singer, J. & Verdel, A. (2007). *Retrieval of reflections from seismic background-noise measurements*. Geophysical Research Letters, **34**, L04305.
- Green, A. & Greenhalgh, S. (2010). *Comment on "Low-frequency microtremor anomalies at an oil and gas field in Voitsdorf, Austria" by Marc-André Lambert, Stefan Schmalholz, Erik H. Saenger and Brian Steiner, Geophysical Prospecting 57, 393–411*. Geophysical Prospecting, **58**, 335–339.
- Lambert, M.-A., Schmalholz, S. M., Saenger, E. H. & Steiner, B. (2009). *Low-frequency microtremor anomalies at an oil and gas field in Voitsdorf, Austria*. Geophysical Prospecting, **57**, 393–411. doi:10.1111/j.1365-2478.2008.00734.x.
- van Mastrigt, P. & Al-Dulaijan, A. (2008). *Seismic spectroscopy using amplified 3C geophones*. Paper presented at the 70th EAGE Conference & Exhibition, Rome, Italy, Expanded Abstracts, p. B047.
- Nasseri-Moghaddam, A., Cascante, G., Phillips, C. & Hutchinson, D. (2007). *Effects of underground cavities on Rayleigh waves - Field and numerical experiments*. Soil Dynamics and Earthquake Engineering, **27**, 300–313.
- Obara, K. (2002). *Nonvolcanic Deep Tremor Associated with Subduction in Southwest Japan*. Science, **196**, 1679–1681.
- Okada, H. (2003). *The Microtremor Survey Method*. Geophysical Monograph Series No. 12, SEG, Tulsa, USA. ISBN 1-56080-120-4.
- Parolai, S., Bormann, P. & Milkereit, C. (2002). *New Relationship between V_S , Thickness of Sediments, and Resonance Frequency Calculated by the H/V Ratio of Seismic Noise for the Cologne Area (Germany)*. Bull. Seism. Soc. Am., **92**, 2521–2527.

- Riahi, N., Kelly, M., Ruiz, M. & Yang, W. (2009). *Bayesian DHI using passive seismic low frequency data*. Paper presented at the 79th SEG International Conference & Exhibition, Houston, USA, Expanded Abstracts, p. 1607–1611.
- Saenger, E. H., Schmalholz, S. M., Lambert, M.-A., Nguyen, T. T., Torres, A., Metzger, S., Habiger, R., Müller, T., Rentsch, S. & Mendez-Hernández, E. (2009). *A passive seismic survey over a gas field: Analysis of low-frequency anomalies*. *Geophysics*, **74**, O29–O40.
- Schuster, G. T. (2009). *Seismic Interferometry*. Cambridge University Press, New York, USA. ISBN 978-0-521-87124-2.
- Shapiro, N. M., Campillo, M., Stehly, L. & Ritzwoller, M. H. (2005). *High-Resolution Surface-Wave Tomography from Ambient Seismic Noise*. *Science*, **307**, 1615–1618.

2. Impact of surface layers on horizontal-to-vertical spectral ratios of ambient ground-motion - field observations, theory and numerical results

2.1 INTRODUCTION

Underground inhomogeneities can have a strong impact on the characteristics of the ambient seismic wave-field at the Earth's surface. Passive measurements of ambient ground-motion at the surface can therefore provide information on inhomogeneities in the subsurface. This is for example exploited to locate underground cavities (Nasseri-Moghaddam et al., 2007), map the sediment-bedrock interface (Parolai et al., 2002) or estimate continuous S-wave velocity depth-profiles in the case of a horizontally layered subsurface (Fäh et al., 2001; Okada, 2003, and references therein). A very common near-surface inhomogeneity in nature is a low-velocity layer on top of stiffer rocks with higher seismic velocities, as shown in the simplified sketch in Figure 2.1. Many empirical studies have found that such low-velocity layers cause characteristic modifications in the average horizontal-to-vertical spectral ratio (H/V-ratio) of the continuous ambient wave-field (Bonney-Claudet et al., 2006, and references therein). The main observation is a peak in the H/V-ratio curve at frequency f_p , which approximately corresponds to the fundamental S-wave resonance frequency f_{S0} of the surface layer, i.e.

$$f_p \approx f_{S0}. \quad (2.1)$$

The fundamental S-wave resonance frequency of the surface layer for vertically incident S-waves is defined by the first maximum of the S-wave transfer function. The transfer function is given as (e.g., Aki & Richards, 2002)

$$A(f) = \frac{2}{\sqrt{\cos^2\left(\frac{2\pi f h}{\beta_1}\right) + \left(\frac{\rho_1 \beta_1}{\rho_2 \beta_2}\right)^2 \sin^2\left(\frac{2\pi f h}{\beta_1}\right)}}, \quad (2.2)$$

where β_1 , ρ_1 and h denote the S-wave velocity, the mass density and the thickness of the surface layer and β_2 and ρ_2 are the S-wave velocity and the mass density of the underlying

half-space, respectively. Figure 2.2 shows an example of the S-wave transfer function. The S-wave resonance frequencies of the surface layer (maxima of the transfer function) are given by

$$f_{S_n} = (2n + 1) \frac{\beta_1}{4h}. \quad (2.3)$$

The amplitudes of the maxima are controlled by the impedance contrast between surface layer and half-space:

$$A_{S_n} = 2 \frac{Z_2}{Z_1} = 2 \frac{\rho_2 \beta_2}{\rho_1 \beta_1}, \quad (2.4)$$

where Z_1 and Z_2 are the S-wave impedances of half-space and surface layer, respectively, i.e. the product of mass density ρ and S-wave velocity β of the corresponding media. For $n = 0$, equation (2.3) yields the fundamental S-wave resonance frequency

$$f_{S_0} = \beta_1/4h. \quad (2.5)$$

Equation (2.5) is also known as the ‘quarter wavelength rule’ (Pujol, 2003) because it shows that the thickness of the layer h equals a quarter of the fundamental S-wave resonance wavelength. From (2.1) and (2.5) it follows

$$f_p \approx \frac{\beta_1}{4h}. \quad (2.6)$$

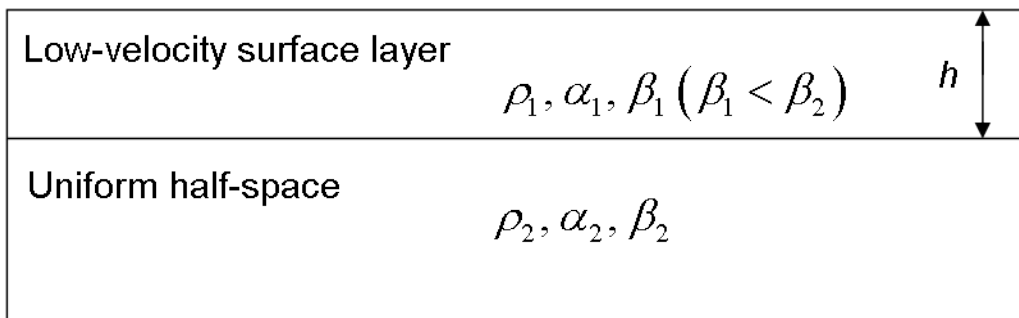


Figure 2.1. Sketch of a low-velocity layer with thickness h on top of a uniform half-space with larger seismic velocities.

In practice, this means that estimating the peak-frequency f_p in the measured H/V-ratio curve can provide not only information on the fundamental S-wave resonance frequency of the site but also on physical properties of the subsurface. The two examples in Table 2.1 show that H/V-peaks in nature can occur in a broad range of seismic frequencies. There are two fun-

damentally different interpretations of the H/V-peak, the body wave and the surface wave interpretation, respectively. As it will be discussed later, both interpretations are able to explain the observed H/V-peaks in ambient ground-motion recordings but are based on different assumptions concerning the composition of the natural wave-field. Characteristics in ambient ground-motion recordings, such as H/V-peaks caused by surface layers, may mask or be misinterpreted as information on other subsurface inhomogeneities that are of interest (e.g. cavities, hydrocarbon reservoirs, CO₂ storage). It is therefore important to be aware of possible surface layer effects when analyzing passive seismic data. In this chapter, a field data example is presented, for which H/V-peaks can be matched with known low-velocity layers. Then, the theoretical background of the phenomenon is briefly reviewed. Finally, numerical results from a two-dimensional (2D) elastic wave propagation model are presented which exhibit the characteristic surface layer effects.

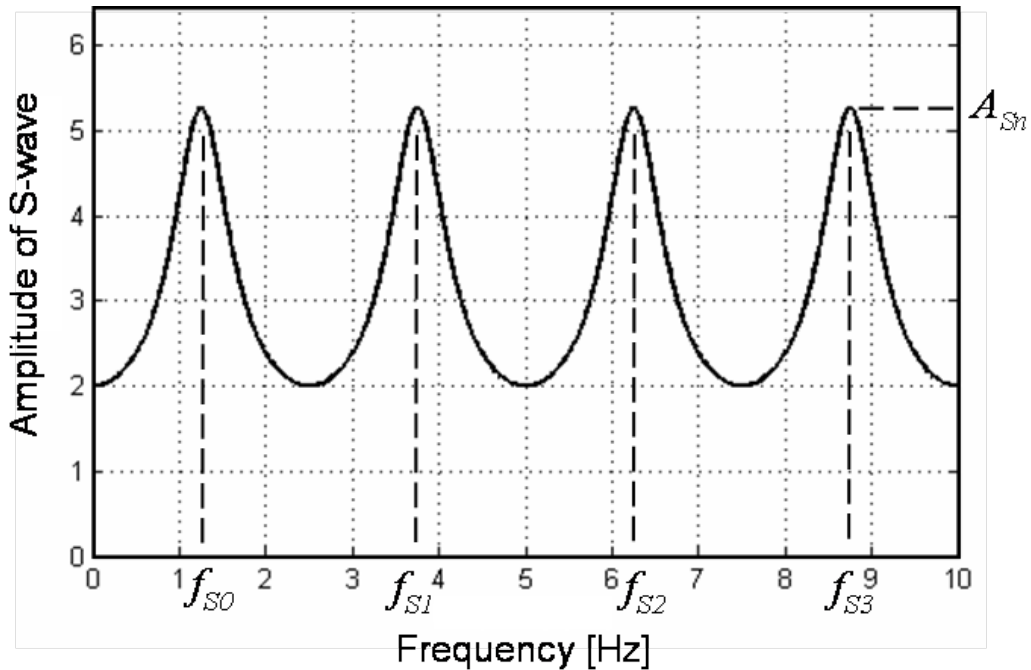


Figure 2.2. Example of the transfer function for a vertically incident S-wave in the case of a low-velocity layer on top of an infinite half-space, as shown in Figure 2.1. Peaks occur at the fundamental S-wave resonance frequency of the layer f_{S0} and its overtones. Parameters are: $\beta_1 = 250$ m/s, $h = 50$ m, $Z_2/Z_1 = 2.6$.

2.2 FIELD DATA

A data example from a low-frequency passive seismic survey conducted in December 2005 at the Voitsdorf oil and gas field in Austria is considered. The vertical S-wave velocity profile

Feature	β_1 [m/s]	h [m]	f_p [Hz]
Soil layer	500	5	25
Sedimentary basin	2000	1000	0.5

Table 2.1. *Example of values for f_p in nature.*

of the measurement site is known from passive array analysis as shown in Figure 2.3a (after Stamm & Fäh, 2006). This profile has been determined applying the frequency-wavenumber analysis described by Okada (2003). The blue lines depict several possible velocity profiles that explain the observed seismic array data with acceptable accuracy and their fluctuation provide information on the uncertainty of the estimated velocities. The red line shows an average of the ensemble of all possible distributions. The red arrows indicate two large velocity discontinuities. The first discontinuity occurs at a depth of only 5 m, where the S-wave velocity increases from 200 m/s to 900 m/s, approximately. The other main discontinuity is at a depth of about 220 m, where the velocity jumps from 1000 m/s to 2900 m/s. The discontinuities define therefore two surface layers with low seismic velocity and thicknesses of approximately 5 m (‘soil layer’) and 220 m (‘low-velocity layer’), respectively. Using the quarter wavelength rule (equation 2.5) and accounting for the uncertainty of the velocity profile in Figure 2.3a, a range for the fundamental S-wave resonance frequency for each of the two surface layers can be determined. These ranges are indicated as shaded areas in Figure 2.3b.

The average H/V spectral ratio curve of ambient ground-motion measured at this site is shown in Figure 2.3b (bold line). The data was recorded with a single three-component seismometer at the centre of the array that was used to determine the S-wave profile shown in Figure 2.3a. A variety of techniques have been proposed in the literature to compute the average H/V-ratio from continuous recordings of ambient ground-motion. Figure 2.4 provides a selection of suggested processing steps together with the corresponding authors. The grey boxes indicate the workflow chosen for this study. The thin lines in Figure 2.3b show the ± 1 standard deviation range derived from the spectral averaging (last step in Figure 2.4). Two main peaks are observed in the H/V-ratio curve, around 1 Hz and 8.5 Hz, respectively. These frequencies are in good agreement with the two ranges for the S-wave amplification frequency, estimated from the velocity profile in Figure 2.3a. The match between the peak-frequencies and the fundamental S-wave resonance frequencies of the surface layers is consistent with the observations of a large number of other ambient ground-motion studies (Bonnetfoy-Claudet et al., 2006, and references therein) and suggests that the measured peaks are indeed related to the presence of the two major velocity discontinuities. The magnitudes of the H/V-peaks seem to be related to the impedance contrast between surface layer and underlying rocks. The magnitude of the soil layer peak at 8.5 Hz is 1.5 times larger than the peak at 1 Hz. Interestingly, the impedance

contrast for the soil layer is also approximately 1.5 times larger than for the discontinuity in 220 m depth. However, these are rough estimates based on seismic velocity changes only because the density distribution is not known.

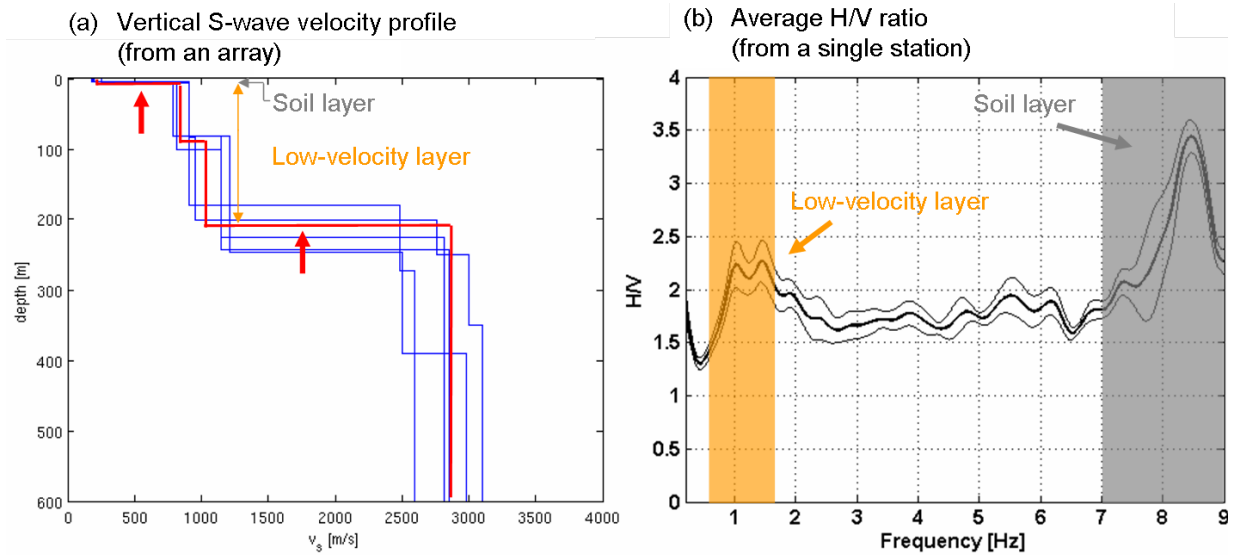


Figure 2.3. (a) Vertical S-wave velocity profile at a site in Austria, derived from passive seismic array data (after Stamm & Fäh, 2006). Blue profiles are different possible solutions that explain the measured data. The red line is an average profile. The red arrows highlight two main velocity discontinuities. (b) Average H/V-ratio curve, measured at the same site as the velocity profile in (a). The peaks around 1 Hz and 8.5 Hz match well with the frequency ranges of S-wave amplification estimated from the subsurface velocity structure in (a).

2.3 THEORY

2.3.1. Body wave interpretation

Nakamura (1989) interpreted the observed peaks in the H/V-ratio curves as an S-wave resonance effect in a surface layer. He claimed that the H/V-ratio curves would approximate the S-wave transfer function of the measurement site, and therefore could directly be used to estimate site amplification factors for earthquake S-waves. The following is a summary of the concept introduced by Nakamura (1989). Figure 2.5 shows a sketch of a horizontal surface layer over a uniform half-space and quantities that are needed to explain Nakamura's concept:

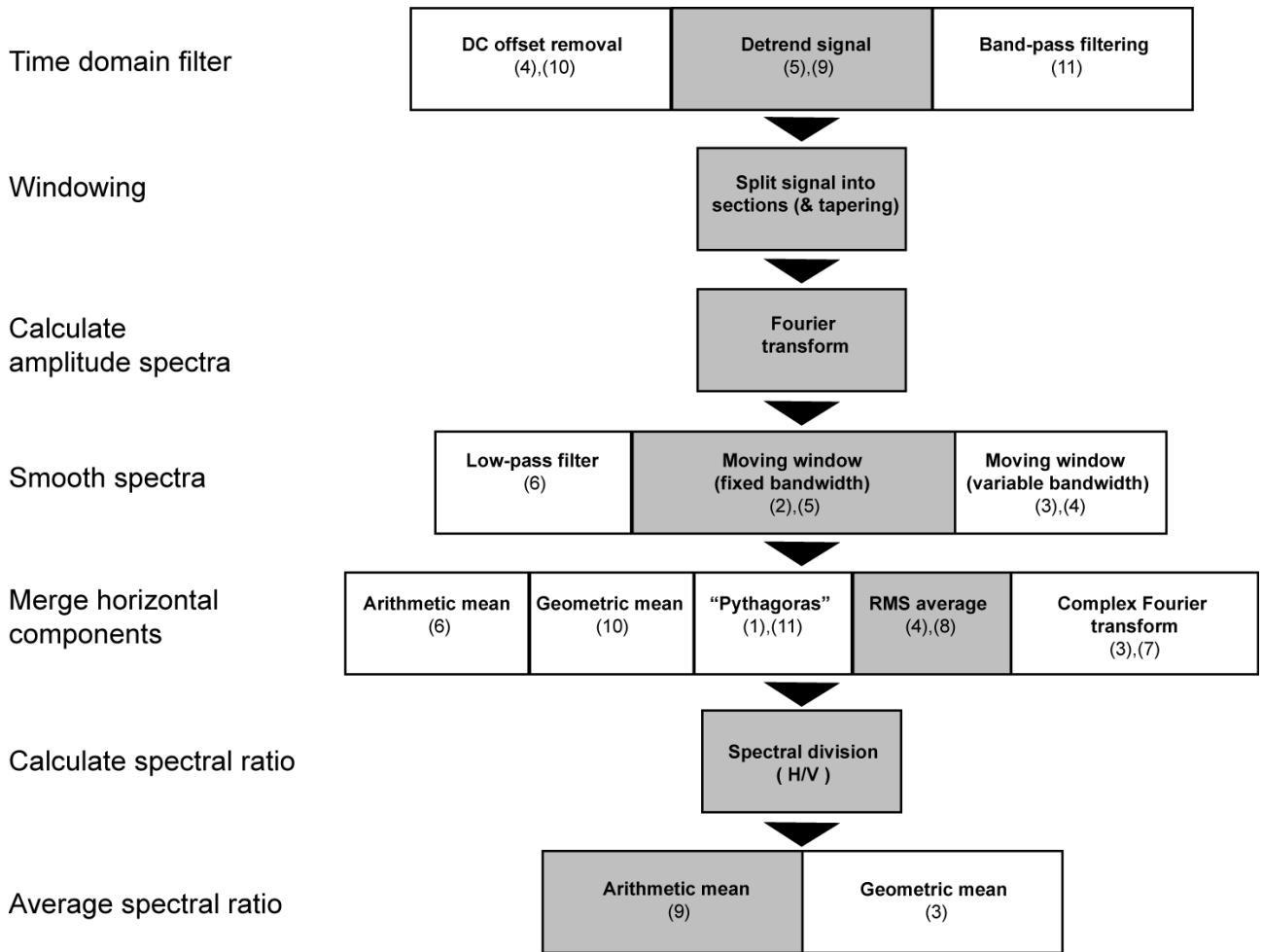


Figure 2.4. Data processing flow-chart to compute average H/V spectral ratios. Different authors have proposed slightly different approaches. The gray boxes denote the steps applied in this study. Numbers correspond to references: (1) Al Yuncha et al. (2004); (2) Almendros et al. (2004); (3) Bard (1999); (4) Bour et al. (1998); (5) Frischknecht et al. (2005); (6) Ibs-von Seht & Wohlenberg (1999); (7) Maresca et al. (2003); (8) Moya et al. (2000); (9) Parolai et al. (2004); (10) SESAME (2004); (11) Teves-Costa et al. (1996).

$H_s(f)$ Amplitude spectrum of the horizontal component of ground-motion at the surface

$H_b(f)$ Amplitude spectrum of the horizontal component of ground-motion at the base of the surface layer

$V_s(f)$ Amplitude spectrum of the vertical component of ground-motion at the surface

$V_b(f)$ Amplitude spectrum of the vertical component of ground-motion at the base of the surface layer

β_1, β_2 S-wave velocity of the surface layer and half-space, respectively

ρ_1, ρ_2 Mass density of the surface layer and half-space, respectively

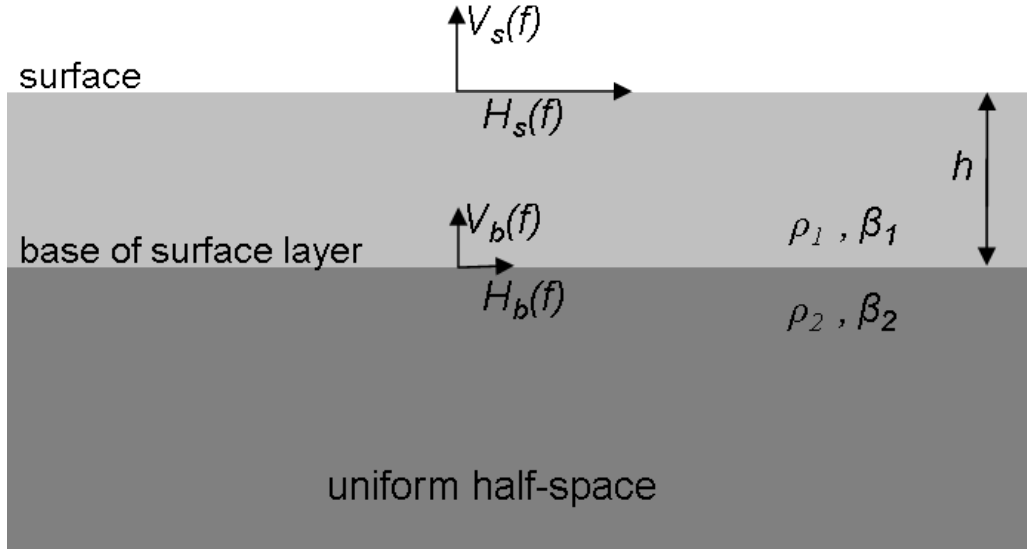


Figure 2.5. *Ground-motion at the surface and at the base of a surface layer.*

Nakamura's interpretation is based on the idea that influences from surface waves can be eliminated and requires the following four assumptions concerning the ambient seismic wave-field:

- (a) The ambient wave-field is a combination of body waves and Rayleigh waves propagating in a surface layer over a uniform half-space. The surface layer has lower seismic velocities than the underlying half-space ($\beta_2 > \beta_1$).
- (b) The difference between the amplitude of the vertical component of motion at the surface and at the base, $V_s(f)$ and $V_b(f)$, is exclusively related to the depth dependency of the Rayleigh wave amplitude. There is no change in amplitude of the vertical component due other effects, such as for example P-wave resonance in the surface layer.
- (c) The depth dependency of Rayleigh wave amplitudes is equal for the vertical and horizontal components of motion.
- (d) The amplitudes of the horizontal and vertical component of motion at the base of the layer, $H_b(f)$ and $V_b(f)$, are equal for ambient ground-motion.

Assumption (d) is also called "Nakamura's hypothesis".

In the case of incident S-waves, e.g. from an earthquake (EQ), the S-wave transfer function (amplification versus frequency) for the surface layer is defined as

$$T_{EQ}(f) = \frac{H_s(f)}{H_b(f)}. \quad (2.7)$$

This is only correct because the wave-field is dominated by S-waves and thus surface wave amplitudes can be neglected. In the case of ambient ground-motion, however, surface waves

are significant and their contribution to the total wave-field can not be neglected. Therefore, $T_{EQ}(f)$ must be corrected for Rayleigh wave motion in order to extract the S-wave transfer function from the ambient wave-field. According to assumption (b), the influence of Rayleigh waves on the vertical component of motion can be written as

$$E_R(f) = \frac{V_s(f)}{V_b(f)}. \quad (2.8)$$

Due to assumption (c), the same Rayleigh wave influence is expected to occur on the horizontal component of motion. Therefore, to correct the S-wave transfer function for the presence of Rayleigh waves in the ambient wave-field (AW), it applies

$$T_{AW}(f) = \frac{T_{EQ}(f)}{E_R(f)} = \frac{H_s(f)V_b(f)}{V_s(f)H_b(f)}. \quad (2.9)$$

This is the S-wave transfer function computed from ambient ground-motion measurements. Nakamura's hypothesis (assumption d) states that the horizontal and vertical component of motion at the base is equal, i.e.

$$\frac{H_b(f)}{V_b(f)} = 1, \quad (2.10)$$

which simplifies equation (2.9) to

$$T_{AW}(f) = \frac{H_s(f)}{V_s(f)} = N_s(f). \quad (2.11)$$

$N_s(f)$ is the ratio between the horizontal and the vertical component of the ambient ground-motion measured at the Earth's surface. If the assumptions (a) to (d) are valid, the local S-wave transfer function can be estimated directly from amplitude spectra measured at one location at the surface (single station measurement).

2.3.2. Surface wave interpretation

The surface wave interpretation is based on the assumption that the ambient wave-field at the Earth's surface is dominated by surface waves. The shape of the H/V-ratio curve is therefore explained by the ellipticity curve (polarization versus period) of Rayleigh waves. Figure 2.6 shows analytical solutions for three different types of ellipticity curves for the fundamental mode Rayleigh wave propagating in a low-velocity layer over a half-space. Type-1 occurs in case of a small impedance contrast ($Z_2/Z_1=2$), type-2 in case of a medium impedance contrast ($Z_2/Z_1=2.5$) and type-3 in case of a large impedance contrast ($Z_2/Z_1=10$) between half-space and surface layer. For the case of large impedance contrasts, there is one particular period for which the vertical component of motion vanishes (at a period of 1 s in Figure 2.6, indicated with an arrow). It was shown that this period corresponds to the inverse of the fundamental

S-wave resonance frequency (f_{S0}) of the surface layer (Konno & Ohmachi, 1998). The vanishing of vertical motion at period $1/f_{S0}$ leads to a singularity in the ellipticity curve. However, this is not the case for the type-2 and type-1 curves, where only a small maximum occurs instead (arrows). The surface wave interpretation states that the observed peaks in the H/V-ratios of ambient ground-motion are caused by the vanishing of the vertical component of motion of Rayleigh waves and therefore only occurs for significant impedance contrasts in the subsurface (type-3 curves). Konno & Ohmachi (1998) show that higher mode Rayleigh waves neither destroy the singularity of the fundamental mode ellipticity nor do they create additional peaks at higher frequencies. The presence of Love waves is expected to strengthen the H/V-peak because the fundamental mode Love wave also occurs at frequency f_{S0} and contributes with additional horizontal ground-motion (Konno & Ohmachi, 1998).

A consequence of the surface wave interpretation is that the observed H/V-peak in ambient ground-motion indicates the fundamental S-wave resonance frequency of the surface layer but does not provide direct information on the magnitude of S-wave resonance (amplification factor). Theoretically, the magnitude of the H/V-peak would be expected to be infinite due to the singularity in the ellipticity curve. However, there is always a small amount of vertical ground-motion in nature and the amplitude of the peak is therefore determined by the composition of the wave-field, the subsurface geology and the data processing (e.g. Fourier transform, smoothing of spectra). This consequence is one of the major differences to Nakamura's body wave interpretation, which suggests that the measured H/V-ratio curve is an approximation for the S-wave transfer function and can, therefore, be used to directly estimate S-wave amplification factors.

2.3.3. Discussion

Both, the body wave as well as the surface wave interpretation are based on assumptions that are questionable or only true for specific conditions. Nakamura's assumptions (b) and (d) may be accepted on the basis of experience (at least as an approximation), but assumption (c) is not justified considering the depth-dependency of the Rayleigh waves' ellipticity. Furthermore, the possible influence of Love waves is completely ignored (assumption a), although Love waves can be a significant part of the ambient wave-field (e.g., Bonnefoy-Claudet et al., 2006). For the surface wave interpretation, on the other hand, it is assumed that the ambient wave-field is dominated by surface waves. This is not always the case though, as pointed out for example by Zhang et al. (2009), who showed that the wave-field between 0.6 and 2 Hz is dominated by continuous P-waves at two sites in California. However, the underlying physical mechanisms of the two different interpretations, i.e. S-wave resonance and development of characteristic Rayleigh wave ellipticities due to the presence of a surface layer, are plausible and expected to occur in nature. The two physical mechanisms are not mutually exclusive but

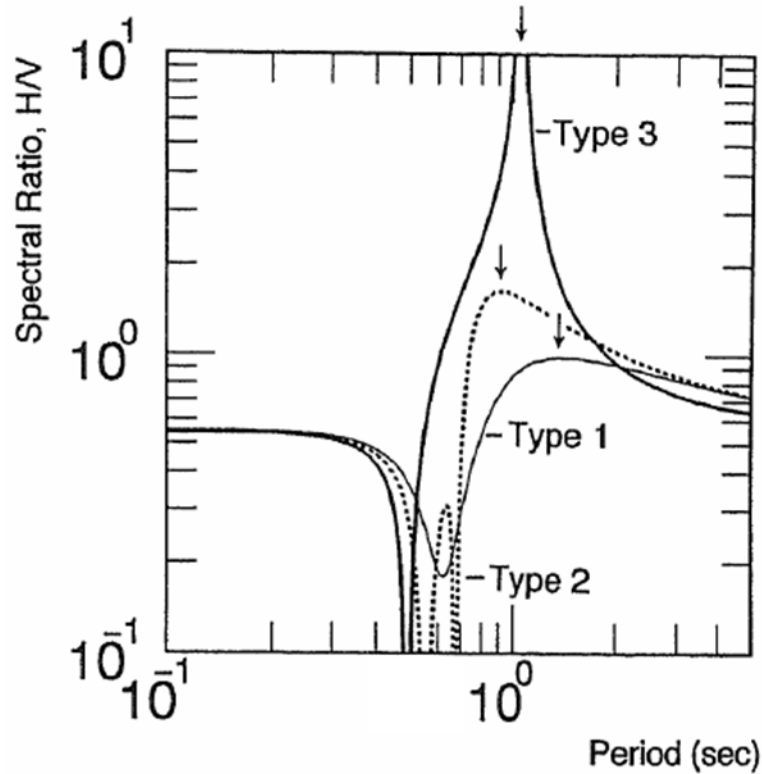


Figure 2.6. *Ellipticity curves of the fundamental mode Rayleigh wave in an elastic layer over a half-space. Type 1: small impedance contrast ($Z_2/Z_1=2$), Type 2: medium impedance contrast ($Z_2/Z_1=2.5$), Type 3: large impedance contrast ($Z_2/Z_1=10$). Arrows indicate the peak period for each of the three curves. After Konno & Ohmachi (1998).*

rather complement each other, where the relative contribution is controlled by the composition of the wave-field and the subsurface geology. The majority of empirical studies have found that (i) the magnitude of the H/V-peak does not well correlate with the S-wave amplification factor of the site and (ii) no clear peaks can be observed at the frequencies of S-wave overtones (Bard, 1999, and references therein). These studies suggest that surface waves contribute significantly to ambient ground-motion H/V-ratios and are not eliminated as claimed by Nakamura (1989). It is therefore critical to consider the H/V-ratio curve computed from ambient ground-motion as an estimate for the S-wave transfer function of the site.

2.4 NUMERICAL MODEL

Numerical modeling is applied to investigate the H/V amplification effect caused by a low-velocity layer on top of a uniform half-space. The numerical algorithm is based on the full 2D elastic wave equations in their first-order velocity-stress formulation (Virieux, 1986). The system of equations is solved with the rotated staggered grid finite-difference technique described in Saenger et al. (2000). The numerical grid is rectangular and all computations are performed with second order spatial finite-difference operators and with a second order explicit time up-

date. A detailed description of the numerical code and its underlying physical and numerical formalism is given in Steiner (2009).

Figure 2.7 shows a sketch of the numerical domain which consists of a 2D isotropic, elastic medium, bounded on three sides by wave absorbing layers to approximate non-reflecting boundaries. The top boundary is a free surface. A surface layer with low seismic velocities exists at the top of the domain. The numerical resolution is 10 m in the horizontal direction and 1.7 m in the vertical direction. The total physical time of the calculation is 60 seconds which corresponds to 400'000 time-steps. An ambient wave-field is generated by a large number of point-sources, randomly distributed in time and space (blue circles). The source locations are distributed between a minimum and maximum distance from the receiver and restricted to a maximum depth. Two different types of source time functions, pulse-like (Figure 2.8a) and sinusoidal (Figure 2.8b), are applied to excite the elastic waves. The source functions are implemented as an additional term in the force balance equation for the vertical and horizontal direction. The random sources build up a diffuse, quasi-stationary wave-field consisting of body and surface waves in the frequency range between 0.5 and 15 Hz. The wave-field is recorded at the indicated receiver-position at the surface.

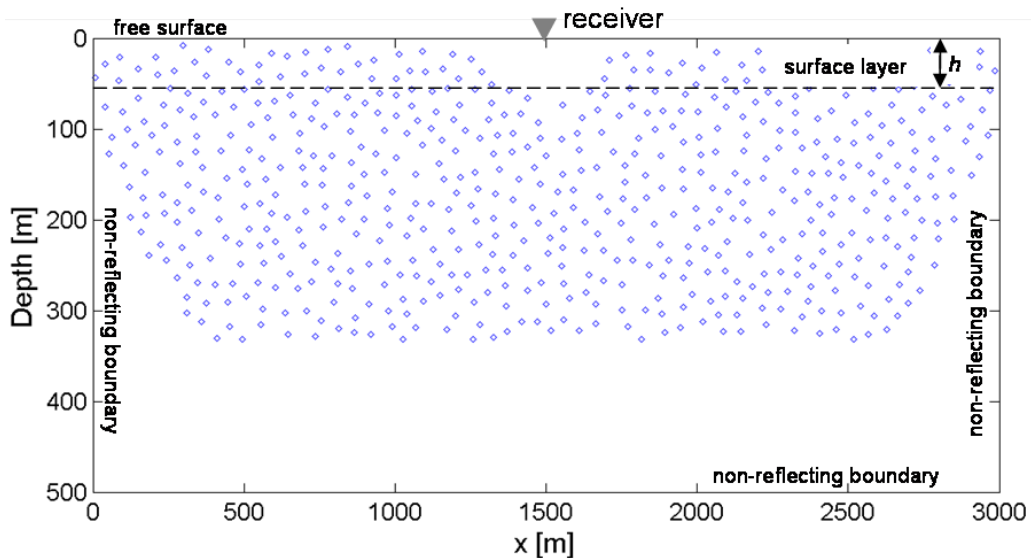


Figure 2.7. Sketch of the numerical domain with a receiver at the surface (triangle) and randomly distributed point sources (blue circles).

Figure 2.9 compares the H/V spectral ratio curves measured at the receiver position for models with surface layers of different thicknesses. The solid black and blue line correspond to a 50 m and 30 m thick surface layer, respectively. For both models, the S-wave velocity of the layer is 250 m/s and the S-wave impedance contrast between underlying half-space and surface

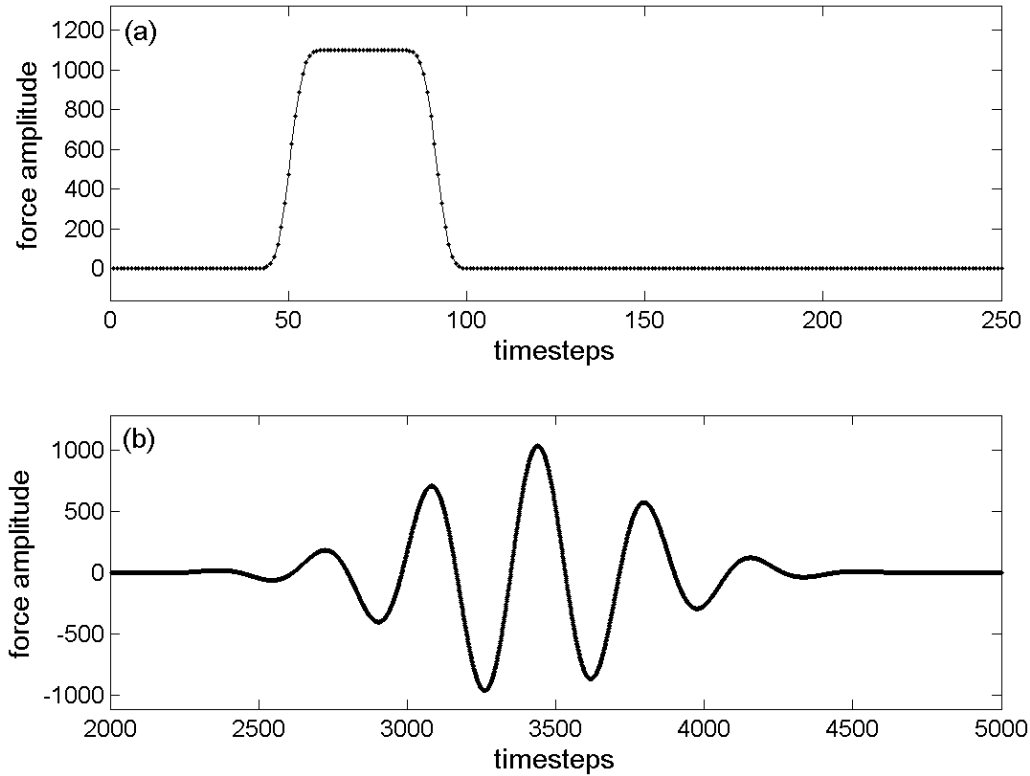


Figure 2.8. *Two different types of source time functions, implemented in the numerical algorithm as an additional term in the force balance equation. (a) Pulse-like source and (b) sinusoidal source.*

layer is 5.2. The solid red line indicates the H/V-ratio curve for a fully homogeneous model, i.e. without surface layer. For each model, the dashed line shows the S-wave amplification due to the presence of the surface layer, analytically derived from the transfer function of vertically incident S-waves. In the case without surface layer, there is no theoretical S-wave amplification and also the modeled H/V-ratio tends to be close to 1 for all frequencies. The significant drop at frequencies below 1 Hz is presumably related to a lack of seismic energy (outside the source frequency range) and must be disregarded for interpretation. In contrast to the uniform model, the presence of a surface layer creates distinct peaks in the H/V-ratio curves (black and blue line). The peak-frequencies match well with the S-wave resonance frequencies of the layer (maxima of corresponding dashed lines). This is in particular true for the fundamental S-wave resonances at 1.25 Hz and 2.08 Hz, respectively. For the overtones, however, small deviations in frequency are observed and additional peaks occur at frequencies that are not related to S-wave resonance (e.g. blue line at 5 Hz). The magnitudes of H/V-peaks at the S-wave overtone frequencies are significantly smaller compared to the fundamental S-wave resonance.

Figure 2.10 investigates the influence of different impedance contrasts between surface layer and underlying media. Three models are compared with impedance contrasts of 10.4 (green), 5.2 (blue) and 1.75 (cyan). The surface layer is 30 m thick and exhibits an S-wave velocity of 250 m/s for all three models. According to the quarter wave-length rule (equation 2.5), the

fundamental S-wave resonance occurs at 2.08 Hz for this model. As shown in Figure 2.10, all three models exhibit an H/V-peak at this frequency. The magnitude of the peak decreases strongly with decreasing impedance contrast, however, a small peak is still observed for the smallest impedance contrast of 1.75. The dashed lines show the amplification of vertically incident S-waves due to the presence of the layer (analytical transfer function). Their maxima align therefore with the fundamental S-wave resonance frequency at 2.08 Hz.

The results of the numerical study show that both, the frequency and the amplitude of the first (dominant) peak in the modeled H/V-ratio curves correspond well with the first (fundamental) peak of the analytical S-wave transfer function of the surface layer. However, the shape of the modeled H/V-ratio peaks is in general broader compared to the analytical S-wave amplification peaks. Additional H/V-peaks are observed at higher frequencies and match with the S-wave resonance overtone frequencies. This suggests that parts of the H/V amplification is indeed caused by S-wave resonance in the surface layer. However, the magnitudes of the additional peaks are significantly smaller than both, the dominant H/V-peak and the peaks of the corresponding S-wave transfer function. This is interpreted as the effect of Rayleigh waves, which boost the dominant peak but tend to destroy any other H/V-peak at higher frequencies due to the shape of their ellipticity curve. These observations reflect that the synthetic ambient wave-field in the models is a combination of both, body and surface waves. For such scenarios it seems to be feasible to estimate fundamental S-wave resonance frequencies and (relative) amplification factors based on the position and magnitude of the dominant peak in the H/V spectral ratio curve. However, estimation of amplification factors is qualitative, does only work around the fundamental frequency (e.g. is not possible for overtones) and may fail in case the wave-field is dominated by surface waves.

It is important to mention that the computation of H/V spectral ratio curves, in particular the mandatory smoothing of the spectra before the spectral division (step 4 in Figure 2.4), has a significant impact on the final shape of the curve. This makes a direct, absolute comparison between the modeled H/V-ratio curves and the analytical transfer function difficult because peak-magnitudes in H/V-ratio curve tend to become too small.

2.5 CONCLUSIONS

A field data example shows peaks in the H/V spectral ratio curve of ambient ground-motion that can be related to the presence of two known S-wave velocity discontinuities in the subsurface (at 5 m and 220 m depth, respectively). The peak-frequencies correlate well with the theoretical fundamental S-wave resonance frequencies for the site, estimated from the S-wave velocity profile using the quarter wavelength rule (equation 2.5). The magnitudes of the peaks provide information on the relative size of the S-wave impedance contrast for the two discontinuities.

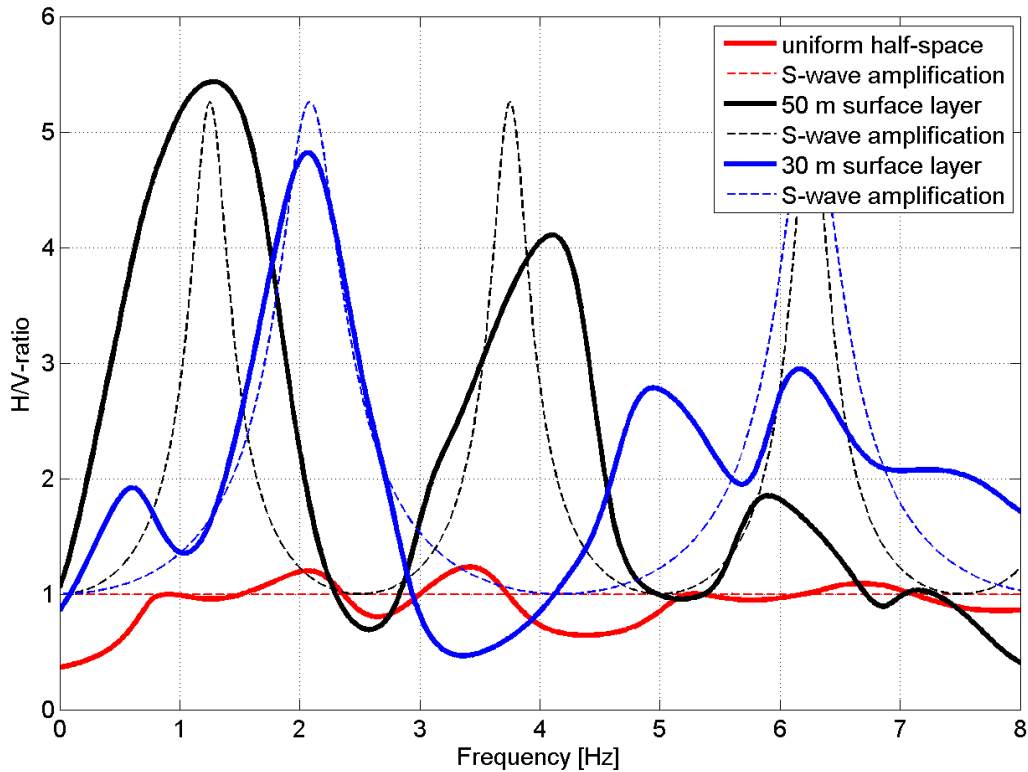


Figure 2.9. *H/V-ratio curves for models with surface layers of different thicknesses (solid black and blue lines). The solid red line corresponds to the fully homogeneous case (no surface layer). The dashed lines indicate the analytical solution for the amplification of vertically incident S-waves (transfer function).*

Two different ways of interpreting H/V-peaks in ambient ground-motion have been proposed in the literature: the body wave interpretation (Nakamura, 1989) and the surface wave interpretation (e.g., Konno & Ohmachi, 1998). Although based on questionable assumptions, the basic underlying physical mechanisms of both interpretations, i.e. S-wave resonance and ellipticity of Rayleigh waves, are plausible and expected to occur in nature. The numerical models presented in this study are able to produce surface layer-related H/V-peaks in synthetic ambient ground-motion data. The characteristic of the modeled H/V-ratio curves suggests that they are caused by both, S-wave resonance and Rayleigh wave ellipticity.

Field data and numerical results indicate that the body and surface wave interpretation are not mutually exclusive. They rather complement each other, where the relative contribution is expected to be controlled by the composition of the wave-field and the subsurface geology. For scenarios with a significant amount of body waves in the ambient wave-field, it seems therefore to be feasible to estimate not only fundamental S-wave resonance frequencies but also relative amplification factors based on the dominant peak in the measured H/V spectral ratio curves. However, estimation of such amplification factors is only qualitative and not possible for S-wave overtones.

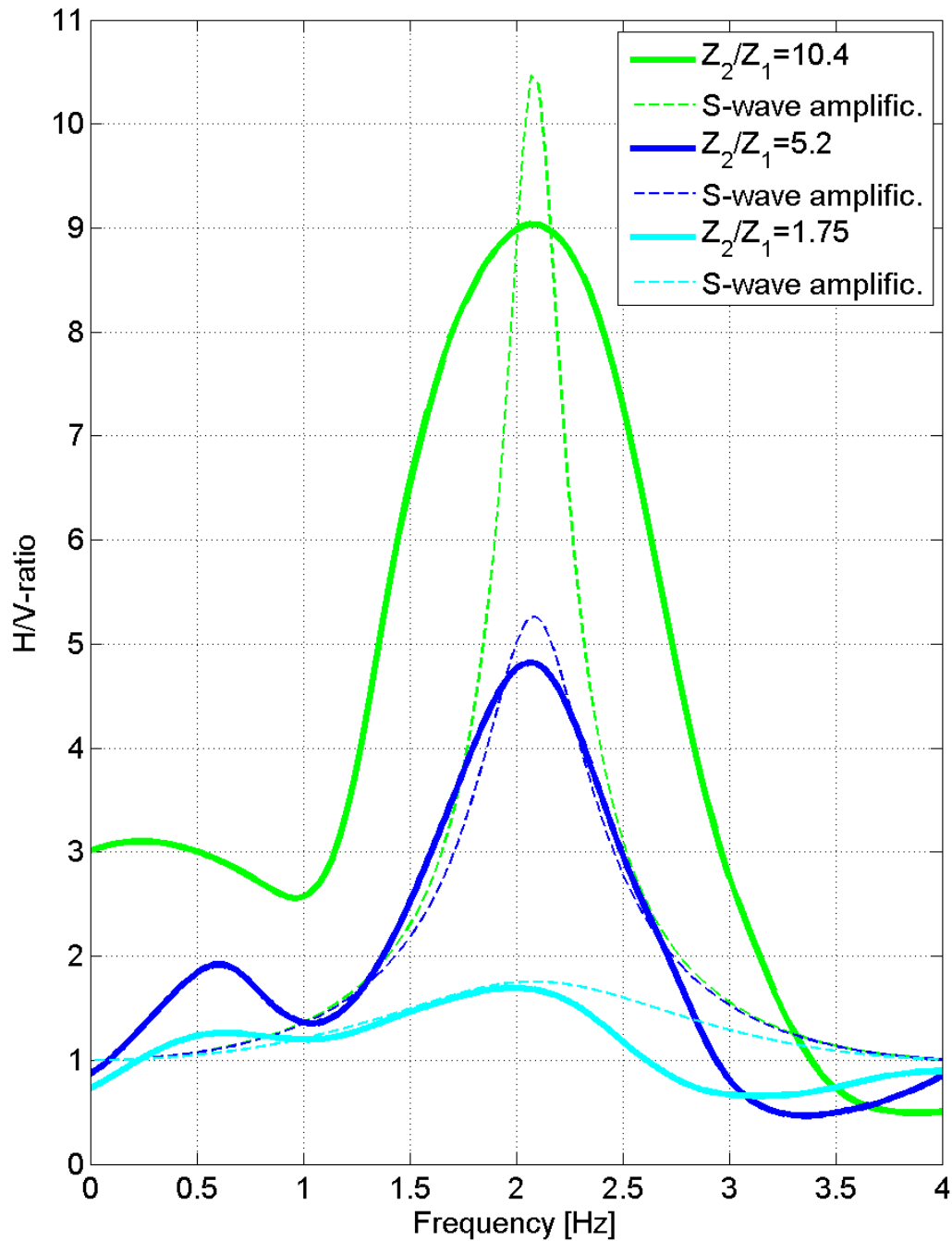


Figure 2.10. *H/V-ratio curves for models with different S-wave impedance contrasts between underlying half-space and surface layer (solid lines). The dashed lines indicate the analytical solution for the amplification of vertically incident S-waves (transfer function).*

References

- Aki, K. & Richards, P. (2002). *Quantitative Seismology (2nd edition)*. University Science Books. ISBN 0-935702-96-2.
- Al Yuncha, Z., Luzon, F., Posadas, A., Martin, J., Alguacil, G., Almendros, J. & Sanchez, S. (2004). *The use of ambient seismic noise measurements for the estimation of surface soil effects: The Motril city case (Southern Spain)*. Pure and Applied Geophysics, **161**, 1549–1559.
- Almendros, J., Luzon, F. & Posadas, A. (2004). *Microtremor analyses at Teide volcano (Canary Island, Spain): Assessment of natural frequencies of vibration using time dependent horizontal-to-vertical ratios*. Applied Geophysics, **161**, 1579–1596.
- Bard, P.-Y. (1999). *Microtremor measurements: A tool for site effect estimation?* In: The Effects of Surface Geology on Seismic Motion (eds K. Irikura, K. Kudo, K. Okada and T. Sasatami) [Balkema, Rotterdam, The Netherlands.], pp. 1251–1279.
- Bonnefoy-Claudet, S., Cotton, F. & Bard, P. (2006). *The nature of noise wavefield and its applications for site effects studies: A literature review*. Earth-Science Reviews, **79**, 205–227.
- Bour, M., Fouissac, D., Dominique, P. & Martin, C. (1998). *On the use of microtremor recordings in seismic microzonation*. Soil Dynamics and Earthquake Engineering, **17**, 465–474.
- Frischknecht, C., Rosset, P. & Wagner, J.-J. (2005). *Towards seismic microzonation 2-D modeling and ambient seismic noise measurements: The case of an embanked, deep alpine valley*. Earthquake Spectra, **21**, 635–651.
- Fäh, D., Kind, F. & Giardini, D. (2001). *A theoretical investigation of average H/V ratios*. Geophys. J. Int., **145**, 535–549.
- Konno, K. & Ohmachi, T. (1998). *Ground-motion characteristics estimated from spectral ratios between horizontal and vertical components of microtremor*. Bull. Seism. Soc. Am., **88**, 228–241.
- Maresca, R. ., Castellano, M., Matteis, R., Saccorotti, G. & P., V. (2003). *Local site effects in the town of Benevento (Italy) from noise measurements*. Pure and Applied Geophysics, **160**, 1745–1764.
- Moya, A., Schmidt, V., Segura, C., Boschini, I. & Atakan, K. (2000). *Empirical evaluation of site effects in the metropolitan area of San Jose, Costa Rica*. Soil Dynamics and Earthquake Engineering, **20**, 177–185.

- Nakamura, Y. (1989). *A method for dynamic characteristics estimation of subsurface using microtremor on the ground surface*. Railway Technical Research Institute, Quarterly Report, **30**, 25–30.
- Nasseri-Moghaddam, A., Cascante, G., Phillips, C. & Hutchinson, D. (2007). *Effects of underground cavities on Rayleigh waves - Field and numerical experiments*. Soil Dynamics and Earthquake Engineering, **27**, 300–313.
- Okada, H. (2003). *The Microtremor Survey Method*. Geophysical Monograph Series No. 12, SEG, Tulsa, USA. ISBN 1-56080-120-4.
- Parolai, S., Bormann, P. & Milkereit, C. (2002). *New Relationship between V_S , Thickness of Sediments, and Resonance Frequency Calculated by the H/V Ratio of Seismic Noise for the Cologne Area (Germany)*. Bull. Seism. Soc. Am., **92**, 2521–2527.
- Parolai, S., Richwalski, S., Milkereit, C. & Bormann, P. (2004). *Assessment of the stability of H/V spectral ratios from ambient noise and comparison with earthquake data in the Cologne area (Germany)*. Tectonophysics, **390**, 57–73.
- Pujol, J. (2003). *Elastic Wave Propagation and Generation in Seismology*. Press Syndicate of the University of Cambridge, Cambridge, UK. ISBN 0-521-52046-0.
- Saenger, E. H., Gold, N. & Shapiro, S. A. (2000). *Modeling the propagation of elastic waves using a modified finite-difference grid*. Wave Motion, **31**, 77–92.
- Ibs-von Seht, M. & Wohlenberg, J. (1999). *Microtremor Measurements Used to Map Thickness of Soft Sediments*. Bull. Seism. Soc. Am., **89**, 250–259.
- SESAME (2004). *Guidelines for the implementation of the H/V spectral ratio technique on ambient vibrations. Measurements, processing and interpretation - WP12*. SESAME European research project (ed. P.-Y. Bard), p. 61ff.
- Stamm, G. & Fäh, D. (2006). *Auswertung der Voitsdorf-Array-Messungen*. Report for Spectraseis. Schweizerischer Erdbebendienst.
- Steiner, B. (2009). *Time reverse modeling of low-frequency tremor signals*. Swiss Federal Institute of Technology, ETH, Zurich, Switzerland. doi:10.3929/ethz-a-005842672.
- Teves-Costa, P., Matias, L. & Bard, P.-Y. (1996). *Seismic behaviour estimation of thin alluvium layers using microtremor recordings*. Soil Dynamics and Earthquake Engineering, **15**, 201–209.
- Virieux, J. (1986). *P-SV-wave propagation in heterogeneous media: Velocity-stress finite-difference method*. Geophysics, **51**, 889–901.

Zhang, J., Gerstoft, P. & Shearer, P. (2009). *High-frequency P-wave seismic noise driven by ocean winds*. *Geophysical Research Letters*, **36**, L09302.

3. Numerical study on detecting wave-field modifications using spectral analysis of ambient ground-motion

Marc-André Lambert, Erik H. Saenger & Stefan M. Schmalholz

ABSTRACT

The quasi-stationary, omnipresent ambient seismic wave-field carries information on the subsurface. Such information can either apply to heterogeneously distributed material properties (e.g. an underground cavity) or to active seismic sources at depth (e.g. volcanic tremor). In both cases, the ambient ground-motion is continuously modified and such modifications can be significant in frequency spectra measured at the surface. We propose a method for detecting the horizontal position (i.e. epicenter) of the subsurface origin of these wave-field modifications. The method uses three attributes extracted from Fourier amplitude spectra of the seismic response at the surface. The first attribute quantifies energy in the vertical component of the wave-field, the second attribute quantifies an integral value of the vertical-to-horizontal spectral ratio and the third attribute quantifies the frequency value of a dominant peak in the vertical component spectrum. We use a finite-difference wave-propagation code to simulate two different types of wave-field modification: (i) models with an embedded inclusion of high attenuation and sources below the inclusion (passive modification), and (ii) models with embedded zones of active seismic emission (active modification). For each scenario we discuss the applicability of the proposed spectral analysis methodology. We further introduce additional complexity, such as shallow structures, realistic subsurface properties and surface noise, to explore limitations of the methodology. The numerical results show that the method is applicable to both types of wave-field modification. Attribute profiles are indicative of the horizontal location of wave-field modifications, also in the case of additional shallow structures and realistic subsurface material properties. However, a complex subsurface can have strong influences on the lateral variation of attribute values and some attributes are then less suited. Surface noise can mask signatures related to subsurface wave-field modifications. F-K filtering is useful to enhance the S/N-ratio and to retrieve signatures in attribute profiles that are otherwise over-

whelmed by noise. Obliquely incident waves on a cross-section in three-dimensional models can reduce the efficiency of F-K filtering considerably. Our simulations provide a theoretical basis to discuss and interpret (i) spectral anomalies observed above hydrocarbon reservoirs, (ii) the possible physical mechanisms of such anomalies and (iii) the applicability of spectral analysis to improve hydrocarbon reservoir detection.

3.1 INTRODUCTION

The quasi-stationary, ambient seismic wave-field is continuously modified through interactions with the subsurface inhomogeneity of the Earth. Consequently, passive ground-motion responses at the Earth's surface carry valuable information about the seismic properties of the subsurface (e.g. [Bonnetfoy-Claudet et al., 2006](#)). Analysis techniques based on frequency spectra proved to be successful in extracting such information because of the complex nature of the ambient wave-field, which includes usually no observable arrivals in the time domain and low signal-to-noise ratios (S/N-ratios). For example, the horizontal-to-vertical (H/V) spectral ratio technique was introduced for estimating earthquake amplification factors from ambient ground-motion in areas with little seismicity ([Bard, 1999](#), and references therein). The shape of H/V spectral ratio curves were also used to invert for the vertical S-wave velocity profile of one-dimensional structures ([Fäh et al., 2003](#), and references therein). More advanced array methods, such as the spatial autocorrelation analysis and the frequency-wavenumber analysis, were developed for the same purpose ([Okada, 2003](#), and references therein). [Nasseri-Moghaddam et al. \(2007\)](#) analyzed frequency domain parameters derived from Fourier amplitude spectra of ambient ground-motion to detect horizontal inhomogeneities, for example a cavity in 50 m depth at a mine site in Canada. All these applications work because seismic wave propagation is sensitive to material properties and, therefore, the ambient wave-field is modified in a characteristic way by the presence of subsurface inhomogeneity.

Similar spectral analysis techniques as described above have recently been suggested in several independent studies as being useful also for the detection of hydrocarbon reservoirs (e.g., [Dangel et al., 2003](#); [van Mastriigt & Al-Dulaijan, 2008](#); [Schechinger et al., 2009](#)). These empirical studies have reported an apparent correlation between spectral patterns in low-frequency (<10 Hz) passive ground-motion recordings at the Earth's surface and the horizontal location of the reservoirs. Therefore, it was speculated that the observed patterns may indeed be related to the presence of subsurface reservoirs and, as a consequence, could be used to improve reservoir detection. The applicability of spectral analyses of passive ground-motion to improve reservoir detection and the possibly responsible physical mechanisms are controversially discussed at present (e.g., [Lambert et al., 2009](#); [Ali et al., 2009](#); [Green & Greenhalgh, 2010](#); [Lambert et al., 2010](#)). However, this current discussion lacks, among other things, a sufficient number of wave propagation studies investigating ambient wave-field modifications. Therefore, we present here a series of numerical wave propagation simulations to investigate if, and how intense, (i) subsurface heterogeneities and (ii) subsurface zones of active seismic sources can modify the ambient ground-motion. These simulations of standard seismic wave propagation provide a theoretical basis to discuss the applicability of spectral analysis for improving reservoir detection as well as potential physical mechanisms.

The physical mechanisms that have been suggested as possible explanation for reservoir-related patterns (for an overview see [Saenger et al. \(2009\)](#)) can roughly be divided into two different groups:

- (i) Modification of the ambient wave-field through interaction with an inhomogeneity (passive modification). Due to partial fluid saturation, reservoirs can be subsurface inhomogeneities with different seismic properties (attenuation, impedances, velocities) compared to surrounding, fully saturated rocks (e.g., [Klimentos, 1995](#); [Dasgupta & Clark, 1998](#); [Korneev et al., 2004](#)). Like for any inhomogeneity, this causes interaction with the ambient wave-field through processes such as reflection, refraction, attenuation, scattering and resonant scattering ([Kallweit & Wood, 1982](#); [Korneev & Johnson, 1996](#); [Liu et al., 2000](#); [Korneev et al., 2004](#); [Korneev, 2008](#); [Goloshubin et al., 2006](#); [Tai et al., 2009](#); [Werby & Gaunaud, 1990](#)). A reservoir, therefore, modifies the ambient wave-field because it acts as a wave-scatterer and -damper if one or more of the seismic properties differ from the ones of the surrounding rocks.

- (ii) Active emission of seismic signals from within the reservoir which is more frequent and/or more intense than from the surrounding rocks (active modification). This might be caused by a number of processes such as, for example, shear failure (e.g. [Rutledge et al., 1998](#)) or oscillating fluids in pore space and fractures ([Beresnev et al., 2005](#); [Korneev, 2008](#); [Frehner et al., 2009](#)). Such processes are possibly, but not necessarily, driven by external seismic waves and in either case trigger active seismic signals that contribute to wave-field modifications.

The first group of mechanisms can be described by the theory of elastic and visco-elastic wave-propagation, while the second group includes additional processes on different scales such as material failure and possible non-linear fluid oscillation and migration. Although different from a physical point of view, the effects on the wave-field can be similar for both groups of mechanisms. For example, a heterogeneous body can be excited by seismic waves and oscillate with its natural frequency. This oscillation may continue even after the incident waves have passed and re-emit seismic waves into the medium. This process is called resonant scattering (e.g. [Werby & Gaunaud, 1990](#)). The heterogeneity can therefore act similar to an active seismic source.

For many ambient ground-motion applications, the location of the signal's origin (be it an active source, a wave-scatterer or a wave-damper) is of main interest. But precise location of the origin is often not an easy task because distinct events in the time traces are absent and therefore standard methods such as earthquake location algorithms cannot be applied straightforward. Several alternative approaches have been proposed. For example, [Brown et al. \(2009\)](#) apply waveform cross-correlation to non-volcanic tremor to measure relative arrival times of P- and

S-waves and then perform a travel time inversion to locate the origin of deep low-frequency earthquakes. [Di Grazia et al. \(2006\)](#) estimate the source location of volcanic tremor considering the spatial amplitude distribution of the measured waveforms at the Earth's surface. [Steiner et al. \(2008\)](#) apply time reverse modeling to synthetic and real data to detect sources of low-frequency microtremors in the subsurface. [Nasseri-Moghaddam et al. \(2007\)](#) considered spatial patterns of frequency domain parameters derived from Fourier amplitude spectra of ambient ground-motion recordings to detect the location of an underground cavity that acts as a source of Rayleigh wave scattering.

In this paper, we introduce a spectral analysis methodology for detecting the origin of quasi-stationary subsurface wave-field modifications and we use numerical simulations to investigate its applicability. Fourier amplitude spectra of the synthetic signals at the surface are used to extract and map spectral attributes. The attributes quantify characteristic features in the data that are indicative of the modification's origin. According to the two groups of physical mechanisms described above, we distinguish two different types of wave-field modification: (i) Models with an embedded inhomogeneity that acts as a wave-scatterer and wave-damper (passive modification), and (ii) models with embedded zones of active seismic emission (active modification). The general aim of this study is to show that the proposed spectral analysis methodology is in principle useful for detecting the origin of both types of wave-field modifications. We introduce additional complexity, such as surface noise or shallow structures, to explore the limitations of the methodology. More specifically, we consider a scenario with realistic subsurface properties obtained from a 3D seismic survey at an oil and gas field in Austria. We regard the known hydrocarbon reservoirs as zones of seismic emission and investigate whether spectral analysis of the resulting surface signals is useful to assess the location of the zones of emission. In the discussion, we address the question whether or not it is physically justified to apply the proposed spectral analysis to real ambient ground-motion recordings in an attempt to increase the probability of detecting hydrocarbon reservoirs.

3.2 METHOD

3.2.1. Data generation

The synthetic data used in this study is generated with a finite-difference wave-propagation code. The numerical algorithm is based on the three-dimensional (3D) elastic wave equation ([Aki & Richards, 2002](#)). The system of equations is solved with the rotated staggered grid finite-difference technique described in [Saenger et al. \(2000\)](#). The numerical domain is rectangular and described by the Cartesian coordinates x , y and z , where x and y are the two principal horizontal directions and z denotes the vertical direction. The domain is limited by non-reflecting boundaries ([Cerjan et al., 1985](#)), except for the top boundary which is a stress free

surface. The medium inside the domain has isotropic properties and is discretized into a rectangular grid with a spacing of 10 m in all three principal directions. Computations are performed with second order spatial finite-difference operators and with a second order explicit time update. The size of the time-step is constrained by the Courant-Friedrich-Lewy condition (Courant et al., 1967) and therefore controlled by the largest wave propagation velocity in the model. The two-dimensional (2D) models assume plane strain conditions to approximate infinite extension in the 3rd dimension.

3.2.2. Data processing

We propose spectral analysis of the medium’s seismic surface response to extract information on subsurface wave-field modifications. Similar techniques have been used for example to detect wave-field scattering caused by buried objects. The synthetic study of Nasser-Moghaddam et al. (2005) introduced frequency domain parameters to quantify the scattered energy of surface waves, caused by a void embedded in a homogenous medium. The parameters were sensitive to the presence of the void and allowed assessing the location, depth and size of the void. Later, the same methodology was successfully applied to real ambient ground-motion data measured at a mine site in Canada to detect a cavity (Nasser-Moghaddam et al., 2007). Tallavó et al. (2009) applied a similar method to detect buried timber trestles using an active seismic source. In our study, we more generally evaluate the potential of spectral analysis techniques to extract from ambient surface signals information on subsurface wave-field modifications.

The modeled time-histories of the particle motion at selected surface grid-points (“receivers”) are transformed into the frequency domain using a discrete Fourier transform algorithm. The absolute values of the transformed signals yield the amplitude spectra $|X(f)|$, $|Y(f)|$ and $|Z(f)|$ for the three principle components. Specific attributes that quantify features of interest in the data can be deduced from those amplitude spectra. Three attributes are used for this study. The first attribute, A_1 , quantifies the signal’s spectral energy on the vertical component of motion. Nasser-Moghaddam et al. (2005) used this attribute to quantify the effect of Rayleigh wave scattering caused by an embedded void. The spectral energy is calculated for each receiver as

$$E_V(k) = \sum_{f_r} |Z(k, f)|^2, \quad (3.1)$$

where $|Z(k, f)|$ is the spectral amplitude as a discrete function of frequency f for receiver number k . The summation is performed over the frequency interval $f_r = [f_1, f_2]$, which is chosen to contain the features of interest. The energy is normalized by its maximum value across the receiver array which yields attribute A_1 :

$$A_1(k) = \frac{E_V(k)}{\max[E_V(k)]}. \quad (3.2)$$

The second attribute, A_2 , quantifies an integral value of the ratio between the amplitude spectrum of the vertical component and horizontal component of motion (V/H-ratio). In the 3D case, the amplitude spectrum of the horizontal component, $H(k, f)$, for each receiver k is computed as the root mean square of the spectra of the two principal horizontal directions:

$$H(k, f) = \sqrt{\frac{|X(k, f)|^2 + |Y(k, f)|^2}{2}}. \quad (3.3)$$

The integral value of the V/H-ratio for receiver number k is given as

$$R(k) = \sum_{f_r} \frac{|Z(k, f)|}{H(k, f)}, \quad (3.4)$$

where the summation is performed over the frequency interval $f_r = [f_1, f_2]$, which can be different from the frequency interval used for attribute A_1 above. Attribute A_2 is obtained by normalizing to the maximum value across the receiver array:

$$A_2(k) = \frac{R(k)}{\max[R(k)]}. \quad (3.5)$$

The third attribute, A_3 , is based on the frequency value f_{\max} corresponding to the maximum amplitude in the vertical component spectrum within the frequency interval $f_r = [f_1, f_2]$. Normalizing by the largest f_{\max} -value among all receivers yields attribute A_3 :

$$A_3(k) = \frac{f_{\max}(k)}{\max[f_{\max}(k)]}. \quad (3.6)$$

Equations (3.2), (3.5) and (3.6) show that the attributes are dimensionless parameters with values in the range $[0, 1]$. The frequency interval $f_r = [f_1, f_2]$ is chosen empirically for each model set-up and can be different for each attribute. Table 3.1 lists the frequency parameters used to calculate the attributes for the models presented in this paper. For interpretation, the attribute values are displayed either as profiles (2D models) or as contour plots (3D model). Spatial averaging of adjacent attribute values (stacking) yields smoothed profiles in the 2D case as it reduces local fluctuations and removes isolated outliers. In particular for the latter we decided to use a running median procedure which is more efficient in removing outliers compared to a moving average procedure based on arithmetic mean values.

3.3 EMBEDDED INHOMOGENEITY

Draganov et al. (2010) proposed a 2D numerical model set-up to test several aspects of passive seismic interferometry for imaging reflectors in a horizontally layered medium. In their Figure 9

Model scenario	A_1, A_3		A_2	
	f_1	f_2	f_1	f_2
Inclusion 2D	1	6	4	6
Emission 2D	2	5	3	5
Emission 3D	2	5	4	6

Table 3.1. Frequency parameters used to calculate attributes A_1 , A_2 and A_3 .

they display a model with random source distribution at depth below the reflectors and with a receiver array at the free surface of the model. Figure 3.1 in our paper shows a similar set-up, but the focus of our study is on the lateral location of an inclusion that exhibits high attenuation rather than on detecting the depth of acoustic impedance discontinuities (reflectors). Our intention is not to study the potential and limitations of interferometry, but we use similar scenarios and data to test the applicability of the above spectral analysis methodology for the detection of an embedded inhomogeneity.

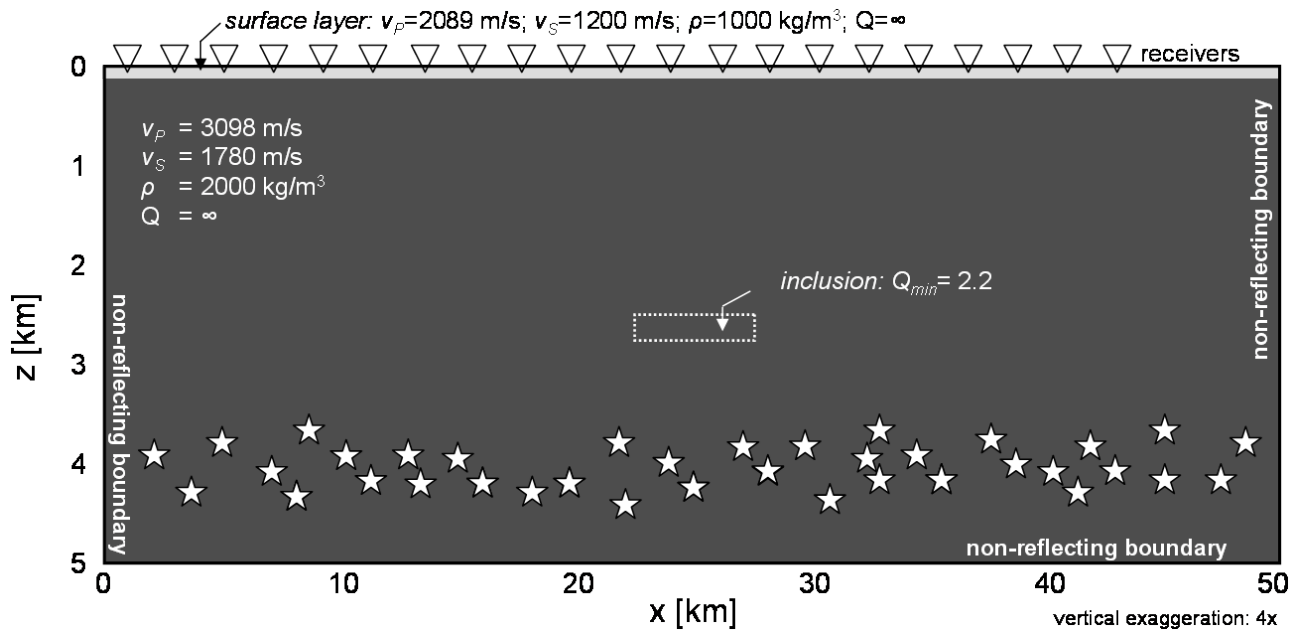


Figure 3.1. Model of the subsurface with an embedded inclusion and a 100 m thick surface layer. The half-space and the surface layer are characterized by their P-wave velocity v_p , S-wave velocity v_s and mass density ρ . The media is fully elastic, except for the inclusion which behaves visco-elastic with a minimum value of Q of 2.2. The subsurface sources are randomly distributed in a depth between 3500 and 4500 m (stars). Vertical exaggeration is 4.

Visco-elastic inclusion in a uniform, elastic medium

First, we consider a model as illustrated in Figure 3.1, but without the low velocity surface layer. The domain consists of a uniform elastic medium with P- and S-wave velocities of $v_P=3098$ m/s and $v_S=1780$ m/s, respectively. The mass density ρ is 2000 kg/m³. At the center of the domain is a rectangular inclusion with a size of 5000 by 250 meters. The material inside the inclusion behaves visco-elastic and therefore acts as a wave damper. The incorporation of visco-elasticity is based on the generalized Maxwell model described by [Emmerich & Korn \(1987\)](#) and [Kristek & Moczo \(2003\)](#). The model is implemented according to equation (4) in [Saenger & Shapiro \(2005\)](#), using the following parameters: $\tilde{Y}_1^{11} = 0.6 v_P^2 \rho$, $\tilde{Y}_1^{44} = 0.6 v_S^2 \rho$ and $\omega_1 = 2\pi \cdot 3\text{Hz}$. This leads to a frequency dependent attenuation with a minimum quality factor Q of about 2.2 at around 2 Hz. All other material properties are the same for the inclusion and its surrounding medium. Three hundred seismic sources are randomly distributed in depth between 3500 m and 4500 m. The sources are implemented in the force balance equation as single body forces with random orientations. The source time functions are Ricker wavelets with random central frequencies between 2 and 5 Hz. The sources are multiply and randomly triggered in time and each source radiates both, P-waves and S-waves. The superposition of the signals creates a quasi-stationary wave-field, composed in depth of P- and S-waves. The calculated total physical time was 67.5 seconds which was numerically discretized with 45'000 time-steps. The triangles in Figure 3.1 schematically illustrate the receiver array at the surface with a receiver spacing of 100 m.

Figure 3.2a shows vertical component seismograms recorded at four different stations of the receiver array. The signal at $x=25$ km is recorded vertically above the inclusion. The other three signals are recorded at locations further away from the inclusion. However, all four waveforms show the stable, quasi-stationary character of the wave-field where transient arrivals are missing. Figure 3.2b displays the corresponding Fourier amplitude spectra. The main part of the energy occurs in the frequency band between 1 and 6 Hz and the general shape of the spectra is defined by the frequency content of the source signals, i.e. the Ricker wavelets.

The contour plot in Figure 3.3a displays the normalized vertical component spectral amplitude $|Z(x, f)|$ as a function of distance x . This spatial spectrogram representation provides information about the frequency content of the wave-field with respect to the surface position. The locations of the lateral boundaries of the embedded inclusion are indicated with dashed grey lines. The spectral amplitudes are slightly reduced vertically above the inclusion, presumably because parts of the direct incident signals experienced some attenuation when traveling through the dissipative inclusion. Figure 3.3b shows the spatial spectrogram of the V/H-ratio, i.e. the spectral amplitude ratio $|Z(x, f)/X(x, f)|$. The region above the inclusion is characterized with generally enhanced V/H values.

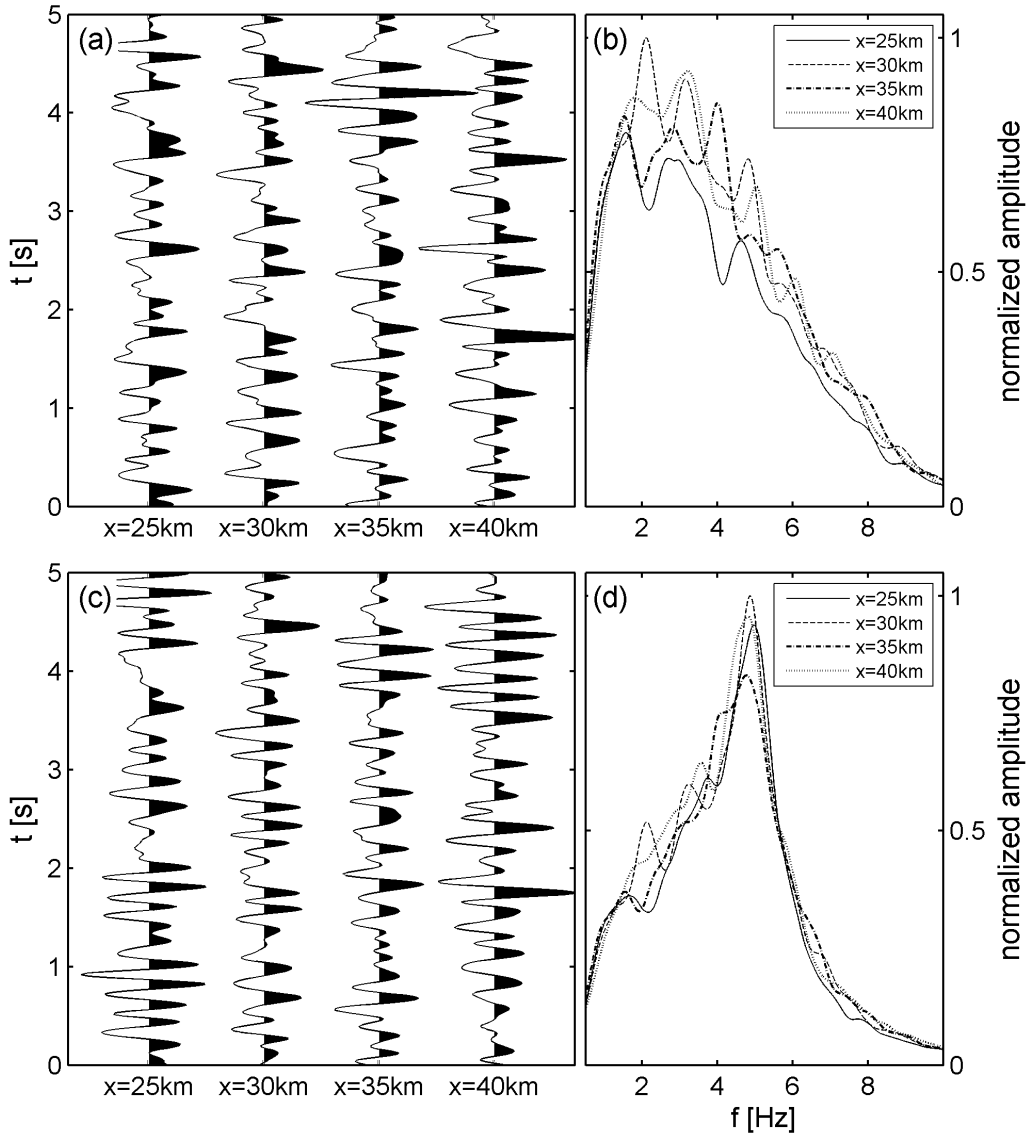


Figure 3.2. Examples of signals recorded at four different stations of the receiver array shown in Figure 3.1. (a) and (b) show the vertical component seismograms and the corresponding Fourier amplitude spectra for the case without surface layer. (c) and (d) show similar data for the case with a surface layer on top of the half-space.

The three spectral attributes introduced in the previous section are calculated for each receiver using the following frequency intervals: $f_r = [1 \text{ Hz}, 6 \text{ Hz}]$ for the attributes A_1 and A_3 , $f_r = [4 \text{ Hz}, 6 \text{ Hz}]$ for attribute A_2 . These frequency intervals are highlighted with arrows in Figure 3.3 and listed in Table 3.1. The dots in Figure 3.4 depict the attribute values computed from 67.5 seconds of continuous waveforms for every 4th receiver position at the surface. Only receivers between $x=8 \text{ km}$ and $x=42 \text{ km}$ are shown because the wave-field close to the boundary of the model domain suffers from reduced source illumination and is therefore excluded from the analysis. The lines show the corresponding running median profiles. To obtain those profiles, the median of the attribute values within a 5000 m wide window is assigned to the location of the centre of the window. Shifting the window along the array by steps of one receiver yields

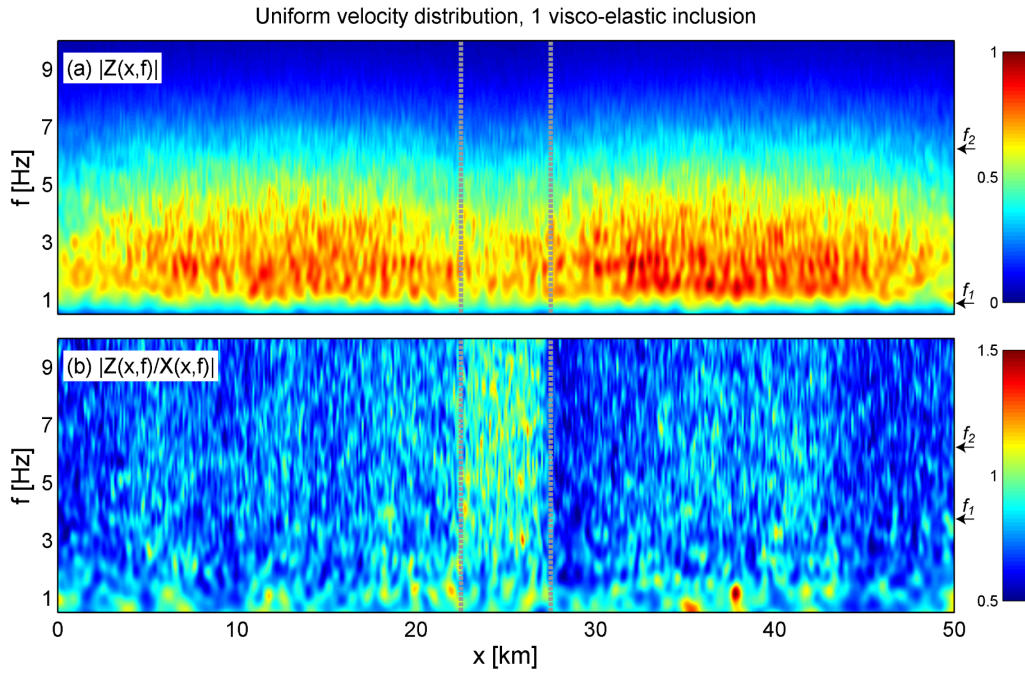


Figure 3.3. *Spatial spectrograms along the free surface of the model without surface layer. (a) Normalized amplitude of vertical component and (b) V/H-ratio. Dashed grey lines indicate the locations of the lateral boundaries of the inclusion at depth. The arrows on the right depict the frequency intervals $f_r = [f_1, f_2]$ used for the attribute calculation.*

the quasi-continuous attribute profiles. Spatial patterns that are related to the presence of the embedded inclusion are expected to occur on a characteristic length scale that is similar to the width of the inclusion itself. Fluctuations on a smaller scale, e.g. isolated outliers, are not expected to be indicative of the inclusion but rather to be related to source characteristics. Therefore, the width of the sliding window for the running median calculation was chosen to be equal to the width of the inclusion, i.e. 5000 m, which reduces fluctuations on smaller scales.

Figure 3.4 shows that attributes A_1 and A_2 are indicative of the subsurface heterogeneity. Both attribute profiles exhibit an anomaly that coincides with the surface projection of the embedded inclusion (highlighted as shaded area bounded by dashed lines). Attribute A_1 shows a broad, negative anomaly and attribute A_2 shows a more confined, positive anomaly. The profile of attribute A_3 does not exhibit any obvious anomalies and is therefore not indicative of the inclusion. These results show that spectral analysis of the quasi-stationary wave-field at the surface, and in particular the use of spectral attribute profiles, is useful to assess the lateral location of the subsurface inclusion. The approach works because the inclusion modifies the ambient wave-field and these modifications can be measured, quantified and mapped along the surface. However, not every attribute is indicative of the origin of the wave-field modification, and therefore, attributes have to be defined carefully to be suitable for the detection of subsurface heterogeneity.

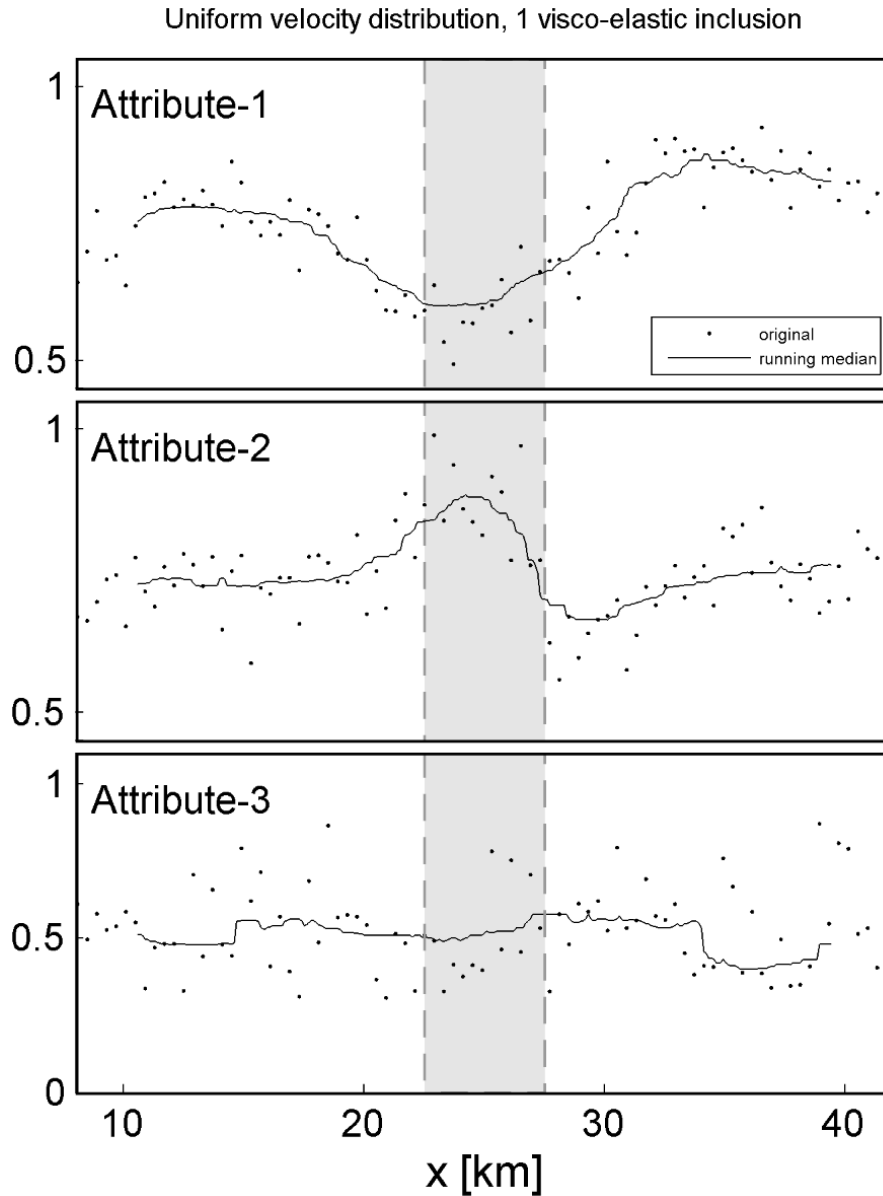


Figure 3.4. Attribute profiles for the model without surface layer. The dots indicate the actual attribute values and the lines are the corresponding running median profiles. The surface projection of the embedded inclusion is highlighted as a shaded area bounded by dashed lines.

Visco-elastic inclusion in elastic medium with surface layer

A possible limitation for the detection of subsurface heterogeneities using spectral analysis of the surface response may arise from strong wave-field modifications introduced by shallow structures. Therefore, a low-velocity surface layer of 100 m thickness is added to the previous model to test whether such shallow inhomogeneity destroys the applicability of spectral attribute profiles for the detection of an embedded inclusion. As shown in Figure 3.1, the model contains the laterally confined inclusion at depth and the laterally persistent surface layer. The P- and S-wave velocities of the layer are 2089 m/s and 1200 m/s, and the density is 1000 kg/m^3 . The

seismic impedance contrast between half-space and surface layer is roughly 3 for both, P- and S-waves. The surface layer behaves fully elastic.

Figure 3.2c shows vertical component seismograms recorded at four different stations of the receiver array. Like in the previous model, all four waveforms show a stable, quasi-stationary wave-field without distinct transient arrivals. However, the corresponding amplitude spectra in Figure 3.2d are distorted compared to the previous model (Figure 3.2b). The general shape of the spectra is no longer controlled by the source wavelets but is mainly related to the presence of the surface layer. Therefore, the vertical amplitude spectra are persistently distorted along the receiver array, as illustrated by the spatial spectrogram in Figure 3.5a. The V/H-ratios displayed in Figure 3.5b exhibit a characteristic feature related to the surface layer. The horizontal-to-vertical spectral ratio of real ambient ground motion, i.e. the inverse of the V/H-ratio, is well-known to show a peak at the fundamental S-wave resonant frequency of the measurement site (Bard, 1999, and references therein). This empirical evidence is for example used for earthquake hazard assessment (e.g. Fäh et al., 1997). For the simple case of a single low-velocity surface layer, the fundamental frequency, f_S , is given by (e.g. Pujol, 2003)

$$f_S = \frac{v_S}{4H}, \quad (3.7)$$

where v_S and H are the S-wave velocity and the thickness of the layer. According to (3.7), f_S equals 3 Hz for the model displayed in Figure 3.1. The distinct and consistent trough around 3 Hz in Figure 3.5b therefore indicates that the wave-field is indeed dominated by effects controlled by the surface layer.

Figure 3.6 shows that the profiles of attribute A_1 and A_2 are indicative of the subsurface heterogeneity. The indication is as significant as for the previous model without surface layer. The profile of attribute A_3 exhibits a weak, positive anomaly that is collocated with the surface projection of the inclusion. Attribute A_3 seems to be sensitive for the inclusion only in the presence of an additional surface layer. This interesting observation needs further investigation which is beyond the scope of this study.

The results of the model with surface layer show that the detection of a deep inhomogeneity is possible despite the presence of a shallow structure that has a significant influence on the characteristic of the surface wave-field. The detection works because of two reasons: First, wave-field modifications caused by the inclusion at depth occur independently of the presence of shallow structures, i.e. the surface layer. Second, only modifications related to the inclusion are confined to its lateral location. Modifications related to the surface layer, on the other hand, occur with the same magnitude at all stations. Although the magnitude of surface layer related modification is much larger compared to modifications introduced by the deep inclusion, the layer does not produce any lateral anomalies that could be misinterpreted as indicative of the inclusion. This synthetic example shows that it is possible to retrieve from

the same data-set information on shallow structures (e.g. the resonance frequency of the site) as well as information on deep inhomogeneities (e.g. the lateral location of an inclusion).

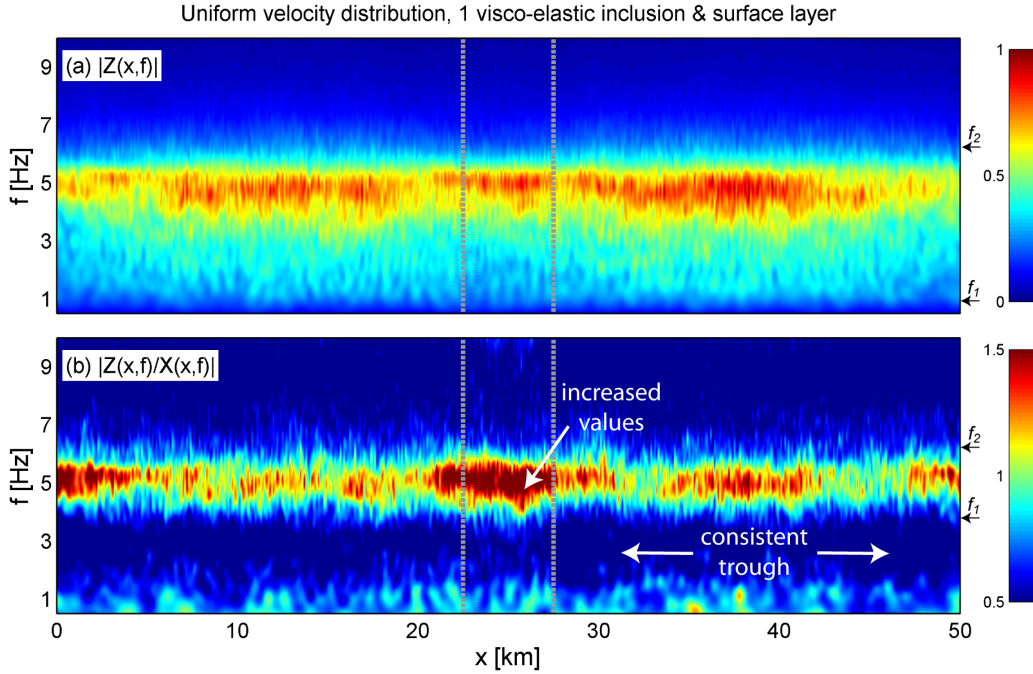


Figure 3.5. *Spatial spectrograms along the free surface of the model with a surface layer on top of the half-space. (a) Normalized amplitude of vertical component. (b) V/H-ratio. Dashed grey lines indicate the locations of the lateral boundaries of the inclusion at depth. The arrows on the right depict the frequency intervals $f_r = [f_1, f_2]$ used for the attribute calculation.*

3.4 EMBEDDED ZONES OF SEISMIC EMISSION

In a second group of models we test the applicability of the spectral analysis methodology to detect zones of continuous active seismic emission embedded in a fully elastic subsurface. The emission is generated by a large number of seismic sources, randomly distributed within the emission zones and randomly activated in time. The sources are implemented as an additional term in the force balance equation for the vertical component and described with a source time function of a Ricker wavelet with central frequency 3 Hz. Each single source radiates P-waves in vertical direction and S-waves with smaller amplitudes in horizontal direction. The superposition of the random signals creates a quasi-stationary wave-field, dominated by vertically traveling P-waves mainly in the frequency band between 1 and 6 Hz.

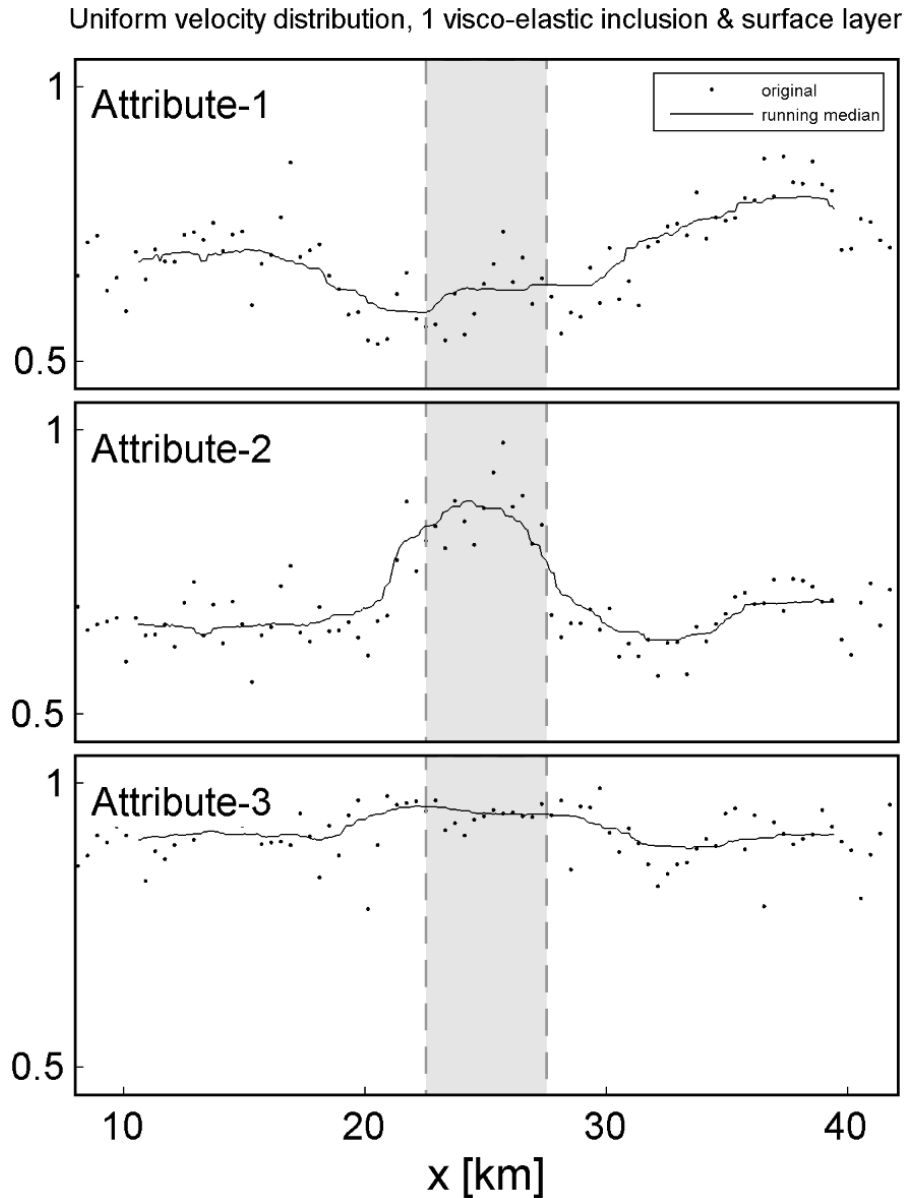


Figure 3.6. Attribute profiles for the model with a surface layer on top of the half-space. The dots indicate the actual attribute values and the lines are the corresponding running median profiles. The surface projection of the embedded inclusion is highlighted as a shaded area bounded by dashed lines.

3.4.1. Two-dimensional models

Uniform velocity distribution, one source zone

We consider a model with properties as shown in Figure 3.7a, but with only source zone-1 being active. The model domain is 16 km long and 3 km deep and filled with an isotropic, elastic medium that has a uniform P-wave velocity of 3098 m/s. Mass density and Poisson's ratio are constant values of 2000 kg/m³ and 0.25, respectively. Zone-1 is the origin of continuous seismic emission and on average there are 8 active sources per second. The dominant wavelength of the signals is around 1 km and therefore in the same order of magnitude as the depth of the

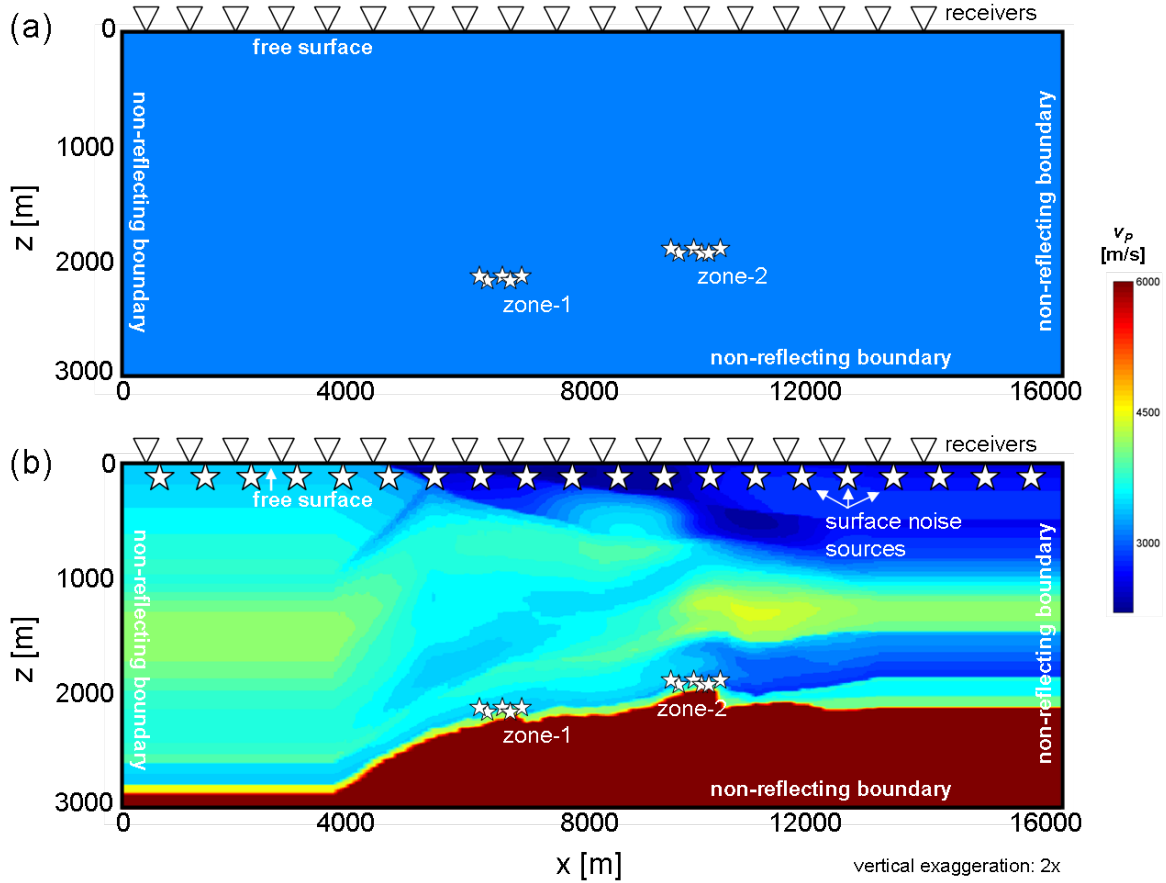


Figure 3.7. Sketches of elastic 2D model domains with two embedded zones of continuous seismic emission. (a) Model with uniform material properties. (b) Realistic model with P-wave velocities, v_p , obtained from a 3D seismic survey at a site in Austria. The stars at the surface schematically illustrate sources of noise. Note the vertical exaggeration of 2.

source zone. A receiver array is located at the free surface of the model with a receiver spacing of 20 m.

Figure 3.8 displays the spatial spectrogram across the receiver array for the vertical component of the wave-field and the V/H-ratio, respectively. Figure 3.8a shows that the largest vertical amplitudes and the highest associated peak-frequencies occur vertically above the zone of seismic emission (depicted with dashed lines) and they both tend to decay laterally in both directions. V/H-ratios in Figure 3.8b show three distinct maxima above the zone of emission but also two maxima away from the emission at low frequencies.

The three attributes are computed using the frequency intervals given in Table 3.1 and indicated as arrows in Figure 3.8. The attribute values are displayed as a function of distance x in Figure 3.9. The dots depict the actual values for every 4th receiver position, computed from 35 seconds of continuous waveforms. The lines show the corresponding running median profiles. The width of the sliding window for the running median calculation was 1000 m. This corresponds to the width of the origin of wave-field modification, i.e. the zone of seismic

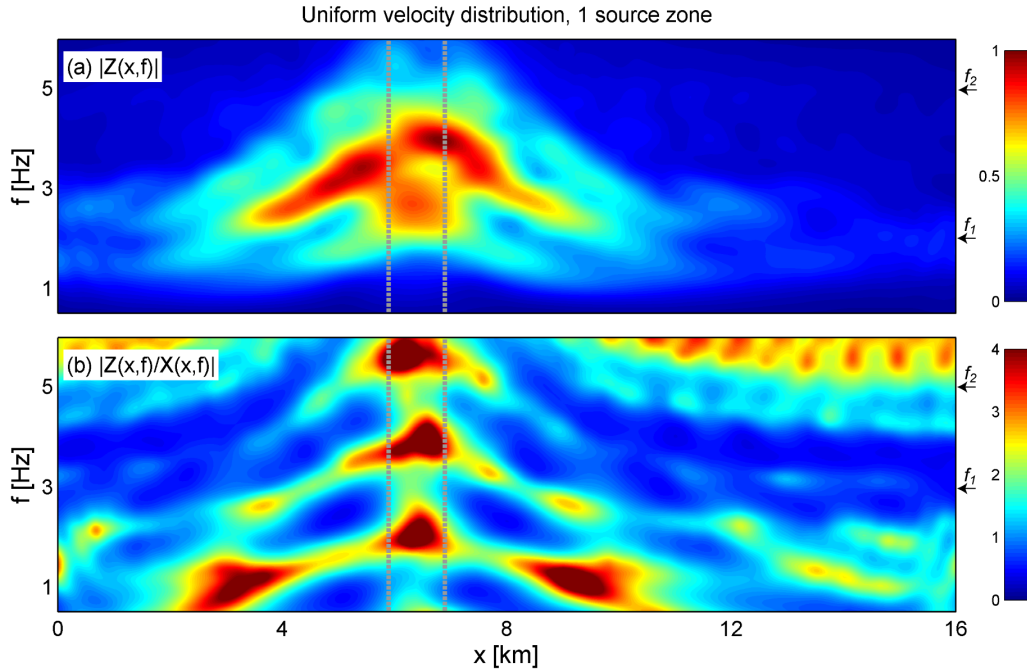


Figure 3.8. *Spatial spectrograms along the free surface of the model with uniform velocity distribution and one embedded source zone. (a) Normalized amplitude of vertical component. (b) V/H-ratio. Dashed lines highlight the surface projection of the lateral boundaries of the source zone at depth. Arrows on the right depict the frequency intervals $f_r = [f_1, f_2]$ used for the attribute calculation.*

emission. As shown in Figure 3.9, fluctuations on smaller scales are reduced and the outliers of attribute A_3 , highlighted with arrows, are removed by the running median procedure.

All three attributes show one large positive anomaly that is collocated with the surface projection of the embedded source zone. The three attributes are therefore indicative of the source zone and the applied spectral analysis of the surface response is suitable to assess the lateral location of the zone.

Uniform velocity distribution, two source zones

We introduce a second zone of seismic emission in the model to investigate the effects of source zone interactions on the shape of the attribute profiles. As shown in Figure 3.7a, the second zone of emission (zone-2) is implemented at a distance of around 3 km from zone-1. Both, the lateral distance between the two source zones and their embedment depth are in the same order of magnitude as the dominant wavelength of the source signals. The two zones are characterized by the same intensity of seismic emission. Figure 3.10a shows the spatial spectrogram of the wave-field's vertical component at the surface. Large spectral amplitudes are not only confined to the lateral location of the embedded sources but also occur between the zones of seismic emission. This is generated by positive interference of signals originating from the two different zones. Also the distribution of V/H-ratios in Figure 3.10b shows a more complicated pattern

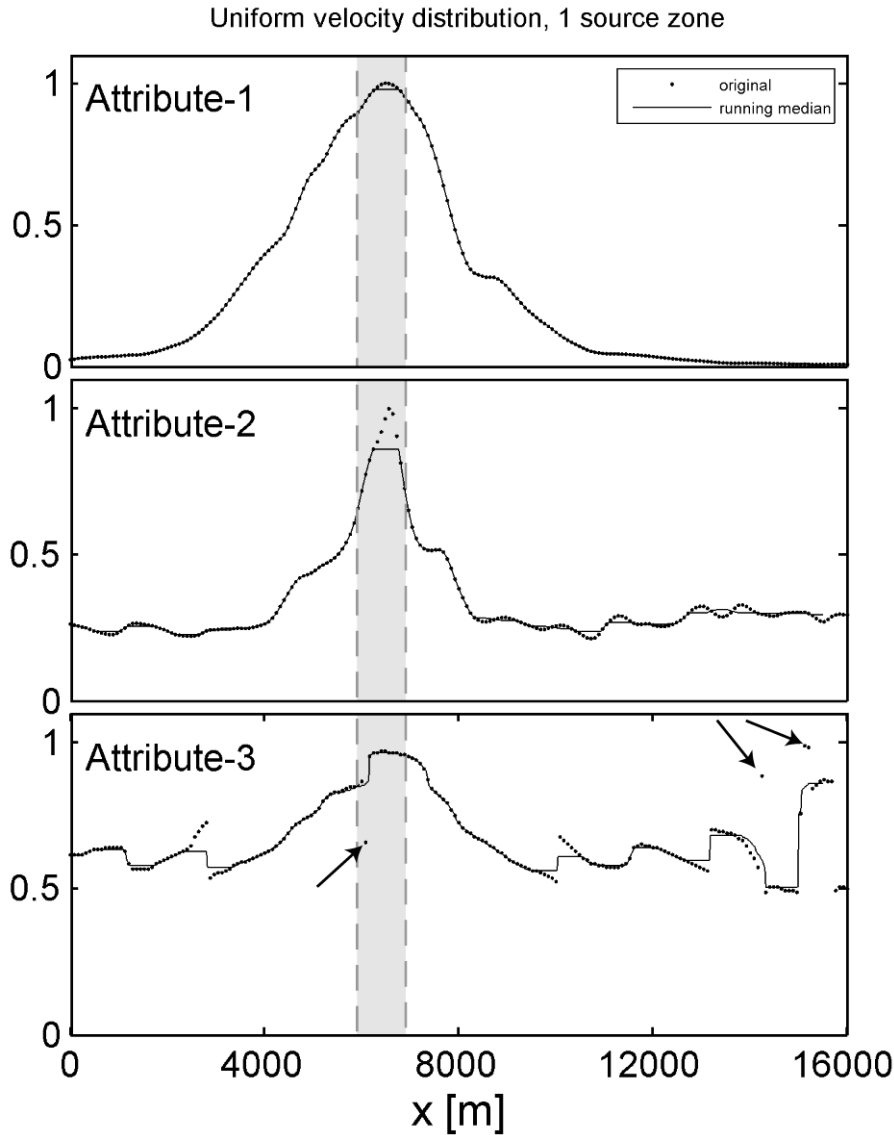


Figure 3.9. Attribute profiles for the model with uniform velocity distribution and only one embedded zone of seismic emission. The dots mark the actual attribute values and the lines indicate the running median profiles. The surface projection of the source zone is highlighted as a shaded area bounded by dashed lines. Arrows indicate examples of outliers that are removed after the running median calculation.

compared to the case with only one source zone. There are several isolated peaks located mostly, but not exclusively, above the two zones of emission.

The spatial pattern of attribute A_1 in Figure 3.11 shows two anomalies whose maxima coincide with the location of the two source zones. However, the spatial resolution is limited as the anomalies tend to merge into one broad anomaly. The resolution provided by attribute A_2 is better and the locations of the individual source zones are clearly indicated by distinct anomalies. The sharp characteristic of anomalies of A_2 was also observed for the model with only one source zone (Figure 3.9) and is therefore a general property of this kind of sources zones. The profile of attribute A_3 is distorted and exhibits many outliers. However, the run-

ning median profile recovers a clear anomaly associated with zone-1. The original attribute values (dots) also indicate an anomaly above zone-2, but the median profile does not preserve a distinct anomaly.

The model of two separated zones of seismic emission identifies limitations in detection capabilities associated to particular attributes: Attribute A_1 offers only limited resolution and therefore struggles to indicate individual source zones that are located too close to each other. Patterns of attribute A_3 are susceptible to distortions caused by interference of signals from multiple zones of emission. For scenarios with two source zones embedded in the medium, attribute A_2 is most significant to assess the lateral locations of the zones.

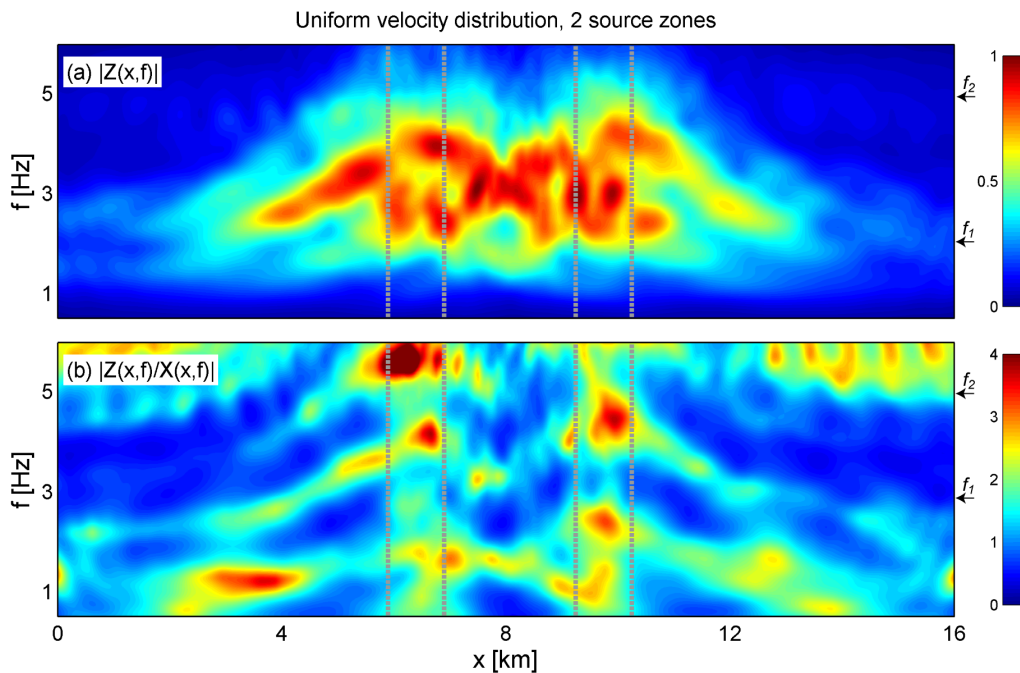


Figure 3.10. *Spatial spectrograms along the free surface of the model with uniform velocity distribution and two embedded source zones. (a) Normalized amplitude of vertical component. (b) V/H-ratio. Dashed lines highlight the surface projection of the lateral boundaries of the source zones at depth. Arrows on the right depict the frequency intervals $f_r = [f_1, f_2]$ used for the attribute calculation.*

Realistic velocity distribution, two source zones

We further extend the complexity of the model by introducing a more realistic velocity distribution, as shown in Figure 3.7b. We use the P-wave velocity model obtained from a 3D seismic survey at an oil and gas field in Voitsdorf, Austria. The total length of the profile was 9 km, covering the range from $x=4$ km to $x=13$ km in Figure 3.7b. The velocities were linearly extrapolated for the model domain beyond those coordinates. Density and Poisson's

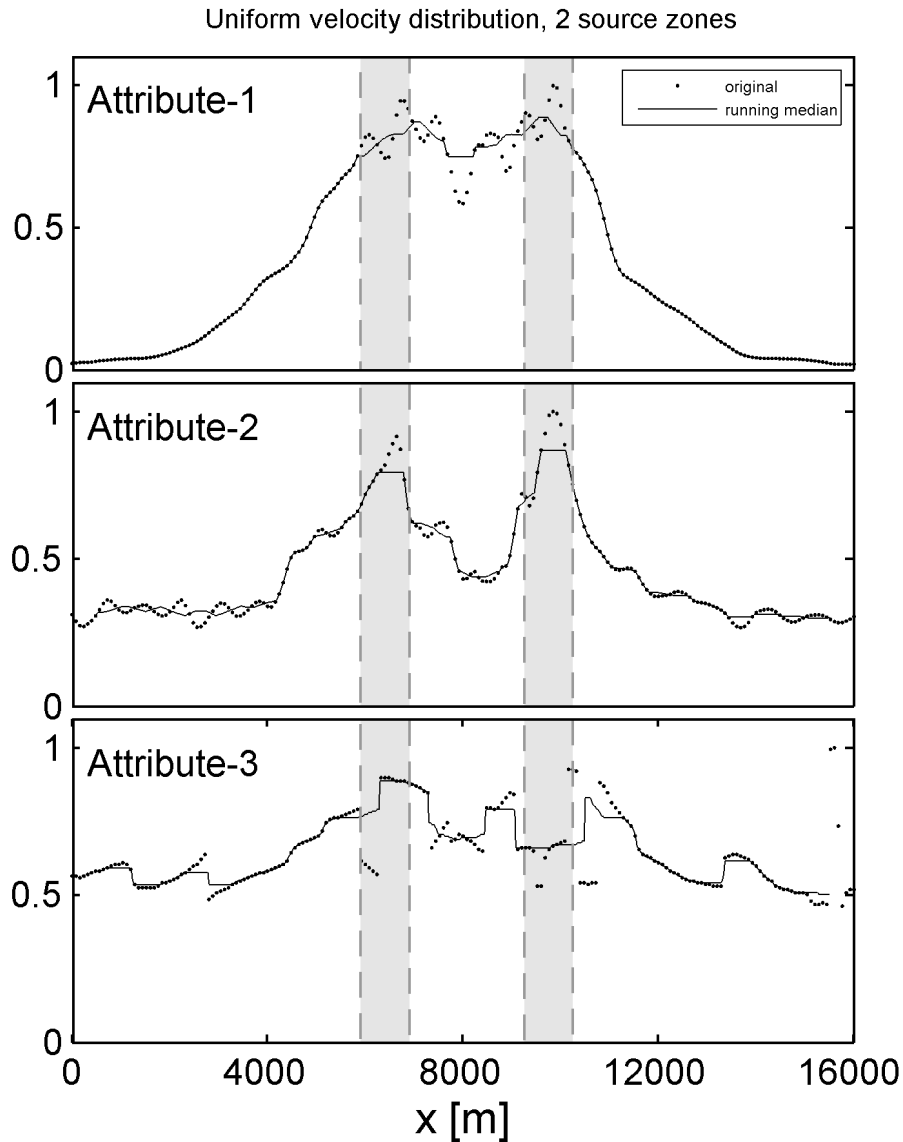


Figure 3.11. Attribute profiles for the model with uniform velocity distribution and two embedded zones of seismic emission. The dots mark the actual attribute values and the lines indicate the running median profiles. The surface projection of the source zones are highlighted as shaded areas bounded by dashed lines.

ratio of the isotropic, elastic medium are kept constant with values of 2000 kg/m^3 and 0.25 , respectively. Similar to the uniform model in the previous section, there are two active zones of seismic emission embedded in the subsurface. These zones coincide with the actual positions of two known hydrocarbon reservoir in the Voitsdorf area. This fact will become important for the discussion in the context of reservoir detection, later in this paper. The surface noise sources indicated in Figure 3.7b are switched off in a first stage.

Figure 3.12 displays the attribute profiles. Similar to the uniform model above, there are generally elevated values of attribute A_1 across both embedded source zones. However, in this case only zone-2 is indicated by a clear maximum and the location of zone-1 is not detectable when analyzing this profile alone. Attribute A_2 is indicative of both source zones, but the

associated anomalies are less pronounced compared to the uniform model, in particular for zone-1. The largest values of attribute A_3 occur directly above the two source zones; however, a qualitative interpretation does not reveal consistent, significant anomalies that can be regarded as reliable indicators for the source locations.

The results of this model show that a complex velocity distribution in combination with two spatially separated source zones can strongly reduce the significance of observed attribute patterns. However, the attribute profiles still contain information on the location of the zones of seismic emission and advanced interpretation methods, such as a quantitative statistical analysis, may allow interpreting such information more reliably.

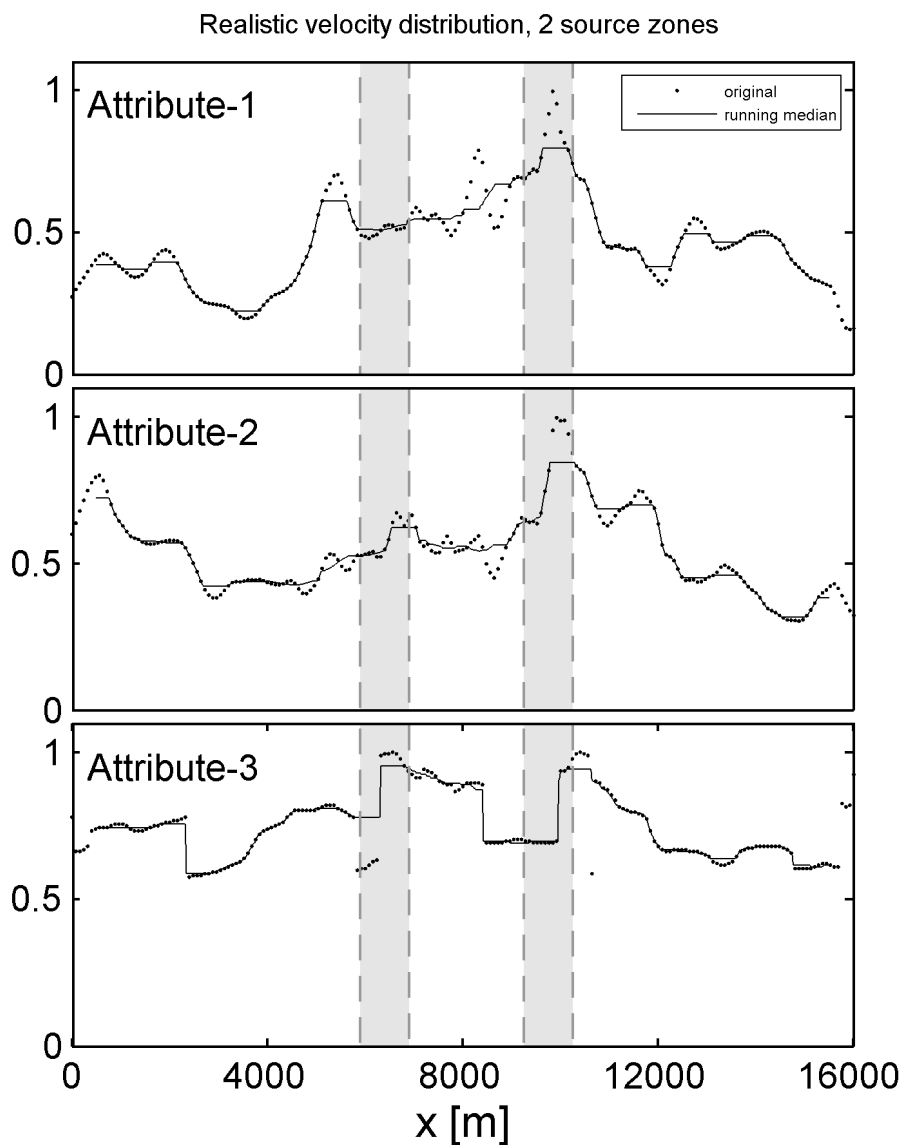


Figure 3.12. Attribute profiles for the model with realistic velocity distribution and two embedded zones of seismic emission. The dots mark the actual attribute values and the lines indicate the running median profiles. The surface projection of the source zones are highlighted as shaded areas bounded by dashed lines.

Surface noise

In real world situations the ambient seismic wave-field is often dominated by signals originating from local surface noise sources (e.g. movements of trees caused by wind, industrial machinery, traffic). We therefore introduce additional noise sources at the model's free surface and study their effect on the attribute values. The noise is modeled by randomly distributed point sources in the top 50 m of the model domain (white stars in Figure 3.7b). Each source is a single force with random orientation. The source time functions are Ricker wavelets with random central frequencies between 1 and 10 Hz, randomly placed in time. The characteristic of the noise wave-field is strongly affected by the near-surface properties of the velocity model. This is demonstrated by the running median profile of attribute A_1 computed from surface noise data alone (simulation without seismic emission at depth). As shown in the top panel of Figure 3.13, this profile (thin line) matches well the distribution of the normalized inverse square of the medium's seismic velocity at the surface (bold line). The normalized inverse square is the same for P- and S-wave velocities because Poisson's ratio is constant across the domain. The reason for the match is the fact that the amplitude of a seismic disturbance is inversely proportional to the propagation velocity in an isotropic elastic solid (e.g. Aki & Richards, 2002). Attribute A_2 is not sensitive for this effect because it cancels out when computing the V/H-ratio. This is shown by the profile in the middle panel of Figure 3.13 which is almost constant with distance. Attribute A_3 , computed from the surface noise data alone, does not show any interpretable patterns related to the properties of the medium. Since this attribute quantifies the spectral frequencies of dominant signals, the values are expected to be controlled by the local, randomly generated frequency content of the surface noise. The local scattering of the values observed for all three attributes (dots in Figure 3.13) reflects the random nature of the surface noise model.

Figure 3.14 shows the attribute profiles of the model with both, embedded zones of seismic emission in the subsurface and strong noise at the surface (model domain is shown in Figure 3.7b). The magnitude of the surface noise is chosen to yield an average S/N-ratio of 0.1 at the surface. The sum of the energy recorded at all surface receivers that originates from the two embedded source zones is therefore ten times smaller compared to the sum of the energy that is introduced by the surface noise sources. The individual attribute values (dots) and the shape of the corresponding running median profiles (thin solid lines) are almost identical to the results presented for the model with surface noise only (Figure 3.13). This indicates that, for such a scenario, shallow structures and surface noise have an overwhelming influence and control the shape of the attribute profiles. Signatures related to the seismic emission at depth are masked by the dominant nature of the surface noise and it is not possible to detect the source zones based on the results shown in Figure 3.14. However, the signatures are just masked and not

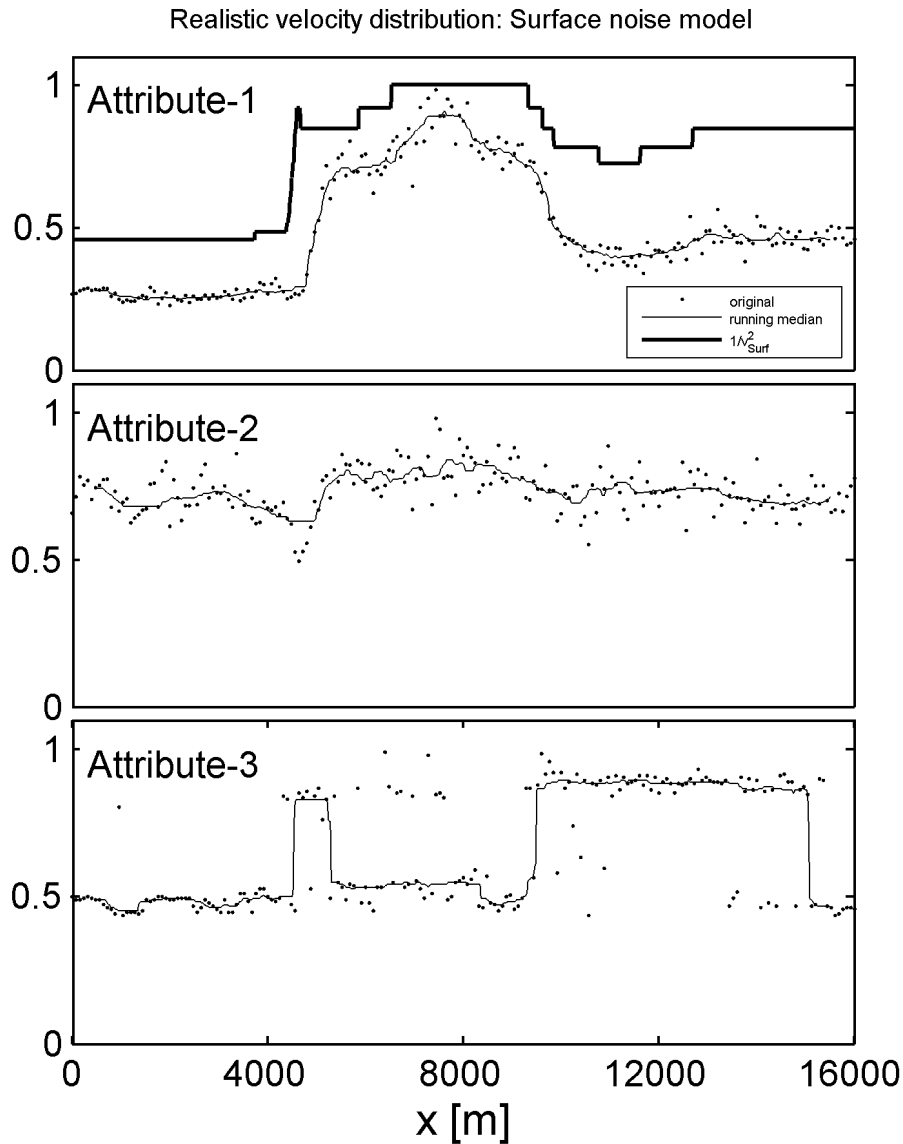


Figure 3.13. Attribute profiles for the surface noise model. The model domain is shown in Figure 3.7b. The two embedded zones of seismic emission were switched off and only the surface noise sources were active. Dots mark the actual attribute values and the lines indicate the running median profiles. The bold line in the top panel shows the normalized inverse square of the seismic velocity along the surface (same for P- and S-waves).

lost. The information related to the presence of the source zones is still in the data and can be recovered by applying appropriate processing techniques.

Frequency-wavenumber (F-K) filters are routinely applied to conventional seismic data to suppress surface noise such as for example ground roll (Yilmaz, 1987). Here, we use F-K filtering to reduce surface noise in the synthetic data. The filter removes signals with apparent velocities of 6000 m/s and less, which includes the surface waves and body waves propagating along the surface. The running median attribute profiles computed from the filtered data are shown as bold dash-dotted lines in Figure 3.14. Attributes A_1 and A_2 reveal pronounced anomalies that

are collocated with the two embedded seismic source zones. The result for attribute A_3 is less significant, but also for this attribute the result has improved for the filtered data.

This model demonstrates that signatures from deeper sources can be masked by strong surface noise in unprocessed data. However, information related to deep sources is still present and F-K filtering is a useful means for recovering such information in attribute profiles.

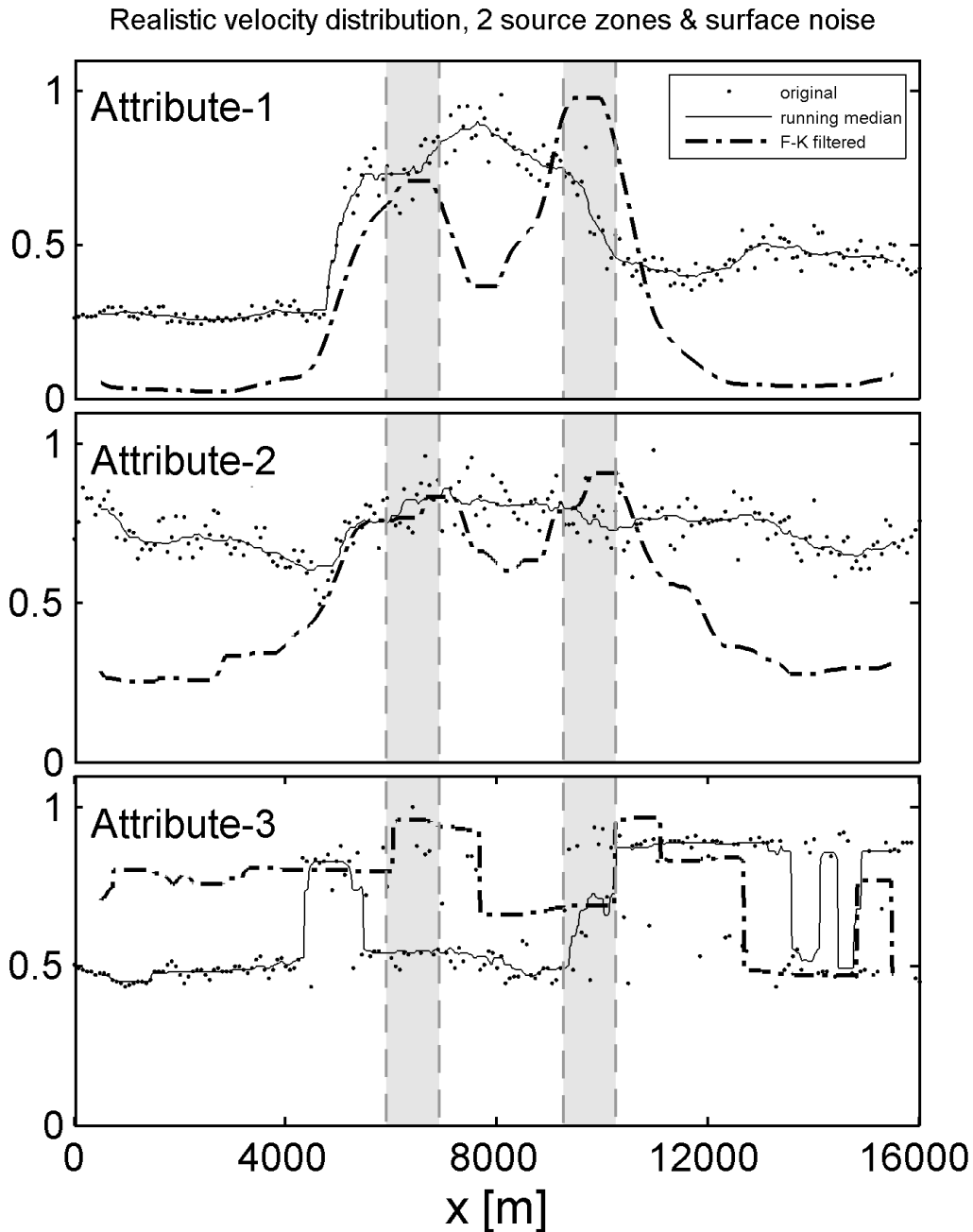


Figure 3.14. Attribute profiles for the model with realistic velocity distribution, two embedded zones of seismic emission and additional surface noise. The dots mark the actual attribute values and the thin solid lines indicate the running median profiles. Bold, dash-dotted lines show the running median profiles computed from the data after F-K filtering. The surface projection of the source zones are highlighted as shaded areas bounded by dashed lines.

3.4.2. Three-dimensional model

We create a more realistic scenario by extending the previous model to three dimensions. Such a model is closer to real world because it is based on the full 3D Greens' functions and allows considering out-of-plane effects. Specifically, we are interested in the limitations of F-K filtering applied to a 2D cross-section extracted from the 3D model. F-K filtering applied to a cross-section is expected to be less effective for the 3D case because surface waves with oblique incidence can not be removed by the filter. This shortcoming does not occur in the 2D case above.

The numerical domain of the 3D model is 20 km long, 10 km wide and 5 km deep. It is divided into cubic cells of 10 by 10 by 10 meters. This leads to a total number of $(1000)^3$ grid-points. The total physical time of the calculation was 22.5 seconds, corresponding to 15'000 time-steps. Such large-scale models are computationally expensive and it is mandatory to use a parallel code on a high-performance computing cluster.

The realistic P-wave velocity distribution of the medium is obtained from the same 3D seismic survey in the Voitsdorf area as for the 2D model above. Mass density and Poisson's ratio are constant values of 2000 kg/m^3 and 0.25, respectively. Figure 3.15 shows a part of the 3D model domain. The two depth slices at $z=500 \text{ m}$ and $z=1500 \text{ m}$ and the vertical slice at $y=5400 \text{ m}$ visualize the 3D P-wave velocity distribution. The velocity values are linearly extrapolated for locations beyond $x=13 \text{ km}$. The stars schematically illustrate randomly distributed sources within two separate zones of active seismic emission, indicated as bar-shaped boxes in the subsurface (100 sources per box). These zones coincide with the approximate positions of the two known hydrocarbon reservoir in the Voitsdorf area. A regular receiver grid at the free surface ($z=0 \text{ m}$) with a spacing of 100 m measures the wave-field over time. The vertical slice at $y=5400 \text{ m}$ was used for to the above 2D model (Figure 3.7b).

Two source-zones at depth

Figure 3.16 displays contourplots for attribute A_1 and A_2 across the free surface of the 3D model. The attribute values are computed using the frequency intervals indicated in Table 3.1. The plots show the spatial patterns of the attributes in a map view. The surface projection of the boundaries of the zones of emission at depth is indicated as grey, dashed lines. The results in Figure 3.16 show a generally good match between elevated attribute values and the location of the embedded source zones. Both attributes are therefore useful for mapping the source zones. However, the resolution is limited and the attribute patterns are locally distorted due to effects of the complex velocity distribution in the media. For example, zone-1 between $y=2 \text{ km}$ and $y=5 \text{ km}$ is only poorly indicated.

The dotted lines in Figure 3.17 show the running median attribute profiles extracted from a cross-section through the 3D model. The location of the cross-section is highlighted as a green

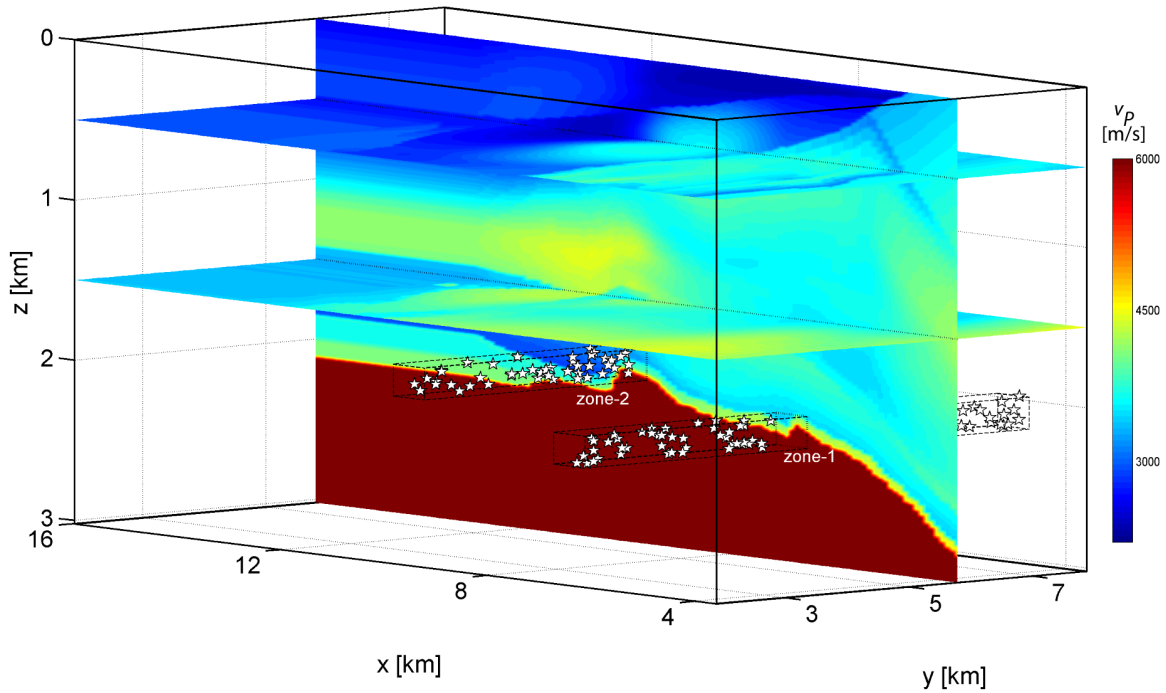


Figure 3.15. *3D model domain with two embedded zones of continuous seismic emission (bar-shaped boxes). The P-wave velocities, v_P , are obtained from a 3D seismic survey at a site in Austria. The slice at $y=5400$ m corresponds to the velocity distribution of the 2D model shown in Figure 3.7b. Note the vertical exaggeration of 2.*

line in Figure 3.16. The same section was already used for the above 2D model with realistic velocity distribution. Both attributes show two distinct anomalies along this profile and the anomalies are collocated with the subsurface source zones (indicated as grey shaded areas in Figure 3.17). The source zone indication in the 3D case is more significant compared to the corresponding results for the noise-free 2D model, shown in Figure 3.12.

Two source-zones at depth and surface noise

Similar to the 2D case above, we introduce surface noise sources in such a way to obtain a data-set with an average S/N-ratio of 0.1. The thin solid lines in Figure 3.17 display the corresponding attribute profiles along the cross-section highlighted in green in Figure 3.16. As for the 2D model, the attribute patterns are mainly controlled by shallow structures and surface noise characteristics. Signatures related to the seismic emission at depth are masked by the dominant nature of the surface noise. In an attempt to recover the masked information, we apply the same 2D F-K filter as for the example of the 2D model with surface noise (i.e. minimum apparent velocity of 6000 m/s). The attribute profiles computed from the filtered data are shown as bold dash-dotted lines in Figure 3.17. The anomaly of attribute A_1 associated with source zone-1 is successfully recovered. The procedure failed for zone-2 where no anomalously increased values are observed. This results in a false negative prediction of the source zone location. The profiles for attribute A_2 indicate both source zones after F-K filtering. However,

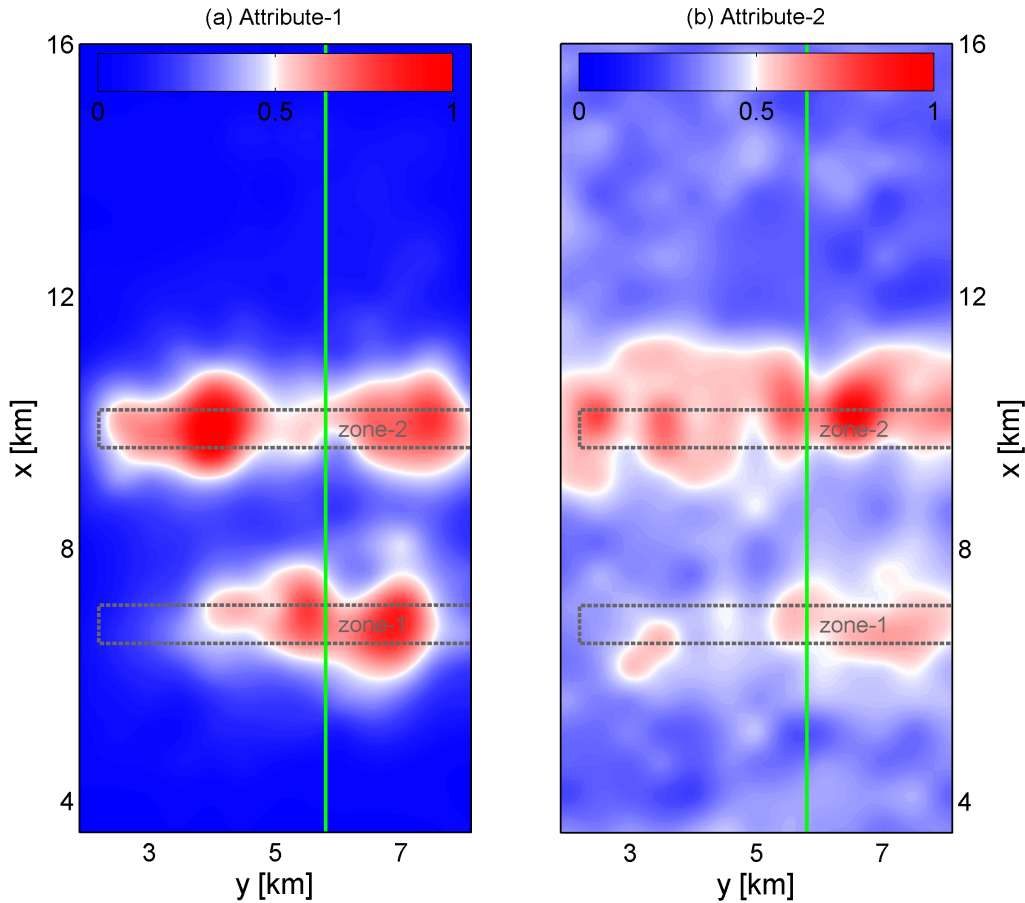


Figure 3.16. Contourplots for attribute A_1 and A_2 across the free surface of the 3D model. Dashed, grey lines indicate the boundaries of the surface projection of the embedded source zones. The green line denotes the location of the profile shown in Figure 3.17 and coincides with the cross-section used for the above 2D model.

the attribute profiles computed from filtered data also exhibit new anomalies at locations where no sources are embedded at depth. This results in a false positive prediction. The results show that F-K filtering applied to a cross-section is less efficient in the 3D case compared to the 2D case. Nevertheless, also in the 3D case signatures related to deep subsurface sources can be recovered from data that is dominated by surface noise. However, the results must be interpreted carefully because both, false negative and false positive predictions can occur.

3.5 DISCUSSION

The interpretation of attribute profiles presented here focuses on the horizontal location of the origin of wave-field modifications and our interpretation is qualitative only. A promising future improvement would be quantitative, statistical correlation analysis as described, for example, in [Avseth et al. \(2005\)](#). Such methods are already successfully applied to enhance the significance of conventional seismic attributes (e.g. [Chopra & Marfurt, 2005](#)). Figure 3.12 shows for a complex case that not all attributes are clearly indicative of all the zones of seismic emission

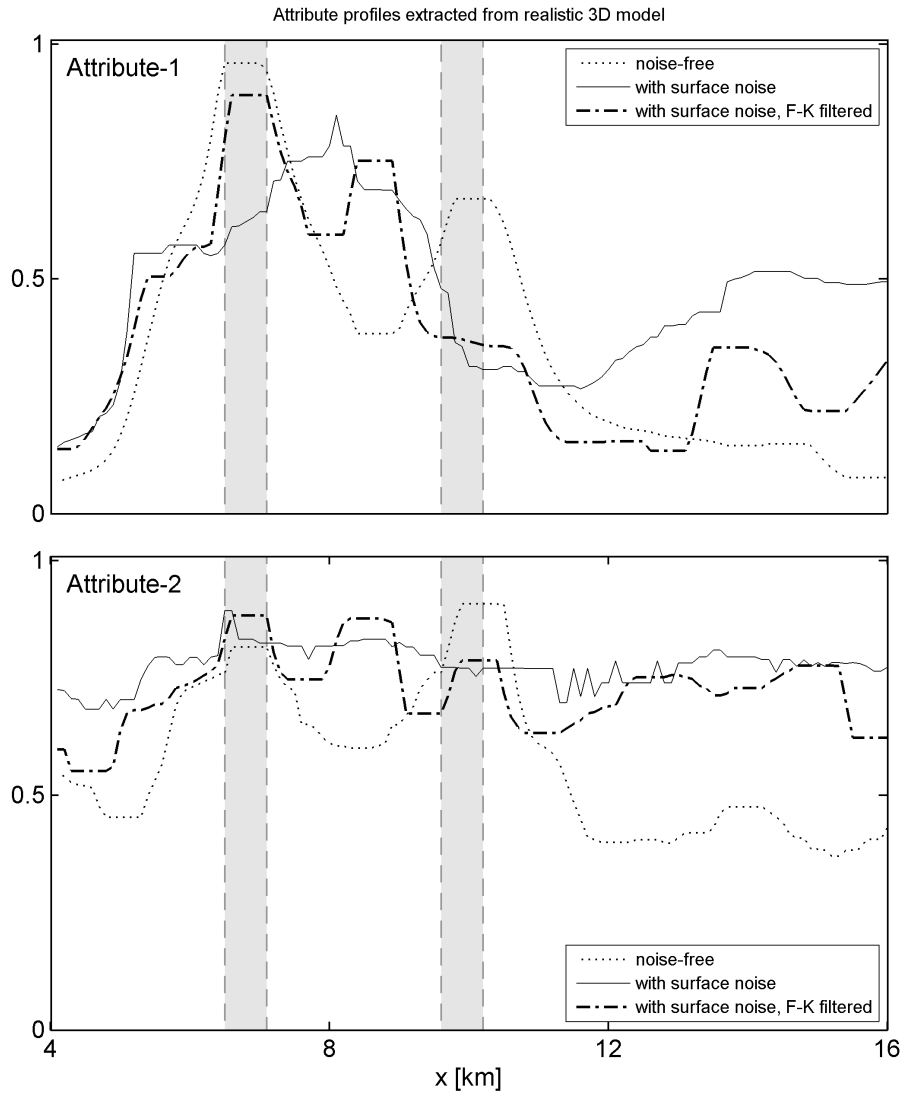


Figure 3.17. Attribute profiles extracted from a cross-section through the 3D model. The location of the cross-section is shown as a green line in Figure 3.16. Dotted lines are the running median profiles for the noise-free model. Thin solid lines show the profiles for the model with additional surface noise. Bold dash-dotted lines show the result of 2D F-K filtering applied to the noise-contaminated data. The surface projection of the source zones are highlighted as shaded areas bounded by dashed lines.

(false negatives). There are also anomalies at locations where in fact is no seismic emission at depth (false positives), for example the peak of attribute A_1 at $x \approx 5500$ m in Figure 3.12. A way to improve the significance of a statistical correlation analysis in such a case consists in a combined, quantitative interpretation of several attributes (Avseth et al., 2005). One possibility is to determine and calibrate a characteristic attributes pattern (“fingerprint”) for a known subsurface feature and then compare this pattern with patterns from data measured in exploration areas where similar features are suspected. This could be applied in regions with a more or less similar geology. Features of interest can include for example cavities (Nasseri-Moghaddam et al., 2007) or hydrocarbon reservoirs, as discussed below.

Applicability to hydrocarbon reservoir detection

The models in the section “Embedded inhomogeneity” consider a visco-elastic inclusion with minimum Q of 2.2 interacting with a quasi-stationary wave-field originating from sources below the inclusion. We argue that this set-up may be considered as a considerably simplified but nevertheless realistic first-order approximation for a hydrocarbon reservoir interacting with the ambient wave-field in nature, mainly because of two reasons. First, there is an omnipresent ambient seismic wave-field in nature which contains body waves in the subsurface. This is also the basic assumption for passive seismic interferometry for imaging reflectors (Draganov et al., 2010). For example, Zhang et al. (2009) showed that the ambient wave-field at low seismic frequencies (between 0.6 and 2 Hz) is dominated by continuous P-wave energy arriving from beneath the station-arrays at two sites in California. Generally, the ambient wave field is a combination of body and surface waves where the actual composition of the wave field varies and has to be determined for each site separately. Second, high attenuation properties of hydrocarbon reservoirs can be observed in nature, especially at low frequencies. For example, Dasgupta & Clark (1998) and Korneev et al. (2004) analyzed active seismic data and found Q -values of 10 and smaller for reservoir rocks. Also, based on White’s model for wave-induced fluid flow (White, 1975), Quintal et al. (2009) showed that Q -values (i) are frequency dependent, (ii) can theoretically be as small as 2 for realistic petrophysical parameter values of sandstones partially saturated with gas and water and (iii) can be approximated with an equivalent visco-elastic model which is the one used in our simulations.

Green & Greenhalgh (2009) argued that it is hardly possible to estimate properties of shallow sediments and simultaneously extract accurate information on deep hydrocarbon reservoirs. The synthetic tests in our study indicate that this must not necessarily be always the case. Information on shallow structures (e.g. the resonance frequency of a shallow sedimentary layer) as well as information on deep inhomogeneities (e.g. an inclusion with high attenuation, representing a reservoir) could be retrieved from the same data-set. The V/H spectrogram in Figure 3.5b shows both, the spectral response of the shallow layer (i.e. the consistent trough around 3 Hz), and the spectral response of the inclusion (i.e. the increased values around 5 Hz above the location of the inclusion). Information on deep and shallow structures is thus complementary and not mutually exclusive. However, the detectability of reservoir-related modifications in real ambient ground-motion depends on the relative strength of such signals at the receiver location. Of course, the spectral attribute approach will fail if surface noise or other non-reservoir related signatures are overwhelming. However, the sole presence of shallow structures and surface noise does not *a priori* make the spectral analysis unsuitable for detecting underground objects.

A method to increase the S/N-ratio consists in F-K filtering applied to array data along a 2D cross-section. A critical issue with sparsely sampled field data consists in spatial aliasing.

This phenomenon introduces spurious signals (artifacts) in the data during the filter process and can lead to meaningless results. This is illustrated in Figure 3.18 for the above example of a 2D model with additional surface noise. The bold solid line shows the F-K filtered profile of attribute A_2 for an array with a receiver spacing of 20 m. This line corresponds to the result in the middle panel of Figure 3.14 where the attribute anomalies could be successfully retrieved after F-K filtering. Increasing the receiver spacing to larger values of 200 m, 300 m and 400 m (circles, crosses and triangles in Figure 3.18) reveals the increasing influence of spatial aliasing and the anomalies are eventually lost. For this particular scenario, a maximum receiver spacing of 200 m is allowed to guarantee a reasonably well performance of the F-K filter. As shown for the 3D model above, another critical issue of F-K filtering consists in surface waves with oblique incidence on the cross-section because such waves are hardly removed by a 2D F-K filter. This problem can be overcome with a densely spaced 2D receiver array (e.g. a regular grid) and a 3D F-K filter ($f - k_x - k_y$ domain).

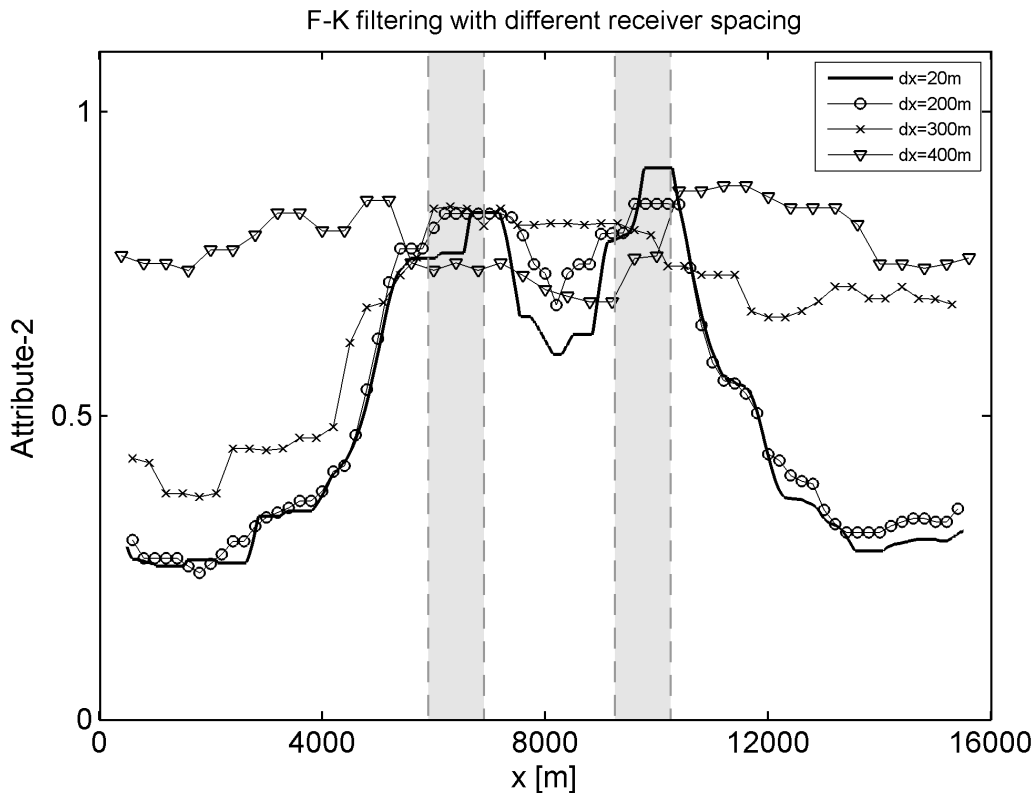


Figure 3.18. Profiles of attribute A_2 computed from the data after F-K filtering with different receiver spacing (model with realistic velocity distribution, two embedded zones of seismic emission and additional surface noise). The bold solid line is derived from a densely spaced receiver array and clearly indicates the two zones of emission. The other profiles suffer from processing artifacts due to sparse receiver covering and are less significant in terms of source zone indication. The surface projection of the source zones are highlighted as shaded areas bounded by dashed lines.

3.6 CONCLUSIONS

We presented a method to detect the horizontal location of the origin of subsurface quasi-stationary wave-field modifications. The method uses spectral attributes extracted from the seismic response at the surface of the medium. Numerical modeling shows that the method is applicable to both, subsurface heterogeneities interacting with an ambient wave-field (passive modification) and embedded zones of active seismic emission (active modification). Attribute profiles are indicative of the location of wave-field modifications also for models with realistic subsurface material properties and in the presence of additional shallow structures. In particular, the spectral response of both, a low-velocity surface layer and an inclusion with high attenuation could be retrieved from the same data. A complex subsurface can have strong influences on lateral attribute patterns. In such a scenario, not all attributes are equally well suited for locating the effects at depth. Significant surface noise can mask signatures related to such effects. F-K filtering applied to array data along a cross-section is a useful tool to enhance the S/N-ratio and to retrieve the signatures in attribute profiles. The spacing of receivers is a critical parameter and special caution is needed in case of obliquely incident surface waves.

Both fundamental assumptions for the scenario with an embedded inclusion of high attenuation (passive modification) can apply for some hydrocarbon reservoirs. First, there is an omnipresent ambient wave-field which contains body waves from depth. Second, high attenuation of reservoirs in the low-frequency range can be observed. Considering the numerical results in this study, it is physically justified to apply the proposed spectral analysis to real ambient ground-motion recordings in an attempt to increase the probability of detecting hydrocarbon reservoirs. We do not claim that the presented models explain observed spectral attribute variations across reservoirs. But the models show that seismic wave propagation and scattering in visco-elastic media is a reasonable physical mechanism that can generate spectral anomalies at the surface. These anomalies can be indicative of deep wave-field modifications, despite the presence of shallow structures. Moreover, numerical modeling is useful for feasibility assessment and survey planning. Such surveys are an important step to eventually better understand the physics of observed spectral anomalies above reservoirs.

This paper discusses an application to possible reservoir-related signals. However, the proposed methodology can be applied to locate the origin of any detectable quasi-stationary wave-field modification. This may include for example volcanic tremor, non-volcanic tremor and shallow heterogeneities acting as surface wave scatterer.

ACKNOWLEDGEMENTS

We thank Rohöl-Aufsuchungs Aktiengesellschaft (RAG) for the permission to publish the geophysical data used for this study. We acknowledge the financial support of the Swiss Commission for Technology and Innovation (CTI) and Spectraseis. E.H. Saenger thanks the DFG (Deutsche Forschungsgemeinschaft) for their support through the Heisenberg Programme (SA 996/1-1).

References

- Aki, K. & Richards, P. (2002). *Quantitative Seismology (2nd edition)*. University Science Books. ISBN 0-935702-96-2.
- Ali, M., Berteussen, K., Small, J., Anjana, B. & Barkat, B. (2009). *Recent Passive Experiments in Abu Dhabi. EAGE Workshop on Passive Seismic: Case Studies and Applications for Field Development and Exploration*. Paper presented at the EAGE Workshop Passive Seismic: Exploration and Monitoring Applications, 2009, Limassol, Cyprus, Expanded Abstracts, p. A36.
- Avseth, P., Mukerji, T. & Mavko, G. (2005). *Quantitative Seismic Interpretation – Applying Rock Physics Tools to Reduce Interpretation Risk*. Cambridge University Press. ISBN 0521816017.
- Bard, P.-Y. (1999). *Microtremor measurements: A tool for site effect estimation?* In: *The Effects of Surface Geology on Seismic Motion* (eds K. Irikura, K. Kudo, K. Okada and T. Sasatami) [Balkema, Rotterdam, The Netherlands.], pp. 1251–1279.
- Beresnev, I. A., Dennis Vigil, R., Li, W., Pennington, W. D., Turpening, R. M., Iassanov, P. P. & Ewing, R. P. (2005). *Elastic waves push organic fluids from reservoir rock*. *Geophysical Research Letters*, **32**, L13303.
- Bonnefoy-Claudet, S., Cotton, F. & Bard, P. (2006). *The nature of noise wavefield and its applications for site effects studies: A literature review*. *Earth-Science Reviews*, **79**, 205–227.
- Brown, J. R., Beroza, G. C., Ide, S., Ohta, K., Shelly, D. R., Schwartz, S. Y., Rabbel, W., Thorwart, M. & Kao, H. (2009). *Deep low-frequency earthquakes in tremor localize to the plate interface in multiple subduction zones*. *Geophysical Research Letters*, **36**, L19306.
- Cerjan, C., Kosloff, D., Kosloff, R. & Reshef, M. (1985). *A nonreflecting boundary condition for discrete acoustic and elastic wave equations*. *Geophysics*, **50**, 705–708.

- Chopra, S. & Marfurt, K. (2005). *Seismic attributes – A historical perspective*. *Geophysics*, **70**, 3S0–28S0.
- Courant, R., Friedrichs, K. & Lewy, H. (1967). *On the partial difference equations of mathematical physics*. *IBM Journal*, **March 1967**, 215–234.
- Dangel, S., Shaepman, M. E., Stoll, E. P., Carniel, R., Barzandji, O., Rode, E.-D. & Singer, J. M. (2003). *Phenomenology of tremor-like signals observed over hydrocarbon reservoirs*. *J. Volcanol. Geothermal Res.*, **128**, 135–158.
- Dasgupta, R. & Clark, R. A. (1998). *Estimation of Q from surface seismic reflection data*. *Geophysics*, **63(6)**, 2120–2128.
- Di Grazia, G., Falsaperla, S. & Langer, H. (2006). *Volcanic tremor location during the 2004 Mount Etna lava effusion*. *Geophysical Research Letters*, **33**, L04304.
- Draganov, D., Ghose, R., Ruigrok, E., Thorbecke, J. & Wapenaar, K. (2010). *Seismic interferometry, intrinsic losses and Q -estimation*. *Geophysical Prospecting*, **58**, 361–373.
- Emmerich, H. & Korn, M. (1987). *Incorporation of attenuation into time-domain computations of seismic wave-fields*. *Geophysics*, **52**, 1252–1264.
- Fäh, D., Ruettener, E., Noack, T. & Kruspan, P. (1997). *Microzonation of the city of Basel*. *Journal of Seismology*, **1**, 87–102.
- Frehner, M., Schmalholz, S. M. & Podladchikov, Y. (2009). *Spectral modification of seismic waves propagating through solids exhibiting a resonance frequency: a 1-D coupled wave propagation–oscillation model*. *Geophys. J. Int.*, **176**, 589–600.
- Fäh, D., Kind, F. & Giardini, D. (2003). *Inversion of local S -wave velocity structures from average H/V ratios, and their use for the estimation of site-effects*. *Journal of Seismology*, **7**, 449–467.
- Goloshubin, G., Vanschuyver, C., Korneev, V., Silin, D. & Vingalov, V. (2006). *Reservoir imaging using low frequencies of seismic reflections*. *The Leading Edge*, **May 2006**, 527–531.
- Green, A. & Greenhalgh, S. (2010). *Comment on "Low-frequency microtremor anomalies at an oil and gas field in Voitsdorf, Austria" by Marc-André Lambert, Stefan Schmalholz, Erik H. Saenger and Brian Steiner*, *Geophysical Prospecting* **57**, 393–411. *Geophysical Prospecting*, **58**, 335–339.

- Green, A. G. & Greenhalgh, S. (2009). *Microtremor spectra: a proven means for estimating resonant frequencies and S-wave velocities of shallow soils/sediments, but a questionable tool for locating hydrocarbon reservoirs*. *First Break*, **July 2009**, 43–50.
- Kallweit, R. S. & Wood, L. C. (1982). *The limits of resolution of zero-phase wavelets*. *Geophysics*, **47**, 1035–1046.
- Klimentos, T. (1995). *Attenuation of P- and S-waves as a method of distinguishing gas and condensates from oil and water*. *Geophysics*, **60(2)**, 447–458.
- Korneev, V. (2008). *Slow waves in fractures filled with viscous fluid*. *Geophysics*, **73**, N1–N7.
- Korneev, V., Goloshubin, G. M., Daley, T. M. & Silin, D. B. (2004). *Seismic low-frequency effects in monitoring fluid-saturated reservoirs*. *Geophysics*, **69**, 522–532.
- Korneev, V. & Johnson, L. R. (1996). *Scattering of P and S Waves by a Spherically Symmetric Inclusion*. *Pure and Applied Geophysics*, **147(4)**, 675–718.
- Kristek, J. & Moczo, P. (2003). *Seismic wave-propagation in viscoelastic media with material discontinuities: A 3D fourth-order staggered-grid finite-difference modelling*. *Bull. Seismol. Soc. Am.*, **93(5)**, 2273–2280.
- Lambert, M.-A., Schmalholz, S. M., Saenger, E. H. & Steiner, B. (2009). *Low-frequency microtremor anomalies at an oil and gas field in Voitsdorf, Austria*. *Geophysical Prospecting*, **57**, 393–411. doi:10.1111/j.1365-2478.2008.00734.x.
- Lambert, M.-A., Schmalholz, S. M., Saenger, E. H. & Steiner, B. (2010). *Reply to comment on "Low-frequency microtremor anomalies at an oil and gas field in Voitsdorf, Austria" by Marc-André Lambert, Stefan M. Schmalholz, Erik H. Saenger and Brian Steiner*, *Geophysical Prospecting* 57, 393–411. *Geophysical Prospecting*, **58**, 341–346.
- Liu, Y., Wu, R.-S. & Ying, C. F. (2000). *Scattering of elastic waves by an elastic or viscoelastic cylinder*. *Geophys. J. Int.*, **142**, 439–460.
- van Mastrigt, P. & Al-Dulaijan, A. (2008). *Seismic spectroscopy using amplified 3C geophones*. Paper presented at the 70th EAGE Conference & Exhibition, Rome, Italy, Expanded Abstracts, p. B047.
- Nasseri-Moghaddam, A., Cascante, G. & Hutchinson, D. (2005). *A New Quantitative Procedure to Determine the Location and Embedment Depth of a Void Using Surface Waves*. *Journal of Environmental and Engineering Geophysics*, **10(1)**, 51–64.

- Nasseri-Moghaddam, A., Cascante, G., Phillips, C. & Hutchinson, D. (2007). *Effects of underground cavities on Rayleigh waves - Field and numerical experiments*. Soil Dynamics and Earthquake Engineering, **27**, 300–313.
- Okada, H. (2003). *The Microtremor Survey Method*. Geophysical Monograph Series No. 12, SEG, Tulsa, USA. ISBN 1-56080-120-4.
- Pujol, J. (2003). *Elastic Wave Propagation and Generation in Seismology*. Press Syndicate of the University of Cambridge, Cambridge, UK. ISBN 0-521-52046-0.
- Quintal, B., Schmalholz, S. & Podladchikov, Y. Y. (2009). *Low-frequency reflections from a thin layer with high attenuation caused by interlayer flow*. Geophysics, **74**(1), N15–N23.
- Rutledge, J. T., Phillips, W. S. & Schusseler, B. K. (1998). *Reservoir characterization using oil-production-induced microseismicity, Clinton County, Kentucky*. Tectonophysics, **289**, 129–152.
- Saenger, E. H., Gold, N. & Shapiro, S. A. (2000). *Modeling the propagation of elastic waves using a modified finite-difference grid*. Wave Motion, **31**, 77–92.
- Saenger, E. H., Schmalholz, S. M., Lambert, M.-A., Nguyen, T. T., Torres, A., Metzger, S., Habiger, R., Müller, T., Rentsch, S. & Mendez-Hernández, E. (2009). *A passive seismic survey over a gas field: Analysis of low-frequency anomalies*. Geophysics, **74**, O29–O40.
- Saenger, E. H. & Shapiro, S. A. (2005). *Seismic effects of viscous Biot-coupling: Finite difference simulations on micro-scale*. Geophysical Research Letters, **32**, L14310.
- Schechinger, B., Goertz, A., Artman, B., Lambert, M.-A., Koerbe, M. & Krajewski, P. (2009). *Extracting subsurface information from ambient seismic noise – an example from Germany*. Paper presented at the 79th SEG International Conference & Exhibition, Houston, USA, Expanded Abstracts, pp. 1617–1621.
- Steiner, B., Saenger, E. & Schmalholz, S. (2008). *Time reverse modeling of low-frequency microtremors: Application to hydrocarbon reservoir localization*. Geophys. Res. Lett., **35**, L03307. doi:10.1029/2007GL032097.
- Tai, S., Puryear, C. & Castagna, J. P. (2009). *Local frequency as a direct hydrocarbon indicator*. Paper presented at the 79th SEG International Conference & Exhibition, Houston, USA, Expanded Abstracts, p. 2160–2164.
- Tallavó, F., Cascante, G. & Pandey, M. (2009). *Experimental and numerical analysis of MASW tests for detection of buried timber trestles*. Soil Dynamics and Earthquake Engineering, **29**, 91–102.

- Werby, M. F. & Gaunaurd, G. C. (1990). *Resonance scattering from submerged elastic spheroids of high aspect ratios and its 3-dimensional interpretation*. Journal of the Acoustical Society of America, **88**(2), 951–960.
- White, J. E. (1975). *Computed seismic speeds and attenuation in rocks with partial gas saturation*. Geophysics, **40**(2), 224–232.
- Yilmaz, O. (1987). *Seismic Data Processing, Volume 2*. SEG. ISBN 0931830400.
- Zhang, J., Gerstoft, P. & Shearer, P. (2009). *High-frequency P-wave seismic noise driven by ocean winds*. Geophysical Research Letters, **36**, L09302.

4. Low-frequency microtremor anomalies at an oil and gas field in Voitsdorf, Austria ¹

Marc-André Lambert, Stefan M. Schmalholz, Erik H. Saenger & Brian Steiner

ABSTRACT

Results of a passive microtremor survey at an oil and gas field in Voitsdorf, Austria, are presented. The survey consists in six parallel profiles approximately 9 km long over two hydrocarbon reservoirs. For each profile the seismic wavefield was recorded synchronously at 11 in-line stations. The measurements were conducted with broadband seismometers and lasted, for each profile, at least 12 hours overnight. Data interpretation is based on a comprehensive data set and on the analysis of four different spectral attributes. These attributes quantify the characteristic features of the wavefield's Fourier spectra in the low-frequency range ($<10\text{Hz}$). One attribute quantifies the spectral energy in the vertical wavefield component, another attribute quantifies the maxima in vertical-to-horizontal spectral ratios and two attributes describe the frequency shifts of peaks within the spectra of vertical and horizontal wavefield components. Due to temporal variations of the signals we combine the long-term measurements (several hours of continuous records) of multiple profiles. This procedure considerably enhances the consistency of each spectral attribute and makes them suitable to quantify lateral variations of the wavefield. The results show that using a combination of several attributes significantly increases the reliability of detecting anomalies in the microtremor wavefield that are presumably caused by hydrocarbon reservoirs. A numerical study of two-dimensional seismic wave propagation is applied to investigate the peak frequency shift attributes. The results of the study indicate that the attributes may contain information on the depth of hydrocarbon reservoirs, assuming that the reservoir acts as a (secondary) source of low-frequency seismic waves.

¹This chapter was published in *Geophysical Prospecting* (Lambert et al., 2009)

4.1 INTRODUCTION

The movement of the Earth's surface generated by ambient seismic background noise and its corresponding frequencies above 1 Hz are usually referred to as microtremors (Bard, 1999, and references therein). Near-surface geological structures can characteristically modify the spectral content of microtremors. Examples are resonant amplification due to a soft soil layer (Nogoshi & Igarashi, 1971; Nakamura, 1989; Al Yuncha et al., 2004) and two-dimensional resonance patterns in mountain valleys (Roten et al., 2006). Such modifications of the microtremor wavefield are especially stable in the spectral ratio of the horizontal (H) over vertical (V) component of ground motion (H/V-ratio) and have been used to assess the S-wave velocity distribution in near-surface sediments in particular during the last 20 years (Fäh et al., 1997; Bour et al., 1998; Parolai & Galiana-Merino, 2006). This methodology has also been adapted for assessing deeper subsurface structures. For example, Ibs-von Seht & Wohlenberg (1999) related variations of the peak frequency of H/V-ratios to depth-variations of the sediment-basement contact at more than a 1000 m depth. These studies indicated that microtremors can contain useful information about subsurface geological structures.

Low-frequency (<10 Hz) spectral anomalies in surface microtremor signals have recently been used as hydrocarbon indicators (Dangel et al., 2003; Holzner et al., 2005; Akrawi & Bloch, 2006; Birialtsev et al., 2006; Rached, 2006; Suntsov et al., 2006). Dangel et al. (2003) investigated microtremor data to locate hydrocarbon bearing structures in the subsurface and found an empirical relationship between low frequency spectral anomalies in microtremor wavefields and the presence of hydrocarbon reservoirs, mainly for sites in the Middle East. Also, applications of low-frequency spectral analysis for hydrocarbon detection have been reported in Russian literature since the early 1990s (Aroutunov et al., 1998). Most of those empirical observations are based on the vertical component of the microtremor wavefield. However, Lambert et al. (2007) and Saenger et al. (2007) reported a coincidence between anomalies in the vertical-to-horizontal spectral ratio (V/H-ratio) and the reservoir locations. Spectral ratios are especially useful because they show much less temporal noise variations than single component, or absolute, spectra (Bard, 1999, and references therein).

Motivated by these observations we carried out a microtremor survey at an explored oil and gas field near Voitsdorf, Austria. We used this field as a test site to investigate correlations between spatial anomalies in the measured microtremor signals and the reservoir location. The aim was also to evaluate the observations reported by previous microtremor studies at oil and gas fields (Dangel et al., 2003; Lambert et al., 2007; Saenger et al., 2007). In the first part of this paper we present the findings of the Voitsdorf survey. We explain data processing, which includes the calculation of four spectral attributes. We also show how spatial attribute anomalies are extracted and used to locate the reservoirs. The second part of the paper presents a numerical study of two dimensional wave propagation, which generates patterns similar to

those observed in two of the spectral attributes. At the end of the paper we shortly discuss the possible origin of the observed anomalies. They are caused by either anthropogenic or natural mechanisms. Anthropogenic mechanisms may be related to production noise at the surface or within the reservoir (e.g., pumps, induced micro-earthquakes, global fluid flow). Natural mechanisms may be related to the partial saturation of the reservoir rocks, which can lead to pore-fluid oscillations (Frehner et al., 2007) and/or abnormally high attenuation compared to the surrounding, fully saturated, rocks (Quintal et al., 2007). The results indicate that passive low-frequency spectral analysis combining several spectral attributes can significantly increase the probability of locating the reservoirs.

4.2 THE VOITSDORF SURVEY

4.2.1. Study site

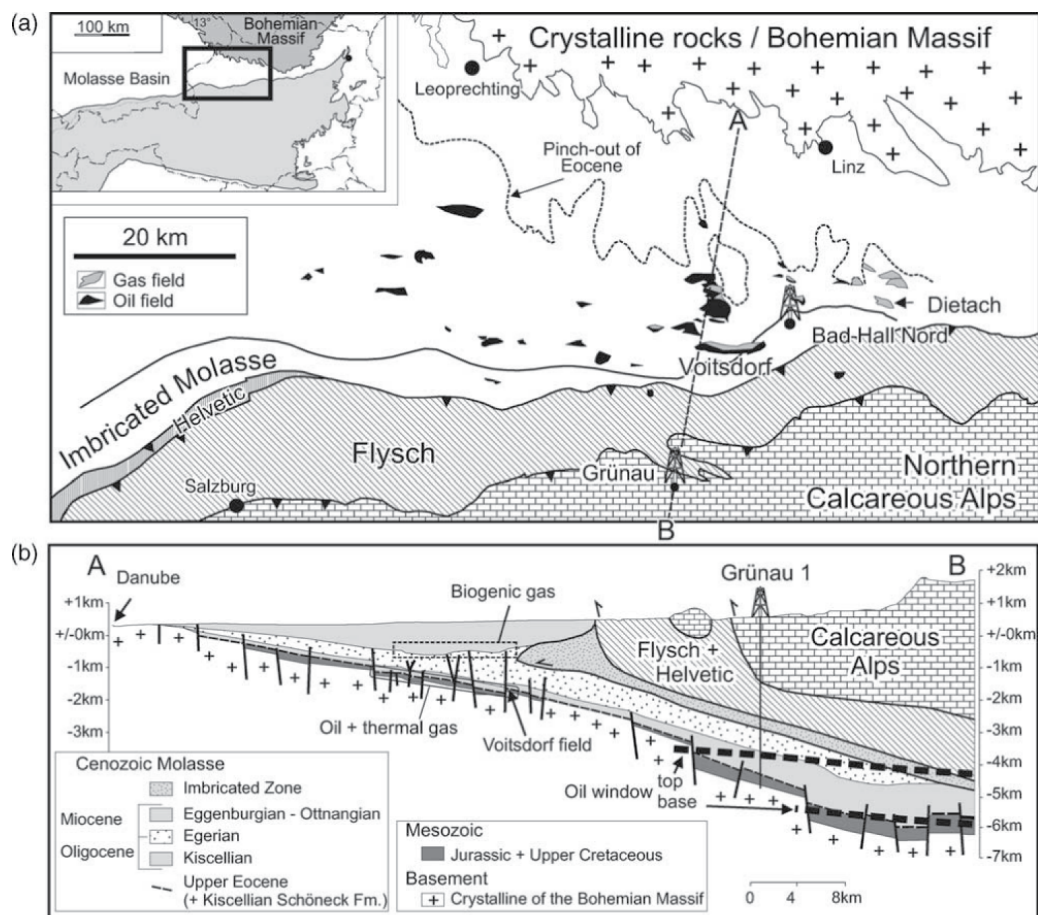


Figure 4.1. Taken from *Sachsenhofer et al. (2006)*. (a) Geological overview of Upper Austria and location of the Voitsdorf oil and gas field. (b) Cross-section through the Alpine Foreland Basin, showing the position of the Voitsdorf field.

The microtremor survey presented in this study was performed at the Voitsdorf oil and gas field in Upper Austria. The measurements were conducted from 30 March to 5 April 2007. A detailed geological overview of the Voitsdorf area is given in [Sachsenhofer et al. \(2006\)](#). Voitsdorf is situated in the Alpine Foreland Basin oil and gas province in central Europe (Fig. 4.1). The Alpine Foreland Basin stretches along the northern margin of the Alps from Geneva to Vienna. Sedimentation began in the late Eocene with the deposition of fluvial and shallow marine sandstones, shales and carbonates (molasse). During Oligocene and Miocene, several hundred metre thick, deep marine, turbiditic sequences were deposited in the eastern part (including the Voitsdorf area), whereas the western part of the basin was dominated by a prograding-retrograding delta system. The southern part of the basin was overthrust by the Alpine nappes.

Exploration of the Alpine Foreland Basin oil and gas province resulted in the discovery of almost 200 relatively small fields, most of them located in southeastern Germany and Upper Austria (Fig. 4.1a). The Voitsdorf field is one of the larger fields in this province. It is operated by Rohöl-Aufsuchungs AG (RAG) since the early 1960s and is still producing. The oil reservoir rocks consist mainly of Upper Eocene sandstones that lie on older sedimentary formations of a few tens of metre thickness. These formations are in contact with the underlying crystalline basement in a depth between 2 and 2.5 km. The hydrocarbons mainly originate from lower Oligocene formations (e.g., Schöneck formation). The oil window is in a depth between 4 and 6 km and therefore the oil source is located beneath the Alpine nappes, resulting in long-distance migration to the present reservoir (see Fig. 4.1b). The hydrocarbons are typically trapped on the upthrown side of steeply dipping E/W-striking faults. Recent exploration revealed another, smaller oil reservoir approximately 2 km south of the main reservoir. Here, the reservoir rocks are in direct contact with the basement. In this study we investigate both the northern and the newly discovered southern reservoir.

The area around Voitsdorf is dominated by farmland and forest. The population density is relatively high and there are small villages every few kilometres. Highway A9 crosses the survey area from north to south. The nearest large town is Wels, 20 km north of Voitsdorf with approximately 60 000 residents.

4.2.2. Data acquisition

The field equipment comprised thirteen Guralp CMG-3ESP portable three-component (3C) broadband seismometers, each equipped with an internal 24-bit digitizer and an external GPS receiver to allow precise synchronization of the measurements. Figure 4.2 shows a picture of such a device. The seismometers are based on the electromagnetic force feedback principle and have a flat frequency response from 30 s to 50 Hz with a sensitivity of 1500 V/m/s. Up to 25 Hz, the instrument noise remains below the New Low Noise Model ([Peterson, 1993](#)). Figure 4.2

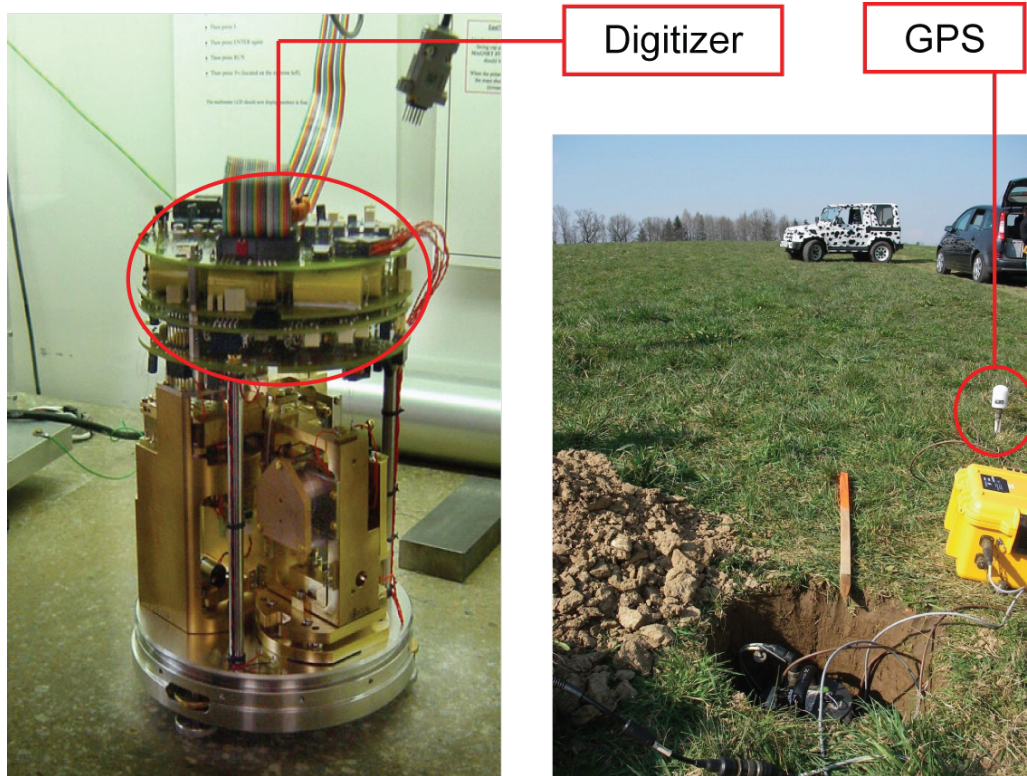


Figure 4.2. *Portable broadband seismometer and set-up in the field.*

shows how the seismometers were installed in holes of approximately 60 cm depth to improve coupling to the ground and to reduce surface noise and wind influence.

Figure 4.3 shows the six parallel profiles that were measured, each consisting in 10 regular in-line stations. The large icons in Fig. 4.3 represent three reference stations that were additionally deployed in a cross-line direction. This set-up yields synchronized data for 11 in-line and 2 cross-line stations. Each of the profiles has a length of approximately 9 km and an in-line seismometer spacing of 1 km (outer stations) and 0.5 km (inner stations), respectively. The profiles are grouped into southern lines (1 to 3) and northern lines (4 to 6), with an overlap of about 4km. The cross-line spacing is 500 m. Each line crosses both reservoir locations and lies perpendicular to the reservoirs' extension.

Each seismometer outlay continuously recorded the microtremor wavefield for at least 12 hours during the night. In the morning, the regular stations were shifted to the next profile to record the following night. The reference stations recorded continuously for three days over the southern reservoir (RS-S; for line 1 to 3) and were then moved to the northern reservoir (RS-N; for line 4 to 6) where they recorded for another three days. The reference stations are used to monitor regional variations of the wavefield.

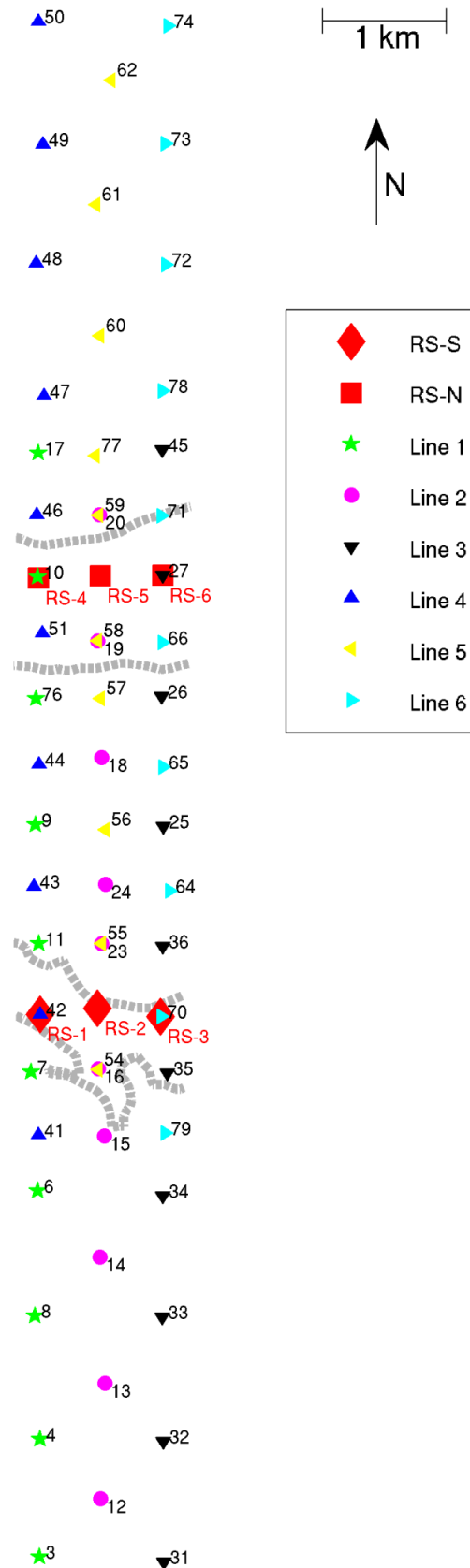


Figure 4.3. Acquisition layout. Six profiles (Lines 1–6) have been measured across the two hydrocarbon reservoirs. Stations are marked with different colours for each profile. A 2-digit identifier is indicated for each station. Three additional reference stations are marked as red diamonds (for lines 1–3) and as red squares (for lines 4–6). The reservoir contours are given as dashed lines (information provided by Spectraseis).

4.3 ANALYSIS OF SPECTRAL ATTRIBUTES

4.3.1. Data example

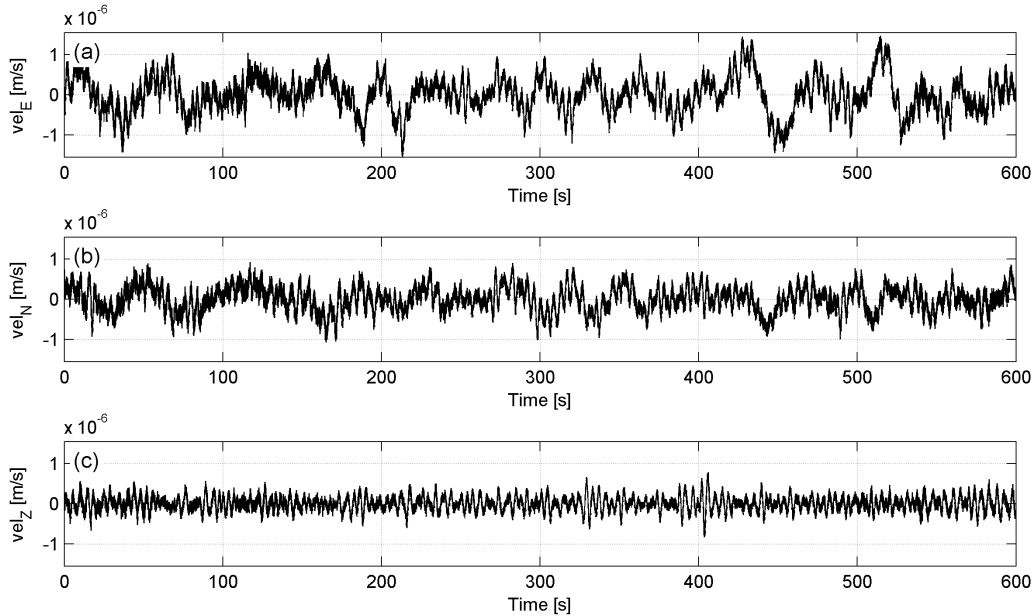


Figure 4.4. Data section from station 59: ground particle velocity (m/s) versus time (seconds) for the three components (a) east/west, (b) north/south and (c) vertical. A ten minute window at 5:00 a.m. is shown (compare with Fig. 4.5).

Figure 4.4 shows a representative record of the microtremor wavefield in the survey area. The record shows 10 minutes from measurement point 59 (line 5) and represents a relatively quiet time period from 5:00 a.m. to 5:10 a.m. of 4 April 2007. The three signals correspond to the east/west (Fig. 4.4a), north/south (Fig. 4.4b) and vertical component (Fig. 4.4c) of the velocity field.

Figure 4.5 shows spectrograms of the data recorded at station 59 from 04:00 a.m. to 09:00 a.m. of 4 April 2007. Figure 4.5a displays the spectrogram for the amplitude of the vertical particle velocity component (V) versus time and frequency. Figure 4.5b shows the spectrogram for the average horizontal component (H), which is the geometric mean of the two horizontal components, east/west and north/south. Figure 4.5c shows the vertical-to-horizontal spectral ratio of the wavefield (V/H-ratio).

The amplitudes of the wavefield (V and H) generally increase during the day (Fig. 4.5), reflecting the diurnal pattern of anthropogenic noise. Two other typical characteristics are narrowband continuous signals (e.g., at 12.5 Hz) and broadband short-time interferences (transients). Both features are related to artificial noise such as industrial machinery or traffic. Most

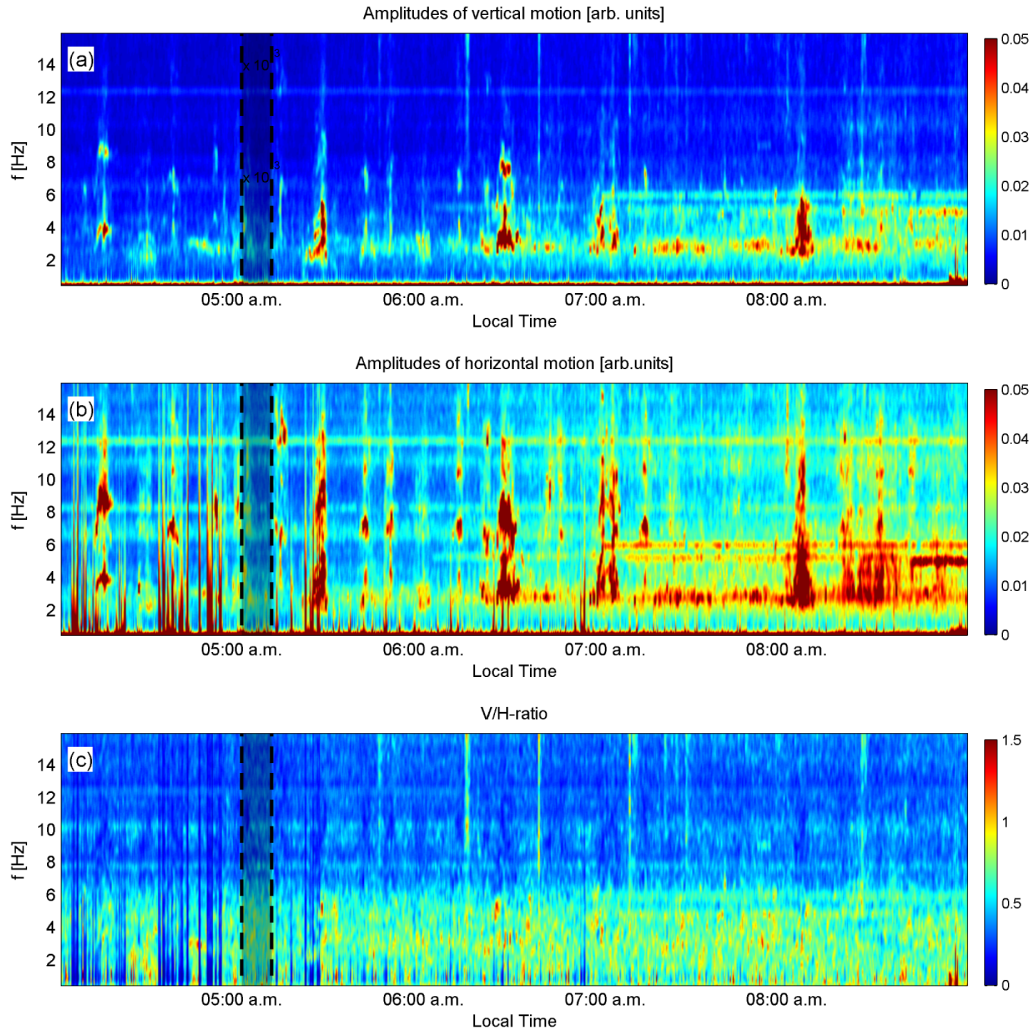


Figure 4.5. Spectrograms of the wavefield at station 59. (a) Vertical component, (b) horizontal component and (c) V/H-ratio. The grey shaded area at 5:00 a.m. highlights the signals used for Figs 4.4 and 4.6.

interesting for this study are features that have a relatively broad frequency range and also show continuity in time, e.g., the enhanced amplitudes between 1 and 5 Hz in Fig. 4.5c. Such signals are most probably produced by natural sources and/or geological conditions. Another typical feature is the so called ocean wave peak. This ubiquitous signal, around 0.14 Hz, originates from ocean waves interacting with coast structures (e.g., Friedrich et al., 1998). The amplitude of this signal is usually in orders of magnitudes higher than compared to the rest of the ambient seismic spectrum. It is visible in Figs 4.5a and 4.5b as a red line at low-frequencies.

Compared to the single component spectrograms, the V/H ratio spectrogram, Fig. 4.5c, looks considerably different. It exhibits much less temporal variability. The day-night cycle is less pronounced and the short-time transients as well as the high-energy ocean wave peak are not present.

4.3.2. Spectral attributes

We consider the spatial distribution of spectral attributes of the surface microtremor wavefield to locate hydrocarbon reservoirs (Saenger et al., 2007). Here, we use four different attributes, which are briefly introduced in the following paragraphs. Attribute 1 is an integral value under the power spectral density curve of the vertical component. Integrating within a specified bandwidth quantifies an anomaly proportional to energy since the integral value has units of the square of particle velocity. Attribute 2 is the peak amplitude of the V/H-ratio, which quantifies the magnitude of a dominant maximum in the V/H spectral ratio in the low-frequency range. These two attributes have been applied in previous studies (Lambert et al., 2007; Saenger et al., 2007) and directly depend on the signal-strength of ground motion. This might be a drawback in areas with temporally varying and/or very high anthropogenic noise influence. Artificial noise sources (e.g., pumps or traffic) may contribute additional energy to the seismic spectra and bias the estimate of the attribute values. Therefore, we introduce attributes 3 and 4, the peak frequencies of the vertical and horizontal spectrum, respectively, which focus on the frequencies rather than the amplitudes in the low-frequency band. Figure 4.6 shows the four attributes calculated from a time window extracted from station 59. The corresponding time signals are shown in Fig. 4.4.

Attribute 1: Energy anomaly in the vertical particle velocity

Attribute 1 is based on the observation of energy accumulation of the microtremor motion in the low-frequency range above reservoirs (Dangel et al., 2003). Figure 4.6a illustrates the integration technique used to quantify low-frequency anomalies visible in the power spectral density plot. The method considers only the vertical component of the microtremor wavefield. Temporal noise variations are taken into account by extracting the amplitude minimum (diamond in Fig. 4.6a) for each power spectrum at the low-frequency end, here between 1 and 1.7 Hz. The integral above the level defined by this minimum value is considered for attribute 1. The frequency value of this minimum also defines the lower boundary of the integration range. The upper boundary is a fixed frequency, here 5 Hz. The integration interval was empirically defined to be between the very strong ocean wave peak and the strong anthropogenic noise and therefore varies for different surveys (Saenger et al., 2007).

Attribute 2: Peak amplitude of V/H-ratio

This attribute is based on the observation that the hydrocarbon-related energy anomaly is usually stronger in the vertical component compared to the horizontal components (Lambert et al., 2007). Therefore, we use the V/H spectral ratio (Fig. 4.6b), in contrast to the well-known H/V-ratio, which is widely used to identify soft soil layers from passive seismic data

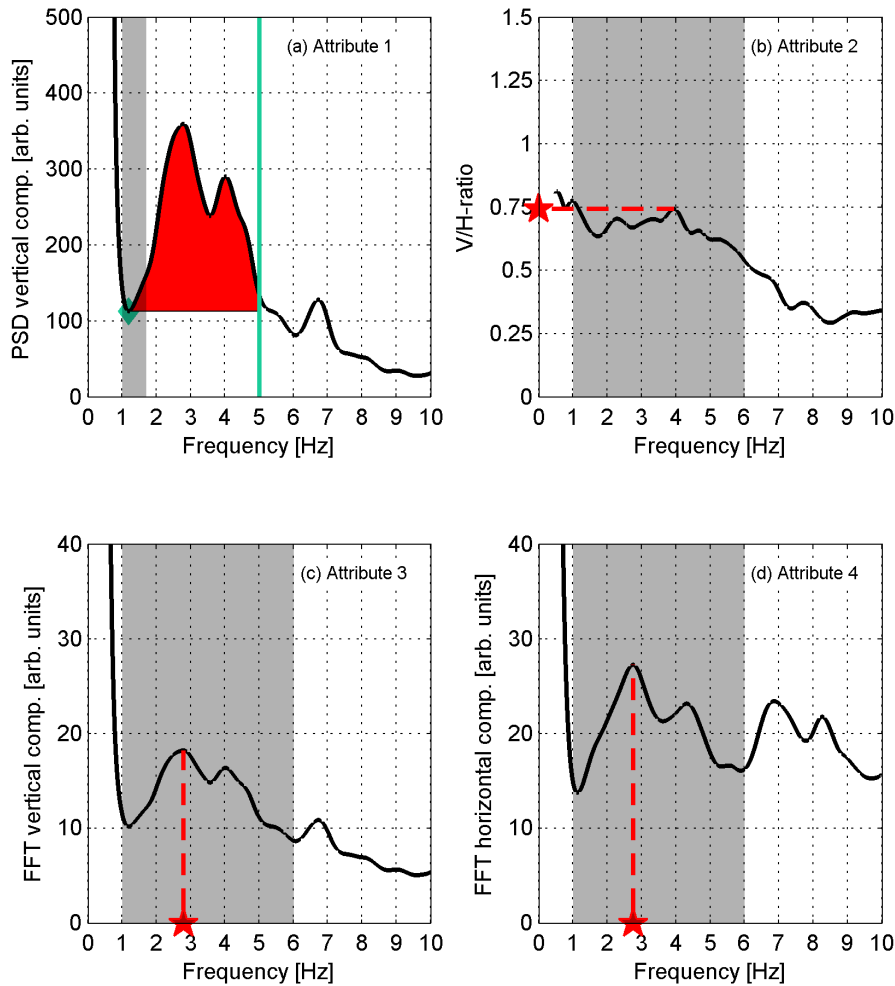


Figure 4.6. *Spectral attributes of the ambient wavefield used in this study (from measurement 59, as an example). (a) Attribute 1 quantifies an anomaly of the power spectral density of the vertical component in the low-frequency range (red area). (b) Attribute 2 is defined as the peak amplitude of the V/H spectral ratio (red star). (c) Attribute 3 refers to the peak frequency of the Fourier amplitude spectrum of the vertical component (red star). (d) Attribute 4 refers to the peak frequency of the combined Fourier amplitude spectrum of the two horizontal components (red star). The shaded regions of the graphs indicate the frequency band considered to calculate parameters needed for the attributes.*

sets (e.g., [Ibs-von Seht & Wohlenberg, 1999](#); [Fäh et al., 2001](#)). The V/H spectrum includes all three components of the measured signal. After the Fourier transform, the spectra are smoothed by a weighted moving average using the Hann window. Smoothing avoids instability due to division by infinitesimal values during the calculation of the V/H-ratio. The spectra of the two horizontal components are combined, by the geometric mean, to an average horizontal spectrum. The peak amplitude of the V/H-ratio is extracted by scanning through the V/H spectrum, searching for the amplitude of dominant peaks in the 1–6 Hz range (red star in Fig. 4.6b). The 1–6 Hz frequency range is chosen because it lies between the ocean wave peak and the anthropogenic noise band and is therefore characterized by a relatively low seismic noise level.

Attributes 3 and 4: Peak frequency of the vertical and horizontal spectrum

We define the peak frequency as the value, in Hz, where a maximum appears. For microtremor spectra (and spectral ratios), these quantities are usually more stable than the corresponding peak amplitudes (e.g., [Teves-Costa et al., 1996](#); [Bour et al., 1998](#)). Figures 4.6c and 4.6d show the peak frequency (red star) for the vertical and the horizontal ground motion signal extracted from station 59. The Fourier amplitude spectra are calculated and smoothed as described in the previous section. Again, the spectra of the two horizontal signals are averaged. The maxima within the 1–6 Hz frequency range are then used to determine the values for attributes 3 (using vertical particle velocity) and 4 (using horizontal particle velocity).

4.3.3. Attribute profiles

Figure 4.7 shows in-line profiles of the spectral attributes. Each circle represents an attribute value based on the spectra of 30 minutes of continuous recording from 5:00 a.m. to 5:30 a.m. at one particular station. The spectra were derived by averaging the spectra of 45 consecutive time sections with a length of 40 seconds each (no overlap of the sections). This procedure considerably decreases computational time. A window length of 40 seconds was chosen to provide sufficient resolution in the low-frequency domain. The full time-domain record was used to compute the spectra and no systematic elimination of artificial noise was performed on the data set.

While the values from stations on different measurement lines originate from different days, the measurements within a line are synchronous. Therefore, those values are connected in Fig. 4.7 (dotted lines) and represent the attribute profiles for the six measurement lines during the chosen time window. The grey areas in Fig. 4.7 show the location of the reservoirs from interpretations of active seismic and well log data. The northern boundaries of the reservoirs are defined by known faults. The southern boundaries are defined by the oil-water contact. For the southern reservoir the oil-water contact has yet to be precisely defined and the reservoir location is therefore indicated with a grey fading boundary towards the south. Note that the reservoir extensions are not exactly the same for each profile (see Fig. 4.3). Therefore, the cross-line projection of the maximum extents based on all profiles is indicated in Fig. 4.7.

4.3.4. Spatial variability of the attribute profiles

The thick lines in Fig. 4.7 indicate for each attribute the crossline stack of the six individual measurement lines. After a linear interpolation between the in-line stations the individual profiles were averaged by the arithmetic mean. The averaged profile was smoothed by a weighted moving average using the Hann window. This procedure is reasonable since all profiles lie

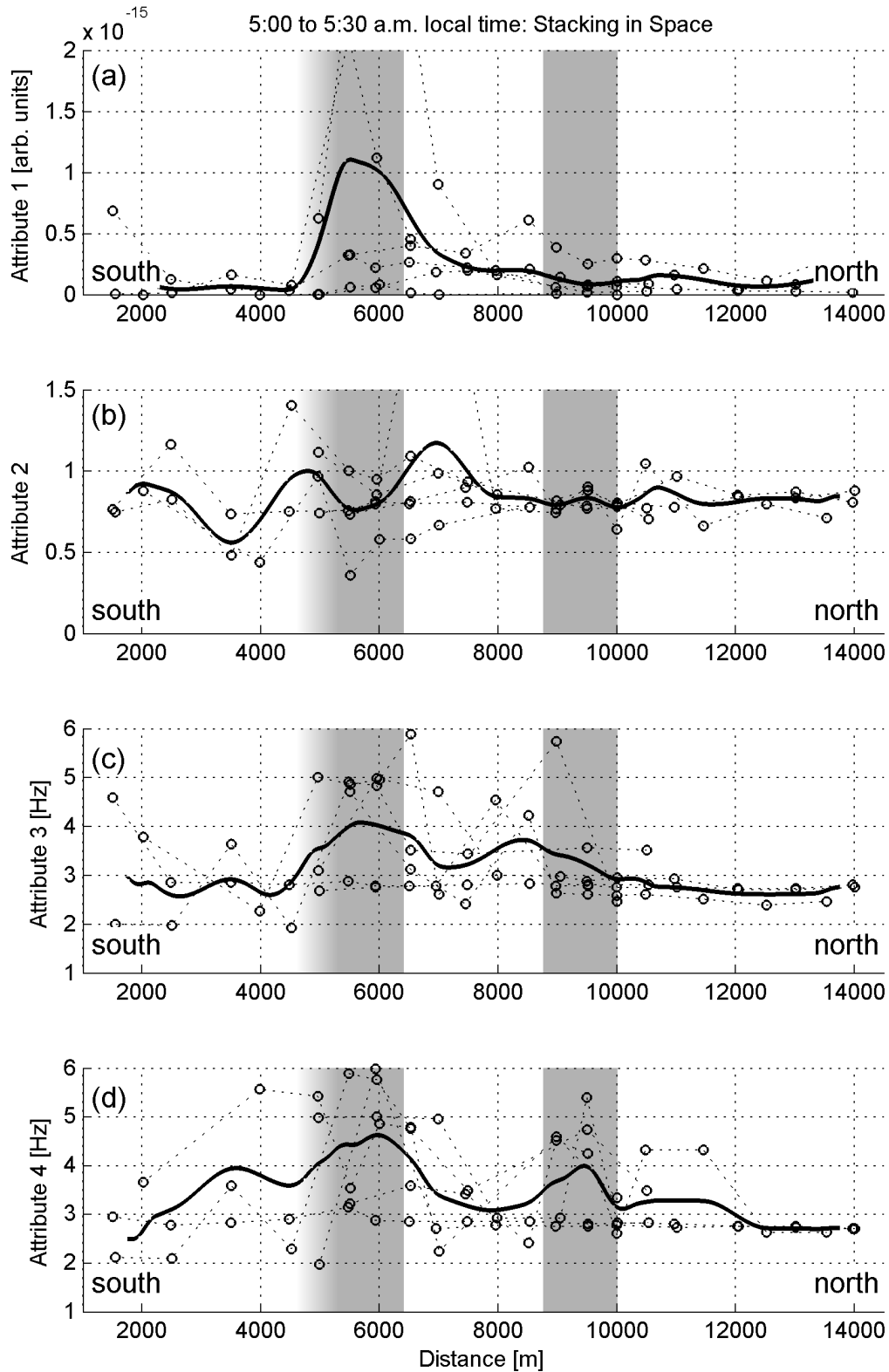


Figure 4.7. Profiles of all six measurement lines for (a) attribute 1, (b) attribute 2, (c) attribute 3 and (d) attribute 4 (dotted lines). The individual values (circles) are calculated per station from the 30 minute time section between 5:00 a.m. and 5:30 a.m. The thick line represents for each attribute the arithmetic average of the six profiles (cross-line stack). Grey areas indicate the reservoir locations (cross-line projection of the maximum extents).

parallel to each other, perpendicular to the reservoir extension and very close together compared to their length (500 m spacing, 9 km length).

The stacked profile for attribute 1 (Fig. 4.7a) shows a distinct peak at a distance of about 6000 m in the in-line direction. However, this anomaly is only seen in two of the six individual profiles. The values of attribute 2 (Fig. 4.7b) show a more stable pattern. The individual profiles are more or less flat around a value of 1. Only the southern part of the profiles shows two lines with an anomalous behaviour. The individual profiles of attributes 3 and 4 (Figs 4.7c and 7d) are quite rough. However, high values cluster around 6000 m and 9500 m. Therefore, the corresponding average profiles show two major anomalies, especially pronounced on the horizontal component (attribute 4, Fig. 4.7d).

Generally, the attribute values from different profiles can vary significantly. Spatial stacking compensates for these variations and produces more consistent anomalies compared to single measurement lines.

4.3.5. Temporal variability of the attribute profiles

The time window from 5:00 a.m. to 5:30 a.m., which was used to calculate the attribute profiles shown in Fig. 4.7, reflects only a small part of the available data set. The question is whether the attribute values observed in this 30-minute snapshot are representative for the corresponding measurement site or not. We therefore focus on line 1 to compare the results derived from various time windows. Line 1 lies centrally across the southern reservoir and, at its northern end, also covers the northern reservoir (see Fig. 4.3). We calculated attribute profiles for 11 consecutive time windows with a length of 30 minutes between midnight and 05:30 a.m. (full time-domain record used). The dotted lines in Fig. 4.8 show the profiles derived from each of the 11 time windows (circles give the actual value of the attribute at each station) while the thick line indicates the stacked section of all time windows. We computed the stacked section after the same procedure that was used in the previous section for the computation of the cross-line stack. The grey areas show the locations of the reservoirs on measurement line 1 (note that they are slightly different compared to the cross-line projection in Fig. 4.7).

The stacked profile of attribute 1 exhibits a strong anomaly at a distance of about 5500 m (Fig. 4.8a). Attribute 2 behaves very stable in time (dotted profiles look very similar) and the profiles do not show clear lateral anomalies (Fig. 4.8b). Attributes 3 and 4 (Figs 4.8c and 4.8d) exhibit characteristic spatial patterns despite showing rather strong variations in time.

4.3.6. Characteristic profiles

It has previously been shown that stacking both in the space and time-domain increases the stability of the attribute values. Therefore we compute cross-line stacks (similar to the thick lines in Fig. 4.7) for various time windows and stack them. The resulting characteristic profile

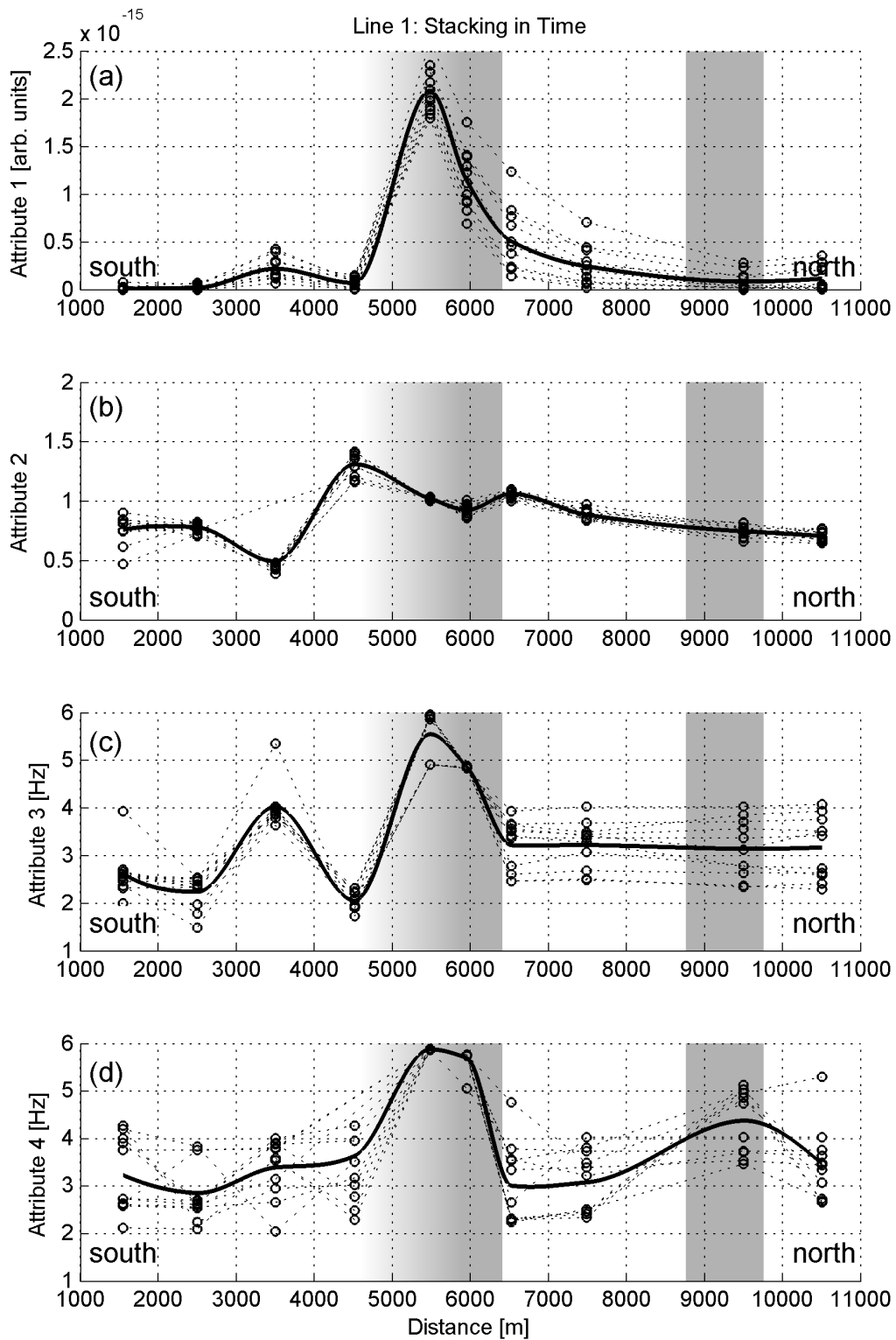


Figure 4.8. Comparison of 11 profiles along measurement line 1 for (a) attribute 1, (b) attribute 2, (c) attribute 3 and (d) attribute 4 (dotted lines). Each profile was computed from a different time interval (see text). The thick line represents for each attribute the arithmetic average of the 11 profiles (stack in time-domain). Grey areas indicate the reservoir locations for measurement line 1.

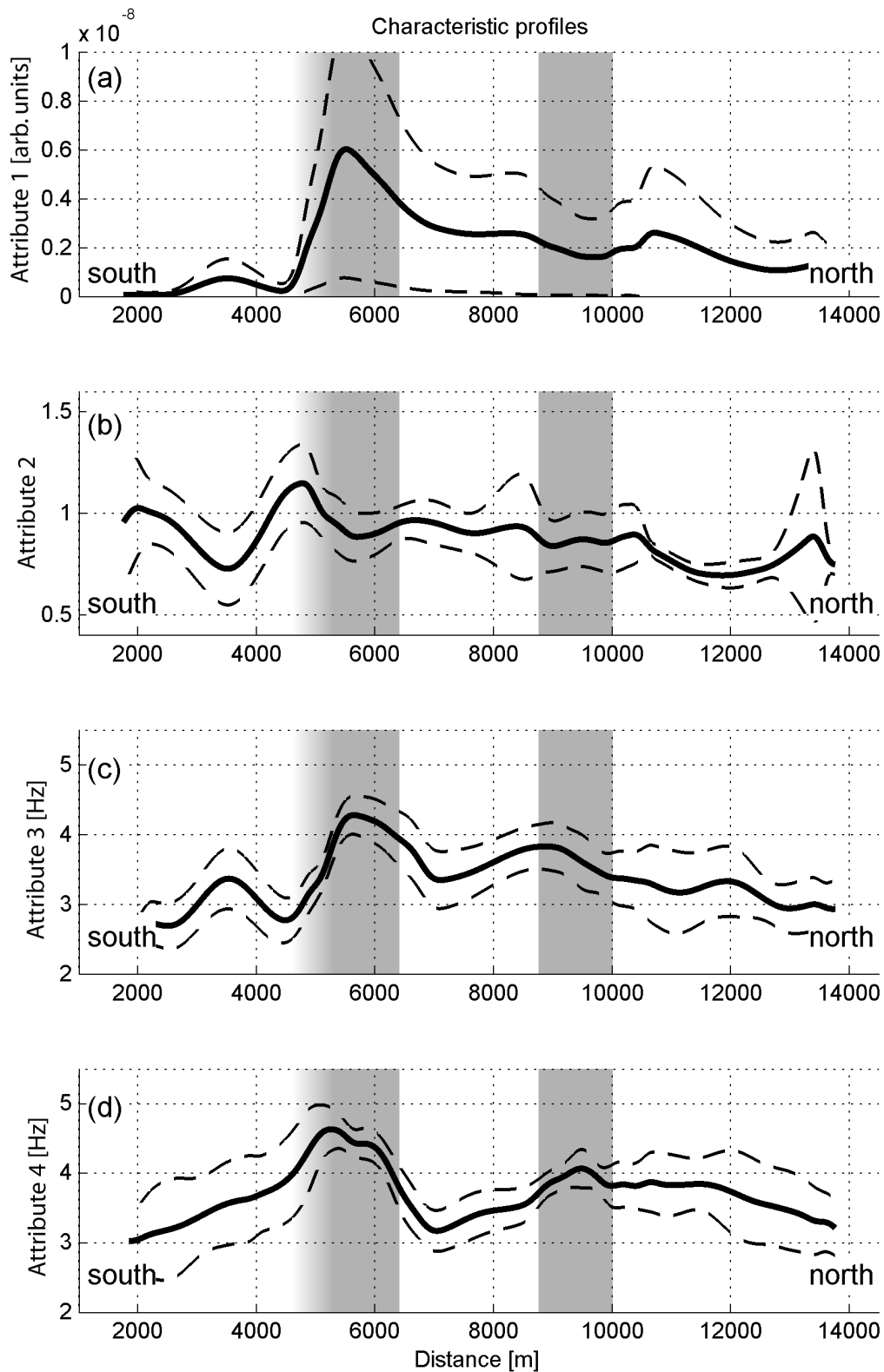


Figure 4.9. Characteristic profile of (a) attribute 1, (b) attribute 2, (c) attribute 3 and (d) attribute 4, derived from nighttime measurements (solid line). Dashed lines indicate the corresponding plus/minus 1 standard deviation. Grey areas indicate the reservoir locations (cross-line projection of the maximum extents).

represents an average in-line pattern of the attributes based on all the available data of the chosen time period. For example, the solid line in Fig. 4.9a is the characteristic profile of attribute 1 for the time period between midnight and 5:30 a.m. and therefore comprises 11 x 30 minutes of data at each of the 66 stations of the survey. The dashed lines in Fig. 4.9a indicate the plus/minus 1 standard deviation range from the time average. Figure 4.9(b–d) display the characteristic profiles for the attributes 2, 3 and 4. Each characteristic profile is calculated from the same 363 hours of data.

The characteristic profile of attribute 1 (Fig. 4.9a) shows two anomalies, one at an in-line distance of 5500 m and another one at 11 000 m. The southern anomaly has a very large amplitude. Both anomalies vary considerably in time as shown by the large standard deviations. Figure 4.9b shows a mostly flat profile for attribute 2. There is only one significant (in terms of standard deviation) anomaly at 4500 m. The peak at 13 500 m is not significant (very large standard deviation). The characteristic profile of attribute 3 (Fig. 4.9c) shows three significant anomalies (at 3500 m, 5500 m and 9000 m). The largest anomaly is at 5500 m and has a small standard deviation. Therefore it is not only pronounced but also consistent in time. There are two significant anomalies in the characteristic profile of attribute 4 (Fig. 4.9d). The southern anomaly is a relatively narrow peak with a large amplitude. The northern anomaly has a much broader shape. However, both anomalies are consistent in time.

Only nighttime measurements have been used for the profiles shown in Fig. 4.9 (time window from midnight to 5:30 a.m.). The reason is that daytime measurements are dominated by anthropogenic noise, particularly traffic noise from the adjacent highway. This makes it difficult to reliably analyse the data and often leads to unstable results (not shown here).

4.4 DISCUSSION OF FIELD RESULTS

4.4.1. Reservoir location

Figure 4.9 shows an important property of the measured microtremor wavefield: the characteristic profiles of the attributes 2, 3 and 4 exhibit smaller temporal variation (given by the standard deviation) than spatial variation (given by the magnitude of the anomalies), which makes those attributes suitable to quantify lateral variations of the wavefield. This is the case even though the full data set was used and no elimination of artificial noise was performed. For attribute 1 the temporal variations are rather large and therefore the observed anomalies are less significant.

The characteristic profiles show several significant spatial anomalies that overly the reservoirs. For example, the largest and most significant anomalies of attributes 1, 3 and 4 are located at a distance of 5500 m in the in-line direction (Figs 4.9a, 4.9c and 4.9d). This also agrees with the location of the southern reservoir. A second example is the two broad anomalies

of attributes 3 and 4 (Figs 4.9c and 4.9d). Despite their considerable width, the maxima of those anomalies can be located at 9500 m, which is over the northern reservoir. Attributes 1 and 2 are not sensitive for the northern reservoir. This shows that making a prediction for the reservoir locations based on the anomalies of only one attribute is not reliable. However, combining the results of several attributes significantly increases the probability of detecting the reservoir locations.

Typically, the wavelength of S- and surface waves at low frequencies (1 to 6 Hz) is several hundreds of metres. For P-waves even larger values apply. Based on the concept of the Fresnel zone, the maximum lateral resolution for the reservoir would be expected to be in the same order of magnitude as the wavelength of the measured signals, i.e., several hundreds of metres. Therefore, passive low-frequency spectral analysis is considered as a possible method for detecting reservoirs rather than resolving reservoir contours in detail. Other geophysical methods (like for example reflection seismic) would still be required to image the geological structures with a higher resolution.

4.4.2. Observations on individual attributes

The anomalies of attribute 1 show very strong temporal variations (Fig. 4.9a). This may reflect the unstable nature of the microtremor wavefield in a populated area like Voitsdorf. On the other hand it may also indicate time-variations of the hydrocarbon related tremor itself, a behaviour that has also been observed by [Saenger et al. \(2007\)](#).

Attribute 2 does not reveal conclusive results. The observed anomalies are small in amplitude and difficult to correlate with the reservoir locations (Figs 4.7b, 4.8b and 4.9b). However, the significant anomaly at 5000 m may be associated with the southern reservoir. More information on the southern reservoir boundary is needed for a reliable conclusion. This attribute is, nevertheless, of interest for future studies since its considerable temporal stability is a fundamental and promising property that should be investigated in more detail. The temporal stability of spectral ratios is also visible in Fig. 4.5c and it suggests that spectral ratios are less affected by seismic source characteristics (compared to the spectra of single components) and therefore, they can particularly emphasize site specific properties. Note that attribute 2 has been successfully applied in another case study ([Saenger et al., 2007](#)).

Attributes 3 and 4 clearly locate the southern as well as the northern reservoir (Figs 4.9c and 4.9d). However, not all the individual profiles in Figs 4.7 and 4.8 exhibit the anomalies. This suggests that the strength of the anomaly's source varies considerably with time. Therefore, it is clear from a statistical point of view that long measurements (several hours) have a higher potential to yield stable results. This is especially important for noisy areas like Voitsdorf. Attributes related to spectral ratios (e.g., attribute 2) are less affected by this issue and 30 minutes of data seems sufficient to extract a stable value (Fig. 4.8b).

The anomaly measured over the southern reservoir is stronger and narrower compared to the northern reservoir (Figs 4.9c and 4.9d). This agrees with the fact that the southern reservoir is expected to have a smaller spatial extension in the in-line direction (see Fig. 4.3). The large amplitude could be explained by the fact that the southern reservoir has been discovered only recently whereas the northern reservoir has been produced for more than 40 years. This could cause different signal strengths of the northern and southern reservoir, where the southern reservoir is expected to exhibit a higher signal strength.

4.5 NUMERICAL STUDY ON FREQUENCY PATTERNS

We performed a theoretical study of seismic wave propagation to better understand the observed anomalies of the peak frequency attributes (attributes 3 and 4). We assume that a subsurface object, here the reservoir, can act as a (secondary) source of seismic energy (Kouznetsov et al., 2005; Holzner et al., 2005; Turuntaev et al., 2006; Zhukov et al., 2007; Korneev, 2008). A time reverse modelling study by Steiner et al. (2008) effectively indicates the two Voitsdorf reservoirs as the origin of low-frequency seismic signals.

For a vertically acting single body force in a homogeneous, isotropic, unbounded medium the wavefield is analytically described by the corresponding solution for the elastodynamic Green function (Aki & Richards, 2002). However, we chose a numerical approach in order to also take into account the free surface of the Earth and to have the possibility in the future to implement arbitrarily complex structures within the medium. The numerical algorithm solves the two-dimensional (2D) elastic wave equation, which is transformed into the first-order velocity-stress formulation (Virieux, 1986). The rotated staggered grid finite-difference technique by Saenger et al. (2000) is applied. The numerical grid is rectangular. All computations are performed with second-order spatial finite-difference operators and with a second-order explicit time update. According to Bohlen & Saenger (2006), the scheme and the chosen modelling parameters are adequate to solve this type of problem (also with respect to the accuracy of surface waves). Here, the model domain is a 2D homogeneous medium (Fig. 4.10a) with a free surface at the top and wave absorbing layers at the three other boundaries to simulate an infinite half-space (Cerjan et al., 1985). The seismic velocities are $V_P=3000$ m/s (P-wave) and $V_S=1500$ m/s (S-wave). A seismic source is located in the centre of the domain at a depth of $D=2000$ m. This source is represented as a short-time low-frequency signal, induced by a vertically acting single body force. The source time function is a Ricker wavelet with a central frequency of 3 Hz.

At the free surface, the particle velocities are recorded over time. These time signals capture the elastic disturbance that was generated by the seismic source and then propagated through the medium. The modelled signals are transformed into the frequency domain and displayed as spatial spectrograms (amplitude versus frequency versus distance) as shown in Fig. 4.10b for

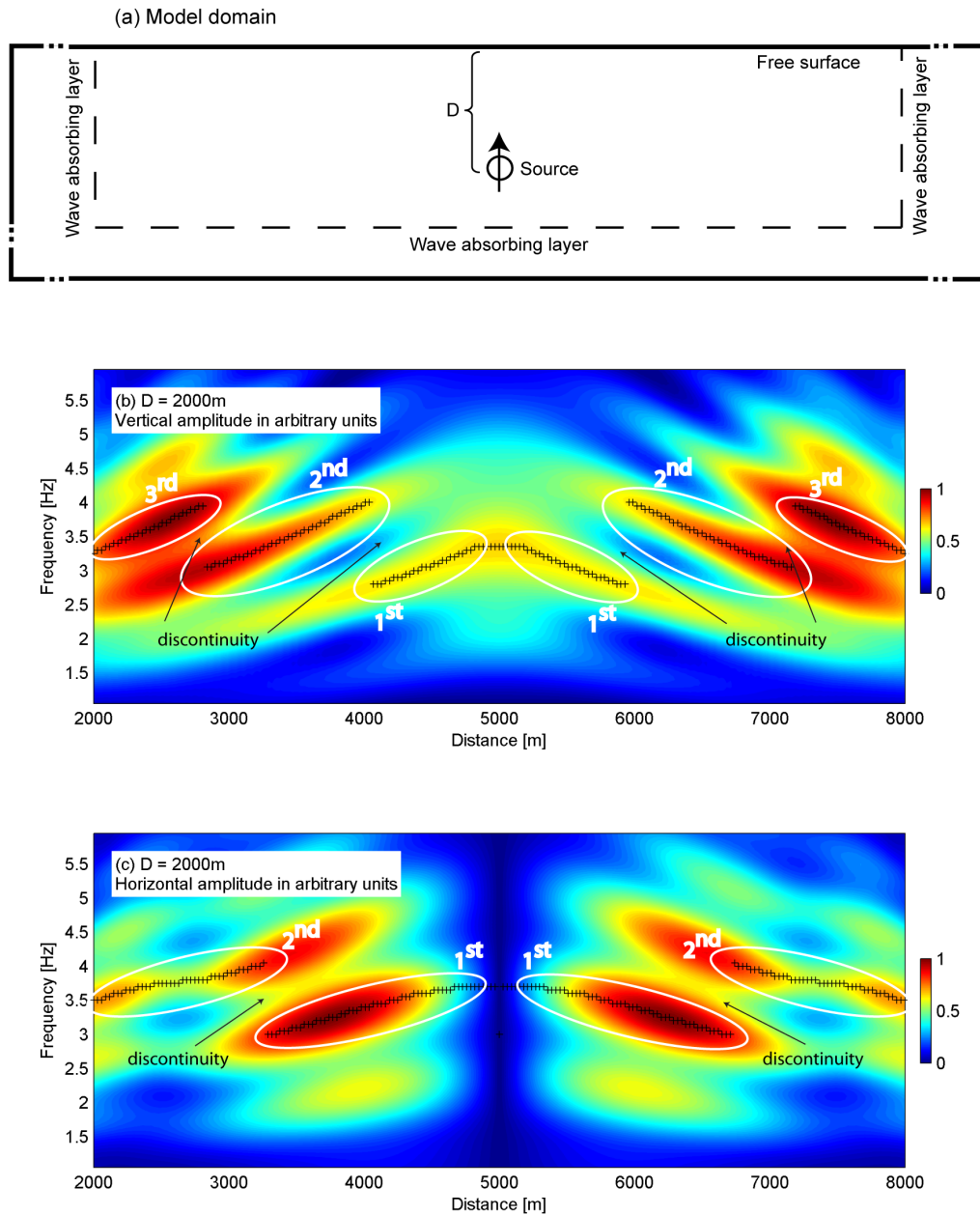


Figure 4.10. Numerical results for a low-frequency source in a homogeneous half-space. (a) Sketch of the model with the source at depth D . (b) Normalized spatial spectrograms of the vertical component of the synthetic wavefield measured at the free surface for a source depth of $D=2000$ m. Black crosses indicate the values of attribute 3. (c) Same as (b) but for the horizontal component and attribute 4.

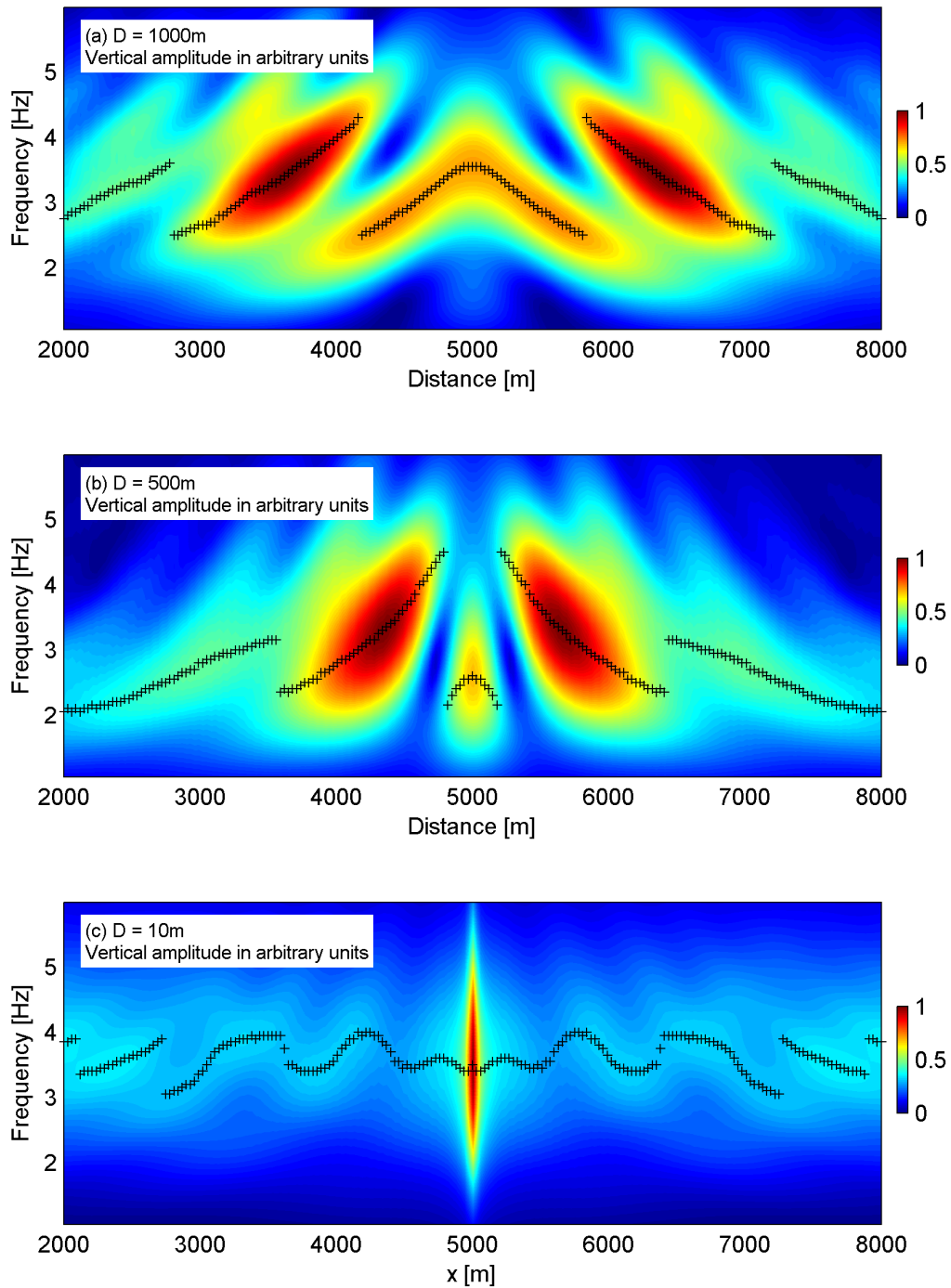


Figure 4.11. Normalized spatial spectrograms of the vertical component of the synthetic wavefield measured at the free surface for a source depth of (a) $D=1000$ m, (b) $D=500$ m and (c) $D=10$ m, respectively. The spectrograms are significantly different for different source depths. A sketch of the corresponding model domain is shown in Fig. 4.10a.

the vertical component of the wavefield. The corresponding values of attribute 3 are indicated with black crosses. They lie around 3 Hz vertically above the source ($x=5000$ m) and decrease with increasing distance from the source along the surface. This is highlighted with two ellipses (labelled as 1st) and forms a positive anomaly vertically above the source. A second branch of high amplitudes at higher frequencies becomes dominant at $x \approx 4000$ m and $x \approx 6000$ m (ellipses labelled as 2nd) and a third one at about $x \approx 2700$ m and $x \approx 7300$ m (ellipses labelled as 3rd). The profile of attribute 3 exhibits four distinct discontinuities.

Figure 4.10c shows a similar pattern in the horizontal component of the wavefield. However, the slope of the anomaly of attribute 4 is less steep compared to the anomaly of attribute 3 shown in Fig. 4.10b and there are only two discontinuities in the profile. Figure 4.10 also illustrates that high attribute values are not necessarily related to high amplitudes of ground motion. For example at $x = 5000$ m there is a local maximum of attribute 4 but a minimum of seismic amplitudes (Fig. 4.10c).

Figure 4.11 Normalized spatial spectrograms of the vertical component of the synthetic wavefield measured at the free surface for a source depth of (a) $D=1000$ m, (b) $D=500$ m and (c) $D=10$ m, respectively. The spectrograms are significantly different for different source depths. A sketch of the corresponding model domain is shown in Fig. 4.10a. Figure 4.11 shows the effect of source depth on attribute 3 by comparing the spatial spectrograms of the vertical component for $D=1000$ m, $D=500$ m and $D=10$ m. The anomaly of attribute 3 above the source becomes narrower for shallow sources (Figs 4.10b and 4.11) and disappears for sources close to the surface (Fig. 4.11c).

A frequency pattern as shown in Figs 4.10 and 4.11 is mainly controlled by the lateral change of the traveltime difference between P- and S-wave arrivals. The wavelets of the emitted P- and S-waves have a similar shape and therefore appear like multiples in the modelled time signal. Multiple wavelets manifest themselves in the amplitude spectrum as periodic peaks and notches (Yilmaz, 1987). The greater the wavelet separation in time (= the greater the distance from the source), the closer the peaks and notches in the amplitude spectrum. This behaviour can be observed in the spectrograms of Figs 4.10 and 4.11 and leads to the characteristic peak frequency anomaly above the source. Therefore, such an anomaly can only be generated by a source with a preferred directionality (emitting P- and S-waves). For example, an isotropic P-wave source (explosion) does not show such a pattern. A comparison with the analytical solution for a homogeneous, isotropic, unbounded medium (Aki & Richards, 2002) indicates that near-field effects and the presence of a free surface only play a minor role.

The numerical study shows that seismic signals emitted by a subsurface source can generate characteristic spectral patterns along the free surface. For a vertically acting single body force, these spectral patterns look similar to those measured above the two Voitsdorf reservoirs, namely that the values of attributes 3 and 4 are decreasing with increasing distance from the

source (Figs 4.9c and 4.9d). The numerical results have also been cross-checked with two other numerical codes (not shown here); one is a displacement-stress finite difference code used in Saenger et al. (2000) and one is a finite element code using implicit time integration where the free surface condition is automatically satisfied by the so-called natural boundary condition (Frehner et al., 2008).

4.6 DISCUSSION ON THE ORIGIN OF THE SIGNALS

A relevant question is whether the measured attribute anomalies are caused by natural mechanisms or by production noise. Generally, it can be distinguished between production noise at the surface (e.g. pumps, pipelines, etc.) and production noise at depth (e.g., global fluid flow, induced micro-earthquakes). Steiner et al. (2008) applied time reverse modelling on the Voitsdorf data set to locate the focusing of seismic energy at low frequencies. They found a significant focusing at the reservoir locations. Figure 4.12 shows one of their results for measurement line 1. For the southern reservoir, the strongest energy anomaly occurs right at the assumed southern boundary of the reservoir location. Note that this anomaly coincides with the V/H anomaly in Fig. 4.9b. The results of time reverse modelling support the proposition that there is low-frequency seismic emission originating from the reservoir areas.

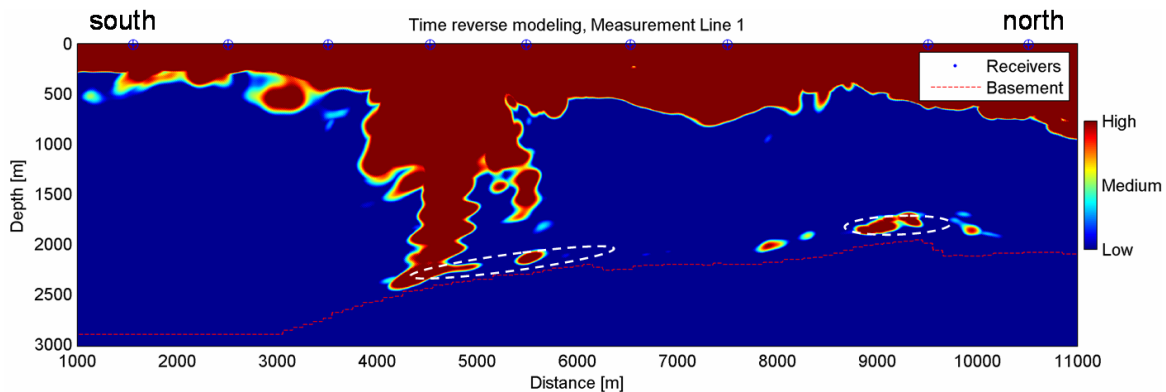


Figure 4.12. Result of time reverse modelling for the cross-section along measurement line 1 (modified after Steiner et al. 2008). The dashed ellipses show the approximate reservoir locations for measurement line 1.

Another argument is based on the numerical results shown in the previous section. Figure 4.11 compares the spatial spectrograms for different source depths D . As pointed out by Fig. 4.11c, the model does not predict the typical anomaly if the source is close to the surface. Figure 4.11 also shows that the spectral patterns change characteristically with source depth. The anomaly of attribute 3 becomes narrower and has steeper slopes for shallow sources, which

might be used as a potential depth-indicator for reservoirs. All these arguments suggest that the source that causes the attribute anomalies is located at reservoir depth and not at the Earth's surface.

It is hard to exclude production noise within the reservoir as a cause for the observed signals because of the ambiguity in terms of source location. However, several physical mechanisms were proposed as a possible explanation for the natural emission of low-frequency signals. For instance, [Korneev \(2007\)](#) detected primary scattered and trapped circumferential waves in forms of sharp resonant peaks in seismic records, which can be explained by resonant effects in fractures partially filled with fluids. [Frehner et al. \(2007\)](#) considered the interaction of seismic background noise with oscillating pore fluids to cause low-frequency amplification in the seismic spectrum. Based on this idea, [Saenger et al. \(2007\)](#) discussed a theoretical model that explains why the seismic energy is mainly polarized on the vertical component. The basic idea is that pore fluid oscillations driven by background waves generate P- and S-waves, where the P-waves are emitted mainly in a vertical direction. Another hypothesis is low-frequency reflections caused by abnormally high attenuation in the reservoir and the corresponding increase of the reflection coefficient ([Quintal et al., 2007](#)). For all proposed rock physical mechanisms it is assumed that the reservoir rocks exhibit a partial saturation (e.g., with oil and water) while the rocks around the reservoir are fully saturated (e.g., with water only). The partial saturation of the reservoir rocks can then generate characteristic oscillations and/or high attenuation due to a wave induced flow; processes that are not active in fully saturated rocks. However, the impact of the various physical mechanisms is still open to debate and was not the main objective of this study.

4.7 CONCLUSIONS

The analysis of a comprehensive data set from a passive seismic survey over two hydrocarbon reservoirs in Voitsdorf, Austria, indicates that spectral attributes are suitable to quantify lateral variations of the microtremor wavefield (because temporal variations are smaller than spatial variations). Regarding hydrocarbon reservoirs, a distinct localization of the southern reservoir and a less clear localization of the northern reservoir was observed. The localization analysis is based on a combined interpretation of four spectral attributes. Three of those attributes (attributes 1, 3 and 4) show a distinct anomaly above the southern reservoir and attribute 2 shows an anomaly above the assumed southern boundary of the southern reservoir. Anomalies above the northern reservoir are only visible in the profiles of the peak frequency attributes (attributes 3 and 4). The corresponding anomalies are less pronounced and wider compared to the southern reservoir.

Due to the temporal variations of the signals, a processing method was applied that significantly improves the consistency of the results (stacking in time and space domain). This method

considers synchronized long-term measurements (several hours of raw records; no elimination of artificial noise) and combines profiles from multiple measurement lines.

A 2D numerical model for seismic wave propagation was used to investigate the measured anomalies of the peak frequency attributes (attributes 3 and 4). This model is based on the assumption that reservoirs emit seismic energy at low frequencies, induced by a vertical body force. If this assumption is correct, attributes 3 and 4 could be used as a depth-indicator for reservoirs.

The results indicate that passive low-frequency spectral analysis can increase the probability of locating reservoirs significantly. Clearly, more work is needed in the future to better understand the physical causes of the observed spectral anomalies.

ACKNOWLEDGEMENTS

We thank Spectraseis for providing the survey data presented in this study. Rohöl-Aufsuchungs Aktiengesellschaft (RAG) granted access to the Voitsdorf field and provided 3D seismic and other geophysical data referred to in this study. We acknowledge the financial support of the Swiss Commission for Technology and Innovation (CTI) and Spectraseis. Marcel Frehner provided numerical codes, which is gratefully acknowledged. We thank Yuri Podladchikov for valuable help and stimulating discussions. We thank Brad Artman and Ross Newman, from Spectraseis, for fruitful comments on the manuscript. E.H. Saenger thanks the DFG (Deutsche Forschungsgemeinschaft) for their support through the Heisenberg Programme (SA 996/1-1).

References

- Aki, K. & Richards, P. (2002). *Quantitative Seismology (2nd edition)*. University Science Books. ISBN 0-935702-96-2.
- Akrawi, K. & Bloch, G. (2006). *Application of passive seismic (IPDS) surveys in Arabian Peninsula*. EAGE Workshop Passive Seismic: Exploration and Monitoring Applications, Dubai, United Arab Emirates, Extended Abstracts, A28.
- Al Yuncha, Z., Luzon, F., Posadas, A., Martin, J., Alguacil, G., Almendros, J. & Sanchez, S. (2004). *The use of ambient seismic noise measurements for the estimation of surface soil effects: The Motril city case (Southern Spain)*. *Pure and Applied Geophysics*, **161**, 1549–1559.
- Aroutunov, S., Grafov, B. & Sirotinsky, Y. (1998). *ANChAR - an unique technology of direct hydrocarbon field exploration*. *Geoinformatics*, **98**, 12–15.

- Bard, P.-Y. (1999). *Microtremor measurements: A tool for site effect estimation?* In: The Effects of Surface Geology on Seismic Motion (eds K. Irikura, K. Kudo, K. Okada and T. Sasatami) [Balkema, Rotterdam, The Netherlands.], pp. 1251–1279.
- Birialtsev, E., Plotnikova, I., Khabibulin, I. & Shabalin, N. (2006). *The analysis of micro-seisms spectrum at prospecting of oil reservoir on Republic Tatarstan*. Paper presented at EAGE/EAGO/SEG International Conference & Exhibition, Saint Petersburg, Russia, Expanded Abstracts.
- Bohlen, T. & Saenger, E. (2006). *Accuracy of heterogeneous staggered-grid finite-difference modeling of Rayleigh waves*. *Geophysics*, **71**, T109–T115.
- Bour, M., Fouissac, D., Dominique, P. & Martin, C. (1998). *On the use of microtremor recordings in seismic microzonation*. *Soil Dynamics and Earthquake Engineering*, **17**, 465–474.
- Cerjan, C., Kosloff, D., Kosloff, R. & Reshef, M. (1985). *A nonreflecting boundary condition for discrete acoustic and elastic wave equations*. *Geophysics*, **50**, 705–708.
- Dangel, S., Shaepman, M. E., Stoll, E. P., Carniel, R., Barzandji, O., Rode, E.-D. & Singer, J. M. (2003). *Phenomenology of tremor-like signals observed over hydrocarbon reservoirs*. *J. Volcanol. Geothermal Res.*, **128**, 135–158.
- Fäh, D., Ruettener, E., Noack, T. & Kruspan, P. (1997). *Microzonation of the city of Basel*. *Journal of Seismology*, **1**, 87–102.
- Frehner, M., Schmalholz, S. & Podladchikov, Y. (2007). *Interaction of seismic background noise with oscillating pore fluids causes spectral modifications of passive seismic measurements at low frequencies*. Paper presented at the 77th SEG International Conference & Exhibition, San Antonio, USA, Expanded Abstracts, pp. 1307–1311.
- Frehner, M., Schmalholz, S., Saenger, E. & Steeb, H. (2008). *Comparison of finite difference and finite element methods for simulating two-dimensional scattering of elastic waves*. *Physics of the Earth and Planetary Interiors*, **168**. doi:10.1016/j.pepi.2008.07.003.
- Friedrich, A., Krüger, F. & Klinge, K. (1998). *Ocean-generated microseismic noise located with the Gräfenberg array*. *Journal of Seismology*, **2**, 47–64.
- Fäh, D., Kind, F. & Giardini, D. (2001). *A theoretical investigation of average H/V ratios*. *Geophys. J. Int.*, **145**, 535–549.
- Holzner, R., Eschle, P., Zuercher, H., Lambert, M., Graf, R., Dangel, S. & Meier, P. (2005). *Applying microtremor analysis to identify hydrocarbon reservoirs*. *First Break*, **23**, 41–46.

- Korneev, V. (2007). *Imaging of Subsurface Objects Using Resonant Seismic Emission*. Paper presented at the 77th SEG International Conference & Exhibition, San Antonio, USA, Expanded Abstracts, pp. 1113–1117.
- Korneev, V. (2008). *Slow waves in fractures filled with viscous fluid*. *Geophysics*, **73**, N1–N7.
- Kouznetsov, O., Chirkin, I., Dryagin, V., Aroutunov, S. & Meltschouk, B. (2005). *Induced seismoacoustic emission - basis for new technologies of fluid identification*. Paper presented at the 67th EAGE International Conference & Exhibition, Madrid, Spain, Expanded Abstracts, Z-99.
- Lambert, M., Schmalholz, S., Saenger, E. & Podladchikov, Y. (2007). *Low-frequency anomalies in spectral ratios of single station microtremor measurements: Observations across an oil and gas field in Austria*. Paper presented at the 77th SEG International Conference & Exhibition, San Antonio, USA, Expanded Abstracts, pp. 1352–1356.
- Lambert, M.-A., Schmalholz, S. M., Saenger, E. H. & Steiner, B. (2009). *Low-frequency microtremor anomalies at an oil and gas field in Voitsdorf, Austria*. *Geophysical Prospecting*, **57**, 393–411. doi:10.1111/j.1365-2478.2008.00734.x.
- Nakamura, Y. (1989). *A method for dynamic characteristics estimation of subsurface using microtremor on the ground surface*. Railway Technical Research Institute, Quarterly Report, **30**, 25–30.
- Nogoshi, M. & Igarashi, T. (1971). *On the amplitude characteristics of microtremor (Part 2)*. *Journal of the Seismological Society of Japan*, **24**, 26–40.
- Parolai, S. & Galiana-Merino, J. (2006). *Effect of transient seismic noise on estimates of H/V spectral ratios*. *Bull. Seism. Soc. Am.*, **96**, 228–236.
- Peterson, J. (1993). *Observations and modeling of background seismic noise*. Open-file report 93-322, US Geological Survey, Albuquerque, USA.
- Quintal, B., Schmalholz, S., Podladchikov, Y. & Carcione, J. (2007). *Seismic low-frequency anomalies in multiple reflections from thinly-layered poroelastic reservoirs*. Paper presented at the 77th SEG International Conference & Exhibition, San Antonio, USA, Expanded Abstracts, pp. 1690–1695.
- Rached, G. (2006). *Surface passive seismic in Kuwait*. EAGE Workshop Passive Seismic: Exploration and Monitoring Applications, Dubai, United Arab Emirates, Extended Abstracts, A27.

- Roten, D., Faeh, D., Cornou, C. & Giardini, D. (2006). *Two-dimensional resonances in Alpine valleys identified from ambient vibration wavefields*. *Geophys. J. Int.*, **165**, 889–905.
- Sachsenhofer, R., Gratzner, R., Tschelaut, W. & Bechtel, A. (2006). *Characterisation of non-productible oil in Eocene reservoir sandstones (Bad Hall Nord field, Alpine Foreland Basin, Austria)*. *Marine and Petroleum Geology*, **23**, 1–15.
- Saenger, E., Torres, A., Rentsch, S., Lambert, M.-A., Schmalholz, S. & Mendez-Hernandez, E. (2007). *A hydrocarbon microtremor survey over a gas field: Identification of seismic attributes*. Paper presented at the 77th SEG International Conference & Exhibition, San Antonio, USA, Expanded Abstracts, pp. 1277–1281.
- Saenger, E. H., Gold, N. & Shapiro, S. A. (2000). *Modeling the propagation of elastic waves using a modified finite-difference grid*. *Wave Motion*, **31**, 77–92.
- Ibs-von Seht, M. & Wohlenberg, J. (1999). *Microtremor Measurements Used to Map Thickness of Soft Sediments*. *Bull. Seism. Soc. Am.*, **89**, 250–259.
- Steiner, B., Saenger, E. & Schmalholz, S. (2008). *Time reverse modeling of low-frequency microtremors: Application to hydrocarbon reservoir localization*. *Geophys. Res. Lett.*, **35**, L03307. doi:10.1029/2007GL032097.
- Suntsov, A., Aroutunov, S., Mekhnin, A. & Meltschouk, B. (2006). *Passive infra-frequency microseismic technology - Experience and problems of practical use*. EAGE Workshop Passive Seismic: Exploration and Monitoring Applications, Dubai, United Arab Emirates, Extended Abstracts, A25.
- Teves-Costa, P., Matias, L. & Bard, P.-Y. (1996). *Seismic behaviour estimation of thin alluvium layers using microtremor recordings*. *Soil Dynamics and Earthquake Engineering*, **15**, 201–209.
- Turuntaev, S., Burchik, V. & Turuntaev, D. (2006). *Microseismic background study for gas field exploration*. Paper presented at the 76th SEG International Conference & Exhibition, New Orleans, USA, Expanded Abstracts, pp. 115–119.
- Virieux, J. (1986). *P-SV-wave propagation in heterogeneous media: Velocity-stress finite-difference method*. *Geophysics*, **51**, 889–901.
- Yilmaz, O. (1987). *Seismic Data Processing, Volume 2*. SEG. ISBN 0931830400.
- Zhukov, A., Loginov, K., Shneerson, M., Shulakova, V., Kharisov, R. & Ekimenko, V. (2007). *Nonlinear properties of vibrator-generated wavefields and their application to hydrocarbon detection*. *The Leading Edge*, **26**, 1395–1402.

5. Spectral analysis of ambient ground-motion - Noise reduction techniques and a methodology for mapping horizontal inhomogeneity

Marc-André Lambert, Tung Nguyen, Erik H. Saenger & Stefan M. Schmalholz

ABSTRACT

Inhomogeneities in the subsurface interact with and modify seismic waves. As a consequence, the quasi-stationary, ambient ground-motion response at the Earth's surface carries valuable information about underground inhomogeneities. Extracting and interpreting such information by analyzing low-frequency passive measurements is not an easy task because distinct events in the time traces are usually absent in ambient ground-motion recordings and the signal-to-noise ratio is low. This paper presents four processing techniques to reduce anthropogenic noise effects and proposes a methodology for extracting and mapping passive seismic characteristics that help detect horizontal inhomogeneity. The methodology uses Fourier amplitude spectra to calculate four independent spectral attributes that quantify signatures of interest in the data. The methodology is applied to a noisy data-set acquired at an oil and gas field in Austria. Two horizontally separated hydrocarbon reservoirs are considered as possible inhomogeneities in the subsurface. Results show that anthropogenic noise is successfully removed from the data, enhancing the signal-to-noise ratio. Attribute profiles are extracted and show stable patterns that are apparently related to stationary site properties. Correlation between patterns of spectral attributes at the Earth's surface and the horizontal location of the reservoirs is not as clear as reported in case-studies across other oil or gas fields. This paper discusses an application for hydrocarbon exploration. However, the proposed methodology is suitable to quantify and map signatures related to any subsurface inhomogeneity (e.g. underground cavities) or seismic source (e.g. volcanic tremor) that is of interest and has a measurable impact on the ambient ground-motion at the Earth's surface.

5.1 INTRODUCTION

Different case studies and numerical simulations have shown that embedded inhomogeneities of seismic properties can have significant effects on the seismic surface response of a medium (Rechtien & Stewart, 1975; Gucunski et al., 1996; Campman et al., 2004; Phillips et al., 2004). Consequently, the quasi-stationary, ambient seismic wave-field at the Earth's surface is affected by the seismic properties of the subsurface. Inhomogeneities modify the ambient wave-field through different types of interactions, such as wave reflection and refraction, mode conversions, amplitude damping or resonant scattering. If strong enough, the resulting response can be measured at the Earth's surface and provide information on the inhomogeneity itself. For example, Parolai et al. (2002) extracted information from ambient ground-motion to map the sediment-bedrock interface down to depths of more than 1000 m in the Cologne area in Germany. Nasseri-Moghaddam et al. (2007) successfully analyzed anomalous patterns in ambient ground-motion measured at the surface to detect a cavity in 50 m depth at a mine site in Canada. They also tested active sources, such as explosives and sledge hammer, but concluded that the passive, ambient ground-motion is the only seismic source that can provide enough energy in the low-frequency range for their test. Due to the complex nature of the ambient wave-field, including a low signal-to-noise ratio (S/N-ratio) and no observable arrivals in the time traces, Nasseri-Moghaddam et al. (2007) found Fourier amplitude spectra in particular to be sensitive to the presence of the cavity. Therefore, frequency domain parameters were introduced for detecting underground inhomogeneity.

Several independent studies have attempted to apply similar spectral analysis techniques to detect hydrocarbon reservoirs (e.g. Dangel et al., 2003; Zhukov et al., 2007; van Mastrigt & Al-Dulaijan, 2008; Schechinger et al., 2009). These studies have reported an apparent correlation between spectral patterns in low-frequency (<10 Hz) passive ground-motion recordings at the Earth's surface and the horizontal location of reservoirs. It was speculated that the observed patterns may indeed be related to the presence of reservoirs in the subsurface and therefore could be used for reservoir detection. However, the applicability of spectral analyses to passive data and the basic physical justification of using such analyses to detect reservoirs are controversially discussed at present (e.g. Lambert et al., 2009; Ali et al., 2009; Green & Greenhalgh, 2010; Lambert et al., 2010). The study presented here analyzes low-frequency passive data that was measured across two reservoirs and attempts, amongst other things, to map patterns in the data that are collocated with reservoirs. With the aim of avoiding potential misinterpretation, we state here the hypothesis considered in this study and we provide several arguments for justifying its consideration in order to motivate the presented data analysis:

“Hydrocarbon reservoirs can have different seismic properties (e.g. impedance, velocity, attenuation) at different frequencies (e.g. attenuation due to wave-induced fluid flow) than the surrounding rocks and physical processes can occur in reservoirs (e.g. microseismicity, fluid flow, fluid oscillation) that occur with different intensity than in the surrounding rocks. The presence of hydrocarbon reservoirs, therefore, modifies the ambient seismic wave-field and these modifications can be detected by applying spectral analysis to passive ground-motion measurements at the Earth’s surface.”

This hypothesis is plausible to consider because of two basic observations: First, continuous natural seismic signals in the low-frequency range are present at reservoir depth. Such signals can for example originate from earthquakes of various magnitudes and hypocenter locations (including microseismicity). However, apart from transient events there is also evidence of continuous seismic motion at reservoir depths. [Zhang et al. \(2009\)](#) showed that the ambient seismic wave-field between 0.6 and 2 Hz is dominated by continuous P-wave energy arriving from beneath the station-arrays at two sites in California. Similar observations have been made in northern Canada, where stable consistent signals of 0.5-1 Hz P-waves from far-away source areas in the northwest Pacific and central Atlantic are often the largest source of ambient ground-motion ([Koper et al., 2009](#)). In addition, reservoirs are constantly perturbed by surface waves. Ubiquitous oceanic microseisms propagate as Rayleigh waves through entire continents and are used to determine seismic velocities down to a depth of 20 km ([Shapiro et al., 2005](#)). [Draganov et al. \(2007\)](#) demonstrate the feasibility of using natural ambient ground-motion for exploration purposes. They used cross-correlations of passive recordings at frequencies between 2 and 10 Hz to retrieve P-wave reflections with travel-times as great as 2 seconds at a proven, non-producing gas reservoir situated deep within Saudi Arabia’s Rub’ al Khali desert.

Second, hydrocarbon reservoirs are underground inhomogeneities and can therefore interact with and modify the seismic wave-field. The contrast in seismic impedance between reservoirs and surrounding rocks is usually small, but attenuation contrasts can be substantial. The attenuation behavior of reservoirs at seismic frequencies was theoretically explained by energy dissipation due to wave-induced fluid flow in partially saturated porous rocks ([White, 1975](#)). Laboratory experiments confirmed a strong, frequency-dependent increase of attenuation in partially saturated rock samples compared to dry or fully saturated samples ([Spencer, 1981](#); [Paffenholz & Burkhardt, 1989](#)). Results from field data suggested that quality factors (Q), the inverse of attenuation, can be as small as 10 inside reservoirs (e.g. [Klimentos, 1995](#); [Dasgupta & Clark, 1998](#); [Korneev et al., 2004](#)). Fully saturated sediments around reservoirs typically have much larger Q -values in the order of a few tens to several hundreds. [Korneev et al. \(2004\)](#) used laboratory and field data to show that attenuation contrast can be associated with an increase in reflectivity. Wave propagation phenomena associated with high attenuation and the related increase in reflectivity are utilized in seismic exploration for direct hydrocarbon indication,

for example within the framework of low-frequency shadows below gas reservoirs (Chopra & Marfurt, 2005). Also, Korneev et al. (2004) consider frequency-dependent reflection of waves due to frequency-dependent attenuation within the reservoir. Kallweit & Wood (1982) and Tai et al. (2009) investigate peak-frequency shifts and amplitude distortion caused by overlapping reflections from top and bottom of a thin layer (tuning effect). Resonant scattering, excited by seismic waves, causes an inhomogeneity to oscillate with its natural frequency and to re-emit waves into the medium (Korneev & Johnson, 1996; Liu et al., 2000; Korneev, 2008). All these phenomena are frequency-dependent and particularly observed at low seismic frequencies (e.g. Korneev et al., 2004; Chapman et al., 2006; Goloshubin et al., 2006; Quintal et al., 2009). In addition to pure wave propagation phenomena, effects like seismically-induced shear failure (e.g. Obana & Kodaira, 2009) or oscillating fluids in pore spaces and fractures (Beresnev et al., 2005; Korneev, 2008; Frehner et al., 2009) might also occur and excite seismic signals that contribute to wave-field modifications in the vicinity of a reservoir.

Therefore, the critical question for evaluating the aforementioned hypothesis of reservoir-related modifications in ambient ground-motion is not whether such modifications do occur, but rather whether or not they are strong enough to be detectable in ground-motion recordings at the Earth's surface and distinguishable from other, non-reservoir related modifications. Since the hypothesis refers to hydrocarbon reservoirs in general, and reservoirs can be (i) of different size, (ii) composed of different types of reservoir rocks and fluids, (iii) surrounded by different types of rocks, (iv) located in different tectonic stress regimes and (v) located in areas with different natural and anthropogenic ambient wave-fields, this question should be evaluated for each reservoir separately. For example, Hanssen & Bussat (2008) and Ali et al. (2010) presented case-studies in Libya and Abu Dhabi, respectively, which concluded that the analyzed ground-motion is not influenced by the presence of known hydrocarbon reservoirs. However, their results seem to be dominated by anthropogenic noise and near-surface effects which they did not successfully remove from the data prior to interpretation. Therefore the studies are not able to falsify the hypothesis for these reservoirs. Results from other case-studies are more positive with respect to the hypothesis but unfortunately these studies either (i) offer only limited conclusiveness because of high anthropogenic noise and/or complex geology (Lambert et al., 2009; Saenger et al., 2009; Schechinger et al., 2009), (ii) only provide an incomplete description of the applied processing methods (van Mastrigt & Al-Dulaijan, 2008) or (iii) present only isolated measurements (Dangel et al., 2003). Therefore, these studies are not able to verify the hypothesis.

In this paper we propose processing techniques that allow suppressing the effects of anthropogenic noise on passive seismic signals. The techniques are designed to take into account the small number of synchronized data points and the coarse spatial sampling that have been typical for low-frequency passive seismic surveys. In addition, we present a methodology to extract and

quantify features in the data that can contain subsurface information. The aim of this study is to improve the methods for spectral analysis of ambient ground-motion at oil or gas fields, eventually providing more conclusive results pro or contra reservoir-related signatures. Data from a survey conducted at an oil and gas field in Voitsdorf, Austria, is used to demonstrate the processing techniques. First, we explore the passive data-set, discriminating between features of obvious anthropogenic origin (“noise”) and features of interest that have been proposed to potentially contain reservoir-related information (“signal”). Similar to [Nasseri-Moghaddam et al. \(2005\)](#), we then introduce spectral attributes that help quantify and map these signals in space and time. The main part of the paper explains how the data is processed to enhance the signal-to-noise ratio by reducing noise influences. Single station methods and linear array methods are presented. Finally, results from cleaned data are discussed.

5.2 DATA

The data for this study was acquired by Spectraseis in 2007 and 2008 at the Voitsdorf oil and gas field in Austria which is operated by Rohöl-Aufsuchungs Aktiengesellschaft (RAG). More than 50 three-component broadband seismometers continuously recorded the ambient ground motion (particle velocity) with a sampling rate of 100 Hz. The seismometers were synchronized using GPS clocks and recorded at nighttime in an attempt to minimize anthropogenic noise. The geometry of three different station arrays is shown in [Figure 5.1](#). The blue dots depict two parallel linear arrays (L1 and L2) with a length of 11.5 km each and 250 m average in-line spacing between seismometers. The white dots show the stations of a 11x3 km rectangular grid-array (G1) with 1 km seismometer spacing. Lines L1 and L2 were acquired in 2008 during the night of March 29 to 30 and March 30 to 31, respectively. The grid recorded during the night from April 1 to April 2 of the same year. The magenta triangles show stations that were deployed one year earlier, in spring 2007. Dashed orange lines indicate the surface projection contours of the two reservoirs in the survey area. The reservoirs’ depth is approximately 2 km. Roads are shown in gray. Green and yellow colors illustrate the topography which varies between 400 m and 550 m above mean sea level. A description of the Voitsdorf oil and gas field and the geological setting of the area can be found in [Lambert et al. \(2009\)](#).

5.2.1. Anthropogenic noise

Three noise-types of anthropogenic origin can be identified from the data:

- (A) Local transient noise
- (B) Stationary narrow-band noise
- (C) Correlated transient noise

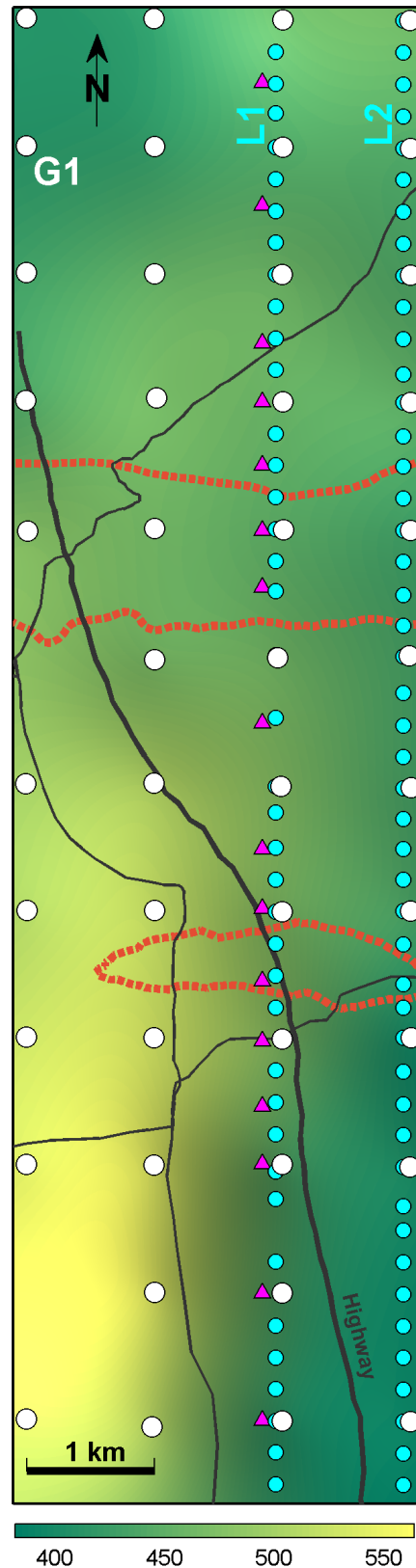


Figure 5.1. Geometry of the seismometer arrays deployed in spring 2008. White dots indicate stations of the rectangular grid-array (G1). Blue dots show the stations of two densely spaced linear arrays (L1 and L2). Reservoir contours are indicated as dashed orange lines. Roads are shown in gray. Green and yellow colors illustrate the topography of the area (values in meter AMSL). The magenta triangles indicate stations of the 2007 experiment.

Noise-types A and B are visible in the data example displayed as vertical-component spectrogram in Figure 5.2a. The spectrogram is generated from 30 minutes of data by computing the Fourier amplitude spectra for a 20 s moving time interval shifted by 1 s time steps. Each time interval is windowed with a 10% Hanning taper. The four high-amplitude (red) vertical lines at the times $t=250$ s, $t=800$ s, $t=935$ s and $t=1000$ s correspond to noise-type A. They are caused by non-stationary noise sources near to the recording station, most likely related to cultural activities like farming, traffic or construction work. Instrumental irregularities can give rise to similar noise signatures. The spectrogram also exhibits a high-amplitude horizontal line at a frequency of $f=3.3$ Hz. This signature is caused by a stationary, monochromatic noise source, possibly a pump operating at this particular frequency and is classified as noise-type B. The right panel in Figure 5.2a shows the two-dimensional (2D) histogram of the spectrogram amplitudes (frequency of occurrence plotted versus spectral amplitude and seismic frequency). This representation can be interpreted as an empirical estimate of the probability density function (PDF) of the amplitudes displayed in the spectrogram to the left. Looking at only one particular seismic frequency, the amplitude distribution generally resembles a log-normal distribution. However, for some frequencies, long tails of higher amplitudes exist (e.g. around 5 Hz). The black line highlights the maximum and the magenta line the expectation value (arithmetic mean) of the PDF. Both lines represent a different characteristic spectrum for the 30 minute interval. In this example, the arithmetic mean amplitude is larger than the maximum PDF amplitude for all frequencies. This is due to noise-type A which contributes a few very large amplitudes (outside the amplitude-range displayed in the histogram plot) which boost the arithmetic mean. Because of its stationary characteristic, the narrow-band noise at 3.3 Hz (B) gives rise to a spike in both, the arithmetic mean spectrum as well as the maximum PDF spectrum.

An example of noise-type C is shown in the six minutes long ground-motion sample displayed in Figure 5.3. The vertical component velocity waveforms measured along line L2 are band-pass-filtered between 1 and 6 Hz. The red lines highlight transient events across the survey line with a move-out of approximately 25 m/s (90 km/h). Such a low apparent velocity can not be explained by propagating seismic waves of any type but rather by moving seismic sources, in this case vehicles driving on a nearby road.

5.2.2. Features of interest

The frequency band between approximately 0.2 and 6 Hz is often characterized by a low level of ambient background noise. Below 0.2 Hz the wave-field is overwhelmed by the large amplitudes of the ubiquitous oceanic microseisms (Cessaro, 1994, and references therein). Above 6 Hz anthropogenic noise usually becomes dominant (Bonnetoy-Claudet et al., 2006). Therefore, frequencies between 0.2 and 6 Hz are expected to offer the highest potential to reveal features

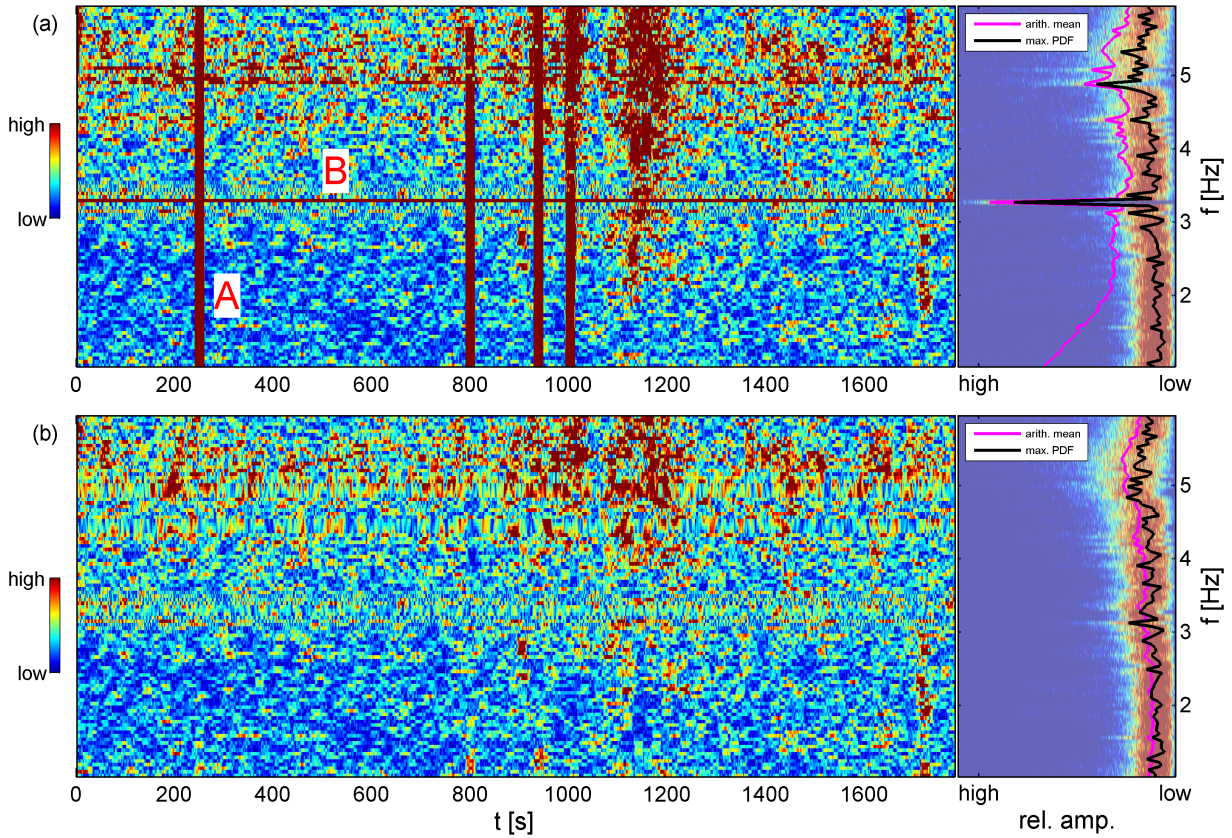


Figure 5.2. 30 minutes section of a vertical-component ground-velocity spectrogram in the frequency range of 1-6 Hz from a representative station. The panels on the right-hand side show the statistical distribution of the spectrogram amplitudes as a two-dimensional histogram (empirical probability density function, PDF). Magenta and black lines indicate the arithmetic mean spectrum and the maximum PDF spectrum, respectively. (a) Raw data that include signals of noise type A and B. (b) Cleaned data after temporal normalization and spectral despiking.

of interest that are otherwise masked by noise. Figure 5.4a displays the empirical PDF of the spectral amplitudes estimated from synchronized vertical component velocity data from the ensemble of all 48 stations of line L2 measured between midnight and 00:30 a.m. The data has been processed using temporal normalization and spectral despiking (these processing techniques are described in section 5.3). Figure 5.4a provides an overall statistical impression on the spectral amplitudes in the survey area. A feature of elevated amplitudes is visible roughly between 1 and 4 Hz. Similarly, the PDF of the ratio between the spectral amplitudes of vertical and horizontal ground motion (V/H-ratio), in Figure 5.4b, suggest that some stations exhibit elevated V/H-amplitudes around 2 Hz. It was suggested that these or similar features could carry information on reservoir-related modifications in the wave-field (Dangel et al., 2003; van Mastrigt & Al-Dulaijan, 2008; Saenger et al., 2009; Lambert et al., 2009). Four spectral seismic attributes are used in this study to quantitatively describe these features and to map their distribution in space and time.

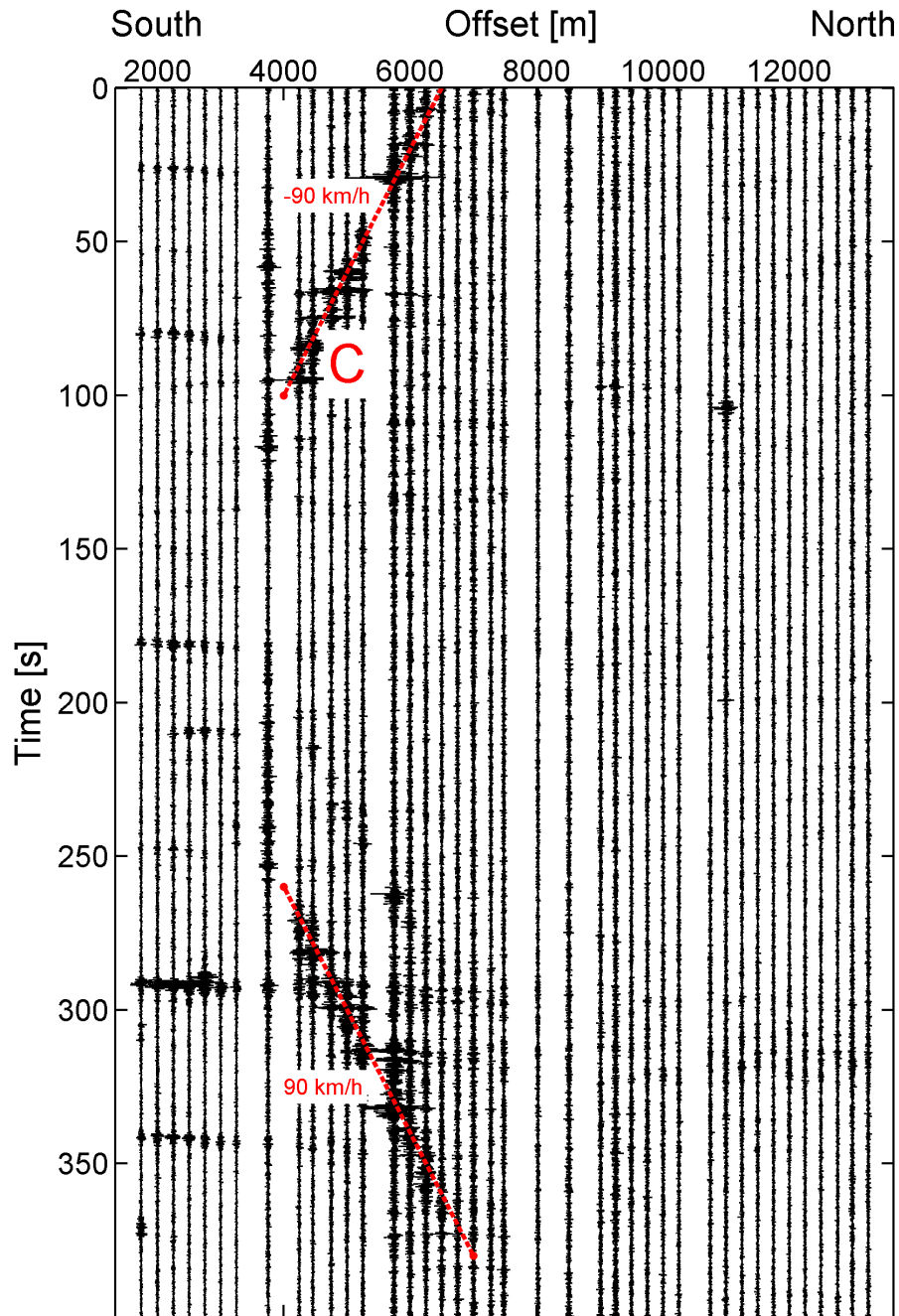


Figure 5.3. 6 minutes of band-pass-filtered (1-6 Hz) vertical component velocity waveforms measured across line L2 (relative amplitudes). The red lines highlight signals that can be attributed to vehicles driving on a nearby road (noise-type C).

5.2.3. Spectral attributes

Seismic attributes are defined as the quantitative measure of a seismic characteristic of interest (Chopra & Marfurt, 2005). Attributes describe, with a single value, a characteristic of the wave-field at one particular position at a given time. These values can be displayed, used for further processing (like stacking, averaging, normalizing, etc.) or interpreted in a quantitative, statistical manner. We choose to operate in the frequency domain because quasi-stationary modifications of a passive signal with no observable arrivals and low S/N-ratio appear more

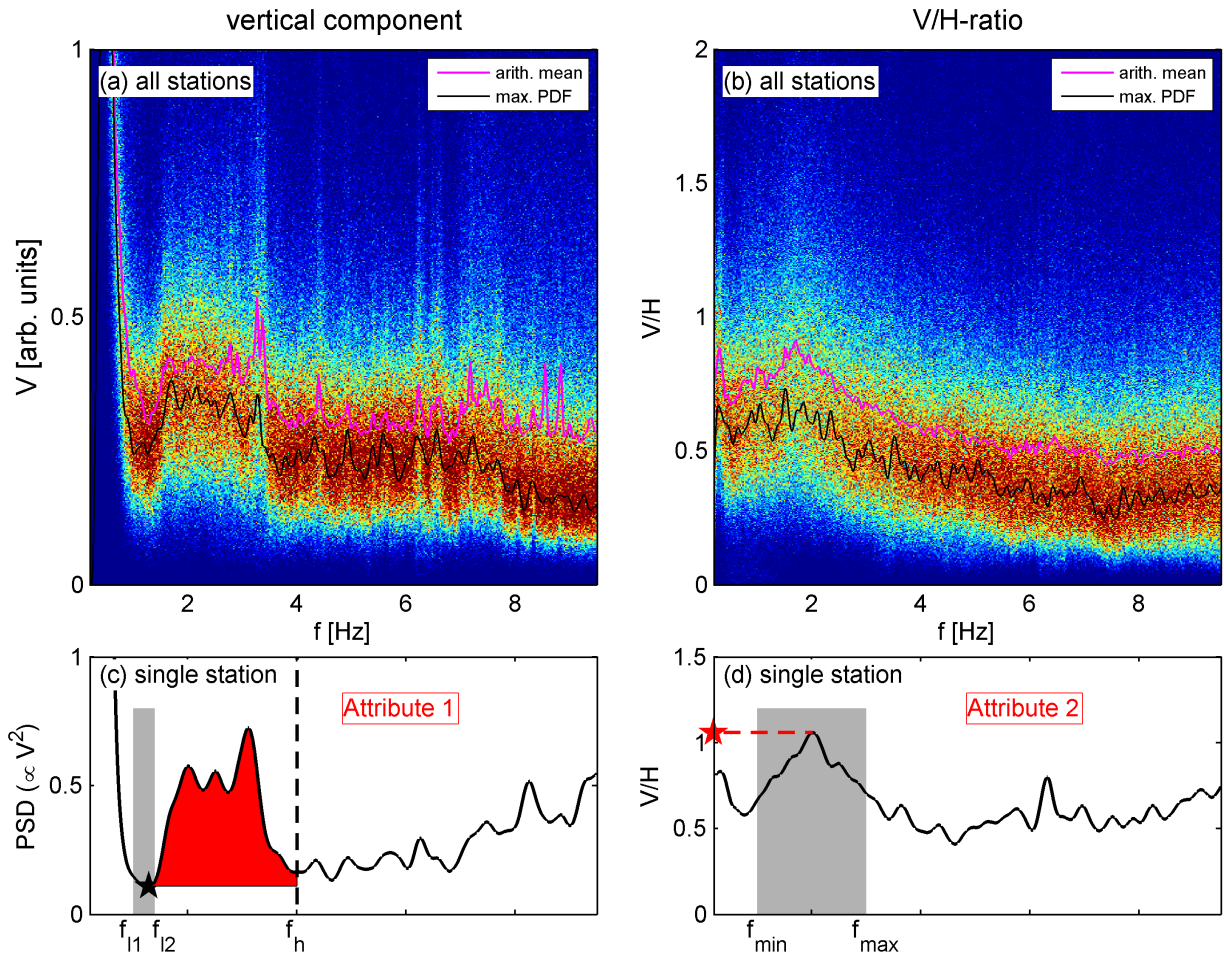


Figure 5.4. (a) 2D histogram of the spectral amplitude distribution of vertical ground motion recorded with all 48 stations of line L2 between midnight and 00:30 a.m. The magenta and black lines indicate the arithmetic mean spectrum and the maximum PDF spectrum, respectively. (b) Same as (a) but for the vertical-to-horizontal spectral amplitude ratio. (c) Sketch for definition of Attribute 1. The attribute value is given by the red area below the power spectral density curve of the vertical ground velocity component. (d) Sketch for definition of Attribute 2. The attribute value is given by the dominant maximum in the V/H spectral ratio of ground motion.

conspicuously in its frequency spectrum (Nasseri-Moghaddam et al., 2007). Similar to Nasseri-Moghaddam et al. (2005), we define and extract spectral attributes from the measured spectra. Spectral seismic attributes allow tracking changes in spectra in time and space. Even small deviations can be detected, something that would be more difficult by just a visual inspection of the spectra. Spectral attributes are useful to simplify the temporal and spatial analysis of a complex phenomenon like the ambient wave-field.

The attributes chosen for this study are Attribute 1 to 4 from Lambert et al. (2009) because they quantify the features of interest identified in the previous section. In the following, Attributes 1 and 2 are used to demonstrate analysis methods and noise-removal techniques. Figures 5.4c and 5.4d schematically illustrate the definition of the attributes. Attribute 1 is an integral value under the power spectral density (PSD) curve of the vertical component of

ground motion and therefore quantifies energy in a chosen frequency band (red area). Only the area above a certain amplitude level contributes to the attribute value. This level is defined from the data by the minimum PSD (black star) within a narrow frequency band, defined by f_{l1} and f_{l2} , at low frequencies. The upper integration boundary is given by the fixed frequency f_h (dashed line), above which anthropogenic noise is expected to become dominant. Attribute 2 quantifies the dominant maximum (red star) of the V/H-ratio in the frequency range between f_{min} and f_{max} . To compute the V/H-ratio, the data is cut into 40 s long time windows, detrended and processed with a 10% Hanning taper and with a fast Fourier transform algorithm. The resulting amplitude spectra are smoothed using a 0.1 Hz running frequency window and the two horizontal components are combined using the root mean square average. Finally, the vertical-to-horizontal spectral ratios for each of the 40 s windows are arithmetically averaged over the window ensemble.

The Attributes 3 and 4 are based on frequency values, in Hz, of dominant peaks in a given frequency interval $[f_{min}, f_{max}]$ of the amplitude spectrum of vertical and horizontal ground motion, respectively. These frequency-based quantities are expected to be more stable than amplitudes and provide complementary information on a spectral feature. For example, [Nasseri-Moghaddam et al. \(2007\)](#) show with synthetic data that scattered waves from a buried inhomogeneity not only exhibit energy concentrations but also characteristic frequency patterns at the surface (“ripples”) which are sensitive to the location, depth and size of the inhomogeneity. Attributes 3 and 4 are described in [Lambert et al. \(2009\)](#) and will be used at the end of this paper for the evaluation of the cleaned data-set.

The parameters needed to calculate the attributes (f_{l1} , f_{l2} , f_h , f_{min} and f_{max}) are empirically determined with respect to the characteristics of the data in order to capture the feature of interest. For this study, the parameters have been chosen based on the representative spectral distribution shown in Figure 5.4a and 5.4b. The values are given in Table 5.1.

Attribute 1	f_{l1}	f_{l2}	f_h
	1.0 Hz	1.4 Hz	4.0 Hz
Attribute 2	f_{min}	f_{max}	
	1.0 Hz	3.0 Hz	
Attribute 3	f_{min}	f_{max}	
	1.0 Hz	6.0 Hz	
Attribute 4	f_{min}	f_{max}	
	1.0 Hz	6.0 Hz	

Table 5.1. Parameters used to calculate the four attributes. The parameters are determined based on the data shown in Figure 5.4a and 5.4b.

5.2.4. Spatial and temporal patterns of raw-data attributes

Figure 5.5a shows values of Attribute 1 versus distance along line L1 computed from raw data of 7 consecutive time-windows of 30 minutes duration from 00:30 a.m. to 05:00 a.m. The apparent gap of one hour between 03:00 a.m. and 04:00 a.m. occurs due to adjustment of the clocks for daylight-saving time which coincidentally took place in that particular night. The black line in Figure 5.5c shows a stack of the profiles (arithmetic mean) in Figure 5.5a. Magenta dots are results from measurements conducted one year earlier, spring 2007. The error bars indicate the ± 1 standard deviation range of the values from 7 consecutive time-windows for the 2007 survey. Figures 5.5b and 5.5d display the results for Attribute 2. Figure 5.5 suggest that:

- (i) Spatial patterns of Attribute 1 and 2 are independent from each other. There is no obvious correlation between their spatial patterns.
- (ii) Temporal and spatial variations of Attribute 2 are smaller compared to Attribute 1.
- (iii) Spatial patterns of Attribute 1 and 2 are relatively consistent in time (on an hourly scale as well as on a yearly scale) and therefore presumably contain a significant amount of site specific information. An exception to this is the major anomaly of Attribute 1 at an offset of 5500 m.

Figure 5.6a shows a map view of the distribution of Attribute 1 in the survey area. The values were computed from 30 minutes of raw data measured with grid G1. White dots depict the measurement locations and roads are shown in gray. Many stations showing high values of Attribute 1 are located close to a highway, the busiest road in the area and hence one of the major anthropogenic noise sources. Note that the major anomaly of Attribute 1 observed at an offset of 5500 m along line L1 (Figure 5.5a and 5.5c) occurs where the line intersects the highway and is therefore expected to be strongly affected by anthropogenic signals. In fact, Lambert et al. (2009) have already suspected (based on results of the 2007 data) that this anomaly is caused by a strong and unstable source, possibly related to cultural activities. This view is now supported with the more comprehensive data-set of 2008.

5.3 NOISE FILTERING

Anthropogenic noise has been discriminated from signals of interest in the previous section. Spectral attributes were introduced to quantify the interesting signals in order to describe and analyze their spatial patterns. Raw data suggested that attribute values provide site specific information and also that they can be strongly affected by anthropogenic noise. It is therefore crucial to reduce the unwanted noise effects as much as possible prior to analyzing attribute

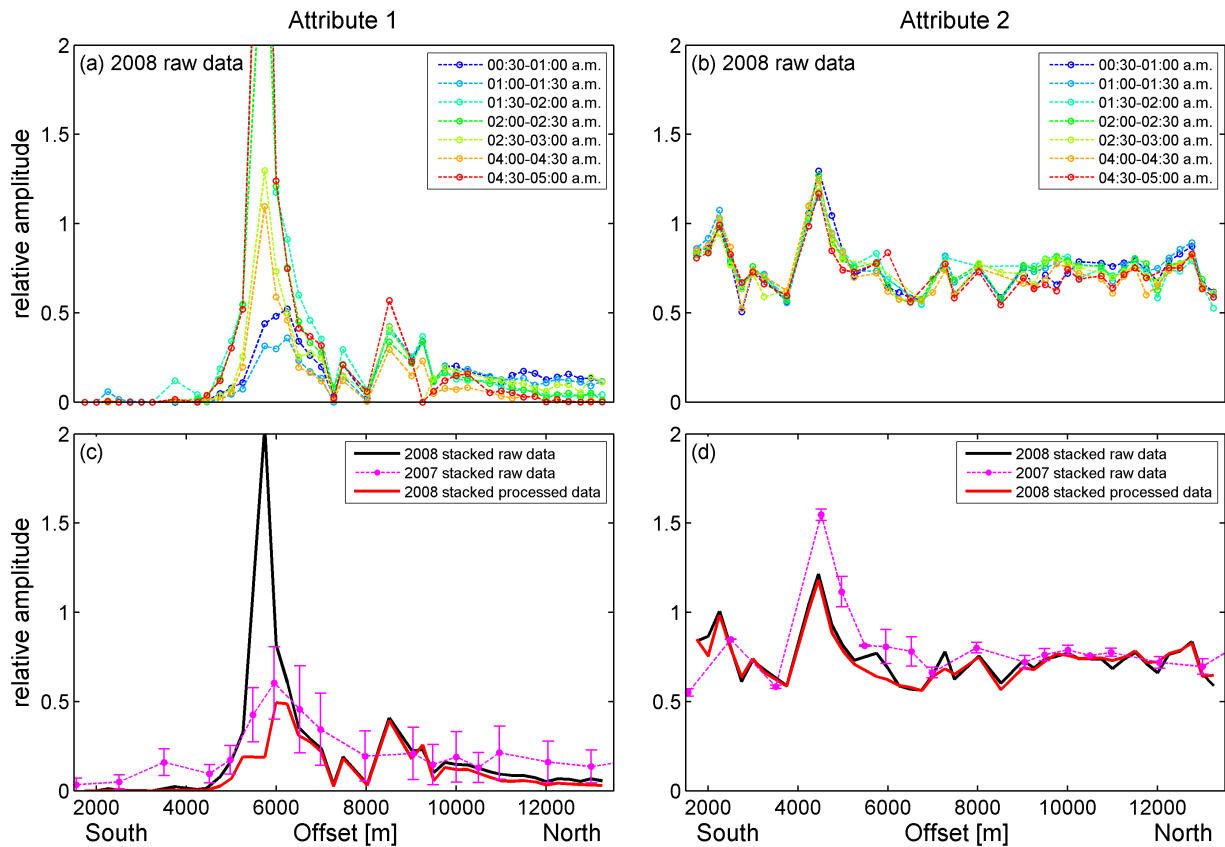


Figure 5.5. Attribute profiles across line L1. (a) Attribute 1 computed from raw data of 7 consecutive time-windows. (c) Black line: Stack of the profiles shown in (a). Magenta dots with error bars: Stacked attribute values and standard deviations from the 2007 data-set. The red line shows the stacked profile computed from 2008 data, processed with temporal normalization and spectral despiking. (b),(d) Corresponding results for Attribute 2.

patterns. Four techniques are presented which are applied to systematically suppress the noise-types A, B and C and therefore enhance the S/N-ratio. We distinguish between techniques individually applied to recordings from single stations and techniques that take advantage of a collection of synchronized recordings from linear arrays. The latter techniques are applied to attribute sections, a representation of the attribute values in the 2D time-space domain.

5.3.1. Single station techniques

The processing techniques introduced in this section are designed to remove noise of type A and B from ground motion recordings of individual stations. Figure 5.2 shows an example where this goal has been successfully achieved. Local transient noise (A) as well as the stationary narrow-band noise at $f=3.3$ Hz (B) have disappeared in the cleaned spectrogram in Figure 5.2b. The rest of the wave-field has been preserved during the noise-removal process. The arithmetic mean spectrum and the maximum PDF spectrum of the cleaned data exhibit a similar shape because the transient noise, responsible for boosting the arithmetic mean values in Figure 5.2a,

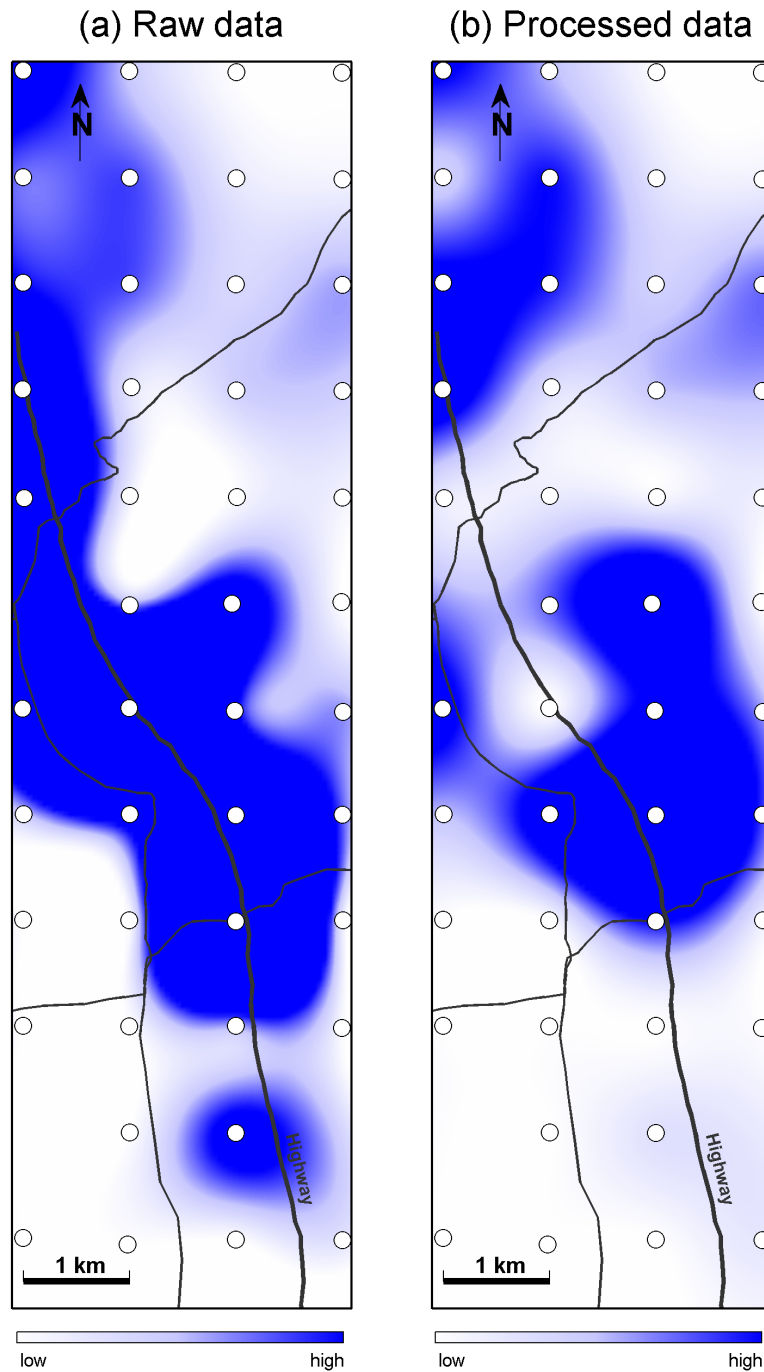


Figure 5.6. (a) Map view of the spatial distribution of Attribute 1 computed from raw grid-array data using a standard triangle-based interpolation algorithm. (b) Attribute map computed from data that has been processed using single-station techniques. White dots depict the measurement locations. Roads are shown in gray.

is omitted. The noise-filtering procedures leading to the result in Figure 5.2b are described in the following.

Temporal normalization to remove noise-type A

Benson et al. (2007) have introduced several methods to reduce the effects of local, non-stationary noise sources, earthquakes and instrumental irregularities on recorded ambient noise.

We use a modified version of their “running-absolute-mean normalization” to suppress local transient noise in our data (noise-type A). Our method first computes the band-pass filtered waveform amplitudes in the target frequency range (i.e. the frequency interval from which attributes will be computed). The weighted moving average (WMA) of the absolute amplitudes is then computed from the band-passed data using a moving Hanning window of fixed width. Finally, the original data is weighted at the centre of each window by the inverse of the corresponding WMA value. For a time-series x_j , the WMA for sample n is given as

$$WMA_n = \frac{1}{2N+1} \sum_{j=n-N}^{n+N} \frac{1}{2} \left[1 + \cos \left(\frac{\pi(j-n)}{N} \right) \right] |x_j|. \quad (5.1)$$

The width of the normalization window ($2N+1$) determines how much amplitude information is retained. A one-sample window ($N=0$) will normalize all amplitudes to a value of 1 and preserves only the sign of the signal, while a very long window ($N \rightarrow \infty$) will approach a re-scaled version of the original waveform. [Benson et al. \(2007\)](#) used a rectangular window instead of the Hanning window. The Hanning window function puts more emphasis to the amplitudes in the centre of the window and creates a smoother WMA function. However, comparisons with a rectangular window have shown only minor differences in the final result. In contrast to the method proposed by [Benson et al. \(2007\)](#), only WMA values greater than a threshold are considered for the normalization. The threshold is given as the p -th percentile of all WMA values. The WMA of the three components are summed up before computing the percentile and the full data-set (signals from all stations) is used to determine the percentile. Samples whose corresponding WMA does not exceed the threshold remain untouched. This is an important generalization of the method because it allows restriction of the normalization procedure to those time windows that are really affected by transient noise. A threshold equal to the 0th percentile ($p=0$) corresponds to Benson et al.’s method and normalizes the full data record.

The example in [Figure 5.7](#) illustrates the procedure. The heavily noise-contaminated vertical-component broad-band data in [Figure 5.7a](#) is first band-pass filtered in the target frequency range of 0.5 to 6.5 Hz ([Fig. 5.7b](#)). The massive noise feature between $t=250$ s and $t=450$ s has disappeared in the band-passed data, because this feature occurs at frequencies outside the target range. The weighted moving average of the absolute amplitudes of the band-passed data is shown in [Figure 5.7c](#). The WMA was computed using [equation 5.1](#) with a value of $N=100$ which corresponds to a window width of 2 s. The dashed line indicates the threshold corresponding to the 95th percentile, i.e. 5% of all WMA values are above the threshold. [Figure 5.7d](#) shows the broad-band data after normalization, i.e. the raw data of [Figure 5.7a](#), weighted by the inverse of the WMA values that exceed the threshold in [Figure 5.7c](#). The transient noise is still visible in the normalized broad-band data; however, band-pass filtering this data

between 0.5 and 6.5 Hz reveals that the transient noise has been successfully removed in the target frequency range. This final result of the temporal normalization procedure, free from transient contamination, is shown in Figure 5.7e. The amplitude spectra of the raw and the normalized data are displayed in Figure 5.7f. Stationary noise like the narrow spike at 3.3 Hz could not be reduced by temporal normalization. Other methods have to be applied for this purpose and an example of such a method will be demonstrated in the next section. The data example in Figure 5.7 points out the importance of band-pass filtering the data before computing the moving average values. If the WMA had been computed directly from the raw data in Figure 5.7a, the final result in Figure 5.7e would exhibit strongly muted amplitudes in the area of the massive high-frequency noise feature between $t=250$ s and $t=450$ s.

The proposed temporal normalization algorithm automatically identifies and removes non-stationary noise from the data. In contrast to other techniques with the same aim, like cutting unstable time windows from the data (e.g. [SESAME, 2004](#); [Schechinger et al., 2009](#)), it preserves the full data continuity and creates no time gaps in the record. This makes it attractive as a pre-processing tool for applications that require continuously sampled data, like for example cross-correlation of diffuse wave-fields for estimating Green functions (e.g. [Benson et al., 2007](#)) or time-reverse modeling for tremor source detection (e.g. [Steiner et al., 2008](#)). Also the methods introduced later in this paper benefit from the preservation of the continuous waveform record. In addition, temporal normalization is data-adaptive and flexible. Three parameters can be adjusted to optimize the result and to account for the characteristics of the input data. These parameters are the target frequency range f_t , the width of the normalization window (defined by N) and the percentile for the threshold of the WMA values (defined by p). The target frequency range for this study is fixed between 0.5 and 6.5 Hz. For the other two parameters we found that a normalization window of 2 s ($N=100$) and a threshold corresponding to the 95th percentile ($p=95$) works well for this data-set.

Spectral despiking to remove noise-type B

Stationary narrow-band noise (highlighted as “B” in Figure 5.2a and 5.8a) is identified and removed with a method we call spectral despiking. In a first step, frequency-windows that contain stationary noise are identified in the Fourier spectra. In a second step, the amplitudes in the noise windows are removed and the gaps restored by a spline interpolation.

For the first step, the noise identification, we chose to adopt an algorithm introduced by [Bruni et al. \(2008\)](#) to automatically detect vertical scratches in old motion picture films. Such scratches appear on film images as lines with limited width and significant energy and therefore look similar to noise-type B in spectrogram representations as the one shown in Figure 5.2a. In fact, both types of signals not only qualitatively look similar but they are quantitatively described by the same mathematical function. The characteristic of the image defect due to a

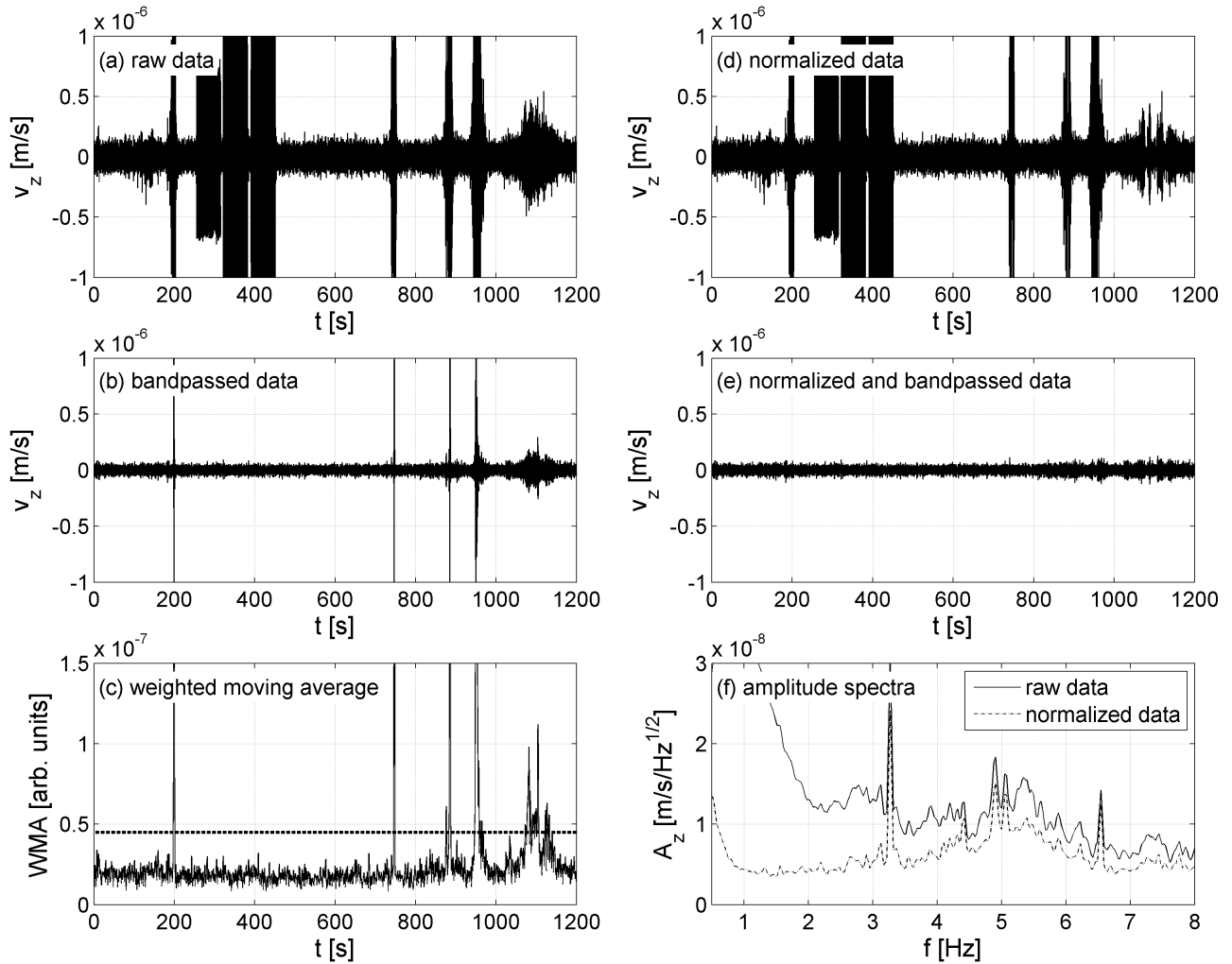


Figure 5.7. Example of temporal normalization applied to heavily noise-contaminated data. (a) Raw vertical-component broad-band velocity seismogram. (b) Data from (a) band-pass filtered between 0.5 and 6.5 Hz, showing four major transient events. (c) Weighted moving average of the filtered data in (b) and threshold for the normalization weights (dashed line). (d) Broad-band data from (a) after temporal normalization using the weighted moving average values exceeding the threshold shown in (c). (e) Data from (d) band-pass filtered between 0.5 and 6.5 Hz, showing that the transient signals have successfully been removed by the normalization procedure. (f) Amplitude spectra of the raw and the normalized data.

film scratch is controlled by a light diffraction effect (Bruni et al., 2004). It is produced by the projector light that passes through the thin vertical slit (i.e. the scratch) of the film material during the projection and/or scanning process. Due to this physical process, the intensity of the image defect, L , as a function of the horizontal distance y (perpendicular to the scratch) is described with a sinc-function as follows

$$L(y) = b_p \text{sinc}^2 \left(\frac{y - c_p}{m} \right), \quad (5.2)$$

where b_p is the maximum intensity, c_p the horizontal location of the maximum intensity and m a measure of the width of the defect on the image. On the other hand, the Fourier transform, $H(f)$, of an infinite sinusoidal signal, $h(t) = A \cdot \cos(2\pi f_0 t)$, multiplied with a boxcar function of finite duration T , has the form

$$H(f) = \frac{AT}{2} \text{sinc} \left(\frac{f - f_0}{1/T} \right), \quad (5.3)$$

where A and f_0 are the maximum amplitude and the frequency of the sinusoid, respectively. The corresponding power spectral density, $P(f)$, is proportional to the square of the Fourier amplitude spectrum

$$P(f) \propto |H(f)|^2 = \left(\frac{AT}{2} \right)^2 \text{sinc}^2 \left(\frac{f - f_0}{1/T} \right). \quad (5.4)$$

Comparing Equations 5.2 and 5.4 reveals that both, the intensity of an image defect and the power spectral density of a sinusoidal signal with finite duration have exactly the same mathematical form. As a consequence, the algorithm by Bruni et al. (2008) to detect scratches in motion picture films is also applicable to identify stationary, monochromatic signals (like noise-type B) in ground-motion spectrograms.

Bruni et al. (2008) apply the detection algorithm to the film images' vertical cross-section $c(y)$, which is defined as the mean value of the intensities in the column at distance y of the digitized image. In this one-dimensional cross-section, scratches on the image occur as peaks with maxima at locations c_p . Bruni et al. (2008) suggested applying the following three criteria to detect such peaks:

- (1) The width of the peak, $2m$, must not exceed a maximum value of w (in Hertz).
- (2) The relative magnitude of the peak, Δ_p , must exceed the average E of all relative peak-magnitudes in the cross-section.
- (3) The area, A_p , of a sinc^2 -function fitted to the peak must exceed the area of the function $\bar{b}_p \text{sinc}^2 \left(\frac{y - c_p}{m} \right)$, where \bar{b}_p is the least perceptible intensity value for a scratch in the considered image.

Similarly, these criteria can be applied for identifying noise-type B from ground-velocity spectrograms. For this purpose, the squared arithmetic mean spectrum of the data window (which is proportional to the mean PSD) is used in place of the images' cross-section $c(y)$. In [Bruni et al. \(2008\)](#) the least perceptible intensity, \bar{b}_p , in criterion (3) is defined as $\bar{b}_p = \frac{E}{d}$ with $d=0.98$. However, d is in our case a fitting parameter that has to be adjusted to account for the data characteristics and the Fourier transform window length. Values of $d=0.4$ and $w=0.3$ Hz are chosen for this study.

Figure 5.8 shows an example of the noise-identification algorithm applied to data that has been cleaned beforehand from transient noise using temporal normalization. The vertical-component velocity spectrogram in Figure 5.8a exhibits several narrow-band signals that can be assigned to noise-type B. These signals are represented as peaks in the arithmetic mean spectrum (magenta line in Figure 5.8b). The peaks at $f=4.5$ Hz, $f=11.4$ Hz and $f=12.5$ Hz were identified as noise-type B by the proposed algorithm applying the detection criteria and parameter values above. The widths of the peaks define the “peak-windows” and are given by the points where the peak's slope exceeds 50% of the maximum gradient on both sides of the peak (indicated by the blue dotted lines in Fig. 5.8b). The arithmetic mean spectrum is used because it allows detecting stationary narrow-band noise that is intermittently present during the recorded period of time. Applied to the maximum PDF spectrum (black line in Figure 5.8b), the noise at $f=4.5$ Hz would have been missed by the algorithm. Once the stationary noise is identified, the amplitudes in the peak-windows are removed and the spectral gaps restored by a spline interpolation.

Results from single station processing

The spectrograms in Figure 5.2 illustrate that temporal normalization and spectral despiking successfully remove noise of type A and B from single station data. The impact of single station noise removal on attribute values is shown in Figures 5.5 and 5.6. The red lines in Figures 5.5c and 5.5d show the stacked attribute profiles along line L1, computed from data that has been cleaned using temporal normalization and spectral despiking. The major anomaly of Attribute 1 at an offset of 5500 m, which is dominated by anthropogenic noise from the nearby highway, has been strongly reduced by the cleaning procedure. The patterns of Attribute 2 have only slightly changed after data cleaning. This is consistent with the evidence that the horizontal-to-vertical spectral ratio of ground-motion (and its reciprocal) is in general much less sensitive to source effects and therefore more robust against noise influence than absolute spectra ([Bard, 1999](#), and references therein). Figure 5.6b shows a map view of Attribute 1 computed from data that has been processed with the single station techniques. Compared to the result from raw data in Figure 5.6a, the highway signature has been significantly reduced. However, an influence from the highway is still visible.

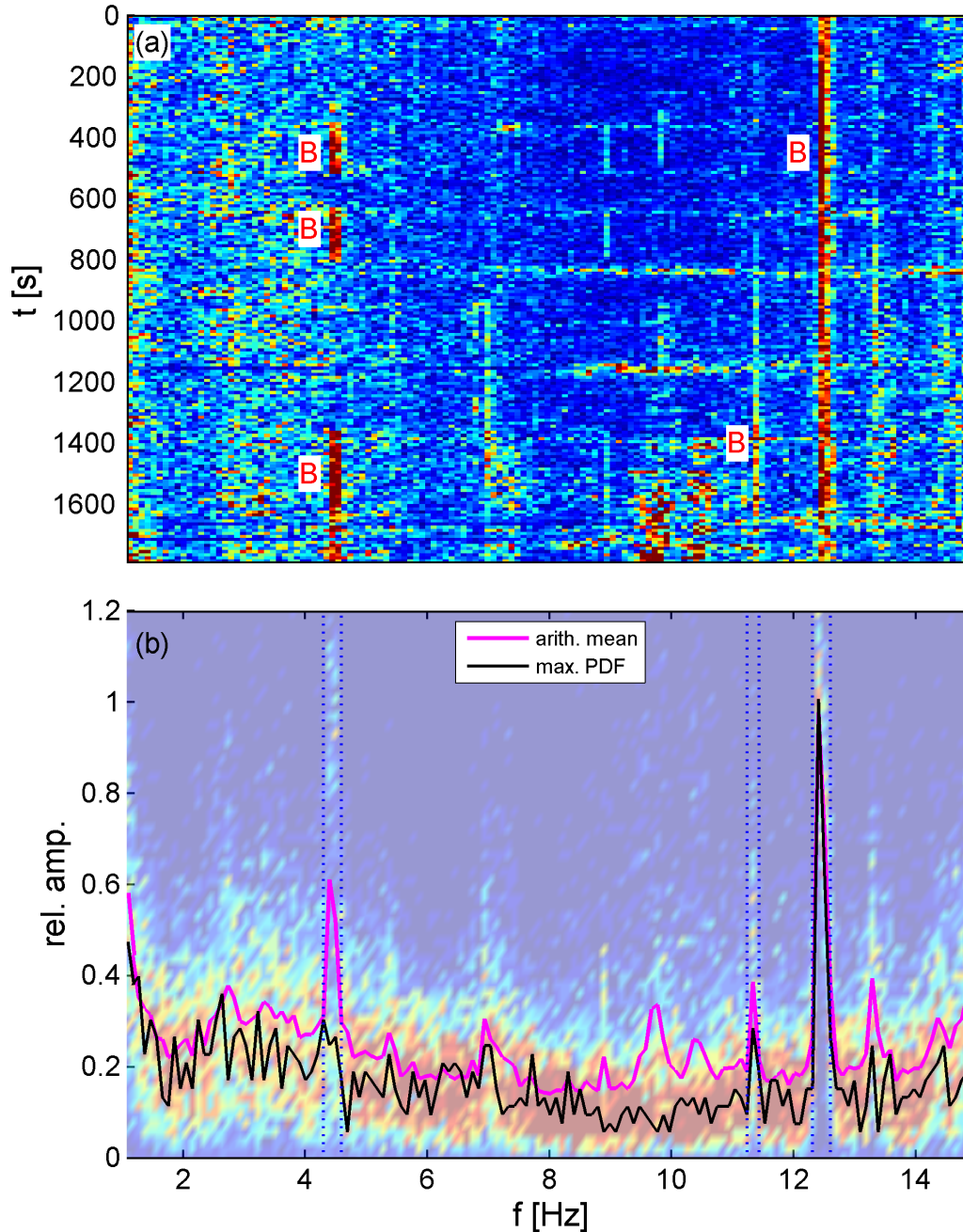


Figure 5.8. *Example of spectral despiking. (a) Vertical-component velocity spectrogram which serves as input for the spike detection algorithm. Significant narrow-band noise is labeled with “B”. (b) The average amplitude spectrum used for spike detection (magenta line) is computed as the arithmetic mean through time of the spectrogram amplitudes in (a). The statistical amplitude distribution is shown as a 2D histogram. The black line shows the maximum PDF spectrum. Dashed blue lines depict the frequency windows in which significant spikes have been detected.*

Although the single station noise cleaning procedures successfully reduced the amount of anthropogenic noise in the data, it is likely that significant anthropogenic energy is still present. This applies in particular for data recorded across line L1 which runs closely along the highway and picked up significant noise in its southern part. We therefore focus in the remaining of this article on data from line L2 that is in general less affected by anthropogenic noise.

5.3.2. Linear array techniques

Array methods are widely-used in seismic data processing and analysis (for an overview see [Rost & Thomas \(2002\)](#)). The advantage of array data is the simultaneous description of the wave-field in time and space. This allows improving the S/N-ratio (e.g., F-K dip filter, beam forming) and separating seismic phases from each other (e.g., frequency-wave number analysis). Unfortunately, due to high costs of delicate instruments, low-frequency passive seismic array measurements are often performed by only a couple of dozens of seismometers deployed at a spacing of a few hundred meters instead of the dense arrays with thousands of geophones used in active seismic surveys. Because of the small number of synchronized data points and the coarse spatial sampling, many effective filtering tools cannot be directly applied to passive seismic data-sets. To address these difficulties, we compute spectral attributes quasi-continuously over time. This is implemented by shifting a short time window through the data record by a given time step. At each step an attribute value representing the time window is calculated. As a result, 2D attribute sections can be generated for the linear arrays, showing the variation of the attribute in both time and space. The benefit of this approach is that consistent trends on the section can be more easily recognized. Moreover, 2D filtering techniques to reduce noise effects can be applied to the sections. Figure 5.9a shows a section for Attribute 1 measured across line L2. Ninety minutes of a noisy time interval (day time) has been processed, using a 20 second moving time window advanced by 1 second time steps. A noisy time interval has been chosen for demonstration purposes to emphasize the impact of anthropogenic noise. Local transient noise (type A) appears as randomly distributed, isolated high values in the section. An example is highlighted with a red circle in Figure 5.9a. Correlated transient noise (type C) spreads as high amplitudes across the line. Several type-C events appear in the section in Figure 5.9a with an estimated apparent velocity just above 100 km/h (presumably caused by traffic nearby). In the following, we introduce two 2D filtering techniques that we found useful to suppress features in attribute sections that are caused by type-A and type-C noise, respectively.

Total variation denoising

[Rudin et al. \(1992\)](#) proposed a total variation based algorithm for removing noise from images. The total variation is defined as the sum of the lengths of the gradient vectors of an image. Given an observed intensity function f , [Rudin et al. \(1992\)](#) reconstruct the clean image u assuming $f = u + \eta$, where η is an additive noise. They propose to minimize the following function

$$J(u) = \int_{\Omega} \left| \vec{\nabla} u \right| + \lambda \int_{\Omega} (f - u)^2 \quad (5.5)$$

for a certain tuning parameter $\lambda > 0$. The term $\int_{\Omega} \left| \vec{\nabla} u \right|$ denotes the total variation of u in the image domain Ω , and $\int_{\Omega} (f - u)^2$ is a measure for the deviation between the observed (noisy) image and the reconstructed image. The minimization problem 5.5 has a unique solution which can be approximatively derived by an iterative algorithm, known as the Rudin-Osher-Fatemi algorithm. For $\lambda \rightarrow \infty$ the solution will be identical to the observed image. For $\lambda \rightarrow 0$, on the other hand, the solution will exhibit zero variation, i.e. the intensity will be constant in the image domain. The tuning parameter λ must be adjusted in a way to obtain the optimum trade-off between these two end-members. Total variation denoising is a standard image processing tool to reduce noise in images reconstructed from data obtained by electronic means, for example data transmission. Figure 5.9d and 5.9e illustrate the effect of total variation denoising applied to a contaminated picture of the Matterhorn. Applied to attribute sections, total variation denoising is capable of effectively removing features related to locale transient noise. This is shown in Figure 5.9b, where isolated high values in the section (e.g. the noises of type A marked with a red circle in Figure 5.9a) have disappeared after denoising. A value of $\lambda=0.05$ was used for the examples shown in Figure 5.9 and for all other results in this paper.

F-K filter applied to attribute sections

As shown in Figure 5.9b, the noise of type C is still present in the attribute section after total variation denoising. It appears as strong transient events, spreading across the section. We assume that the signals of interest are quasi-stationary with time because they presumably are controlled by site specific information on the subsurface. The signals and the type-C noise should, therefore, have distinctive trends in the frequency-wavenumber (F-K) domain. The F-K amplitude spectrum of the section is shown in Figure 5.9f. Indeed, the transient and the stationary events are clearly separated into vertical ('Noise') and horizontal ('Signal') trends. The type-C noise can therefore be filtered out by muting those amplitudes in the F-K domain that correspond to apparent velocities greater than a certain threshold v_t . It is important to point out that using attribute sections instead of recorded waveforms is the key that allows the use of an F-K filter. In this application, the filter must be regarded as an image processing tool to remove certain linear trends rather than the traditional F-K filter used in active seismic to remove incident phases with certain apparent velocities. The latter is not applicable to our data-set because of the coarse sensor coverage which leads to severe artifacts due to spatial aliasing. The F-K filter applied to attribute sections does not suffer from this issue. In the example of Figure 5.9, a threshold of $v_t=1$ m/s was chosen. Therefore, all amplitudes outside the bow tie shaped area indicated with green lines in Figure 5.9f must be muted; however, a tapered muting function is used in practice to avoid artifacts related to spectral leakage. After transforming the filtered data back into the time-space (t-x) domain, the noise has been

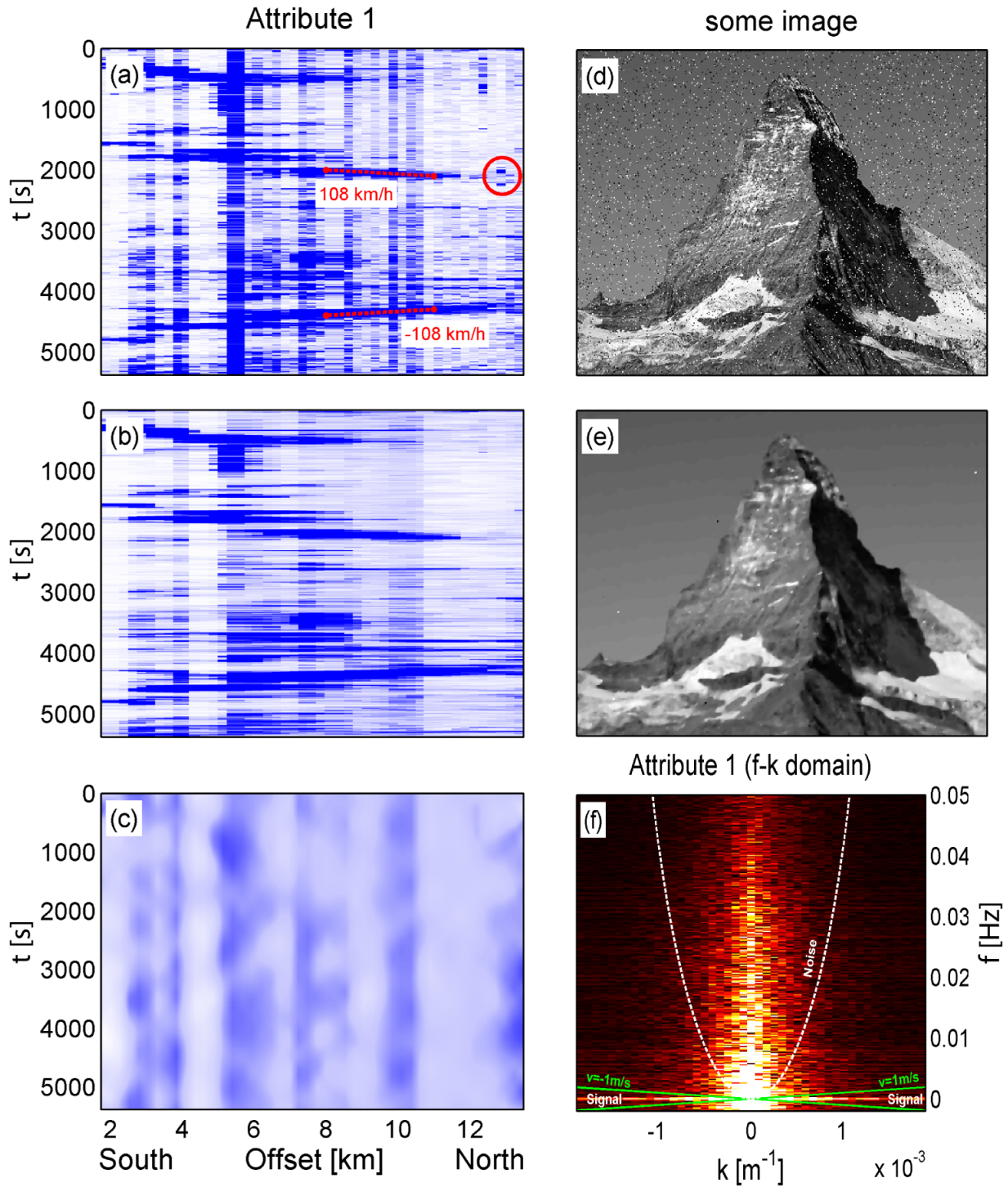


Figure 5.9. Total variation denoising and F-K filtering applied to attribute sections. (a) Ninety minutes of a raw section for Attribute 1 measured across line L2. Isolated (circle) and correlated (dashed line) transients are clearly visible. (b) Section after total variation denoising. Isolated transient noise has been effectively removed. (c) Section after total variation denoising and F-K filtering. Correlated transients have disappeared but quasi-stationary trends in the section are preserved. (d), (e) Illustration of the effect of total variation denoising on an arbitrary, noisy image. (f) Amplitude spectrum of section (b) in the F-K domain. Transient and stationary events are clearly separated into vertical ('Noise') and horizontal ('Signal') trends.

effectively removed and only the quasi-stationary signals in the section are preserved (Figure 5.9c).

5.4 DISCUSSION

Cleaned attribute sections as shown in Figure 5.9c are useful for a qualitative, visual interpretation of the data because consistent trends on a section can be well recognized even by eye. However, for a quantitative evaluation, the time axis of the section is collapsed to generate an average attribute profile. The arithmetic mean through time is used to average the attribute values. This procedure is illustrated in Figure 5.10 for the cleaned attribute section of Figure 5.9c. The resulting profile in Figure 5.10b represents the attribute's characteristic pattern across the linear array for the considered time interval where anthropogenic noise effects have been minimized. The focus when interpreting such profiles is on relative, lateral variations of the attributes. Cleaned attribute profiles are therefore displayed in arbitrary units and only provide information on the spatial variation but not on the attribute's absolute magnitudes.

The colored dashed lines in Figure 5.11 are seven average profiles along line L2 for each of the Attributes 1-4 computed from the night-time interval between midnight and 4:00 a.m. Each individual profile was derived from a cleaned, 30 minutes long attribute section as indicated in the figure's legend. The processing parameters shown in Table 5.2 were used for noise cleaning. The section from 2:00 a.m. to 2:30 a.m. is contaminated by a regional earthquake of magnitude 4.2 and therefore not used for the analysis. The profiles in Figure 5.11 are scaled individually to make lateral variations comparable. The attribute patterns look similar for each 30 minutes window. This shows that the results are reproducible on an hourly scale and that the patterns are controlled by stationary site conditions, rather than by transient noise. All four attributes show stable results; however, the temporal fluctuations of Attribute 2 are smaller compared to the other three attributes. Its spatial pattern is almost identical for each time window. This is explained by the fact that Attribute 2 is based on spectral ratios and residual transient noise is cancelled out by the spectral division.

For a comparison, the black dashed lines in Figure 5.11 show attribute profiles computed from the raw data of line L2 (midnight to 4:00 a.m., without earthquake window). The cleaning procedures have a strong influence on Attribute 1's spatial pattern. Several peaks that are related to anthropogenic noise are removed in the cleaned profiles. Attribute 2 is less affected by the noise cleaning. This is an expected result because spectral ratios of ground-motion are less affected by transient, anthropogenic noise than the absolute spectra. However, it is interesting that also the Attributes 3 and 4 are only little influenced by the noise cleaning. Attributes 3 and 4 are quite robust with regards to anthropogenic noise, presumably because they are based on frequency values rather than spectral amplitudes.

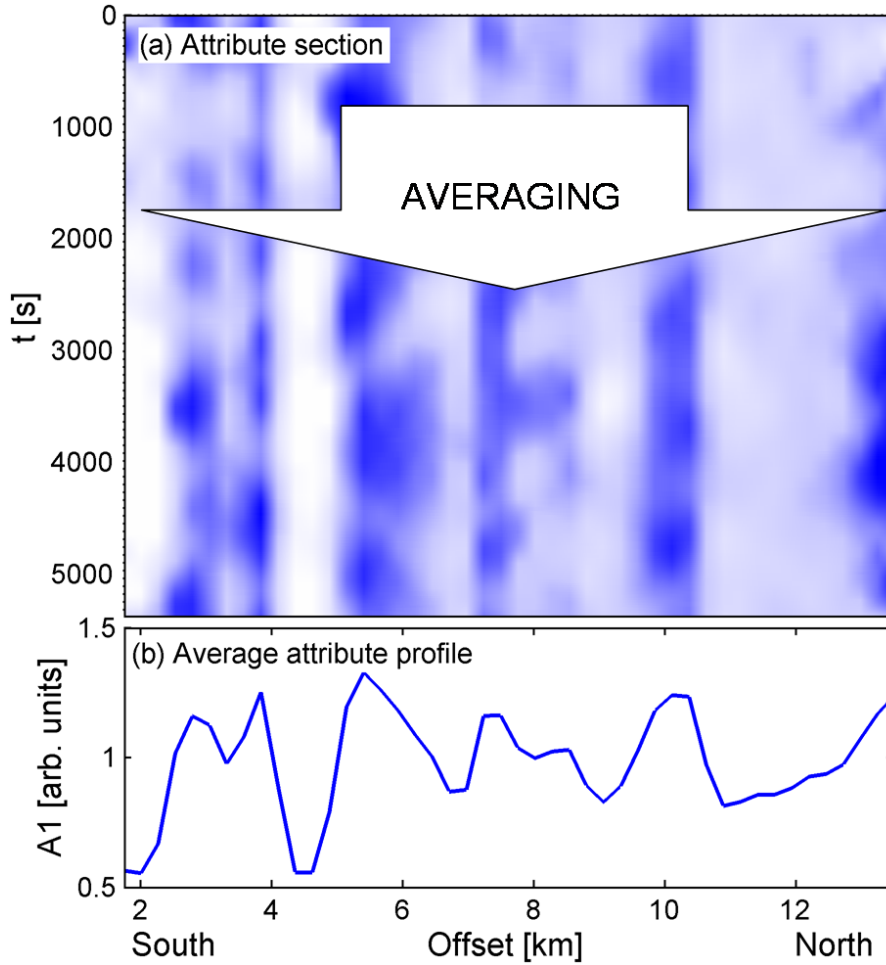


Figure 5.10. (a) Example of a cleaned section of Attribute 1. (b) Attribute profile generated by averaging the section in (a) through time using the arithmetic mean.

Temporal normalization	f_t	N	p
	0.5-6.5 Hz	100	95
Spectral despiking	d	w	
	0.4	0.3 Hz	
Total variation denoising	λ		
	0.05		
F-K filter	v_t		
	1.0 m/s		

Table 5.2. Processing parameters used for the noise reduction techniques.

The magenta lines in Figure 5.11 are the attribute profiles presented as the final result of the survey in 2007 (Lambert et al., 2009). The profiles were derived as an interpolated stack of several parallel linear arrays projected onto the same profile. As a result, most of the measurement locations are not coincident with the stations of the survey in 2008 but are shifted up to 1 km in the cross-line direction. A detailed description of the survey in 2007 is given

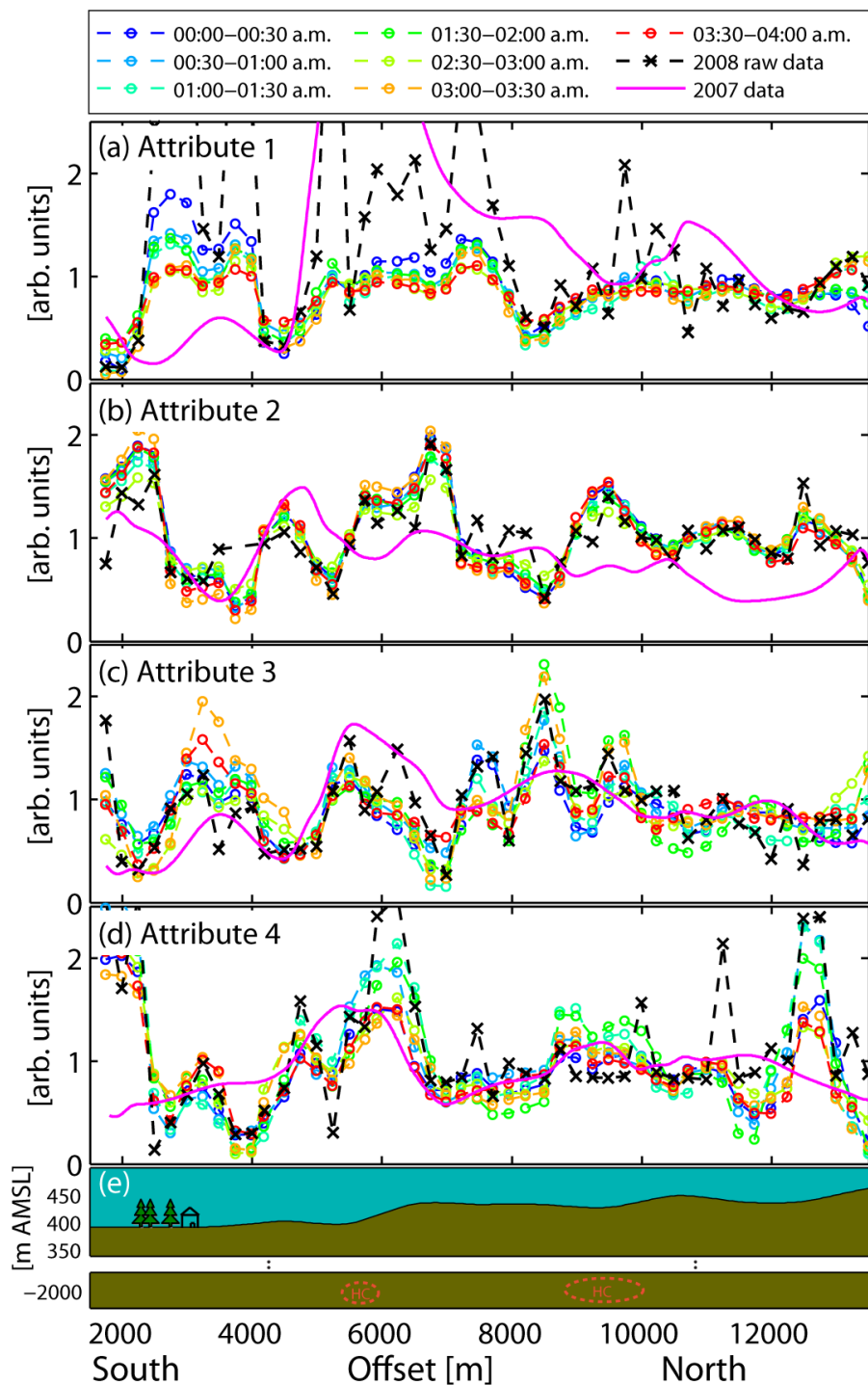


Figure 5.11. (a)-(d) Profiles along line L2 for each of the four attributes computed from different 30 minutes windows of the 2008 survey (colored dashed lines). Each profile was derived by averaging a cleaned attribute section as shown in Figure 5.10. The black dashed lines show attribute profiles computed from raw data of the same time windows. The magenta lines are characteristic attribute profiles computed from data of the survey in 2007. Note that all profiles are scaled individually to make lateral variations comparable. (e) Topography of the survey area displayed with a vertical exaggeration of 8:1 and locations of the hydrocarbon (HC) reservoirs along the profile.

in [Lambert et al. \(2009\)](#). Differences between the 2007 and 2008 data can be explained by (i) temporal changes in noise conditions, (ii) sensors not being at the exact same position for each survey and associated different local surface noise or near-surface effects, and (iii) differences in data processing. Particularly in the case of the spectral-ratio based Attribute 2, where anthropogenic noise influence is expected to be small, we suspect that local near-surface effects are responsible for deviations between the results of 2007 and 2008. Interestingly, profiles of Attributes 3 and 4 exhibit similar features for both data-sets. The features are characterized by increased values, centered at an offset of 5500 m and, less pronounced, at 9000 m. These anomalies can neither be well explained by local surface noise sources nor by local near-surface effects because the two data-sets were not recorded at the exact same station locations. [Lambert et al. \(2009\)](#) pointed out that the positions of the anomalies coincide with the locations of the two reservoirs in the survey area projected to the surface. However, Attribute 4 also exhibits two pronounced anomalies in the 2008 data-set (at an offset of 2000 m and 12500 m) which are not present in the older data-set.

Figure 5.11e shows the locations of the hydrocarbon reservoirs along the survey line and the topography in the survey area with a vertical exaggeration of 8:1. Anomalies of cleaned attribute profiles appear to contain consistent information on site-specific geological properties, but correlations between the attribute patterns and reservoir locations are not very distinct. The topography of the survey area has not had an obvious impact on the attribute patterns neither. This is different compared to the case-study presented in [Hanssen & Bussat \(2008\)](#), where energy-based attributes (such as our Attribute 1) were found to correlate with topography. Near-surface structures, such as for example unconsolidated soil layers can amplify the ambient ground-motion at specific frequencies ([Bard, 1999](#), and references therein). Such effects may cause some of the observed attribute patterns in Figure 5.11. However, based on the passive seismic data alone it is not possible to resolve the ambiguity between near-surface effects, residual surface noise and effects from deeper horizontal inhomogeneities such as hydrocarbon reservoirs. If detailed information on near-surface structures and reservoir properties are available, a possible approach to overcome this issue will consist in statistical classification and pattern recognition methods applied to passive seismic attributes. Such methods are already applied in active seismic for quantitative predictions of hydrocarbon probabilities ([Avseth et al., 2005](#)). A first attempt of using statistical methods to compute hydrocarbon probability maps from passive seismic data was presented in [Riahi et al. \(2009\)](#). Another approach would consist in modeling the seismic response related to shallow structures. As shown in [Artman et al. \(2010\)](#), the modeled response could then be removed from the data in an additional processing step. However, for such a procedure, the physical properties of the near-surface structures should be accurately known.

The flowchart in Figure 5.12 summarizes the methodology and the processing steps we propose for suppressing anthropogenic noise from passive seismic data and for extracting significant attribute profiles. Data from each station is corrected for the seismometer transfer function and anthropogenic noise of type A and B is removed by temporal normalization and spectral despiking. The statistical spectral amplitude distribution of the full data-set (as shown in Figure 5.4) is used to determine the parameters needed to compute the attribute values (Table 5.1). An important step consists in checking whether these parameters match with the processing parameters used to compute the amplitude distribution (Table 5.2). For example, the target frequency range for temporal normalization f_t must include the integration range of Attribute 1 which is determined by the parameters f_{l1} , f_{l2} and f_h . If this is not the case, the processing parameters have to be re-adjusted and the single station noise removal procedures have to be repeated. This is an iterative processing optimization algorithm. Once the attributes are defined, attribute sections are calculated and total variation denoising and F-K filtering can be applied to them for removing isolated and correlated transient noise (type C). The last step of the array processing consists in averaging the attribute section through time which finally yields the cleaned attribute profile.

Analysis of ambient seismic signals at the Earth's surface for investigating structures in the subsurface became increasingly popular in recent years. In geotechnical engineering, the shape of H/V spectral ratio curves are analyzed to estimate earthquake site-effects (Fäh et al., 2003, and references therein). Also, ambient ground-motion is used to detect shallow horizontal inhomogeneities such as for example cavities (Nasseri-Moghaddam et al., 2007). Seismologists perform surface-wave tomography with low-frequency passive data to determine seismic velocities down to depths of more than 20 km (Shapiro et al., 2005). Exploration geophysics benefits from ambient ground-motion analysis as well: Array methods are applied to invert for the vertical S-wave velocity profile of a horizontally layered subsurface (Okada, 2003). Draganov et al. (2007) used cross-correlations of passive seismic recordings at frequencies between 2 and 10 Hz to retrieve P-wave reflections with travel-times as great as 2 seconds at a gas reservoir in Saudi Arabia. All these applications work because seismic wave propagation is sensitive to material properties and, therefore, the ambient wave-field is modified in a characteristic way by the subsurface inhomogeneity. This, however, imposes limitations of applicability. For example, an underground cavity will not be detectable by analyzing ambient ground-motion at the Earth's surface if its size is too small. Below a critical size, effects caused by the cavity will be weak and overwhelmed by other signals, i.e. the S/N-ratio becomes too small. This example points out the importance of noise reduction procedures for passive seismic data analysis in general. And indeed, most of the applications mentioned above use some sort of pre-processing to clean the data before the analysis.

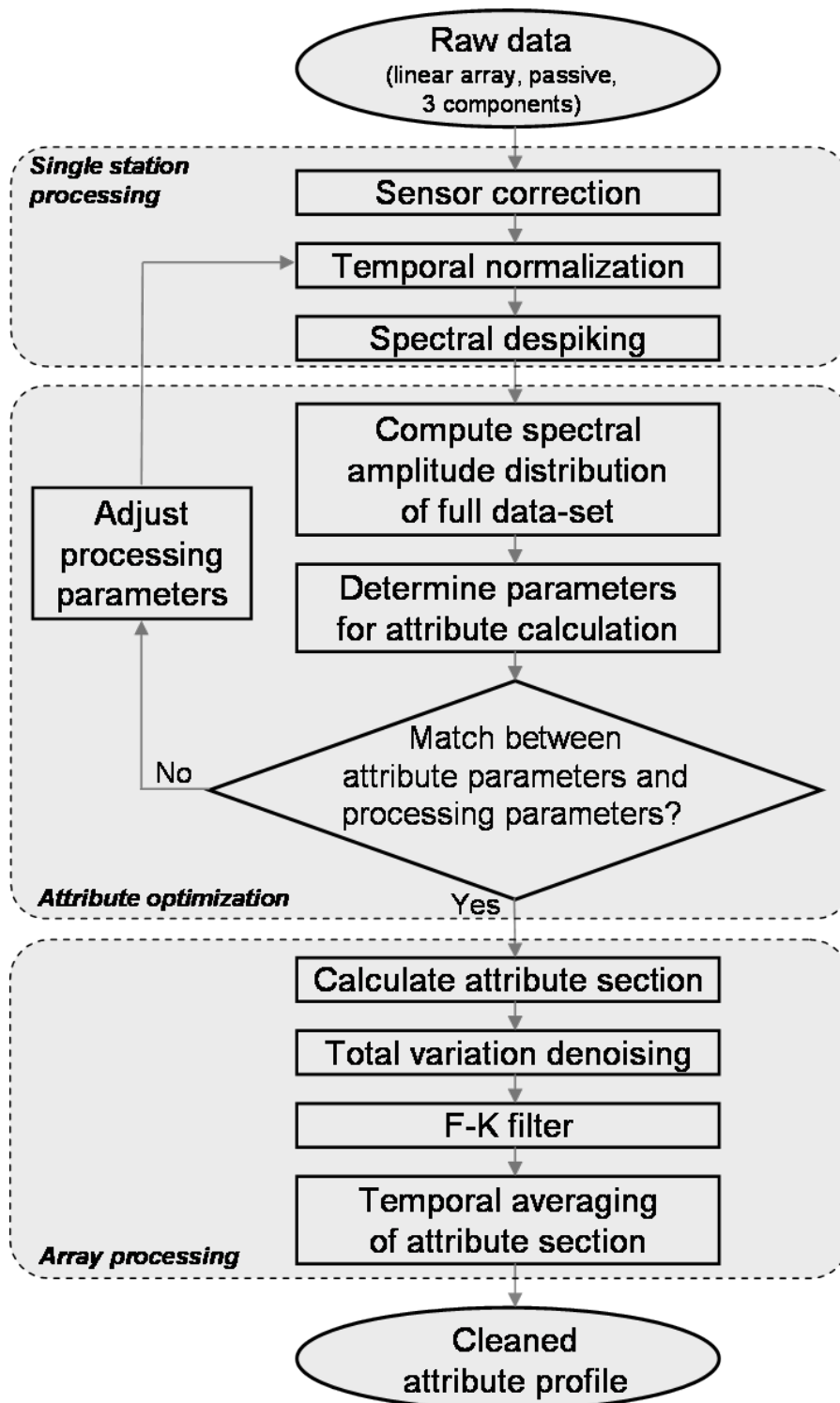


Figure 5.12. Methodology and workflow proposed for suppressing anthropogenic noise from passive data and for creating significant attribute profiles.

Another type of application of ambient seismic signals is the analysis of tremor signals originating from depth. For example, characteristic long-period seismicity at active volcanoes (volcanic tremor) has been found useful for eruption forecasting (Chouet, 1996). A different type of low-frequency tremor has recently been discovered also in non-volcanic regions and was found to provide useful insights on processes in deep subduction zones (e.g. Obara, 2002; Shelly et al., 2007; Obana & Kodaira, 2009). All these measured tremors are generated by physical processes in the Earth whose exact nature is yet not fully understood and currently the focus of scientific research (Chouet, 1996; Obana & Kodaira, 2009, and references therein).

The application discussed in this paper, i.e. hydrocarbon reservoir detection based on spectral analysis of the ambient wave-field at the Earth's surface, is based on the same principles as the applications mentioned above. Due to, for example, partial fluid saturation, reservoirs can be inhomogeneities interacting with and modifying seismic waves that naturally occur at reservoir depth. Similar to the example of embedded cavities, the detectability of such modifications depends on the S/N-ratio of the recorded data. Therefore, we have developed and applied noise reduction techniques similar to those that are already applied in passive seismic (temporal normalization, F-K filter). To account for the peculiarity of the data-set and its application, we have also adopted techniques from other fields than seismic (spectral despiking, total variation method). Clearly, if a reservoir is small, deeply embedded or only exhibits small contrasts in seismic properties compared to the surrounding rocks, detection based on spectral analysis is expected to fail, even after noise reduction. The reservoirs considered in this study have a net thickness of a few tens of meters at most, in a depth of around 2 km. In addition, the area around Voitsdorf features a high anthropogenic noise level and complex surface geology. This could explain why the qualitative correlation of spatial attribute anomalies with the horizontal location of reservoirs is not conclusive and not as clear as reported in case-studies across other oil or gas fields (e.g. van Mastriigt & Al-Dulaijan, 2008).

5.5 CONCLUSIONS

A low-frequency passive seismic data-set acquired at an oil and gas field was investigated. Three surface noise types of anthropogenic origin were identified in the ambient ground-motion recordings: (i) local transient noise, (ii) stationary narrow-band noise and (iii) correlated transient noise. Also, spectral signatures that are expected to be mainly controlled by site specific properties of the subsurface were found in the data. A methodology to extract and map site specific signatures in time and space was presented. The methodology uses Fourier amplitude spectra to calculate four different spectral attributes which quantify the signatures of interest. Results from raw data suggest that anthropogenic noise can strongly affect the attribute values. This applies in particular for Attribute 1 which is based on the spectral energy of the vertical particle velocity field. Therefore, four noise-reduction techniques were presented and

successfully applied to suppress anthropogenic noise and enhance the data's S/N-ratio. Two of the techniques are applicable to recordings of single stations. The other two techniques are two-dimensional filters which are applicable to attribute sections derived from linear arrays. Attributes calculated from cleaned data contain site specific information on the subsurface. Attribute profiles describe lateral variations of ambient ground-motion and are therefore useful to detect horizontal inhomogeneity in the subsurface. Observed attribute patterns might be related to near-surface, site specific structures, but they might also be related to deeper inhomogeneities, such as the hydrocarbon reservoirs. Due to this ambiguity, low-frequency spectral analysis for hydrocarbon detection is in this area not as straightforward as reported for other case-studies. In which environments reservoir-related signatures can be measured at the surface and potentially be used for reservoir detection must be answered empirically through further case-studies at oil and gas fields. The proposed methodology and noise-reduction techniques contribute towards an improved data processing and analysis and may help eventually answer these questions. This paper discusses an application to possible reservoir-related signals. However, the methodology can be useful to detect any horizontal subsurface inhomogeneity (e.g. underground cavities) or seismic sources (e.g. volcanic tremor) that have a measurable impact on the ambient ground-motion at the Earth's surface.

ACKNOWLEDGEMENTS

We thank Rohöl-Aufsuchungs Aktiengesellschaft (RAG) for the permission to access the Voitsdorf oil and gas field. We acknowledge the financial support of the Swiss Commission for Technology and Innovation (CTI) and Spectraseis. E.H. Saenger thanks the DFG (Deutsche Forschungsgemeinschaft) for their support through the Heisenberg Programme (SA 996/1-1).

References

- Ali, M., Berteussen, K., Small, J., Anjana, B. & Barkat, B. (2009). *Recent Passive Experiments in Abu Dhabi. EAGE Workshop on Passive Seismic: Case Studies and Applications for Field Development and Exploration*. Paper presented at the EAGE Workshop Passive Seismic: Exploration and Monitoring Applications, 2009, Limassol, Cyprus, Expanded Abstracts, p. A36.
- Ali, M., Berteussen, K., Small, J. & Barkat, B. (2010). *A Study of Ambient Noise over an Onshore Oil Field in Abu Dhabi, United Arab Emirates*. Bull. Seism. Soc. Am., **100**(1), 392–401.
- Artman, B., Goertz, A., Schechinger, B., Krajewski, P. & Koerbe, M. (2010). *Joint interpretation of multiple passive seismic data volumes*. 72th EAGE meeting, Barcelona, Spain, Expanded Abstracts, p. F009.
- Avseth, P., Mukerji, T. & Mavko, G. (2005). *Quantitative Seismic Interpretation – Applying Rock Physics Tools to Reduce Interpretation Risk*. Cambridge University Press. ISBN 0521816017.
- Bard, P.-Y. (1999). *Microtremor measurements: A tool for site effect estimation?* In: The Effects of Surface Geology on Seismic Motion (eds K. Irikura, K. Kudo, K. Okada and T. Sasatami) [Balkema, Rotterdam, The Netherlands.], pp. 1251–1279.
- Benson, G. D., Ritzwoller, M. H., Barmin, M. P., Levshin, A. L., Lin, F., Moschetti, M. P., Shapiro, N. M. & Yang, Y. (2007). *Processing seismic ambient noise data to obtain reliable broad-band surface wave dispersion measurements*. Geophys. J. Int., **169**, 1239–1260.
- Beresnev, I. A., Dennis Vigil, R., Li, W., Pennington, W. D., Turpening, R. M., Iassanov, P. P. & Ewing, R. P. (2005). *Elastic waves push organic fluids from reservoir rock*. Geophysical Research Letters, **32**, L13303.
- Bonnefoy-Claudet, S., Cotton, F. & Bard, P. (2006). *The nature of noise wavefield and its applications for site effects studies: A literature review*. Earth-Science Reviews, **79**, 205–227.
- Bruni, V., Ferrara, P. & Vitulano, D. (2008). *Removal of Color Scratches from Old Motion Picture Films Exploiting Human Perception*. EURASIP Journal on Advances in Signal Processing. doi:10.1155/2008/352986.
- Bruni, V., Vitulano, D. & Kokaram, A. (2004). *Fast Removal of Line Scratches in Old Movies*. 17th International Conference on Pattern Recognition (ICPR'04, **4**, 827–830.

- Campman, X., Wijk, K., Riyanti, C., Scales, J. & Herman, G. (2004). *Imaging scattered seismic surface waves*. Near Surface Geophysics, pp. 223–230.
- Cessaro, R. K. (1994). *Sources of Primary and Secondary Microseisms*. Bull. Seism. Soc. Am., **84**(1), 142–148.
- Chapman, M., Liu, E. & Li, X.-Y. (2006). *The influence of fluid-sensitive dispersion and attenuation on AVO analysis*. Geophys. J. Int., **167**, 89–105.
- Chopra, S. & Marfurt, K. (2005). *Seismic attributes – A historical perspective*. Geophysics, **70**, 3S0–28S0.
- Chouet, B. (1996). *Long-period volcano seismicity: Its source and use in eruption forecasting*. Nature, **380**, 309–315.
- Dangel, S., Shaepman, M. E., Stoll, E. P., Carniel, R., Barzandji, O., Rode, E.-D. & Singer, J. M. (2003). *Phenomenology of tremor-like signals observed over hydrocarbon reservoirs*. J. Volcanol. Geothermal Res., **128**, 135–158.
- Dasgupta, R. & Clark, R. A. (1998). *Estimation of Q from surface seismic reflection data*. Geophysics, **63**(6), 2120–2128.
- Draganov, D., Wapenaar, K., Mulder, W., Singer, J. & Verdel, A. (2007). *Retrieval of reflections from seismic background-noise measurements*. Geophysical Research Letters, **34**, L04305.
- Frehner, M., Schmalholz, S. M. & Podladchikov, Y. (2009). *Spectral modification of seismic waves propagating through solids exhibiting a resonance frequency: a 1-D coupled wave propagation–oscillation model*. Geophys. J. Int., **176**, 589–600.
- Fäh, D., Kind, F. & Giardini, D. (2003). *Inversion of local S -wave velocity structures from average H/V ratios, and their use for the estimation of site-effects*. Journal of Seismology, **7**, 449–467.
- Goloshubin, G., Vanschuyver, C., Korneev, V., Silin, D. & Vingalov, V. (2006). *Reservoir imaging using low frequencies of seismic reflections*. The Leading Edge, **May 2006**, 527–531.
- Green, A. & Greenhalgh, S. (2010). *Comment on "Low-frequency microtremor anomalies at an oil and gas field in Voitsdorf, Austria" by Marc-André Lambert, Stefan Schmalholz, Erik H. Saenger and Brian Steiner*, Geophysical Prospecting **57**, 393–411. Geophysical Prospecting, **58**, 335–339.
- Gucunski, N., Ganji, V. & Maher, M. (1996). *Effects of obstacles on Rayleigh wave dispersion obtained from the SASW test*. Soil Dynamics and Earthquake Engineering, **15**, 223–231.

- Hanssen, P. & Bussat, S. (2008). *Pitfalls in the analysis of low frequency passive seismic data*. *First Break*, **26**, 111–119.
- Kallweit, R. S. & Wood, L. C. (1982). *The limits of resolution of zero-phase wavelets*. *Geophysics*, **47**, 1035–1046.
- Klimentos, T. (1995). *Attenuation of P- and S-waves as a method of distinguishing gas and condensates from oil and water*. *Geophysics*, **60**(2), 447–458.
- Koper, K., Foy, B. & Benz, H. (2009). *Composition and variation of noise recorded at the Yellowstone Seismic Array*. *Journal of Geophysical Research*, **114**, B10310. doi:10.1029/2009JB006307.
- Korneev, V. (2008). *Slow waves in fractures filled with viscous fluid*. *Geophysics*, **73**, N1–N7.
- Korneev, V., Goloshubin, G. M., Daley, T. M. & Silin, D. B. (2004). *Seismic low-frequency effects in monitoring fluid-saturated reservoirs*. *Geophysics*, **69**, 522–532.
- Korneev, V. & Johnson, L. R. (1996). *Scattering of P and S Waves by a Spherically Symmetric Inclusion*. *Pure and Applied Geophysics*, **147**(4), 675–718.
- Lambert, M.-A., Schmalholz, S. M., Saenger, E. H. & Steiner, B. (2009). *Low-frequency microtremor anomalies at an oil and gas field in Voitsdorf, Austria*. *Geophysical Prospecting*, **57**, 393–411. doi:10.1111/j.1365-2478.2008.00734.x.
- Lambert, M.-A., Schmalholz, S. M., Saenger, E. H. & Steiner, B. (2010). *Reply to comment on "Low-frequency microtremor anomalies at an oil and gas field in Voitsdorf, Austria" by Marc-André Lambert, Stefan M. Schmalholz, Erik H. Saenger and Brian Steiner, Geophysical Prospecting 57, 393–411*. *Geophysical Prospecting*, **58**, 341–346.
- Liu, Y., Wu, R.-S. & Ying, C. F. (2000). *Scattering of elastic waves by an elastic or viscoelastic cylinder*. *Geophys. J. Int.*, **142**, 439–460.
- van Mastriigt, P. & Al-Dulaijan, A. (2008). *Seismic spectroscopy using amplified 3C geophones*. Paper presented at the 70th EAGE Conference & Exhibition, Rome, Italy, Expanded Abstracts, p. B047.
- Nasser-Moghaddam, A., Cascante, G. & Hutchinson, D. (2005). *A New Quantitative Procedure to Determine the Location and Embedment Depth of a Void Using Surface Waves*. *Journal of Environmental and Engineering Geophysics*, **10**(1), 51–64.
- Nasser-Moghaddam, A., Cascante, G., Phillips, C. & Hutchinson, D. (2007). *Effects of underground cavities on Rayleigh waves - Field and numerical experiments*. *Soil Dynamics and Earthquake Engineering*, **27**, 300–313.

- Obana, K. & Kodaira, S. (2009). *Low-frequency tremors associated with reverse faults in a shallow accretionary prism*. Earth Planet. Sci. Lett. doi:10.1016/j.epsl.2009.08.005.
- Obara, K. (2002). *Nonvolcanic Deep Tremor Associated with Subduction in Southwest Japan*. Science, **196**, 1679–1681.
- Okada, H. (2003). *The Microtremor Survey Method*. Geophysical Monograph Series No. 12, SEG, Tulsa, USA. ISBN 1-56080-120-4.
- Paffenholz, J. & Burkhardt, H. (1989). *Absorption and Modulus Measurements in the Seismic Frequency and Strain Range on Partially Saturated Sedimentary Rocks*. Journal of Geophysical Research, **94**, 9493–9507.
- Parolai, S., Bormann, P. & Milkereit, C. (2002). *New Relationship between V_S , Thickness of Sediments, and Resonance Frequency Calculated by the H/V Ratio of Seismic Noise for the Cologne Area (Germany)*. Bull. Seism. Soc. Am., **92**, 2521–2527.
- Phillips, C., Cascante, G. & Hutchinson, D. (2004). *Evaluation of horizontal homogeneity of geomaterials with the distance analysis of surface waves*. Can. Geotech. J., **41**, 212–226.
- Quintal, B., Schmalholz, S. & Podladchikov, Y. Y. (2009). *Low-frequency reflections from a thin layer with high attenuation caused by interlayer flow*. Geophysics, **74**(1), N15–N23.
- Rechtien, R. & Stewart, D. (1975). *A seismic investigation over a near-surface cavern*. Geoprospection, **13**, 235–246.
- Riahi, N., Kelly, M., Ruiz, M. & Yang, W. (2009). *Bayesian DHI using passive seismic low frequency data*. Paper presented at the 79th SEG International Conference & Exhibition, Houston, USA, Expanded Abstracts, p. 1607–1611.
- Rost, S. & Thomas, C. (2002). *Array seismology: Methods and applications*. Reviews of Geophysics. doi:10.1029/2000RG000100.
- Rudin, L., Osher, S. & Fatemi, E. (1992). *Nonlinear total variation based noise removal algorithms*. Physica, **D60**, 259–268.
- Saenger, E. H., Schmalholz, S. M., Lambert, M.-A., Nguyen, T. T., Torres, A., Metzger, S., Habiger, R., Müller, T., Rentsch, S. & Mendez-Hernández, E. (2009). *A passive seismic survey over a gas field: Analysis of low-frequency anomalies*. Geophysics, **74**, O29–O40.
- Schechinger, B., Goertz, A., Artman, B., Lambert, M.-A., Koerbe, M. & Krajewski, P. (2009). *Extracting subsurface information from ambient seismic noise – an example from Germany*. Paper presented at the 79th SEG International Conference & Exhibition, Houston, USA, Expanded Abstracts, pp. 1617–1621.

- SESAME (2004). *Guidelines for the implementation of the H/V spectral ratio technique on ambient vibrations. Measurements, processing and interpretation - WP12*. SESAME European research project (ed. P.-Y. Bard), p. 61ff.
- Shapiro, N. M., Campillo, M., Stehly, L. & Ritzwoller, M. H. (2005). *High-Resolution Surface-Wave Tomography from Ambient Seismic Noise*. *Science*, **307**, 1615–1618.
- Shelly, D. R., Beroza, G. C. & Ide, S. (2007). *Non-volcanic tremor and low-frequency earthquake swarms*. *Nature*, **446**, 305–307.
- Spencer, J. W. (1981). *Stress Relaxations at Low Frequencies in Fluid-Saturated Rocks: Attenuation and Modulus Dispersion*. *Journal of Geophysical Research*, **86**, 1803–1812.
- Steiner, B., Saenger, E. & Schmalholz, S. (2008). *Time reverse modeling of low-frequency microtremors: Application to hydrocarbon reservoir localization*. *Geophys. Res. Lett.*, **35**, L03307. doi:10.1029/2007GL032097.
- Tai, S., Puryear, C. & Castagna, J. P. (2009). *Local frequency as a direct hydrocarbon indicator*. Paper presented at the 79th SEG International Conference & Exhibition, Houston, USA, Expanded Abstracts, p. 2160–2164.
- White, J. E. (1975). *Computed seismic speeds and attenuation in rocks with partial gas saturation*. *Geophysics*, **40(2)**, 224–232.
- Zhang, J., Gerstoft, P. & Shearer, P. (2009). *High-frequency P-wave seismic noise driven by ocean winds*. *Geophysical Research Letters*, **36**, L09302.
- Zhukov, A., Loginov, K., Shneerson, M., Shulakova, V., Kharisov, R. & Ekimenko, V. (2007). *Nonlinear properties of vibrator-generated wavefields and their application to hydrocarbon detection*. *The Leading Edge*, **26**, 1395–1402.

6. Discussion

This thesis analyzes passive recordings of the ambient seismic wave-field at the Earth's surface. Fourier spectra are explored to detect and characterize quasi-stationary subsurface wave-field modifications. Such modifications can be caused by underground seismic sources (active modification) or heterogeneity interacting with the ambient wave-field through processes such as scattering or attenuation (passive modification). Examples of active modification in nature are volcanic tremor (Chouet, 1996) and non-volcanic tremor (Obara, 2002). Passive modification occurs for example in the case of scattered surface waves due to buried inhomogeneities like cavities or timber trestles (Nasseri-Moghaddam et al., 2007; Tallavó et al., 2009). The data in this thesis is analyzed in the frequency domain because information on the subsurface is carried in particular by spectral modulations. As discussed in Chapter 2, peaks in the H/V spectral ratios can for example be indicative of the depth and the impedance contrast of reflectors in a horizontally layered subsurface. In addition, spatial variations of the ambient wave-field can be indicative of the origin of localized subsurface wave-field modifications.

This thesis explores a methodology that uses spectral seismic attributes to quantify and map temporally stable spatial variations of the wave-field. Such variations can help interpreting subsurface properties and processes. The methodology is based on the assumption that occurring wave-field modifications are related to underground features of interest. It should be noted that this is an empirical procedure and does not a priori require a specific physical model. Similar techniques are applied in engineering geophysics, for example to detect the location of underground cavities (Nasseri-Moghaddam et al., 2007). Therefore, the methodology is only applicable if the subsurface target (i.e. the wave-field modifier) causes quasi-stationary signals that are strong enough to be measured at the surface.

An alternative method to extract subsurface information from passive seismic data is seismic interferometry which relies on cross-correlation to retrieve the Green's function between two receivers (Clearbout, 1968; Schuster, 2009). Successful applications of this concept using entirely passive data (i.e. ambient ground-motion) include, among others, surface wave tomography (e.g., Shapiro et al., 2005; Brenguier et al., 2007) and seismic reflection imaging (Draganov et al., 2007). Application of passive seismic interferometry requires in theory a uniform azimuthal coverage of the incident wave-field as well as synchronized measurements. The spectral analysis explored in this thesis is not limited by these constraints. However, there are a number of other critical aspects which are briefly addressed in the following.

Attribute definition. A seismic attribute is a quantitative measure of a seismic characteristic of interest (Chopra & Marfurt, 2005). According to Liner et al. (2004), attributes can be classified into general and specific categories. General attributes have a well-defined basis in physics or geology and are therefore universally applicable. In contrast, specific attributes may be well correlated to a target feature for a given case-study but these correlations do not in general carry over to different areas. The spectral attributes used in this study are specific because they are not based on a particular physical model. What attributes might be useful and how they should be parameterized must therefore be empirically evaluated for each different case. Attributes should be selected on the basis of their capability to provide significant statistical relationships with the target feature (Fournier & Derain, 1995). In this thesis, attributes are defined and parameterized by searching for anomalous patterns in spatial spectrograms or PDF contour plots, as shown in Figures 3.3 and 5.4.

As a consequence of using specific attributes, some attributes may be useful only in certain cases but in others not. In this study, a selection of possible attributes is introduced. In principle, one can think of defining any other attribute that is sensitive for a feature of interest. This may even include a combination of several specific attributes (“fingerprint”) to enhance the contrast between features of interest and their surroundings. For example, Figure 3.12 shows that for complex cases not all the applied attributes are clearly indicative for the zones of seismic emission (false negatives). Moreover, there also exist anomalies at locations where in fact there is no seismic emission in the subsurface (false positives), for example the peak of attribute A_1 at $x \approx 5500$ m. A way to improve the reliability for source zone detection consists of a combined, simultaneous analysis of all three attributes. Multiplication of the three attribute profiles with each other yields a new spatial distribution that incorporates the information from all three attributes. The circles in Figure 6.1 show the combined profile for this case. A comparison with the corresponding individual attribute profiles, shown in Figure 3.12, reveals an improved source zone indication (especially for zone-2). Moreover, the false positives at $x \approx 5500$ m are strongly reduced. A similar result is observed for the model with additional surface noise sources in section 3.4.1 after F-K filtering. The multi-attribute profile in Figure 6.1 (triangles) shows much sharper anomalies associated with the horizontal location of the sources compared to the individual profiles in Figure 3.14 (dash-dotted lines). These examples demonstrate that a combined interpretation of independent attributes can provide useful additional information. Of course, the rule to optimally combine the attributes may in general be more complicated than a simple multiplication.

Noise. Per definition, all signals that do not contain any useful information are considered as noise. Two different causes of noise can be distinguished to address the issue of noise for spectral analysis of ambient ground-motion:

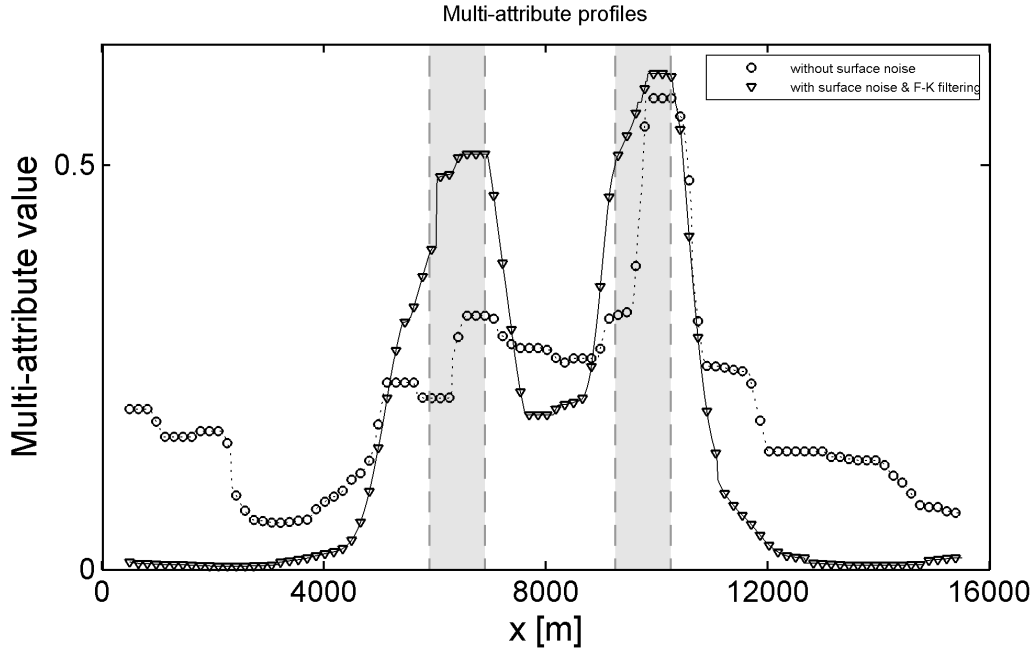


Figure 6.1. *Multi-attribute interpretation. Circles: Multi-attribute profile computed from the profiles shown in Figure 3.12. Triangles: Multi-attribute profile computed from the profiles shown in Figure 3.14. The surface projection of the source zones are highlighted as shaded areas bounded by dashed lines (left=zone-1, right=zone-2).*

- (i) Noise caused by active sources (e.g. local surface sources such as movements of trees caused by wind, infrastructure, traffic, etc.),
- (ii) Passive wave-field modifications caused by subsurface structures that are not of interest (e.g. the shallow near-surface).

In the following, the issue of noise is discussed considering the synthetic example of an embedded inclusion of high attenuation and sources below the inclusion in section 3.3. The values of attribute A_2 in Figure 3.4 are independent of the average strength of the incident wave-field because the attribute values are normalized to their maximum value across the receiver array (equation 3.5). The detectability of the inclusion depends solely on the ratio between the energy of the incident wave-field and the energy of possible additional active noise sources (case (i) above). Noise caused by passive modification (case (ii) above) is zero, since the medium is assumed to be homogeneous. There are seismic environments in nature that are comparable to the one in this model, i.e. where the wave-field in a specific frequency band is composed by a significant amount of body wave energy arriving from depth (e.g. Zhang et al., 2009). Under the assumption that noise caused by passive modification can be neglected, an inclusion in a set-up as indicated in Figure 3.1 can therefore be expected to be detectable in nature (in dedicated areas). Moreover, even if the wave-field was dominated by active noise sources (e.g. cultural noise) the signatures from depth could be retrieved for S/N-ratios as low as 0.1. This is indicated by the results in Figure 3.14. However, passive modification due to subsurface

structures (case (ii) above) remains a critical issue in practice because processing techniques such as F-K filtering are in general not able to remove such noise. Nevertheless, the example of an embedded inclusion and low-velocity surface layer in section 3.3 shows that it is possible, in some cases, to discriminate passive modifications of interest (the anomaly related to the inclusion) from non-relevant passive modification (i.e. the spectral anomalies related to the surface layer). The discrimination worked well in this example because the inclusion and the surface layer have a different horizontal extension. In general, statistical correlation methods may be mandatory to allow discriminating signals based on their spatial patterns.

Resolution. The synthetic examples in this thesis have shown that mapping spectral seismic attributes along the surface allows detecting the horizontal location (“epicenter”) of subsurface wave-field modifications. However, the detection only provided qualitative information and did not allow resolving the exact origin of such modifications. This may eventually be improved by applying quantitative interpretation methods (Avseth et al., 2005). However, the maximum lateral resolution would be expected to be not significantly higher than the wavelength of the measured signals, i.e., several hundreds of meters for the examples considered in this study.

Depth information. The interpretation of attribute profiles focuses in this thesis on the horizontal location of subsurface wave-field modifications. The depth of such modifications was not investigated in detail although attribute patterns can provide depth information as well. For example, the results in Figure 4.11 show that the horizontal patterns of frequency-based attributes (Attributes 3 and 4 in Chapter 4) can be sensitive to the depth of a buried seismic source. Also, the anomalies for attributes A_1 and A_2 in Figure 3.14 (dash-dotted lines, after F-K filtering) are smaller and broader above the source zone-1 (left anomaly) compared to the source zone-2 (right anomaly). This can be explained by the different embedment depth of the two zones, where zone-1 lies roughly 200 m deeper than zone-2 (see Figure 3.7).

Applicability to hydrocarbon exploration

The spectral analysis methodology examined in this thesis is based on the assumption that detectable signals associated with a subsurface target feature exist in the recorded ambient wave-field. This is for example the case when studying volcanic tremor (Chouet, 1996), non-volcanic tremor (Obara, 2002) or scattering of surface waves at buried obstacles (Nasseri-Moghaddam et al., 2007). In the context of hydrocarbon exploration, several studies have reported low-frequency (<10 Hz) spectral signatures that apparently correlate with the location of hydrocarbon reservoirs. Dangel et al. (2003) proposed an empirical relationship between low-frequency spectral characteristics observed in isolated measurements and the presence of reservoirs. Kouznetsov et al. (2005) used surface and borehole data to measure apparent seismic

emission from reservoirs induced by a seismic vibrator at the surface. [Birialtsev et al. \(2006\)](#) reported peaks with abnormally high amplitude in the 1-10 Hz range in the ambient wave-field above oil reservoirs in Tatarstan. [Zhukov et al. \(2007\)](#) investigated non-linear effects in seismic records associated with hydrocarbon-bearing structures and report evidence of natural seismic emission from reservoirs. [van Mastrigt & Al-Dulaijan \(2008\)](#) showed strong correlation of the data with a subsurface hydrocarbon accumulation using low-frequency passive seismic spectroscopy. [Artman et al. \(2010\)](#) applied a methodology to correct the ambient wave-field for the site response and locate the origin of the remaining body waves at the location of a known oil reservoir.

The above studies have neither conclusively proven the existence of low-frequency signals related to the presence of reservoirs nor have they proved the applicability of such signals for improved reservoir detection. However, whether the observations are indeed related to reservoirs or not is worth investigating. The following arguments support a potential applicability of low-frequency passive seismic for hydrocarbon exploration:

- Reservoirs can exhibit significantly different seismic properties than the surrounding rocks at low frequencies. In particular, high attenuation properties of reservoirs have been observed in the field. For example, [Dasgupta & Clark \(1998\)](#) and [Korneev et al. \(2004\)](#) analyzed active seismic data and found Q -values of 10 and smaller for reservoir rocks. Moreover, based on White's model for wave-induced fluid flow ([White, 1975](#)), [Quintal et al. \(2009\)](#) showed that Q -values are frequency dependent and can be as small as 2 for realistic petrophysical parameter values of sandstones partially saturated with gas and water. In the field of conventional seismic, low-frequency effects have been known for a long time ([Castagna et al., 2003](#); [Goloshubin et al., 2006](#)) and are typically explained by visco-elastic effects (e.g. [Chapman et al., 2006](#)).
- There is an omnipresent ambient seismic wave-field in nature which contains body waves from depth. For example, [Zhang et al. \(2009\)](#) showed that the ambient wave-field at low seismic frequencies (between 0.6 and 2 Hz) is dominated by continuous P-wave energy arriving from beneath the station-arrays at two sites in California. Such body waves are expected to experience characteristic modification when propagating across reservoirs with anomalous seismic properties.
- Technical improvements in the last three decades (e.g., portable 3-component seismometers, digital acquisition systems, large data storage capacities) have resulted in a considerable increase of high-quality passive seismic data-sets (including arrays) at oil and gas fields. More comprehensive data can be expected in the future which will further increase the probability of detecting more subtle signatures.

- It is possible to extract temporally stable spatial variations of the ambient wave-field at oil and gas fields (e.g. Chapters 4 and 5 of this thesis). This is an important requirement for an interpretation of the data in terms of stationary site properties (including the subsurface below the station).
- Ambient ground-motion data appear to contain information on reflectors at travel-times as great as 2 s (Draganov et al., 2007), i.e. at typical reservoir depths.

The results of real data analysis presented in this study (Chapters 4 and 5) do not allow for a conclusive evaluation of the applicability of low-frequency passive seismic for hydrocarbon exploration. A qualitative correlation of spatial attribute patterns with the horizontal location of the reservoirs is not as clear as reported in case-studies across other oil or gas fields (e.g. van Mastrigt & Al-Dulaijan, 2008). This may be explained by the thickness of the reservoirs which is a few tens of meters only, in a depth of around 2 km. In addition, the survey area around Voitsdorf features a high anthropogenic noise level and complex surface geology. As demonstrated by the numerical study in Chapter 3, such environments can mask patterns in the data that are related to subsurface features of interest. However, this thesis does not perform a quantitative analysis of observed attribute patterns. Relationships between reservoir locations and attribute patterns are discussed in a purely qualitative way and mainly with respect to the general applicability of the spectral analysis methodology.

The numerical wave propagation simulations in Chapter 3 investigate how and under what conditions subsurface quasi-stationary wave-field modifications can be detected at the surface. This provides a theoretical basis to discuss the applicability of low-frequency passive seismic. Together with the ambient ground-motion study at an oil and gas field and the proposed spectral analysis methodology (Chapters 4 and 5), this thesis contributes towards an eventually better understanding of observed low-frequency spectral anomalies above hydrocarbon reservoirs.

References

- Artman, B., Goertz, A., Schechinger, B., Krajewski, P. & Koerbe, M. (2010). *Joint interpretation of multiple passive seismic data volumes*. 72th EAGE meeting, Barcelona, Spain, Expanded Abstracts, p. F009.
- Avseth, P., Mukerji, T. & Mavko, G. (2005). *Quantitative Seismic Interpretation – Applying Rock Physics Tools to Reduce Interpretation Risk*. Cambridge University Press. ISBN 0521816017.
- Birialtsev, E., Plotnikova, I., Khabibulin, I. & Shabalin, N. (2006). *The analysis of micro-seisms spectrum at prospecting of oil reservoir on Republic Tatarstan*. Paper presented at

- EAGE/EAGO/SEG International Conference & Exhibition, Saint Petersburg, Russia, Expanded Abstracts.
- Brenguier, F., Shapiro, N. M., Campillo, M., Nercessian, A. & Ferrazzini, V. (2007). *3-D surface wave tomography of the Piton de la Fournaise volcano using seismic noise correlations*. *Geophysical Research Letters*, **34**, L02305.
- Castagna, J. P., Sun, S. & Siegfried, R. W. (2003). *Instantaneous spectral analysis: Detection of low-frequency shadows associated with hydrocarbons*. *The Leading Edge*, **22**, 120–127.
- Chapman, M., Liu, E. & Li, X.-Y. (2006). *The influence of fluid-sensitive dispersion and attenuation on AVO analysis*. *Geophys. J. Int.*, **167**, 89–105.
- Chopra, S. & Marfurt, K. (2005). *Seismic attributes – A historical perspective*. *Geophysics*, **70**, 3S0–28S0.
- Chouet, B. (1996). *Long-period volcano seismicity: Its source and use in eruption forecasting*. *Nature*, **380**, 309–315.
- Clearbout, J. (1968). *Synthesis of a layered medium from its acoustic transmission response*. *Geophysics*, **33**, 264–269.
- Dangel, S., Shaepman, M. E., Stoll, E. P., Carniel, R., Barzandji, O., Rode, E.-D. & Singer, J. M. (2003). *Phenomenology of tremor-like signals observed over hydrocarbon reservoirs*. *J. Volcanol. Geothermal Res.*, **128**, 135–158.
- Dasgupta, R. & Clark, R. A. (1998). *Estimation of Q from surface seismic reflection data*. *Geophysics*, **63**(6), 2120–2128.
- Draganov, D., Wapenaar, K., Mulder, W., Singer, J. & Verdel, A. (2007). *Retrieval of reflections from seismic background-noise measurements*. *Geophysical Research Letters*, **34**, L04305.
- Fournier, F. & Derain, J.-F. (1995). *A statistical methodology for deriving reservoir properties from seismic data*. *Geophysics*, **60**(5), 1437–1450.
- Goloshubin, G., Vanschuyver, C., Korneev, V., Silin, D. & Vingalov, V. (2006). *Reservoir imaging using low frequencies of seismic reflections*. *The Leading Edge*, **May 2006**, 527–531.
- Korneev, V., Goloshubin, G. M., Daley, T. M. & Silin, D. B. (2004). *Seismic low-frequency effects in monitoring fluid-saturated reservoirs*. *Geophysics*, **69**, 522–532.

- Kouznetsov, O., Chirkin, I., Dryagin, V., Aroutunov, S. & Meltschouk, B. (2005). *Induced seismoacoustic emission - basis for new technologies of fluid identification*. Paper presented at the 67th EAGE International Conference & Exhibition, Madrid, Spain, Expanded Abstracts, Z-99.
- Liner, C., Li, C.-F., Gersztenkorn, A. & Smythe, J. (2004). *SPICE: A new general seismic attribute*. Paper presented at the 74th SEG International Conference & Exhibition, Denver, USA, Expanded Abstracts, p. 433–436.
- van Mastrigt, P. & Al-Dulaijan, A. (2008). *Seismic spectroscopy using amplified 3C geophones*. Paper presented at the 70th EAGE Conference & Exhibition, Rome, Italy, Expanded Abstracts, p. B047.
- Nasseri-Moghaddam, A., Cascante, G., Phillips, C. & Hutchinson, D. (2007). *Effects of underground cavities on Rayleigh waves - Field and numerical experiments*. *Soil Dynamics and Earthquake Engineering*, **27**, 300–313.
- Obara, K. (2002). *Nonvolcanic Deep Tremor Associated with Subduction in Southwest Japan*. *Science*, **196**, 1679–1681.
- Quintal, B., Schmalholz, S. & Podladchikov, Y. Y. (2009). *Low-frequency reflections from a thin layer with high attenuation caused by interlayer flow*. *Geophysics*, **74**(1), N15–N23.
- Schuster, G. T. (2009). *Seismic Interferometry*. Cambridge University Press, New York, USA. ISBN 978-0-521-87124-2.
- Shapiro, N. M., Campillo, M., Stehly, L. & Ritzwoller, M. H. (2005). *High-Resolution Surface-Wave Tomography from Ambient Seismic Noise*. *Science*, **307**, 1615–1618.
- Tallavó, F., Cascante, G. & Pandey, M. (2009). *Experimental and numerical analysis of MASW tests for detection of buried timber trestles*. *Soil Dynamics and Earthquake Engineering*, **29**, 91–102.
- White, J. E. (1975). *Computed seismic speeds and attenuation in rocks with partial gas saturation*. *Geophysics*, **40**(2), 224–232.
- Zhang, J., Gerstoft, P. & Shearer, P. (2009). *High-frequency P-wave seismic noise driven by ocean winds*. *Geophysical Research Letters*, **36**, L09302.
- Zhukov, A., Loginov, K., Shneerson, M., Shulakova, V., Kharisov, R. & Ekimenko, V. (2007). *Nonlinear properties of vibrator-generated wavefields and their application to hydrocarbon detection*. *The Leading Edge*, **26**, 1395–1402.

7. Conclusions

The omnipresent ambient seismic wave-field at the Earth's surface is a superposition of body and surface waves generated by multiple seismic sources at many different surface and subsurface locations. Moreover, the wave-field is continuously modified by interaction (e.g., reflection, refraction, scattering, attenuation and resonant scattering) with structures like topography, reflectors or underground bodies of anomalous seismic properties (e.g. cavities). Passive recordings of the ambient ground-motion therefore contain information on a variety of subsurface structures and processes.

Spectral analysis is a suitable method to assess the wave-field's characteristic in time, frequency and space. The interpretation of temporally stable, i.e. quasi-stationary, modifications of the wave-field in frequency and space is useful for extracting subsurface information. Modifications can either be caused by interaction with structures (passively) or by seismic sources at depth (actively).

Spectral attributes are a quantitative measure of a spectral characteristic of interest. Mapping spectral seismic attributes along the surface allows detecting the horizontal location of subsurface wave-field modifications. This approach is applicable to both, passive and active modification. Moreover, spectral attributes can be indicative of deep structures, despite the presence of shallow structures that have a strong influence on the wave-field. Information on shallow and deep structures is not mutually exclusive and it is possible to extract both from the same data.

To minimize possible contamination from surface noise sources (e.g. anthropogenic noise) data should be acquired in quiet areas and/or during the most quiet time periods (usually at night). However, in situations where surface noise dominates the wave-field and masks modifications related to deeper features, it is required to apply noise reduction techniques before interpreting the data. Temporal normalization, spectral despiking and F-K filtering applied to attribute sections are examples of techniques that are effective in removing anthropogenic noise from passive seismic data. Noise reduction techniques become more efficient for large and densely spaced receiver arrays. Such arrays, for example in the form of regular grids, are recommended for areas with high anthropogenic noise levels.

Temporally stable attribute patterns at low frequencies are observed in nature, as shown for an oil and gas field in Voitsdorf, Austria. The interpretation of the patterns in terms of subsurface structures and processes was not fully conclusive. More specifically, the discrimination

between modifications due to shallow structures and possible modifications due to the presence of hydrocarbon reservoirs remained ambiguous. However, considering the numerical results in this thesis and the findings of other theoretical and experimental studies, it seems physically justified to apply spectral analysis to ambient ground-motion recordings in an attempt to increase the probability of detecting reservoirs. In which environments low-frequency passive seismic is potentially applicable for hydrocarbon exploration must be answered through further case-studies at oil and gas fields.

Appendices

A. Reply to comment on “Low-frequency microtremor anomalies at an oil and gas field in Voitsdorf, Austria” by Marc-André Lambert, Stefan M. Schmalholz, Erik H. Saenger and Brian Steiner, *Geophysical Prospecting* 57, 393–411 ¹

Marc-André Lambert, Stefan M. Schmalholz, Erik H. Saenger & Brian Steiner

A.1 INTRODUCTION

We welcome the opportunity to respond to Professors Green and Greenhalgh’s analysis of our work in this journal. In addressing their observations we hope to contribute towards a better understanding of our work in general.

Green & Greenhalgh (2010) commented not only on Lambert et al. (2009) but also on peer-reviewed papers, conference proceedings and magazine articles authored by at least one of us, thereby combining formative early work with more advanced results in their critique. Additionally, they commented on publications that none of us has co-authored (e.g., Dangel et al., 2003; Walker, 2008), addressing questions to a scientific community beyond our research group. This reply necessarily focuses only on the work that at least one of us has co-authored.

Green & Greenhalgh (2010) asserted that our conclusion that “the results indicate that passive low-frequency spectral analysis can increase the probability of locating reservoirs significantly” is unfounded. We identify three main arguments in their commentary: i) that our attributes are not applicable to reservoir detection, ii) that the results of our numerical study do not

¹This chapter was published in *Geophysical Prospecting* (Lambert et al., 2010)

fit the data and iii) that our attributes are in fact sensitive to shallow structures and we inadequately consider these potential shallow effects in our work. We first respond to these three main points and then to additional criticism, which is included as discussion within their commentary. Finally, we describe the objectives of our research to put it in the correct perspective and to address Green and Greenhalgh's (2010) assertion that the results of Lambert *et al.* (2009) contradict our earlier work.

A.2 RESPONSE TO SPECIFIC COMMENTS

A.2.1. Attributes 1 and 2

Green & Greenhalgh (2010) expressed the view that our Attributes 1 and 2 do not indicate the two reservoir locations. Based on our qualitative analysis of the correlation between these spectral attributes and reservoir locations, we agree with them. In Lambert *et al.* (2009) we explicitly stated: "Attributes 1 and 2 are not sensitive for the northern reservoir", "For Attribute 1, temporal variations are rather large and, therefore, the observed anomalies are less significant" and "Attribute 2 behaves very stable in time... the profiles do not show clear lateral anomalies". We clearly stated that the profiles of Attributes 1 and 2 are not useful for detecting the two reservoirs at this site. We do not see the supposed contradiction in Lambert *et al.* (2009) because we did not claim that all attributes must show anomalies above both reservoirs in order to increase the probability of detecting reservoirs.

A.2.2. Attributes 3 and 4

Attributes 3 and 4 are based on more stable frequency values rather than on amplitude values, which can vary substantially in experiments utilizing an uncontrolled source. Green & Greenhalgh (2010) wrote that "Lambert *et al.*'s (2009) simplistic physical exploration is both implausible and inconsistent with (our) observations". Our numerical study was in fact a feasibility (or plausibility) study intended to show that seismic signals emitted by a subsurface source in a homogeneous, linear elastic medium with no dispersion can generate spectral patterns along the model's free surface that are similar to the peak-frequency shift pattern identified from the field data for Attributes 3 and 4. Green & Greenhalgh (2010) contrasted our numerical feasibility study for Attributes 3 and 4 with field data of Attribute 2 (V/H values). The objective of our numerical study, using a simplistic parameter space, was to demonstrate a concept; the aim was not to explain the natural wave propagation processes at the Voitsdorf site, nor to reproduce the distribution of all other attributes recorded in the survey. Hence, there is no contradiction with the patterns observed for Attribute 2 in the field data.

To extend the analysis with more realistic complexity, we offer two new numerical simulations and the resulting V/H profiles (Fig. A.1). The top panel shows the modelled distribution of

the peak-frequency attribute due to a single, vertically-acting line source at 2000 m depth. The middle panel is the result from multiple, vertically-acting line sources. The multiple sources are randomly distributed in time and space within a source area in the subsurface to generate a tremor-like signal. The results show that for both source models, there is a considerable peak-frequency shift pattern indicating the location of the subsurface source area (Fig. A.1a,b). Importantly, the corresponding V/H profiles in Fig. A.1(c) are very different. The singular anomaly due to a single source is not only removed for the case of multiple sources (Fig. A.1c, dashed line) but the result does not correspond with the surface projection of the source area (grey area in Fig. A.1c). These results show that our physical justification for the attribute patterns is not inconsistent with observation because the spatial patterns of different attributes can be independent. Therefore, there is no contradiction arising from “not observed” “extraordinarily high V/H values”.

A.2.3. The influence of shallow structures

Green & Greenhalgh (2010) stated that the “very large variations of Attributes 1–4 along lines and between adjacent lines” in our figure 7 “are evidence for the overwhelming influence of local shallow structures”. As described in the paper, Fig. 7 of Lambert et al. (2009) illustrated intermediate processing steps for stacking in space. It showed six profiles for each attribute where each profile has been recorded for 30 minutes by synchronized stations. Each of the six profiles had been recorded on a different day. Therefore, the disputed figure 7 does not show a representative spatial variation of the attributes, because results of adjacent lines are up to 6 days apart and each profile represents only 30 minutes of data. A representative spatial variation was displayed in Fig. 8 of Lambert et al. (2009). Figure 8 showed variations of the four attributes for 11 profiles, each measured for 30 minutes during a continuous time period of 5.5 hours together with the corresponding time average. We are unable to see how the observed spatial variations of the four attributes in these Figs 7 and 8 of Lambert et al. (2009) are “evidence for the overwhelming influence of local shallow structures”. These variations could be due to shallow structures but our numerical feasibility study showed that these variations could equally well originate from deeper sources (Figs 10 and 11 of Lambert et al. (2009) and Fig. 1 in this reply).

The possible influence of shallow structures was not emphasized in Lambert et al. (2009). As we have discussed in other publications (e.g., Lambert et al., 2006; Saenger et al., 2009), we are aware that such effects can strongly affect the data. In the Voitsdorf case study, the limited data on near surface geology available to us makes it difficult to conclude conclusively on the effects of shallow structures. It is well established that the ratio of H/V is less affected by source effects and, therefore, is suitable to analyse shallow structures. We analysed its reciprocal (V/H) in the frequency range of 1–6 Hz and did not find evidence for an “overwhelming influence” of

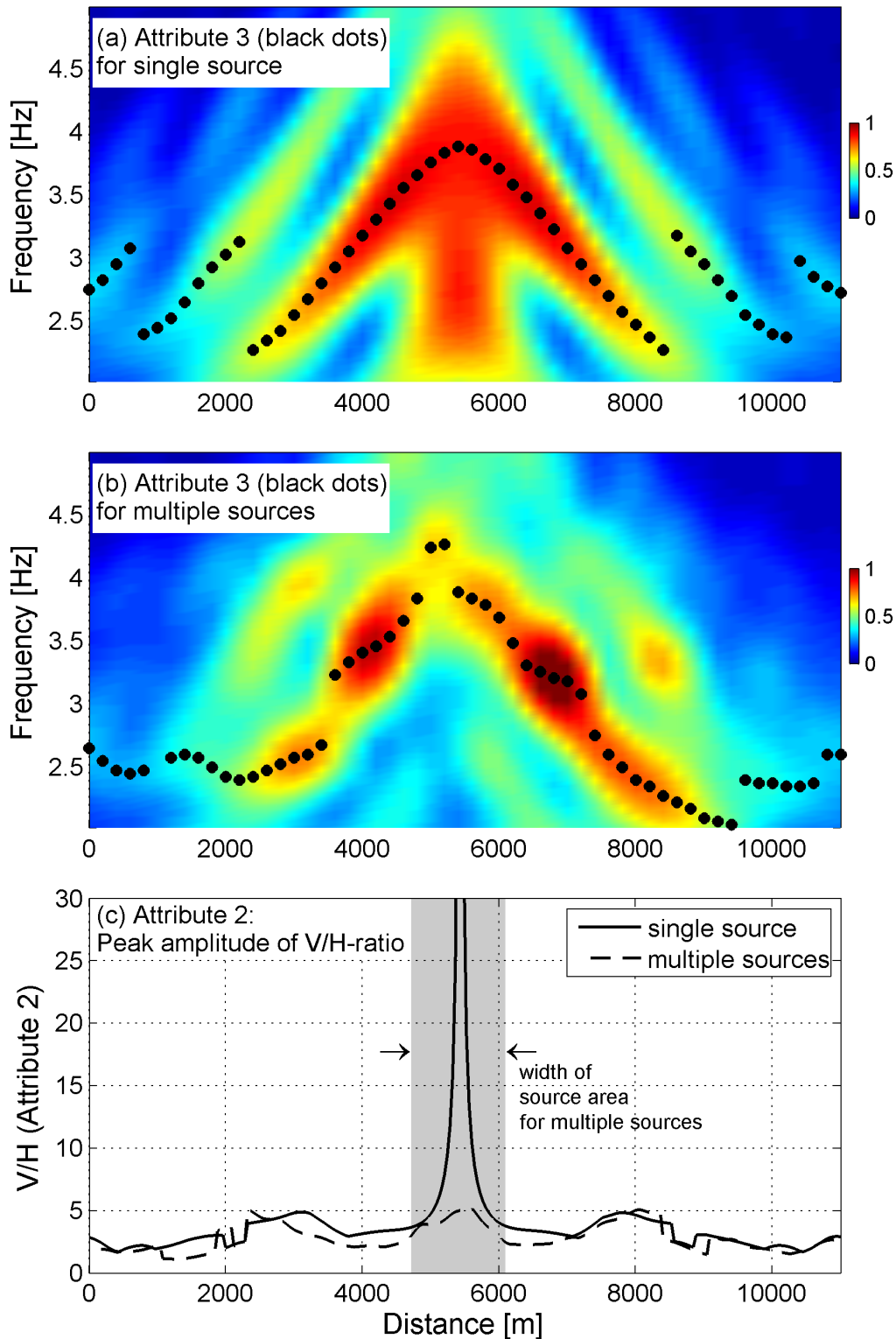


Figure A.1. Results of numerical simulations with two different seismic sources. Details of the model set-up are described in [Lambert et al. \(2009\)](#). a) Normalized spatial spectrogram of the vertical component of the synthetic wavefield at the free surface for a single source. Black dots show the shift of the peak-frequencies (Attribute 3) indicating the source location. b) Same as (a) but for multiple sources (tremor-like signal). c) Profiles of V/H values (Attribute 2) along the model's free surface for the two simulations. Only the single source model exhibits extraordinarily high V/H values (Attribute 2) although for both simulations the patterns of Attribute 3 around the source location are similar (a and b).

shallow structures along the survey lines. Values of V/H were mainly between 0.6–1.2. We chose not to discuss possible shallow structure effects in detail in this paper because we do not present a quantitative correlation analysis among the four attribute patterns and the reservoir locations; instead we focus on the spatial and temporal variation of the attributes.

A.2.4. The Voitsdorf site

[Green & Greenhalgh \(2010\)](#) speculated that we “regard the Voitsdorf site as an ideal location to test the proposed HMS relationship” (the term HMS has been introduced by them for hydrocarbon-microtremor-spectra). On the contrary, the Voitsdorf site in the Alpine Foreland Basin is far from ideal. The site features high anthropogenic noise and complex geology that made our analysis more difficult. Nevertheless, there are good reasons why we chose to study data at this location:

- We have permission from the field operator to publish the data.
- The site offers relatively easy operating access, allowing us to repeat measurements quickly, safely and cost-effectively.
- Good geophysical data (e.g., reservoir model, P-wave velocity model) are available.
- The site is suitable for developing and testing new methods for data filtering, noise cleaning and stacking (e.g., [Nguyen et al., 2008](#)).

For an example of a site more ideally suited to testing the basic hypothesis that low-frequency wavefields can be modified by reservoirs in the subsurface we would refer to [van Mastrigt & Al-Dulaijan \(2008\)](#), who studied a proven nonproducing gas reservoir in an exceptionally quiet location, less conveniently situated deep within Saudi Arabia’s Rub’ al Khali desert.

A.2.5. Selection of applicable literature

Microtremor analysis focusing on reservoir effects is an emerging field. There is currently limited discussion of the topic in the refereed literature. We have sought to address this by submitting our own work for scrutiny and publication by peer-reviewed journals such as this one. [Green & Greenhalgh \(2010\)](#) emphasized two experimental descriptions ([Ali et al., 2007](#); [Berteussen et al., 2008a,b](#); [Hanssen & Bussat, 2008](#)), which did not conclude that the analysed microtremor energy is related to known reservoirs. It would be suspicious if a nascent technique was especially easy to apply, universally applicable, or not subject to complexity or failure. We cannot think of an accepted exploration method about which this could be said. However, not mentioned in Green and Greenhalgh’s (2010) comment are a number of other studies (not

co-authored by us) reporting correlation between the presence of reservoirs and observed low-frequency seismic signals (e.g., [Kouznetsov et al., 2005](#); [Turuntaev et al., 2006](#); [Birialtsev et al., 2006](#); [Zhukov et al., 2007](#)). Moreover, [van Mastrigt & Al-Dulaijan \(2008\)](#) showed correlations between anomalies in passive seismic data and a proven non-producing subsurface reservoir in a remote and unusually quiet location. The results of this study cannot easily be reconciled with the arguments advanced by [Green & Greenhalgh \(2010\)](#) and the articles they cite. In our view, all studies should be considered. While it is correct to be sceptical, one should remain open-minded in the far-from-resolved field of oil and gas exploration.

A.2.6. The nature of 1-10 Hz microtremors

[Green & Greenhalgh \(2010\)](#) argued that there is “compelling evidence for the widely accepted shallow origin of 1–10 Hz microtremors”. We do not disagree that there are many 1–10 Hz microtremors of shallow origin. However, there are also studies showing a dominantly deep origin of microtremors. For example, [Zhang et al. \(2009\)](#) showed that the ambient wavefield between 0.6–2 Hz is dominated by continuous P-wave energy at two sites in California. These P-waves propagate through the Earth and arrive at the stations from beneath the array. We also note that at specific geological locations, such as volcanoes, microtremors can include tremor signals originating from depth (e.g., [Chouet, 1996](#)).

Importantly, [Green & Greenhalgh \(2010\)](#) also wrote that they “do not preclude the possibility of signals from deep structures contributing to microtremor wavefields”. They refer to [Draganov et al. \(2007\)](#) who extracted two-way traveltimes of reflections – also a seismic attribute ([Chopra & Marfurt, 2005](#)) – as great as 2 s from passive seismic data. [Draganov et al. \(2007\)](#) worked with data in a frequency range from 1–80 Hz and stated that “useful information was concentrated between 2 and 10 Hz”. If it is possible to extract attributes such as two-way traveltimes from passive seismic data, then it should, in principle, also be possible to extract other attributes from passive seismic data, such as attributes related to fluid and rock properties of reservoirs.

We emphasize that we did not “claim high-resolution capabilities”, as implied by [Green & Greenhalgh \(2010\)](#) in their final paragraph referencing [Draganov et al. \(2007\)](#). In contrast, [Lambert et al. \(2009\)](#) stated that “...the maximum lateral resolution for the reservoir would be expected to be in the same order of magnitude as the wavelength of the measured signals, i.e., several hundreds of metres”.

A.2.7. Our research organization and earlier work

We have consistently sought to present and discuss our research, results and interpretations at relevant international conferences, such as EAGE and SEG. To do this, we must submit extended abstracts, often six months or more in advance of the presentation. These abstracts present data, results, hypotheses and interpretations at the time they were written. Our re-

search is active and ongoing and the volume and quality of data available to us has increased with time. Accordingly, we have modified some of our earlier hypotheses and interpretations as our understanding has evolved. This normal process of scientific discovery has inevitably led to modified statements, which we do not consider to be contradictions of earlier “assertions”, as suggested by [Green & Greenhalgh \(2010\)](#) and we have made no effort to obscure the progression of our research.

[Green & Greenhalgh \(2010\)](#) described our research collaboration with industry as an “industry-university consortium (IUC)”. In fact, our research in this field is supported by both industry partners and the Swiss Confederation’s innovation promotion agency (CTI, see <http://www.bbt.admin.ch/kti/>). The salaries of PhD students and Post-Doctoral researchers are paid and guaranteed by the CTI.

A.3 CONTEXT FOR THE STUDY AND AIMS OF OUR RESEARCH

Several independent studies (e.g., [Dangel et al., 2003](#); [Zhukov et al., 2007](#); [van Mastrigt & Al-Dulaijan, 2008](#)) have reported an apparent correlation between characteristic patterns, or anomalies, in the spectra of low-frequency passive seismic ground motion recordings and the location of hydrocarbon reservoirs. Our research addresses the question how and to what extent the analysis of passive ground motion can increase the probability of detecting hydrocarbon reservoirs or, more generally, can provide useful information about the subsurface. We refer to the method of analysing passive ground motion in the context of reservoir detection as low-frequency microtremor analysis. Low-frequency microtremor analysis is an emerging methodology both under development and evaluation. As of now, there is no established theoretical and physical model that fully explains the relationship between the recorded data, the ambient seismic wavefield and the physical processes related to the reservoir. So far, only basic and heuristic models have been suggested (e.g., [Saenger et al., 2009](#)). Low-frequency microtremor analysis therefore is currently a statistical method based primarily on empirical observations. One goal of our work is eventually to apply statistical classification and pattern recognition methods (e.g., [Avseth et al., 2005](#)) to passive seismic attributes. Such methods are already applied in active seismics. To apply and evaluate such methods in the context of low frequency microtremor analysis requires:

- 1 Data preprocessing (e.g., filtering, cleaning, stacking etc.).
- 2 Defining, extracting and evaluating attributes for passive data.
- 3 Models providing some physical justification and a better understanding of attributes and their spatial and temporal variation.

- 4 Performing statistical classification and/or pattern recognition (e.g., neural networks) to the passive seismic attributes.
- 5 A large number of case studies to test whether low frequency microtremor analysis can increase the probability of detecting reservoirs for few, many or most case studies.

The work reported in [Lambert et al. \(2009\)](#) focused on points 1) to 3) with the main aim being to introduce and define, for the first time in a peer-reviewed journal, the calculation of four new passive seismic attributes. The attributes presented in the paper are similar to conventional seismic attributes, which are a quantitative measure of a seismic characteristic of interest (e.g., [Chopra & Marfurt, 2005](#)). Attributes can be classified into general and specific categories ([Liner et al., 2004](#)). General attributes have a well-defined basis in physics or geology and are universally applicable. In contrast, specific attributes have a less well-defined basis in physics and may be well correlated to a target feature (e.g., a hydrocarbon reservoir) for a given case study. These correlations often do not carry over to different areas ([Chopra & Marfurt, 2005](#)). The attributes presented in [Lambert et al. \(2009\)](#) are specific. The same attributes can therefore show different patterns across different reservoirs (at different sites) without being in contradiction. Often multiple specific attributes are combined to enhance the contrast between features of interest and their surroundings (e.g., [Avseth et al., 2005](#)). [Lambert et al. \(2009\)](#) therefore also introduced multiple attributes. Not all of these attributes need to, or should be expected to, exhibit anomalous patterns across the same reservoir.

A.4 CONCLUSIONS AND OUTLOOK

Green and Greenhalgh's (2010) claim that results, models and conclusions presented in [Lambert et al. \(2009\)](#) are inconsistent is not justified by their analysis, which reflects an apparent misunderstanding of the reported study and its context. We stand by our conclusion, which stated that "the results indicate that passive low frequency spectral analysis can increase the probability of locating reservoirs significantly". We reiterate the following findings from our study that support this conclusion: i) Attributes 3 and 4 show statistically a stronger variation in space than in time (useful to quantify spatial variations in the passive ground motion) and ii) Attributes 3 and 4 qualitatively indicate a relationship with the reservoir location. We recognize that our conclusion incorporates a subjective assessment with which Professors Green and Greenhalgh are entitled to disagree. However, the analysis presented by [Green & Greenhalgh \(2010\)](#) in their Table 1 is inappropriate, because the question of whether attribute values are anomalous or not should be answered in terms of probability rather than 'yes' or 'no'. Our study suggested that a future statistical classification using the attributes we describe would be a promising approach to improving the probability of detecting reservoirs. This view is now supported by a statistical classification, using a Bayesian methodology, of similar attributes

to compute hydrocarbon probability maps at a different location (Riahi et al., 2009). More conclusive evidence that passive seismic attributes are useful to increase the probability of detecting reservoirs can only be provided by additional studies performing statistical predictions and subsequent verification/falsification by drilling.

References

- Ali, M., Berteussen, K., Small, J. & Barkat, B. (2007). *A low frequency passive seismic experiment over a carbonate reservoir in Abu Dhabi*. *First Break*, **25**, 71–73.
- Avseth, P., Mukerji, T. & Mavko, G. (2005). *Quantitative Seismic Interpretation – Applying Rock Physics Tools to Reduce Interpretation Risk*. Cambridge University Press. ISBN 0521816017.
- Berteussen, K., Ali, M., Small, J., Anjana, B. & Barkat, B. (2008b). *Analysis of low frequency passive seismic data from an experiment over a carbonate reservoir in Abu Dhabi*. Abu Dhabi International Petroleum Exhibition and Conference, Abu Dhabi, UAE, pp. SPE–117925–PP.
- Berteussen, K., Ali, M., Small, J. & Barkat, B. (2008a). *A low frequency, passive seismic experiment over a carbonate reservoir in Abu Dhabi – Wavefront and particle motion study*. 70th EAGE meeting, Rome, Italy, Expanded Abstracts, p. B046.
- Birialtsev, E., Plotnikova, I., Khabibulin, I. & Shabalin, N. (2006). *The analysis of microseisms spectrum at prospecting of oil reservoir on Republic Tatarstan*. Paper presented at EAGE/EAGO/SEG International Conference & Exhibition, Saint Petersburg, Russia, Expanded Abstracts.
- Chopra, S. & Marfurt, K. (2005). *Seismic attributes – A historical perspective*. *Geophysics*, **70**, 3SO–28SO.
- Chouet, B. (1996). *Long-period volcano seismicity: Its source and use in eruption forecasting*. *Nature*, **380**, 309–315.
- Dangel, S., Shaepman, M. E., Stoll, E. P., Carniel, R., Barzandji, O., Rode, E.-D. & Singer, J. M. (2003). *Phenomenology of tremor-like signals observed over hydrocarbon reservoirs*. *J. Volcanol. Geothermal Res.*, **128**, 135–158.
- Draganov, D., Wapenaar, K., Mulder, W., Singer, J. & Verdel, A. (2007). *Retrieval of reflections from seismic background-noise measurements*. *Geophysical Research Letters*, **34**, L04305.
- Green, A. & Greenhalgh, S. (2010). *Comment on "Low-frequency microtremor anomalies at an oil and gas field in Voitsdorf, Austria" by Marc-André Lambert, Stefan Schmalholz, Erik H.*

- Saenger and Brian Steiner, *Geophysical Prospecting* 57, 393–411. *Geophysical Prospecting*, **58**, 335–339.
- Hanssen, P. & Bussat, S. (2008). *Pitfalls in the analysis of low frequency passive seismic data*. *First Break*, **26**, 111–119.
- Kouznetsov, O., Chirkin, I., Dryagin, V., Aroutunov, S. & Meltschouk, B. (2005). *Induced seismoacoustic emission - basis for new technologies of fluid identification*. Paper presented at the 67th EAGE International Conference & Exhibition, Madrid, Spain, Expanded Abstracts, Z-99.
- Lambert, M.-A., Schmalholz, S. M., Saenger, E. H. & Steiner, B. (2009). *Low-frequency microtremor anomalies at an oil and gas field in Voitsdorf, Austria*. *Geophysical Prospecting*, **57**, 393–411. doi:10.1111/j.1365-2478.2008.00734.x.
- Lambert, M.-A., Schmalholz, S. M., Saenger, E. H. & Steiner, B. (2010). *Reply to comment on "Low-frequency microtremor anomalies at an oil and gas field in Voitsdorf, Austria" by Marc-André Lambert, Stefan M. Schmalholz, Erik H. Saenger and Brian Steiner, Geophysical Prospecting 57, 393–411*. *Geophysical Prospecting*, **58**, 341–346.
- Lambert, M.-A., Steiner, B., Schmalholz, S., Holzner, R. & Saenger, E. (2006). *Soft soil amplification of ambient seismic noise – Field measurements and numerical modeling of H/V ratio*. Paper presented at the EAGE Workshop Passive Seismic: Exploration and Monitoring Applications, 2006, Dubai, UAE, Expanded Abstracts, p. A10.
- Liner, C., Li, C.-F., Gersztenkorn, A. & Smythe, J. (2004). *SPICE: A new general seismic attribute*. Paper presented at the 74th SEG International Conference & Exhibition, Denver, USA, Expanded Abstracts, p. 433–436.
- van Mastriigt, P. & Al-Dulaijan, A. (2008). *Seismic spectroscopy using amplified 3C geophones*. Paper presented at the 70th EAGE Conference & Exhibition, Rome, Italy, Expanded Abstracts, p. B047.
- Nguyen, T., Lambert, M.-A., Saenger, E., Artman, B. & Schmalholz, S. (2008). *Reduction of noise effects on low frequency passive seismic data*. Paper presented at the 71st EAGE Conference & Exhibition, Amsterdam, The Netherlands, Expanded Abstracts, p. S038.
- Riahi, N., Kelly, M., Ruiz, M. & Yang, W. (2009). *Bayesian DHI using passive seismic low frequency data*. Paper presented at the 79th SEG International Conference & Exhibition, Houston, USA, Expanded Abstracts, p. 1607–1611.

- Saenger, E. H., Schmalholz, S. M., Lambert, M.-A., Nguyen, T. T., Torres, A., Metzger, S., Habiger, R., Müller, T., Rentsch, S. & Mendez-Hernández, E. (2009). *A passive seismic survey over a gas field: Analysis of low-frequency anomalies*. *Geophysics*, **74**, O29–O40.
- Turuntaev, S., Burchik, V. & Turuntaev, D. (2006). *Microseismic background study for gas field exploration*. Paper presented at the 76th SEG International Conference & Exhibition, New Orleans, USA, Expanded Abstracts, pp. 115–119.
- Walker, D. (2008). *Recent developments in low frequency spectral analysis of passive seismic data*. *First Break*, **26**, 69–77.
- Zhang, J., Gerstoft, P. & Shearer, P. (2009). *High-frequency P-wave seismic noise driven by ocean winds*. *Geophysical Research Letters*, **36**, L09302.
- Zhukov, A., Loginov, K., Shneerson, M., Shulakova, V., Kharisov, R. & Ekimenko, V. (2007). *Nonlinear properties of vibrator-generated wavefields and their application to hydrocarbon detection*. *The Leading Edge*, **26**, 1395–1402.

B. Fourier transform

Consider a discrete time-series x_n consisting of N values, sampled with a time-step of Δt . The total duration of the series is $T = N\Delta t$. For this case, the discrete Fourier transform (DFT) of x_n can be defined as

$$X_k = \Delta t \sum_{n=0}^{N-1} x_n e^{-j2\pi \frac{kn}{N}} \quad k = 0, \dots, N-1, \quad (\text{B.1})$$

where j is the imaginary unit.

This definition of the transform provides the physically correct units of a spectral density for the amplitude spectrum $|X_k|$. For example, if the input time-series has units of m/s , $|X_k|$ will have units of $\frac{m/s}{Hz}$. The corresponding power spectral density is in this case defined as the spectral energy density, $|X_k|^2$, divided by the total duration of the signal:

$$P_k = \frac{1}{T} |X_k|^2 = \frac{\Delta t}{N} \left| \sum_{n=0}^{N-1} x_n e^{-j2\pi \frac{kn}{N}} \right|^2 \quad (\text{B.2})$$

The time-step Δt is often dropped in the definition of the DFT:

$$X'_k = \sum_{n=0}^{N-1} x_n e^{-j2\pi \frac{kn}{N}} \quad k = 0, \dots, N-1. \quad (\text{B.3})$$

This is also a valid notation of the DFT, but without the factor Δt , the correct physical units are not preserved.

The DFT used in this thesis is scaled to the square root of the duration of the time-series:

$$\hat{X}_k = \frac{\Delta t}{\sqrt{N\Delta t}} \sum_{n=0}^{N-1} x_n e^{-j2\pi \frac{kn}{N}} \quad k = 0, \dots, N-1. \quad (\text{B.4})$$

This version of the transform has the advantage that integral values over the amplitude spectra are independent of the duration of the input signal. The physically correct power spectral density is in this case obtained by taking the square of the amplitude spectrum:

$$P_k = |\hat{X}_k|^2 = \frac{\Delta t}{N} \left| \sum_{n=0}^{N-1} x_n e^{-j2\pi \frac{kn}{N}} \right|^2. \quad (\text{B.5})$$

Equations (B.4) and (B.5) are used throughout this thesis to compute amplitude spectra and power spectral densities, respectively. For an input time-series with units m/s , the amplitude spectra therefore have units of $\frac{m/s}{\sqrt{Hz}}$ and the power spectral densities have units of $\frac{(m/s)^2}{Hz}$.

C. Frequency-shift pattern

C.1 OBSERVATION

A numerical model is considered that consists of a single, vertically acting body force in a homogeneous, isotropic medium. The two-dimensional (2D) model domain (Fig. C.1a) has a free surface at the top and wave absorbing layers at the three other boundaries to simulate an infinite half-space (Cerjan et al., 1985). The P- and S-wave velocities are 3000 m/s and 1500 m/s, respectively. The density of the medium is 3000 kg/m³. The seismic source is located at depth $D=2000$ m. The source is represented as a short-time low-frequency signal, induced by a single, vertically acting body force. The source time function is a Ricker wavelet with a central frequency of 3 Hz. The particle velocities are recorded over time at the free surface. The recorded time signals capture the elastic disturbance which was generated by the seismic source and then propagated through the medium. The chosen propagator solves the full 2D elastic wave equation which is transformed into the first order velocity-stress formulation (Virieux, 1986). The rotated staggered grid finite-difference (FD) technique described in Saenger et al. (2000) is applied. The numerical grid is rectangular. All computations are performed with second order spatial finite-difference operators and with a second order explicit time update.

The recorded surface signals are transformed into the frequency domain by a fast Fourier transform and displayed as spatial spectrograms (spectral amplitude as a function of distance and frequency) as shown in Fig. C.1b for the vertical component of the particle velocity. The wave field at the surface is analyzed with a focus on lateral variations of the frequency, in Hertz, of dominant peaks (peak-frequencies). The values of the dominant peak-frequencies are indicated with black crosses in Fig. C.1b. They lie around 3 Hz vertically above the source ($x=5000$ m) and decrease with increasing offset from the vertical projection of the source location onto the surface. This is highlighted with two ellipses (labeled as 1st) and forms a positive anomaly vertically above the source. A second branch of high amplitudes at higher frequencies becomes dominant at $x \approx 4000$ m and $x \approx 6000$ m (ellipses labeled as 2nd) and a third one at $x \approx 2900$ m and $x \approx 7100$ m (ellipses labeled as 3rd). The following sections investigate the question why the seismic wave-field laterally changes its spectral amplitude distribution as shown in Fig. C.1. Several hypotheses are considered as possible explanations. The true explanation is deduced by eliminating one by one all the incorrect hypotheses.

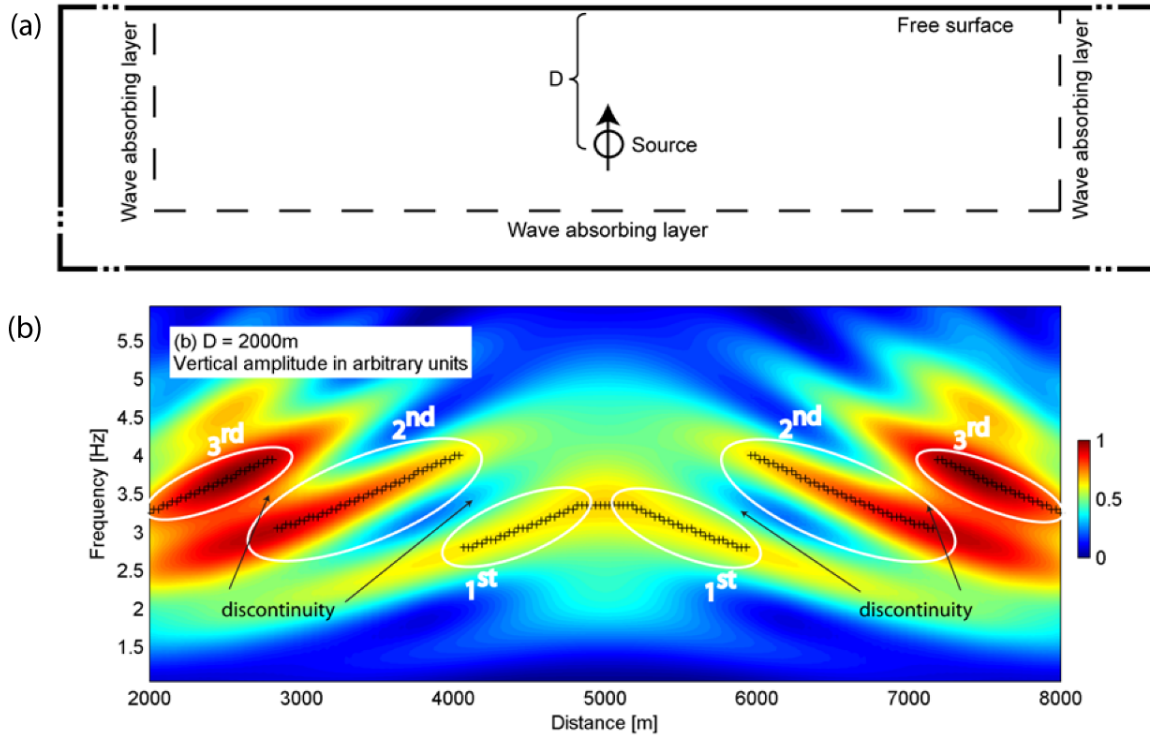


Figure C.1. (a) Sketch of the numerical model and (b) spatial spectrogram for the vertical component of the recorded particle motion at the free surface. The black crosses highlight the peak-frequency shift pattern.

C.2 EXPLANATION

C.2.1. Hypothesis 1: Numerical artefacts

The question is whether or not the lateral peak-frequency shift might be caused by artefacts created by the numerical code, such as numerical dispersion, reflections from the domain boundaries or inaccurate implementation of the free surface. Fig. C.2a-c compares FD simulations with different resolutions. Snapshot of the simulations after 3 seconds are displayed on the left hand side. The corresponding spatial spectrograms for the vertical component of the wave field at the surface is displayed on the right hand side. The model in Fig. C.2a has a low resolution (334x168 gridpoints), the model in Fig. C.2b has an intermediate resolution (1001x1001 gridpoints) and the model in Fig. C.2d has a high resolution (2001x1001 gridpoints). The grid-cells of the models in Fig. C.2a and C.2c are quadratic, while for Fig. C.2b the grid-cell is rectangular with an aspect ratio of 2:1. All other parameters are the same as for the model shown in Fig. C.1. Only slight differences in the spectrograms from the various models can be observed. The badly resolved simulation yields generally stronger amplitudes vertically above the source compared to the other two simulations. However, all the results clearly exhibit the frequency-shift pattern.

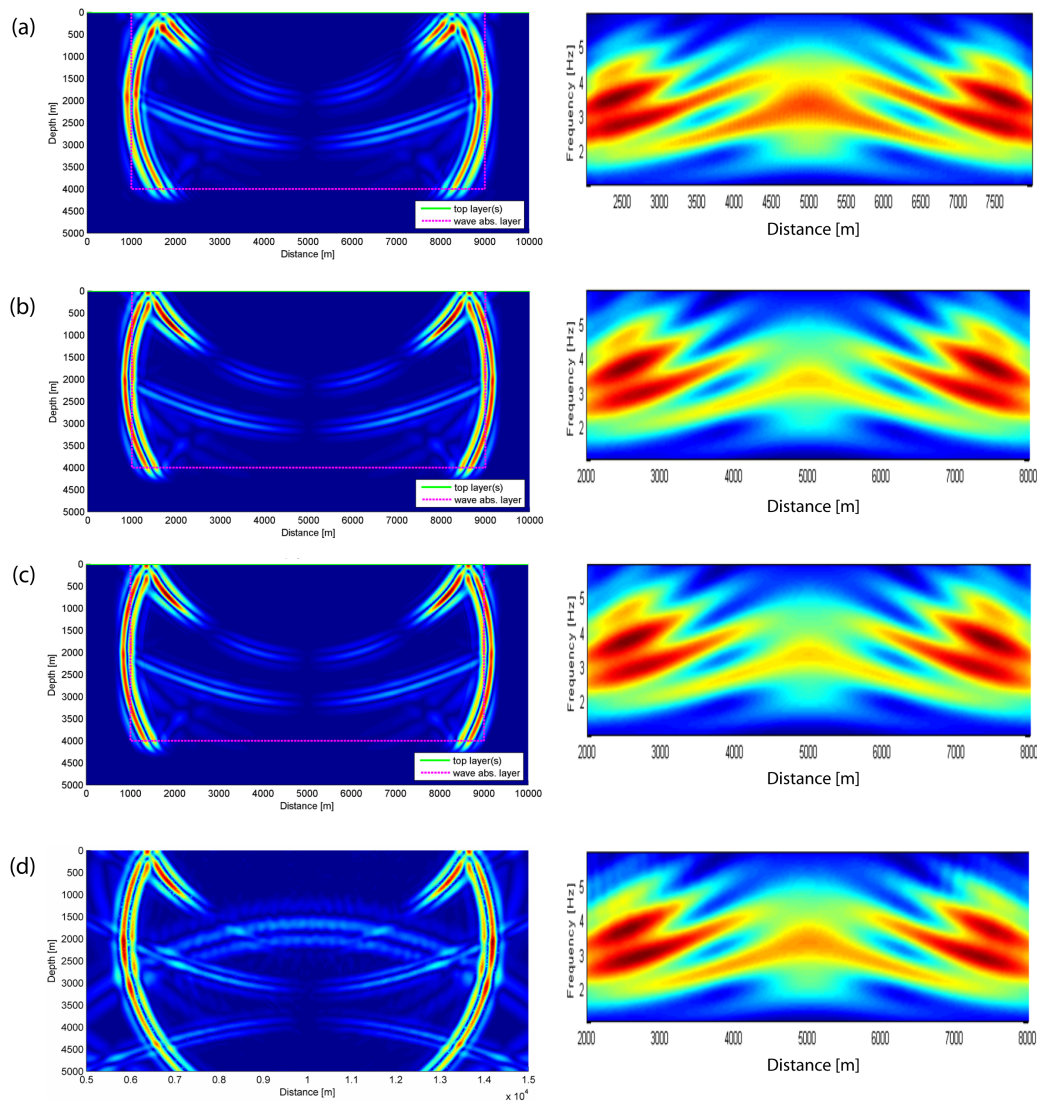


Figure C.2. Snapshots of the simulations after 3 seconds (left) and corresponding spatial spectrograms of the vertical particle velocity at the surface (right). (a) FD model with low resolution. (b) FD model with intermediate resolution. (c) FD model with high resolution. (d) FE model. All simulations exhibit the characteristic peak-frequency shift pattern.

Fig. C.2d shows the same model, but this time solved with a finite element (FE) code using implicit time integration where the free surface condition is automatically satisfied by the so-called natural boundary condition (Frehner et al., 2008). This model does not include non-reflecting boundaries which explains the reflected phases from the bottom of the model domain in the snapshot of Fig. C.2d. Only the signals before the arrival of the first bottom-reflection were used to compute the spatial spectrogram shown in Fig. C.2d. However, also this data clearly reveals the characteristic frequency-shift pattern.

Based on the observations presented in Figure C.2, numerical artefacts due to insufficient resolution or badly implemented boundary conditions can be ruled out as an explanation for the frequency-shift pattern.

C.2.2. Hypothesis 2: Effects of the free surface

Figure C.3a shows the frequency-shift pattern measured along the free surface of the model domain. The source is in this model located at $x=3500$ m (at the very left of the figure) and due to the symmetry of the problem only the right hand half of the receiver line is shown. Figure C.3b shows a similar spatial spectrogram, but computed for a horizontal receiver line below the source location (same distance from the source as the receiver line at the free surface). The lateral peak-frequency shift pattern also occurs on the receiver line below the source although it lies fully embedded in the homogenous medium. Therefore, effects due to the presence of a free surface can not be responsible for the observed pattern.

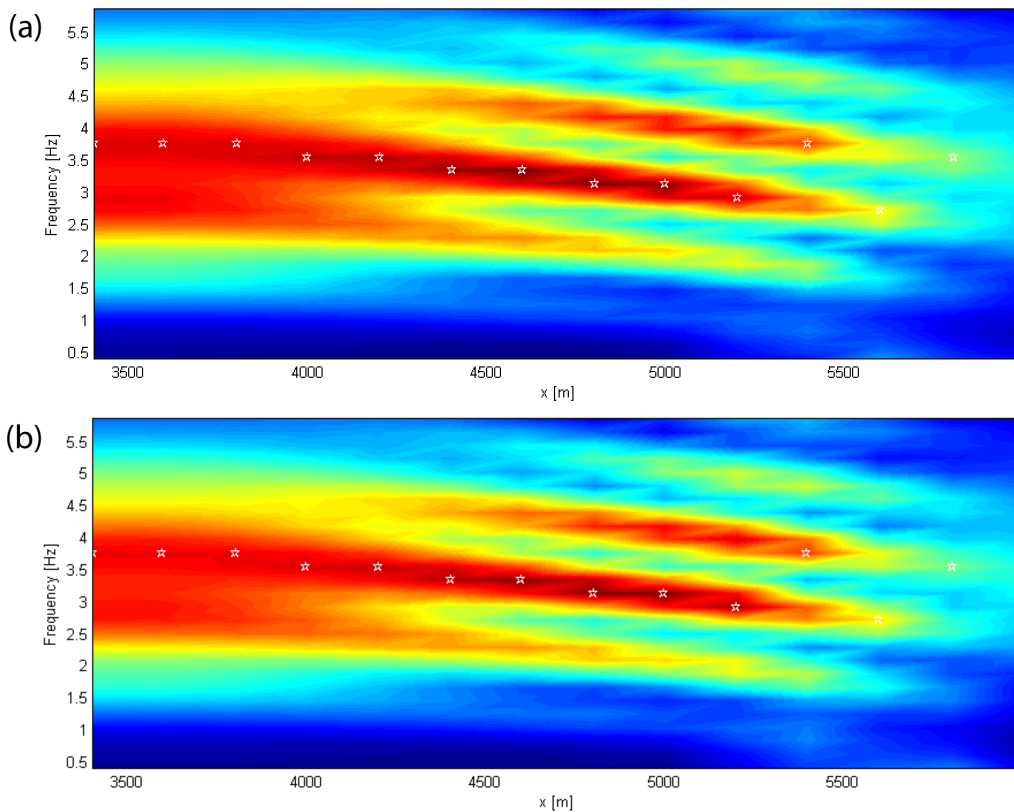


Figure C.3. (a) Frequency-shift pattern along the free surface and (b) along a horizontal receiver line embedded in the medium below the seismic source.

C.2.3. Hypothesis 3: Near-field effects

Another hypothesis states that near-field effects of the seismic source could be relevant to create the frequency-shift pattern. The considered receivers are within a distance from the source of only 2 to 4 times the dominant wave-length of the P-wave and therefore well within the near-field of the seismic source. To test this hypothesis the full mathematical solution of the seismic

wave field for a vertically acting single body force in a homogeneous, isotropic, unbounded medium is considered. The wave-field is analytically described by the corresponding solution for the elastodynamic Green function (Aki & Richards, 2002, p.72). This solution allows to separately calculate the various parts of the radiated wave field, i.e. the far-field P-wave, the far-field S-wave and the near-field terms.

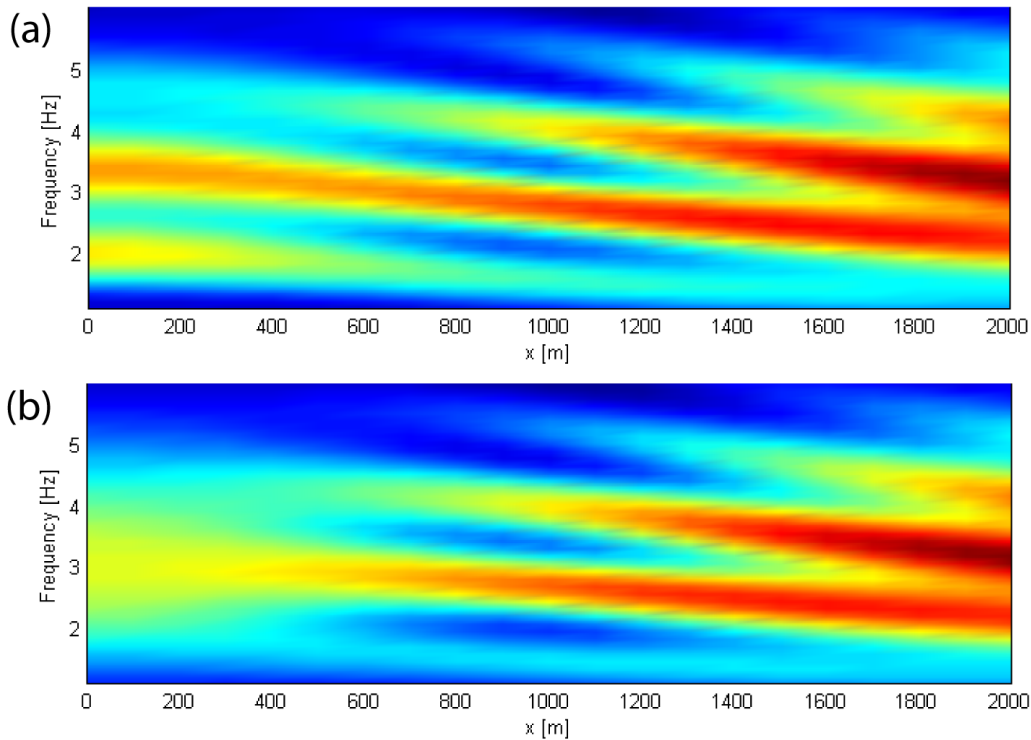


Figure C.4. *Frequency-shift pattern along a horizontal line computed with the analytical solution for a vertically acting body force in a homogeneous medium. (a) Vertical component of the total wave-field. (b) Vertical component of the far-field terms only.*

Figure C.4 compares the spatial spectrogram along a horizontal receiver line for the vertical component of the total seismic field (Fig. C.4a) with the results for only the far-field part (=total field minus near-field terms, Fig. C.4b). Note that the source position is in this case at $x=0$ m and only positive offsets are shown in Fig. C.4 due to the symmetry of the problem. The peak-frequency shift pattern occurs in both cases. This means that the near-field is not the major cause of the observed frequency pattern. However, the near-field terms have a significant influence on the wave field and might be relevant for other applications. For example, near-field effects significantly enhance the amplitudes of the wave field directly above the source (Fig. C.4a). Generally, the analytical solution looks very similar to the results derived from the numerical models (compare Fig. C.2 and Fig. C.4). This supports the earlier conclusion

that neither numerical artefacts nor the free surface are responsible for the frequency-shift phenomenon.

C.2.4. Hypothesis 4: Variation of arrival-time differences

Figure C.5 compares the spatial spectrogram of the wave-field at the surface produced by a FD model with a single vertical body force (Fig. C.5a) with the one produced by a single, isotropic explosion source (Fig. C.5b). The seismic sources in these models are located at $x=3500$ m. The isotropic source produces only one P-wave phase that radiates isotropically, as a circular wave, into all directions. The frequency-shift pattern is not generated by the explosion source. Small peak-frequency variations (stars in Fig. C.5b) are explained by numerical noise. Figure C.6 shows the spatial spectrogram of the far-field P-wave (Fig. C.6a) and the far-field S-wave (Fig. C.6b) along a horizontal receiver line, computed from the analytical solution for a single body force in an unbounded medium (see section C.2.3). Both wave-field parts only contain one seismic phase and don't show the frequency-shift pattern in their spatial spectrogram. These observations suggest that, for creating the frequency shift pattern, it is essential to record at least two seismic phases with different arrival times at the receivers.

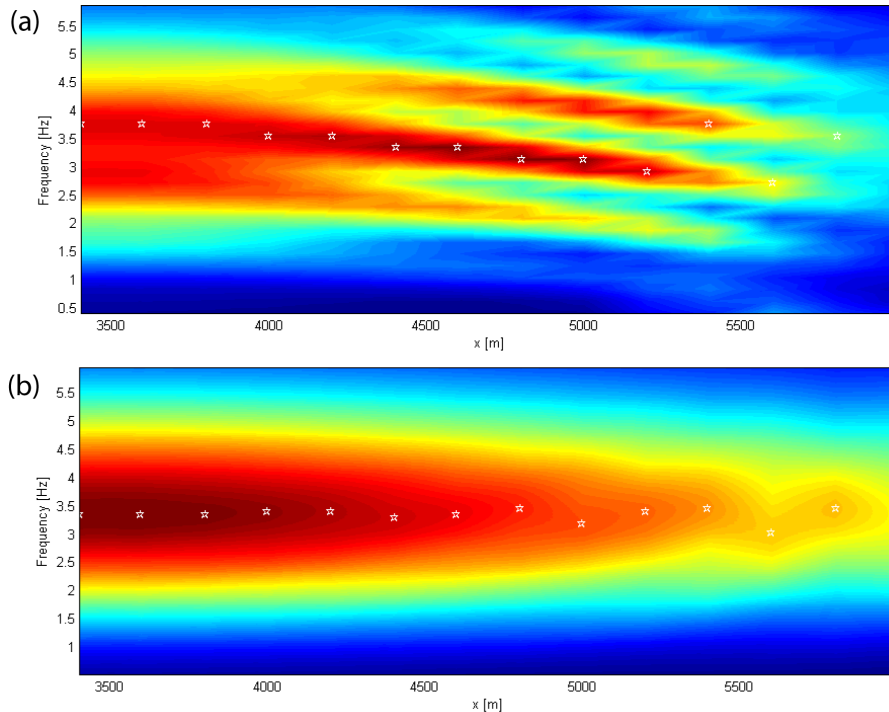


Figure C.5. *Frequency-shift pattern along the free surface of the FD model for different seismic sources. (a) Single, vertically acting body force. (b) Single, isotropic P-wave source (explosion). The peak-frequency shift does not occur in the case of a single, isotropic source.*

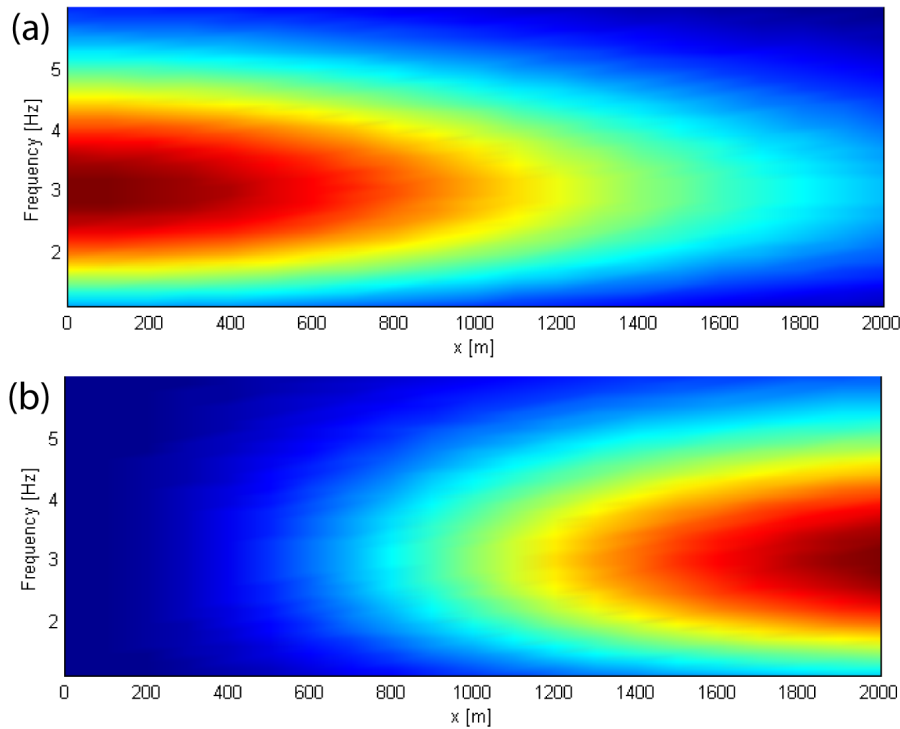


Figure C.6. *Spatial spectrogram along a horizontal line computed with the analytical solution for a vertically acting body force in a homogeneous medium. (a) Vertical component of the far-field P-wave phase. (b) Vertical component of the far-field S-wave phase. The peak-frequency shift pattern does not occur.*

Figure C.7 shows the seismic section used to compute the spatial spectrogram in Fig. C.4a. These are the waveforms of the vertical component of the total wave-field computed by the analytical solution for the single body force in a homogenous, unbounded medium. The P- and S-wave arrivals are clearly visible as two separate hyperbolas with different aperture according to the different P- and S-wave velocity. The arrival-time difference between P- and S-wave increases with increasing distance from the source. Note that this total wave field clearly exhibits the frequency shift pattern as shown in Fig. C.4a.

The following section shows that in fact the lateral change in arrival-time difference between the two phases (P- and S-wave) is responsible for the observed lateral peak-frequency shift pattern. For that purpose, the amplitude spectra of different time-signals consisting of two Ricker wavelets are compared. The wavelets are separated in time by a different time-lag for each signal. For example, Fig. C.8a shows two Ricker wavelets with a time-lag of 0 seconds. This means the two wavelets add up to one single wavelet with again the shape of a Ricker but with twice as large amplitude (Fig. C.8a, left hand side). The corresponding amplitude spectrum looks similar to a lognormal distribution (Fig. C.8a, right hand side). Figure C.8b (left hand side) shows two Ricker wavelets with a time lag of 10 seconds. The corresponding amplitude spectrum has the shape of a lognormal distribution (similar to the amplitude spectrum of

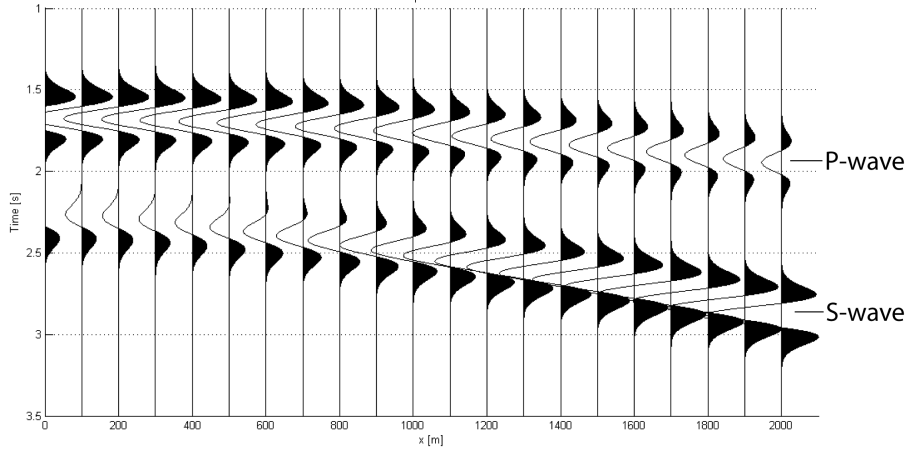


Figure C.7. *Seismic section along a horizontal line computed with the analytical solution for a vertically acting body force in a homogeneous medium. The waveforms show the vertical component of the total wave-field (far-field and near-field; P-wave and S-wave).*

the single wavelet) but overprinted with periodic peaks and notches (Fig. C.8b, right hand side). This alternating pattern of peaks and notches is a well known phenomenon caused by the presence of multiple wavelets in the time signal (Yilmaz, 1987). In signal processing this phenomenon is often referred to as comb filter effect or in acoustics as flanging effect. The greater the wavelet separation in time, the larger the number of peaks and notches in the amplitude spectrum. This is shown in Figure C.8c for two Rickers with a lag of 20 seconds. Picking the frequency of the largest peak for each of the amplitude spectra in Fig. C.8 reveals that the peak-frequency values decrease continuously from spectrum C.8a to C.8b and C.8c. Therefore one can say that the time-lag introduced in Fig. C.8b and C.8c leads to a decrease of the peak-frequency. This effect finally is the explanation for the lateral peak-frequency shift pattern observed for the analytically computed wave field in Fig. C.4 and also for the frequency-shift patterns observed in the numerical results.

Another interesting question is why such periodic peaks and notches are introduced in the amplitude spectra of time-signals that consist of more than only one wavelet. The convolution theorem states that if $g(t)$ and $h(t)$ are functions with Fourier transforms $G(\omega)$ and $H(\omega)$ respectively, then the Fourier transform of their convolution $F(\omega)$ is given by the product of the Fourier transforms $G(\omega)$ and $H(\omega)$:

$$F(\omega) = \sqrt{2\pi}G(\omega)H(\omega), \quad (\text{C.1})$$

where the convolution is defined as

$$f(t) = g(t) * h(t) = \int_{-\infty}^{\infty} g(\tau)h(t - \tau)d\tau. \quad (\text{C.2})$$

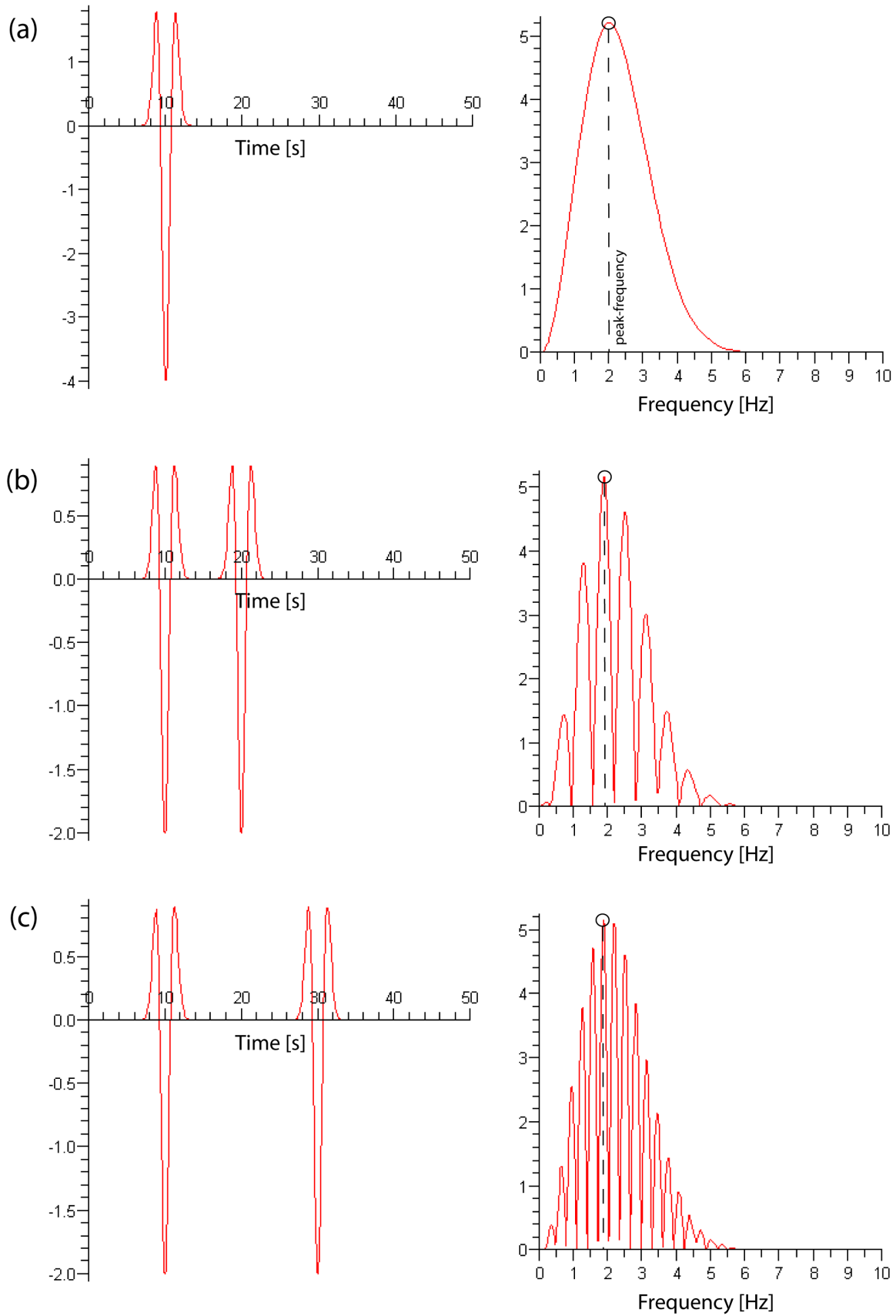


Figure C.8. Ricker wavelets (left) and their corresponding amplitude spectra (right). (a) Superposition of two wavelets centered at $t=10$ s. (b) Superposition of two wavelets centered at $t=10$ s and $t=20$ s, respectively. (c) Superposition of two wavelets centered at $t=10$ s and $t=30$ s, respectively.

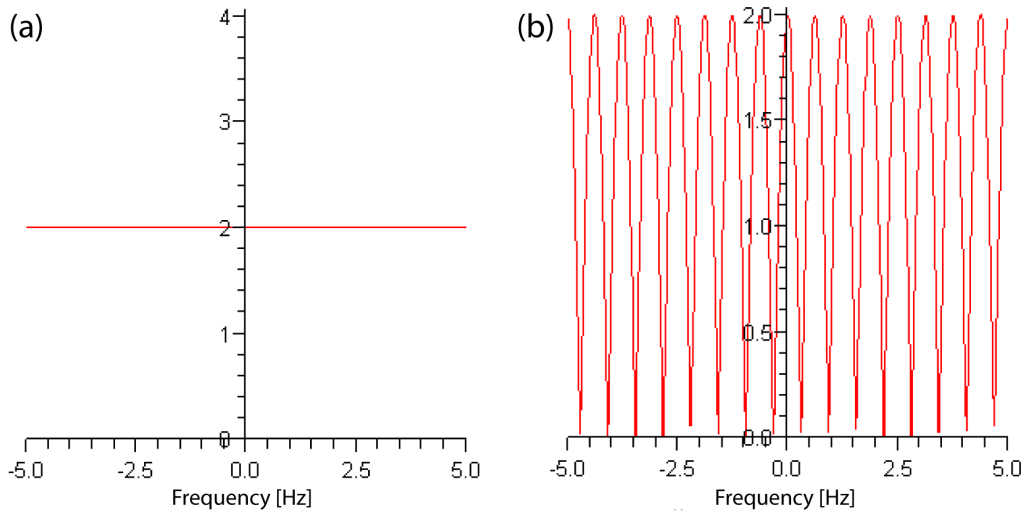


Figure C.9. (a) Amplitude spectrum of one single Dirac pulse. (b) Amplitude spectrum of two Dirac pulses with time lag $\Delta t = 10$ s.

Two Ricker wavelets with a certain time-lag Δt can be represented as the convolution of only one Ricker wavelet with a function that describes two Dirac pulses with time-lag Δt . Therefore, the Fourier transform of the two wavelets is given as the product of the Fourier transform of one Ricker (shown in Fig. C.8a, right hand side) and the Fourier transform of two Dirac pulses with time-lag Δt (shown in Fig. C.9b). This product has the form of a lognormal-distribution, overprinted by peaks and notches due to the shape of the Fourier transform of two Diracs. This is in agreement with the spectra shown in Figs. C.8b and C.8c. The number of peaks and notches increases the larger the time-lag between the two Dirac pulses.

For one single Ricker wavelet, the convolution function consists of only one Dirac pulse. The amplitude spectrum of one single Dirac is white (same value for each frequency) as shown in Fig. C.9a. Therefore, computing the product of the two amplitude spectra yields a spectrum as shown in Fig. C.8a.

C.3 CONCLUSIONS

A peak-frequency shift pattern as shown in Figs. C.1b is mainly controlled by the lateral change of the arrival-time difference between P- and S-wave arrivals. Such a change in arrival-time difference occurs because of the different propagation speed of P- and S-waves. Therefore it can only be generated by a source with a preferred directionality (emitting P- and S-waves). As shown in section C.2.4, an isotropic P-wave source (explosion) does not produce such a pattern. A comparison with the analytical solution for a homogenous, isotropic, unbounded medium indicates that near-field effects and the presence of a free surface only play a minor role. This theoretical study shows that seismic signals emitted by a subsurface source can generate characteristic spectral patterns along the free surface. Numerical artifacts could be

excluded as a possible explanation by cross-checking the results with a finite element code using implicit time integration where the free surface condition is automatically satisfied by the natural boundary condition. Also, the full analytical solution for an unbounded medium leads to similar conclusions.

References

- Aki, K. & Richards, P. (2002). *Quantitative Seismology (2nd edition)*. University Science Books. ISBN 0-935702-96-2.
- Cerjan, C., Kosloff, D., Kosloff, R. & Reshef, M. (1985). *A nonreflecting boundary condition for discrete acoustic and elastic wave equations*. *Geophysics*, **50**, 705–708.
- Frehner, M., Schmalholz, S., Saenger, E. & Steeb, H. (2008). *Comparison of finite difference and finite element methods for simulating two-dimensional scattering of elastic waves*. *Physics of the Earth and Planetary Interiors*, **168**. doi:10.1016/j.pepi.2008.07.003.
- Saenger, E. H., Gold, N. & Shapiro, S. A. (2000). *Modeling the propagation of elastic waves using a modified finite-difference grid*. *Wave Motion*, **31**, 77–92.
- Virieux, J. (1986). *P-SV-wave propagation in heterogeneous media: Velocity-stress finite-difference method*. *Geophysics*, **51**, 889–901.
- Yilmaz, O. (1987). *Seismic Data Processing, Volume 2*. SEG. ISBN 0931830400.

Acknowledgements

This thesis was written at the Structural Geology and Tectonics (SGT) group at ETH Zurich within the framework of a research project funded by Spectraseis, Zurich, and the Swiss Confederation's innovation promotion agency (KTI/CTI). Only due to the generous effort of many people in these three organizations it was possible to complete this work.

I was truly lucky to have such a motivated and committed supervisor like Stefan. His contagious enthusiasm helped me keep going whenever the going got tough. I could count on his support at any time and we spent many good moments at Friday beer and/or Safari bar. Of course, it is impossible to compete with a Bavarian when it comes to beer, but at least I gave my best. Thanks for being a great supervisor over the last four years. A very big 'thank you' also goes to Jean-Pierre, my official "Doktorvater". Although he was not directly involved in my work, I know that many things became possible only because of him.

I wish to thank Erik, for the great collaboration. He took the time to listen to me, trying to understand my (weird??) ideas. This made him the perfect translator between Stefan and me. I am grateful you presented our work at conferences I couldn't attend myself. I also profited a lot from Tungs technical expertise and I very much enjoyed learning more about Vietnamese culture and food. Wish you all the best back in Vietnam or wherever you go. I would like to thank Serge Shapiro for accepting being my external co-referee.

Brian, Beatriz and Marcel are the three fellow PhD students that shared the office with me during most of the time. But we were more than just office mates. We formed a strong team and spent good and bad times together, also outside office hours. Thank you, Brian, for the reliable collaboration and of course for the FD code. Beatriz, I very much enjoyed the regular coffee breaks with you, chatting especially (but not exclusively) about non work-related issues. Thank you, Marcel, for bringing the young, fresh touch into our group and for your open and direct nature. I enjoyed witnessing how an open-air festival is being organized... Thank you all for becoming friends over the past years.

Then, I want to thank the members and former members of the SGT group and associated fellows, namely Ali, Ashgar, Barbara, Claudio, Elie, Ingrid, Liza, Luigi, Maria, Neil, Regula, Santanu, Sarah, Weronika, Yoli (yes, I do like the pasta mensa!) and Yuri. I would also like to thank Spectraseis for the collaboration, and in particular Alex, Brad, David, Fernando, Frank, Martin, Mathieu, Nima, Patrik, Reda, Reto, Rene, Rob, Rodolphe, Ross, Sabrina, Tian. I thank

my colleagues from the master studies (now good "old" friends), Ueli, Joeggu and Saemi. They are co-responsible for me ending up as a geophysicist.

I am thankful to my family, in particular to my parents Annemarie and Guy and my sister Chantal. They always supported my studies and I know I can count on them whatever will happen. Finally I thank you, Mariene, for encouraging and loving me. At the same time you gave me enough space to focus on my thesis, especially in the tough final phase. It was a great help and motivation for me seeing you finishing your PhD one year ago. Besiitos.

Marc-André Lambert

Person

Name	Marc-André Lambert
Birth date	27 th November 1976
Place of origin	Vernier, Switzerland
Nationality	Swiss

Studies & Education

04/2006 - present	PhD at Geological Institute of ETH Zurich, Switzerland Thesis title: “Characterization of ambient ground-motion using spectral analysis techniques - numerical modeling, data processing and application to low-frequency passive seismic” (funded by Swiss Commission of Technology and Innovation, CTI)
10/1997 – 10/2002	Studies of Earth Sciences at ETH Zurich, Switzerland Major subject in Applied & Environmental Geophysics Minor subjects in Seismology, Geomagnetism & Geodynamics, Glaciology
08/1992 – 07/1996	Swiss Matura Type C (university-entrance diploma), Kantonsschule Baden, Switzerland

Work Experience

07/2004 – 03/2006	Data Analyst, Spectraseis AG, Zurich, Switzerland
11/2003 – 03/2006	Research Assistant, Swiss Seismological Service, Zurich, Switzerland
12/2002 - 03/2003	Research Assistant, Institute of Geophysics, ETH Zurich